



InFoMM
Industrially Focused
Mathematical Modelling



Engineering and
Physical Sciences
Research Council

Boston Scientific

Modelling laser-induced vapour bubbles for lithotripsy treatment of kidney stones

---

Sophie Abrahams
sophie.abrahams@maths.ox.ac.uk
Christ Church

October 2023

Supervisors:

Prof. Sarah Waters	Oxford
Prof. Derek Moulton	Oxford
Prof. Robin Cleveland	Oxford
Dr Aditi Ray	Boston Scientific

A thesis submitted for the degree of
Doctor of Philosophy
as part of the centre for doctoral training in
Industrially Focused Mathematical Modelling.

Acknowledgements

Many thanks go to my team of academic supervisors — Sarah Waters, Derek Moulton, Robin Cleveland and Jessica Williams — for their guidance, support and advice over the last four years. It was greatly beneficial to have the diverse knowledge and perspectives that you brought. Thanks also to Ben Turney for providing insight into the application of kidney stone treatment. I am particularly grateful to Bing Yang for the time and energy spent conducting experiments to support my work.

Thank you to my industrial collaborator Boston Scientific who proposed the research topic. Particular thanks to Aditi Ray for allowing the freedom to take the project in my own direction while gently ensuring industrial relevance, and to Jessica Williams for the ongoing input and for the hospitality while in Marlborough.

Special thanks must be given to all of those behind the InFoMM CDT, most importantly, directors Chris Breward and Colin Please. My research project and industrial collaboration with Boston Scientific would not have existed without your hard work. As part of InFoMM, I have been given a range of invaluable skills, both mathematical and otherwise, that will benefit me throughout my career. To my fellow InFoMM students, especially cohort 6, thanks for being great colleagues and friends — my time at Oxford has been very enjoyable thanks to you all.

For encouraging me to pursue mathematics as a second undergraduate degree and then to DPhil level, thank you to my parents, Penny and David. A huge thank you also for the ongoing list of things that you've helped with or given me over the years.

And finally, the last four years as a DPhil student would have been much harder and less fun without my lovely partner Mat. Thank you for cooking and cleaning when I've been too busy and for making sure I take breaks and holidays. Let's hope the next four years are even better!

Abstract

Laser lithotripsy, a common treatment for kidney stones, involves passing a flexible scope containing a laser fibre into the kidney via the bladder and ureter. Within the kidney, laser pulses are fired at the stone to break it into pieces small enough to flush out. During the procedure, laser energy is also transferred to the surrounding liquid, resulting in localised boiling and the production of vapour bubbles. While bubbles can have undesirable effects – for example, causing retropulsion of the stone – they can also be utilised to make stone ablation more efficient. The aim of this work is to contribute to improving the speed and ease of laser lithotripsy kidney stone treatment via mathematical modelling, focusing on the vapour bubbles that form during the treatment.

The size, shape and duration of a laser-induced bubble is dependent on the total energy of the laser pulse and the way in which this energy is temporally distributed. The time dependent power profile of the pulse is referred to as 'pulse shape' and can be manipulated to produce bubbles with desirable properties. Using two different modelling approaches, we predict properties of the bubble as a function of the pulse shape, as well as understanding the physics driving bubble expansion. Previous models of laser-induced bubbles assume the energy transfer from the laser to the fluid to be instantaneous, which is not a good approximation for the ~ 100 µs pulses employed in lithotripsy. To reflect the effect that the laser parameters have on the bubble size, shape and duration, we model the laser as a time and space dependent source of energy in the liquid-vapour fluid system.

Our first model considers the simplified case of a single, spherical vapour bubble in liquid, with phase change at the bubble wall. With this model, we build upon an existing method of coupling the Rayleigh-Plesset equation to an energy equation in the surrounding liquid and an energy flux balance at the bubble wall. Mathematical analysis of the governing equations reveals the physical effects occurring at three stages of bubble expansion and the time-scales at which these stages occur. We then examine the effect on the bubble of varying pulse power, pulse duration, and total pulse energy.

A second modelling approach tackles the challenging problem of breaking spherical symmetry in bubble modelling by utilising the 'volume of fluid' method on an axisymmetric domain. With localised phase change due to laser heating, we are able to reflect the elongated shapes that occur during laser lithotripsy and study how the proportions of the bubble — length and width — as well as its size and duration are affected by the properties of the pulse. Axisymmetry gives the flexibility to introduce solid boundaries near the bubble and measure the effect this has on both the bubble and the boundary.

Through numerical and analytical methods alongside experimental work we develop an understanding of the physical factors driving bubble expansion and provide a framework to guide the future development and clinical usage of lasers.

Statement of Originality

Chapter 2 presents experimental work conducted in collaboration with DPhil candidate Bing Yang (Nuffield Department of Surgical Sciences, University of Oxford), supported by Professor Robin Cleveland (Department of Engineering Science, University of Oxford) and Professor Ben Turney (Nuffield Department of Surgical Sciences, University of Oxford). This work was carried out as follows:

- The aims of the experiment were specified by Sophie Abrahams, including input setting and output data.
- The experiments were set-up and carried out by Bing Yang.
- Details of the experimental method and equipment were written by Bing Yang and edited by Sophie Abrahams.
- The raw data was converted into a usable format by Sophie Abrahams.
- Edge detection functions in MATLAB were used to extract data from the high speed photography images by Sophie Abrahams.
- Analysis, interpretation and presentation of the data was carried out by Sophie Abrahams.

The remaining chapters contain only the original work of Sophie Abrahams.

Contents

1 Introduction and background **3**

1.1 Ureteroscopy and laser lithotripsy 4

1.2 Motivation 7

1.3 Bubble modelling 8

1.4 Overview 11

2 Experimental studies **13**

2.1 P120 laser pulse shapes 14

2.1.1 Method 14

2.1.2 Results 15

2.2 P120 laser-induced bubble photography 18

2.2.1 Method 18

2.2.2 Results 21

2.3 Conclusion 34

3 Spherical bubble model **37**

3.1 Nomenclature 38

3.2 3D model 39

3.2.1 Generalised two-volume fluid model 39

3.2.2 Two-phase bubble model 44

3.3 1D spherical bubble model 49

3.3.1 Laser energy source term 51

3.3.2 Non-dimensionalisation 53

3.3.3 Model reduction 55

3.3.4 Alternative derivation of vapour pressure equation 62

3.3.5 Model summary and change of variable 63

3.3.6 Initial conditions 64

3.4 Numerical method 67

3.4.1 Method of lines 67

3.4.2 Initial conditions 70

3.4.3 Fitting to experimental data . . . 71
3.4.4 Sensitivity to parameter values . . . 72
3.5 Viscous Effects . . . 73
3.6 Conclusion . . . 75

4 Numerical and analytical studies of spherical bubble model 77
4.1 Nomenclature . . . 78
4.2 Model and data comparison . . . 79
4.3 Stages of expansion . . . 80
4.3.1 Stage 1: acceleration . . . 83
4.3.2 Stage 2: continued laser driven expansion . . . 89
4.3.3 Stage 3: deceleration . . . 93
4.3.4 Discussion . . . 99
4.4 Pulse exploration . . . 99
4.4.1 Varying pulse power . . . 99
4.4.2 Varying pulse duration . . . 100
4.4.3 Varying pulse duration and power . . . 101
4.4.4 Discussion . . . 104
4.5 Conclusion . . . 104

5 Axisymmetric bubble model 107
5.0.1 OpenFOAM . . . 109
5.1 Nomenclature . . . 110
5.2 Model . . . 110
5.2.1 Governing equations . . . 110
5.2.2 Phase change . . . 113
5.2.3 Initial conditions . . . 114
5.2.4 Domain and boundary conditions . . . 115
5.2.5 Laser energy source term . . . 118
5.2.6 Numerical method . . . 121
5.3 Results . . . 122
5.3.1 Fibre-boundary distance . . . 123
5.3.2 Single pulse . . . 130
5.3.3 Pulse packet . . . 135
5.3.4 Pulse packet with boundary . . . 137
5.4 Conclusion . . . 139

6 Conclusion **141**

6.1 Model comparison 144

6.2 Future work 148

References **151**

A Parameter values **159**

Chapter 1

Introduction and background

1.1 Ureteroscopy and laser lithotripsy

The kidneys are two fist-size organs that filter the blood, removing waste and producing urine. From the kidneys, urine passes through the tube-like ureters to the bladder. Kidney stones are mineral deposits, most commonly calcium oxalate, that occur in the ureters or cavities of the kidneys. The production of kidney stones occurs when there is an excess of stone-forming chemicals in the urine, and/or a lack of stone-inhibiting chemicals. Kidney stones can cause acute pain [1] and, as of 2016, 13% of the UK population develop them in their lifetime [2], with a recurrence rate of approximately 50% within ten years [1].

One of the most common treatments for kidney stones is ureteroscopy and laser lithotripsy. Lithotripsy, which literally means 'grinding stone', has been utilised in one form or another in the treatment of kidney stones since as early as the 19th century [3]. For lithotripsy by laser, a ureteroscope — a medical device with a small camera and light at the tip of a long hollow shaft — is passed through the urethra and bladder and into the ureter or kidney to the position of the stone, as in Fig. 1.1.1a. As shown in Fig. 1.1.1b, the ureteroscope contains a hollow working channel in which tools, including an optical fibre, are inserted. To break the stone, the laser fibre tip is placed approximately 1 mm away and laser pulses are fired. The pulses either fragment the stone into smaller chunks that can be retrieved individually or 'dust' it into particles so small they can be flushed out. Throughout the procedure, saline flows to the area of the stone through the working channel and flows out between the scope and an outer access sheath to clear dust and debris. Alternative treatments for kidney stones include shock wave lithotripsy, in which shock waves are produced by a machine externally to the body and are focused to the area of the stone, and percutaneous nephrolithotomy, a form of keyhole surgery by which the stone is broken and removed [1].

Ablation of the kidney stone during laser lithotripsy occurs predominantly due to the transfer of thermal energy to the stone, although the exact mechanisms of stone breaking are not known. Laser energy is delivered as a single laser pulse or as a group of smaller 'micropulses' called a pulse packet [6]. The pulse or packet is repeated a specified number of times per second, called the pulse repetition frequency (PRF). The lasers used in lithotripsy are predominantly Holmium:YAG (Ho:YAG), which emits a wavelength of 2100 nm [7]. For a Ho:YAG laser, each pulse or packet has an energy of 0.2–2.0 J, lasts on the order of 100 µs and has a PRF of 5–80 Hz [7]. Other lasers are being explored for their potential use in kidney stone treatment, for example Thulium which emits wavelength of 1908 nm [7].

The 'pulse shape' is the way in which the power of the laser is modulated over time to create the pulses or pulse packets; illustrative examples of pulse shapes are shown in Fig. 1.1.2. For a given amount of energy, the pulse shape determines the way in which this energy is distributed and is known to affect the way in which the stone breaks [8]. For example, a shorter, higher power pulse produces larger stone fragments and a longer, lower power pulse

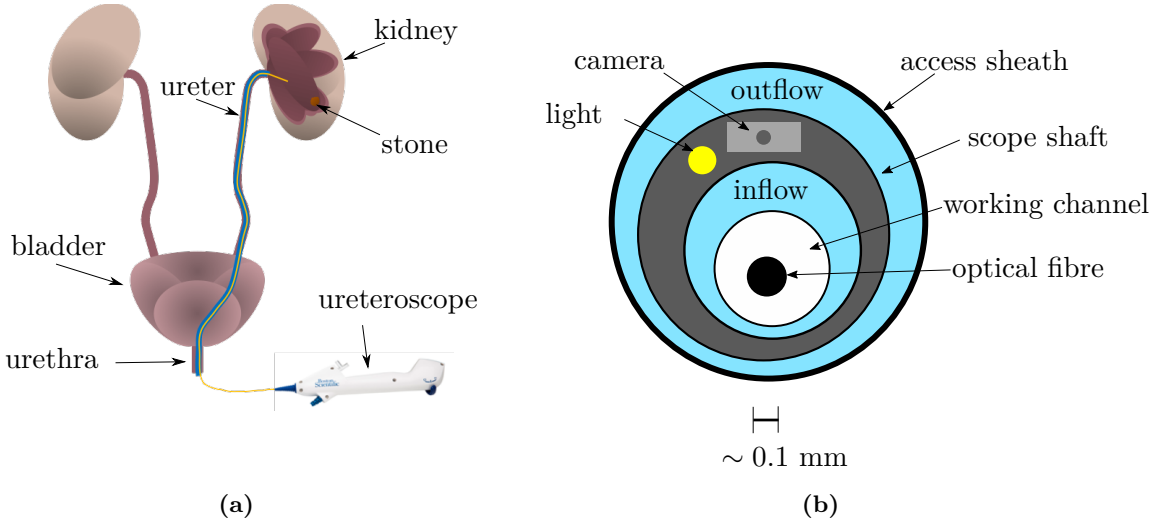


Figure 1.1.1 – (a) A diagram of a ureterescope inserted into the kidney for laser lithotripsy treatment of a kidney stone (not to scale), adapted from an image in [4]. (b) A schematic of the ureteroscope tip, adapted from an image in [5].

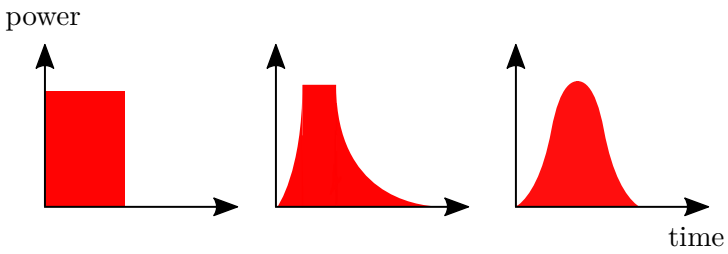


Figure 1.1.2 – An illustrative example of possible shapes — power over time profiles — for a single pulse.

produces smaller, dust-like fragments [8]. Again, the mechanisms causing this varied behaviour are not well understood. The rate, type and ease of stone breaking is also dependent on other factors such as peak laser power, PRF and the number of pulses per packet [8]. Clinical laser systems now offer an increasing choice of laser parameters to allow surgeons more control over the lithotripsy procedure [8, 9].

As the laser is pulsed, not all the energy reaches the stone as some is partially absorbed by the surrounding fluid in the kidney, a mixture of urine and saline from the ureteroscope. The laser energy causes the fluid to heat and boil in a localised region between the fibre and stone. The phase change due to boiling produces vapour bubbles, as shown in Fig. 1.1.3, which can have both beneficial and detrimental effects to the lithotripsy procedure. The primary benefit is considered to be the 'Moses effect' — first exploited by the Lumenis Pulse 120H Holmium Laser System (P120) — which is the phenomenon that laser energy travels significantly further when passing through vapour than when passing through liquid [9, 10]. The Moses effect occurs because the vapour has a negligible absorption rate of laser energy in comparison to the liquid;

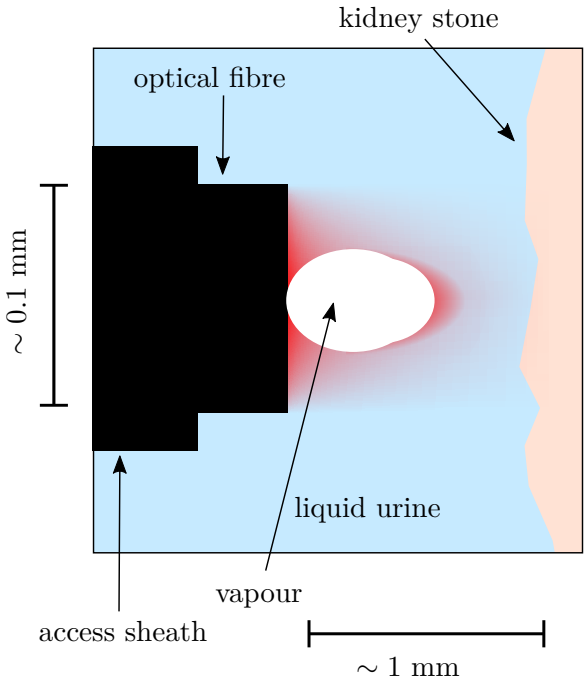


Figure 1.1.3 – A diagram of the laser fibre, stone and vapour bubble within the kidney (not to scale).

for this reason, once a vapour cavity exists between the laser fibre and stone, almost all the laser energy is delivered to the stone [10]. The process of the Moses effect as utilised in laser lithotripsy is depicted in Fig. 1.1.4: 1) the laser pulse begins and an initial amount of energy is taken up in heating the liquid and nucleating a bubble; 2) the bubble expands and laser energy now passes through the vapour, almost without energy loss, heating and vaporising liquid on the far side; 3) if the vapour region becomes large enough to fill the gap between the fibre and stone, laser energy will pass directly to the stone; and 4) the bubble collapses and the process repeats. It is known that the shape of a bubble is determined by the shape of the laser pulse [7]. Most notably, a longer duration pulse creates a more elongated bubble [7]. The pulse shapes and timings can therefore be designed to exploit the Moses effect, for example if an initial pulse is fired that creates a highly elongated bubble, a second pulse can be fired, allowing the energy from the second pulse to travel as far as possible from the fibre [9].

A secondary contribution to stone fragmentation arises from the high pressures generated during bubble expansion [11] and collapse [12]. Damage to a solid surface caused by the production and collapse of bubbles — cavitation damage — is a well documented phenomenon, particularly in relation to underwater machinery [13–15], and it is likely to also play a stone-breaking role in laser lithotripsy. It should be noted that too energetic a collapse may also cause retropulsion — pushing backwards — of the stone, making the process of kidney stone ablation more difficult and time consuming for the surgeon [9].

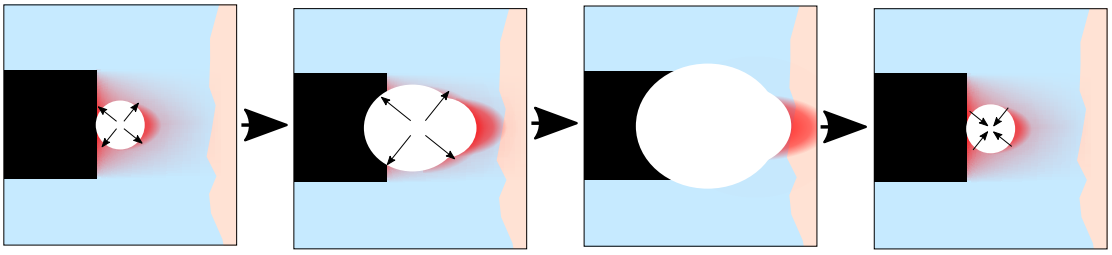


Figure 1.1.4 – A representation of the Moses effect. The process is as follows: 1) the laser pulse begins and an initial amount of energy is taken up in heating the liquid and nucleating a bubble; 2) the bubble expands and laser energy now passes through the vapour, almost without loss, heating and vaporising liquid on the far side; 3) the vapour region becomes big enough to fill the gap between the fibre and stone, and laser energy passes without loss to the stone; and 4) the bubble collapses and the process repeats.

1.2 Motivation

The aim of this work is to contribute to improving the speed and ease of laser lithotripsy kidney stone treatment via mathematical modelling. Although there are many aspects of laser lithotripsy that could be studied and optimised, we focus here on the laser-induced vapour bubbles that form during the treatment. Bubbles are a key part of the energy transfer that occurs between the laser and kidney stone so controlling the bubble dynamics is a necessary part of manipulating the way in which the stone breaks.

The laser parameters and pulse shapes currently used for lithotripsy have largely been determined through experimental methods. Experimental work has already gone some way to understanding the dependence of bubble size, shape and duration on the pulse parameters [7, 16] but mathematical modelling can support and complement experimental work in a number of ways. Firstly, validated models can quickly and cheaply explore the parameter space, reducing the need for experiments. Secondly, quantities such as pressure and temperature fields that are difficult to measure experimentally can be calculated using mathematics. Finally, mathematical analysis of these models can reveal the physical mechanisms underpinning behaviour that is observed experimentally. A deeper understanding of the complicated physics of lithotripsy could be utilised to better design lasers for kidney stone treatment.

A vital step towards control and optimisation of bubbles for lithotripsy is modelling a laser-induced bubble as a function of pulse shape. Through modelling, we aim to predict properties of the bubble, such as size and duration, as well as understanding the physics driving bubble expansion. Introducing solid boundaries near the bubble — for example in the position of a kidney stone — we will consider the impact on the bubble and on the boundary itself by quantifying pressures, velocities and temperatures. Through mathematics, we will develop tools and knowledge to inform the design and use of lasers for lithotripsy.

1.3 Bubble modelling

Multi-phase modelling, of which bubble modelling is a subset, considers flows that consist of two or more different fluids, referred to as 'phases'. Multi-phase models, and consequently bubble models, typically take two approaches: 'interface tracking' and 'interface capturing'. Interface tracking methods consider each phase as a distinct region with their own set of governing equations together with an explicit expression for the position of the boundaries between phases. In contrast, in interface capturing methods all equations hold across the whole domain and a 'phase fraction' gives the proportion of each phase at any location. The locations of boundaries are determined and reconstructed from the phase fraction. 'Phase change' or 'mass transfer', in which one fluid changes into another, can be included in both interface tracking and interface capturing models.

In bubble modelling specifically, behaviour is distinguished between: 1) bubbles containing vapour, originating from a phase change of the liquid; 2) bubbles containing non-condensible gas originating from impurities in the liquid; and 3) bubbles containing a mixture of the two [17]. Ongoing phase change at the bubble wall is a consideration when modelling vapour bubbles, but does not occur with non-condensible gas bubbles. A distinction is also made between bubbles that form due to cavitation and those due to boiling [17]. The term 'boiling' refers to bubbles that occur at higher temperatures where thermal effects, such as latent heat-flow, are significant. The term 'cavitation' usually refers to bubbles that occur at low pressure and at temperatures for which thermal effects are negligible.

In the interface tracking category is the commonly used Rayleigh-Plesset equation, a second-order differential equation in time for the radius of a spherical bubble [18]. This equation originates from a model for an empty or gas-filled bubble, proposed by Lord Rayleigh in 1917 [19]. Rayleigh's model was extended to include the effect of surface tension by Plesset and Zwick [18] to give the widely used Rayleigh-Plesset equation. This equation has been further adapted to include other physical phenomena such as viscosity and compressibility in the liquid surrounding the bubble [20–22]. In general, the nonlinearity of the Rayleigh-Plesset equation means numerical integration is required to determine the bubble radius over time, however analytic solutions have been proposed for special cases [23, 24].

Plesset and Prosperetti [17] coupled the Rayleigh-Plesset equation to a heat equation in the liquid region and a conservation equation for the heat flux at the bubble wall, equating the rate of energy used for phase change to the rate of energy supplied as heat by the liquid. This coupling is employed by others including Flynn [25] and Prosperetti et al. [26], both of which consider the case of acoustically-forced oscillations of a bubble. The equation derived by Prosperetti et al. for the rate of change of pressure within the bubble is similar in form to that which we derive in Chapter 3, however their model applies to a non-condensible gas bubble in cool liquid [26]. This method is again used in the work of Hao and Prosperetti [27],

Akhatov et al. [28], Doinikov et al. [29], and Guedra and Coulouvrat [30], although in some cases the Rayleigh-Plesset equation is replaced with the Keller-Miksis equation to account for liquid compressibility.

Where Rayleigh-Plesset-type models have been applied to laser-induced bubbles, the laser is generally considered to cause bubble nucleation only, effectively modelling the energy input as instantaneous [28, 31, 32]. This assumption neglects not only the time-dependence of the laser heating of the liquid, but also the spatial temperature variations caused by the localised nature of this heating. While an instantaneous pulse may be a reasonable assumption for some purposes, it is not suitable for the ~ 100 µs pulses used in laser lithotripsy, where the modulation of the laser power is known from experimental studies to affect the size, shape and duration of the bubbles [7, 16].

Finding appropriate initial conditions for a laser-induced bubble model is not trivial. The physics of nucleation is complex and it is known that laser radiation in a liquid, in some cases, triggers plasma formation before a vapour bubble appears [33, 34]. In some Rayleigh-Plesset-type models, the initial conditions of the laser-induced bubble are fitted to experimental data [28, 31, 32]. Byun and Kwak employ a separate model for nucleation via plasma formation before moving to a Keller-Miksis-based bubble expansion model [34]. This step is necessary in their case to study the evolution of the pressure shock wave that is initiated during nucleation [34].

Models based on the Rayleigh-Plesset equation are, in most cases, simple in form so can be easily integrated and interpreted. The necessary assumption of spherical symmetry, however, means that there are limitations to the applications of this type of model. Breaking spherical symmetry, but also in the category of interface tracking, is the 1971 work of Plesset and Chapman on the collapse of a bubble against a solid, flat boundary [13]. The collapse of a bubble in a fluid near a solid surface is of interest in many applications, including lithotripsy treatment of kidney stones, due to the formation of a high-speed jet of liquid towards the surface during collapse and the subsequent surface damage, known as cavitation damage. The introduction of a solid boundary near a bubble breaks spherical symmetry and hence increases the difficulty of modelling. Plesset and Chapman simplify the problem by assuming axisymmetry, an initially spherical bubble, and an inviscid, incompressible liquid surrounding the bubble [13].

The problem of a collapsing bubble near a boundary has since been studied using a variety of numerical and experimental methods. Zhang and Duncan [35], Tong [36] and Klaseboer et al. [37] all apply the boundary integral method or boundary element method (BEM), another interface tracking method. The BEM reduces the complexity of the problem by only solving for the evolution of the vapour-liquid boundary [36]. Deviating from interface tracking methods, Blake [38], Blake et al. [39] and Supponen et al. [40] determine quantities associated with the collapse of a bubble against a boundary using a single parameter. Blake uses the Kelvin Impulse, a measure of the inertia of a bubble, to determine the motion of the centre of the bubble during collapse [38], while Blake et al. use the same measure to determine

the direction and speed of the liquid jet [39]. Supponen et al. define an anisotropy parameter, a dimensionless version of the Kelvin Impulse, which is used to determine if the jet formed on collapse is weak (never impacts other side of bubble), intermediate (impacts other side of bubble during last phase of collapse) or strong (impacts bubble early in collapse) [40]. The anisotropy parameter can also be used to predict jet impact time, jet speed, bubble displacement at impact, and bubble volume at impact [40].

The interface capturing approach to multi-phase modelling has no limitations in terms of geometry and bubble shape. However, interface capturing models can be complicated and require intensive numerical methods of solution. In this category is a strand of bubble modelling that stems from Drew's 1983 model for a two phase flow which consists of seven equations — conservation of mass, momentum and energy for each phase plus an equation for the evolution of the phase fraction — to which averaging is applied to give a macroscopic picture [41]. Saurel and Abgrall developed the work of Drew, introducing compressibility but reducing the complexity by assuming a short pressure relaxation time [42]. Heat and mass transfer between phases were introduced by Zein et al. but with the simplification that both phases share the same velocity field, to give a six equation model [43]. A nine equation model was also given by Zein et al. for the case of three fluid phases: liquid, gas and vapour [44]. Zein et al. applied the six equation model, both with and without the inclusion of phase change, to the case of the collapse and rebound of a laser-induced vapour bubble, giving very good agreement to experimental data [43].

The volume of fluid (VOF) method is another strand of interface capturing modelling, in which the fluids are assumed to be immiscible. This method is characterised by solving one set of equations across all fluid phases, on a domain discretised into cells [45–47]. Since the fluids are immiscible, only one is present at any location, therefore only one value of pressure, temperature and velocity exist at any location [45–47]. The interface between phases is determined by locating the cells partly filled by different fluids; in these cells a volume average of each field value is obtained [47]. The VOF approach is therefore simpler than that of Drew and Zein et al. in which the fluids can be miscible and each has a separate pressure, temperature and velocity field. [41, 43]. The VOF method has been applied to bubble modelling, in many cases via the open source computational fluids package OpenFOAM [46, 48, 49]. The papers of Nabil and Rattner [46] and Shi et al. [49] are of particular interest as they model bubbles occurring due to localised heating and boiling, in both cases at a heated wall.

As with Rayleigh-Plesset-type models, when interface capturing models are applied to laser-induced bubbles, the laser is generally considered only to cause bubble nucleation and does not influence the bubble dynamics after this point [44, 50–54]. Some models further simplify the problem by neglecting mass flux between the bubble and surrounding liquid [52, 54] while others overlook bubble expansion, focusing instead on collapse and rebound [44, 50, 51, 53].

A 2023 preprint by Zhao et al. is the only known model of laser-induced bubbles that considers both expansion and collapse and includes the spatiotemporal nature of the laser

heating [55]. Their model uses an interface capturing method of multi-phase modelling called the level-set method [55]. This method uses a signed distance function that measures distance from the phase boundary such that the value of the function is zero on the interface, positive in the liquid and negative in the vapour. Zhao et al. simulate the different conditions that create the so-called 'pear shaped' and 'elongated' bubble shapes, validating the results against experiments [55]. The work of Zhao et al. shows a promising alternative route, using a method not utilised in this thesis, for modelling laser-induced bubbles for the optimisation of lithotripsy kidney stone treatment.

1.4 Overview

We begin this thesis with a presentation of two experiments in Chapter 2, conducted to motivate and validate the mathematical work that follows. The first experiment records the shape of the pulses produced by the Pulse 120H Ho:YAG (P120) laser system, a commonly used laser system in kidney stone lithotripsy. The second experiment records the bubbles produced by the same pulses: via high speed photography we extract data about the bubble including the change in volume over time. Together, the two experiments give information about the effect of the laser parameters on bubble dynamics. Most importantly, the experimental data is used to fit and validate the mathematical models.

In the remaining chapters, two mathematical models of laser-induced bubbles are presented, employing some of the methods described in Sec. 1.3. In both cases, the bubble is modelled as a region of pure water vapour within a region of liquid water, with bubble dynamics studied as a function of pulse shape. Our first model, presented in Chapter 3, uses an interface tracking method for the case of a spherically symmetric bubble. General equations are derived in 3D then reduced to 1D with the assumption of spherical symmetry, such that the position of the vapour-liquid interface is determined just by the bubble radius. With a further reduction under the assumption of spatially uniform pressure and temperature within the bubble, we arrive at the Rayleigh-Plesset equation coupled to three further differential equations. These three additional equations model: an energy flux balance at the bubble wall; conservation of energy in the liquid; and the relationship between pressure and temperature within the bubble. The uniform conditions within the bubble mean that spatial variations only occur in the liquid region, allowing a simple change of variable to convert the moving liquid domain to a fixed domain. A quick and straightforward numerical method of solution is possible on this fixed domain.

A numerical and mathematical analysis of the spherical model is given in Chapter 4. We begin with a comparison to the experimental data from Chapter 2, from which we determine the regime in which the spherical model gives reasonable predictions. The governing equations and numerical solutions are then probed to determine the physical effects occurring at three stages

of bubble expansion and the time-scales at which these stages occur. This type of mathematical analysis is novel in the application to laser-induced bubbles. Finally, the model is used to predict the bubble size and duration as parameters of the pulse are varied. In particular, we examine the effect of varying pulse power, pulse duration, and total pulse energy.

Breaking the spherical symmetry, a second model is presented in Chapter 5, using the interface capturing VOF method. Our model is closely related to those of Nabil and Rattner [46] and Shi et al. [49]. Using an axisymmetric domain, this method and geometry allows more freedom than the spherical model in the shape of the bubble and gives us the flexibility to introduce solid boundaries, for example, in the positions of the laser fibre and stone. This model does not rely on the assumption of spatially uniform pressure and temperature within the bubble, as in the spherical model, but does have other simplifications. We outline the governing equations and the method of solution using the computational fluid dynamics package OpenFOAM. A number of simulation are carried out under different conditions to show the potential of VOF modelling for laser-induced bubbles and lithotripsy. With the axisymmetric model, the simulations reflect the elongated shape of the bubbles seen experimentally, and we explore how the bubble length and width vary with pulse shape. Introducing a solid boundary perpendicular to the laser fibre, in the position of a kidney stone, we measure the temperatures, pressures and velocities generated at the boundary under different conditions.

The application in this thesis is identical to that of Zhao et al. and their model has many similarities to that presented in Chapter 5. We both make the obvious choice to work in an axisymmetric geometry. We both consider ongoing phase change throughout the expansion and collapse of a bubble, not only during nucleation, recognising the importance of this time dependent phase change to recover the elongated bubble shape seen in lithotripsy. We derive similar governing equations to those of Zhao et al. aside from the method of reconstructing the liquid-vapour interface; as described in Section 1.3, Zhao et al. use the level-set method whereas we choose the VOF method. The VOF method is a convenient choice as it is already implemented in some inbuilt solvers in OpenFOAM, and being open-source software, it is possible to adapt solvers for this present work and for future development. However, the work of Zhao et al. shows a promising alternative route for modelling laser-induced bubbles for the optimisation of lithotripsy kidney stone treatment.

In both models, the laser acts as a source of thermal energy in the liquid region and, unlike the existing literature on laser-induced bubbles, we require the effect of the laser to be considered past the point of bubble nucleation. For this reason, the laser heating of the liquid in our models is both time and space dependent, adding considerable complexity to the models. Time and space dependent heating is novel in a Rayleigh-Plesset based model. Localised heating has been modelled using VOF methods, for example at a heated wall, but has not been applied to laser induced bubbles.

Chapter 2

Experimental studies

To complement and validate the mathematical work presented in the following chapters, two experiments were conducted to: 1) record the power-over-time profiles of the laser pulses used in the lithotripsy treatment of kidney stones, and 2) capture the dynamics of the vapour bubbles induced by these pulses. The experiments were undertaken by colleagues in the Nuffield Department of Surgical Sciences, University of Oxford. Preparation, analysis and presentation of the experimental data was completed by the author and contributes to the original work of this thesis.

Experiments were conducted with a Pulse 120H Ho:YAG (P120) laser system (Lumenis, Israel) coupled to a compatible 230 µm diameter laser fibre (Moses 200 D/F/L, Lumenis, Israel). This laser system and fibre combination was chosen as it is commonly used in laser lithotripsy. The P120 emits pulses in two modes: single pulse and 'Moses' double pulse. In the first case, a single pulse is emitted at a specified pulse repetition frequency (PRF), with the choice of a 'short', 'medium' or 'long' pulse. In the Moses mode, two pulses are emitted in quick succession, with this double pulse repeated at the specified PRF. Two Moses settings are available, 'Moses Contact' (MC) which is designed to be used with the fibre tip less than 1 mm from the stone, and 'Moses Distance' (MD) which is designed to be used at distances of around 2 mm [56]. Measurements of all five pulse types — short, medium, long, MC and MD — were taken at set energies from 0.2 J to 2.0 J. The bubbles produced by each pulse type and energy were captured by high speed photography.

2.1 P120 laser pulse shapes

2.1.1 Method

The temporal power profiles of the laser pulses — referred to as the pulse 'shape' — were measured using a photodetector (PDA10T, Thorlabs, NJ, USA), with bandwidth set to 1 MHz. A 1.5 µm long pass filter (FEL1500, Thorlabs, NJ, USA) was used to remove light from the visible spectrum while allowing the 2.1 µm wavelength light from the P120 to be measured. The voltage output from the photodetector was recorded by a digital oscilloscope (DSOX4024A, Keysight Technologies, CA, USA). Measurements were conducted in air and, because the direct beam could destroy the detector, the laser was aimed at a matt white target with the photodetector positioned to capture the reflected light, as shown in Fig. 2.1.1. The target surface was positioned approximately 30 cm from the fibre tip. An angle of 45° was set between the fibre tip, target surface and photodetector. The distance between the photodetector and the target surface was adjusted for each laser setting, varying between 30 cm and 100 cm to ensure there was sufficient strength of signal to be measured but that the sensor was not saturated. Similarly, the angle of orientation of the photodetector in relation to the target surface was varied between 0° and 60° for each laser setting to correct the strength of signal. The laser was fired continuously and the oscilloscope triggered by an edge trigger on the signal,

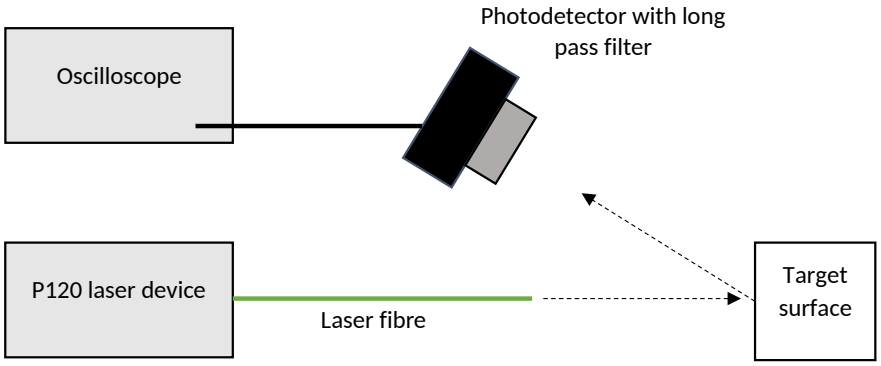


Figure 2.1.1 – Experimental setup for capturing laser pulse profiles.

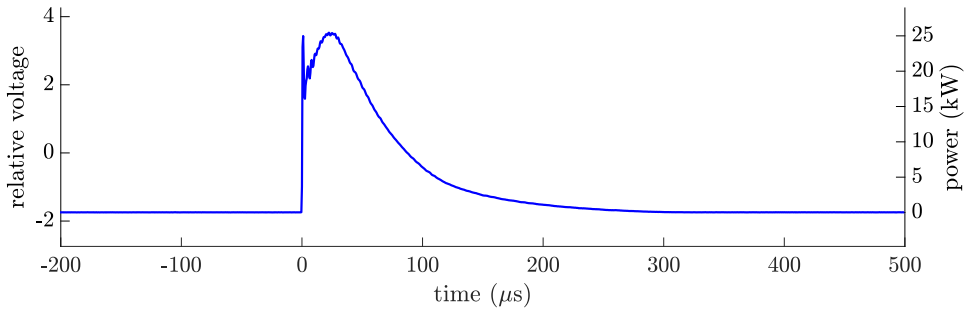


Figure 2.1.2 – An example of a pulse profile captured by the method shown in Fig. 2.1.1 for the case of a 1.0 J short pulse. The left-hand axis displays voltage as measured by the oscilloscope relative to an unknown background voltage. The right-hand axis displays the corresponding power output of the laser as calculated by the method detailed in Sec. 2.1.1.

averaged over 30 pulses at 2 MHz sampling rate.

An example of one measured pulse profile is shown in Fig. 2.1.2; the output data from the oscilloscope is in terms of voltage relative to a background value, displayed by the left hand axis. The data was manually shifted against the vertical axis such that the value is zero when the laser is off. To convert to watts, a multiplicative factor was introduced, ensuring that the integral of the power curve was equal to the specified pulse energy. The right hand axis of Fig. 2.1.2 displays the power scale.

2.1.2 Results

2.1.2.1 Single pulses

The P120 pulse shapes are plotted in Fig. 2.1.3 for short, medium and long pulses. Figure 2.1.3b zooms in on the first 50 µs for the case of the short pulses. All measured pulses begin with a spike of approximately 1 µs, followed by a smooth rise to a maximum and then an exponential decay. The spike is caused by laser saturation after the pulse is initiated by flashlamp. The growth phase then occurs due to continued pumping of the lasing material until a maximum power is reached. Finally, the decay of power occurs when pumping ends.

Comparing pulses of the same energy, a medium pulse extends over a longer duration

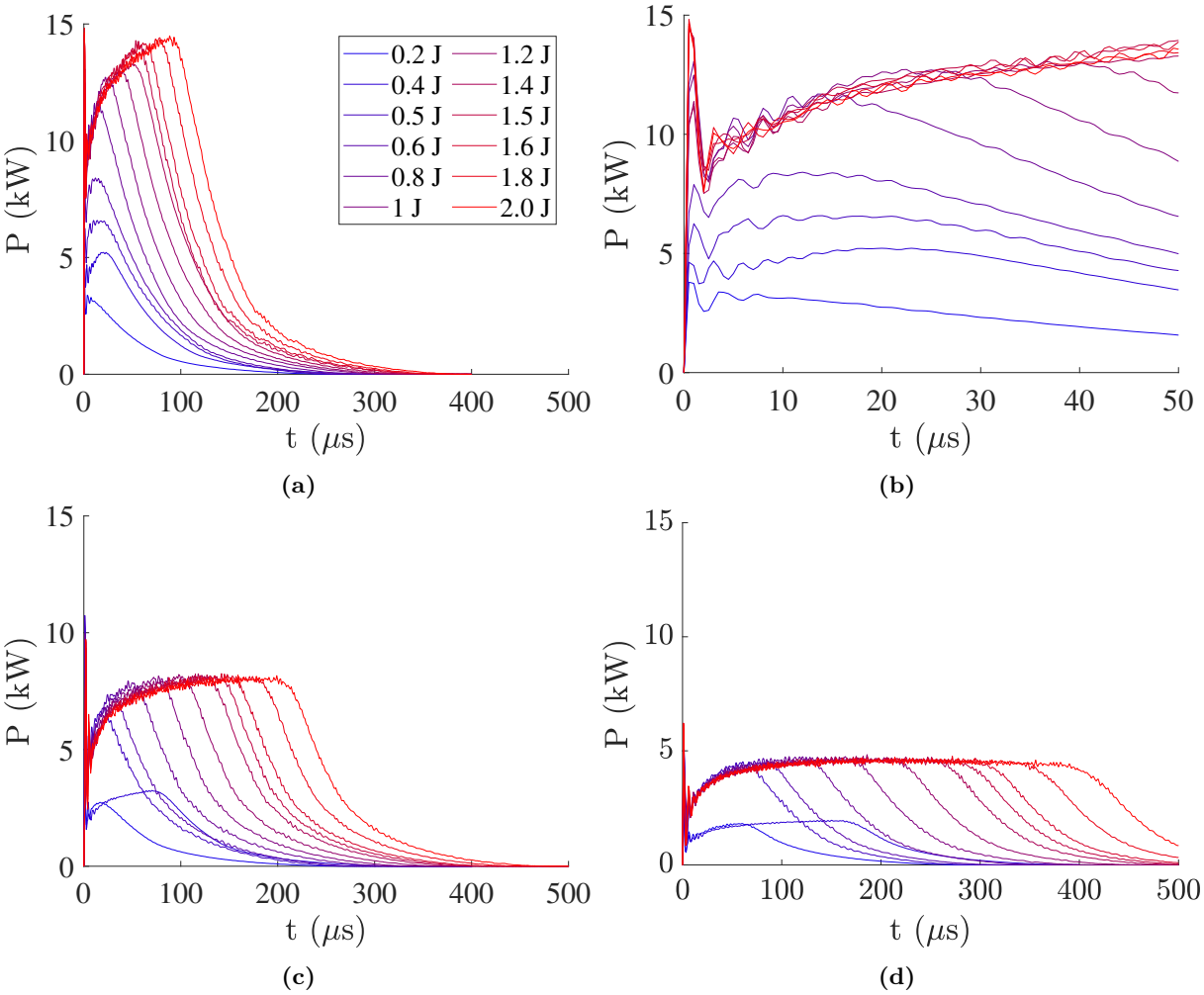


Figure 2.1.3 – Power, P, against time, t for (a) short, (c) medium and (d) long P120 pulses. A close-up of the initial spike for the case of short pulses is shown in (b).

than a short pulse, and a long pulse over a longer duration still. It is notable that the distribution of energy is qualitatively different between the three pulse types. The short pulses rise to peak power at $10 - 100$ µs then immediately decay, ending at $200 - 350$ µs. Peak power of the short pulses varies from 4 kW for the lowest energy 0.2 J pulse, and increases significantly with pulse energy up to 15 kW for a 2.0 J pulse.

In contrast to the short pulses, the long pulses rise to peak power where they remain at a plateau before decaying. The majority of the long pulses have a similar peak power of around 5 kW, with higher energy pulses spending longer time at the peak in order to achieve the desired energy. The 0.2 J and 0.4 J long pulses differ in form to their higher energy counterparts, with a much lower peak power of about 2 kW. Laser systems such as the P120 are typically comprised of multiple laser units; it is likely that not all units are utilised for the 0.2 J and 0.4 J long pulses resulting in a lower peak power than the higher energy long pulses that use all laser units.

The medium pulses qualitatively lie between short and long pulses in terms of maximum power and duration. Medium pulses of 0.8 J and higher almost reach a plateau at 8 kW but continue to rise a little until their descent. The 0.5 J and 0.6 J medium pulses appear to follow a similar profile at first but drop away before reaching 8 kW. Similarly to the long pulses, the behavior is very different for the lowest two energies 0.2 J and 0.4 J, with a peak of less than 4 kW.

The shapes and time-scales of the single pulses agree well with the limited studies of the P120 pulses by Ventimiglia et al. [57] and Aldoukhi et al. [16], giving confidence in the accuracy of our experimental results. However, we obtain slightly higher power values for 0.2 J short and medium pulses than Ventimiglia et al. [57]. The discrepancy may come from measuring voltage and converting to power with the assumption of a known total pulse energy, rather than directly measuring power output as in the work of Ventimiglia et al. [57].

2.1.2.2 Moses pulses

Fig. 2.1.4 shows the power over time profile for Moses pulses with the top row showing MC and bottom row showing MD. Fig. 2.1.4a and Fig. 2.1.4c show the full double pulse while Fig. 2.1.4b and Fig. 2.1.4d zoom in on the first 30 µs.

As with the single pulses, all measured Moses pulses begin with a spike of approximately 1 µs. The power of each Moses double pulse, after the initial spike, rises to a local maximum then decays — this is referred to as the 'first pulse'. The power then rises again to a second local maximum before decaying to zero — the second rise and fall of power is referred to as the 'second pulse'.

For MC of all energies, after the initial spike, the first pulse peaks at approximately 5 µs and the second pulse peaks at about 200 µs. The lowest three energy MC pulses, 0.2 J, 0.4 J, and 0.5 J, have a second pulse that peaks at a lower power than the first. At 0.6 J the two pulses peak at approximately the same power but for 0.8 J and higher, the second pulse has

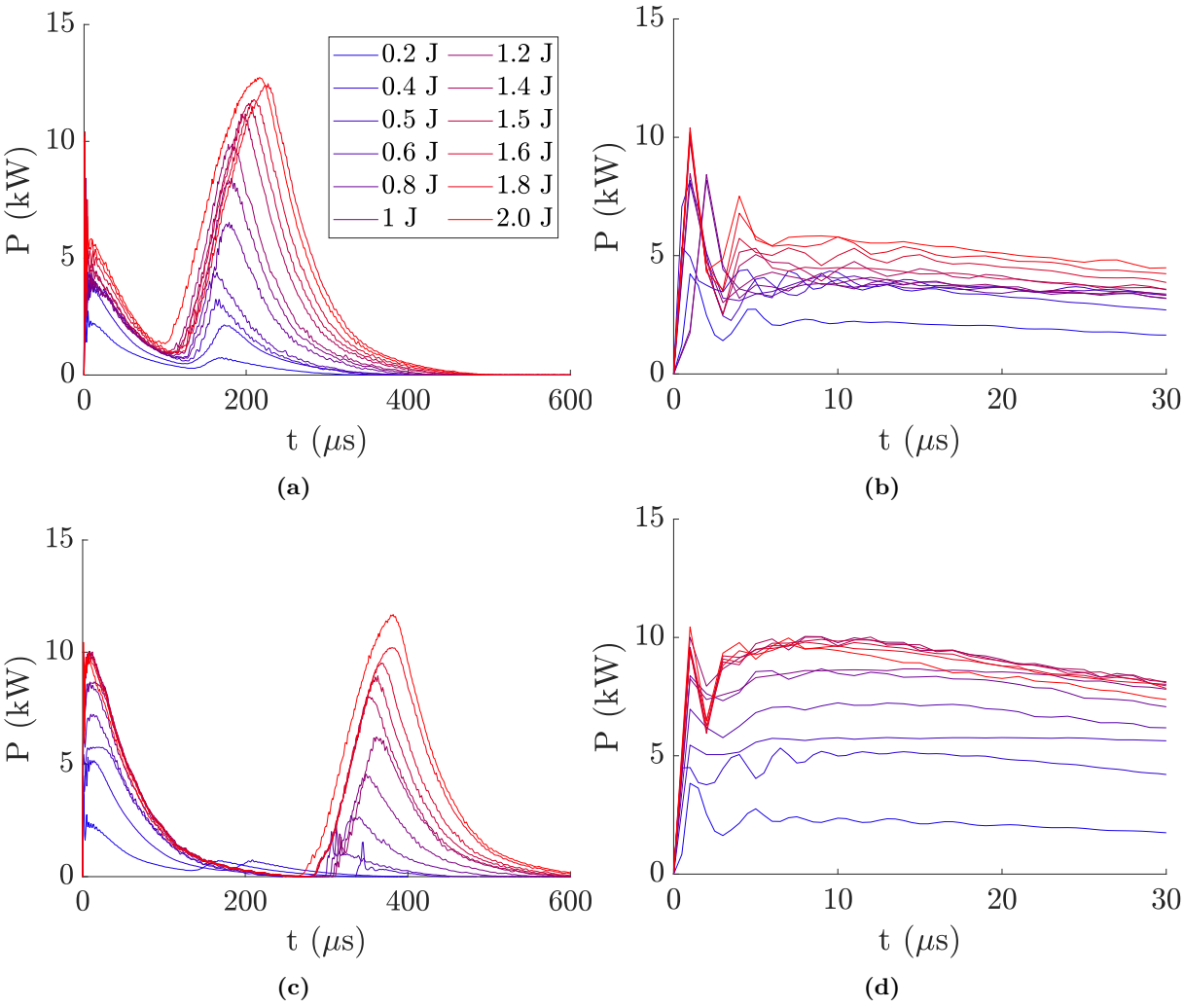


Figure 2.1.4 – Power, P, against time, t for (a) and (b) MC and (c) and (d) MD pulses. The full pulses are shown in (a) and (c) while just the first 200 µs is shown in (b) and (d).

a higher peak power than the first.

All MD pulses also have a first pulse that peaks at around 5 µs, however the time of the second pulse varies. At 0.2 J the second pulse peaks just before 200 µs, making it almost identical to the 0.2 J MC pulse. For 0.4 J, the second pulse peaks a little later, just after 200 µs. For MD pulses of 0.5 J and higher, the second pulse peaks at 350-400 µs, meaning that the two pulses are delivered further apart than their MC counterparts. In terms of peak power of the MD pulses, the second pulse is similar or lower than the first, with the exception of the highest energy 2.0 J pulse where the second pulse has a marginally higher peak power than the first.

2.2 P120 laser-induced bubble photography

2.2.1 Method

The bubbles generated in water by the laser emission were recorded at 2×10^5 frames per second at a resolution of 256×160 pixels using a high-speed video camera (FASTCAM

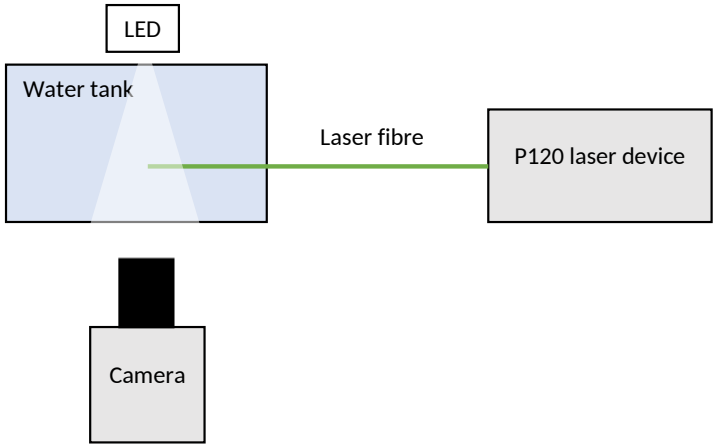


Figure 2.2.1 – Experimental setup for high speed bubble photography.

SA-X2, Photron, Tokyo, Japan) with a shutter speed of 5 µs. A 12× zoom lens was used with a 2× adapter tube (Navitar, NY, USA). The equipment was set up as shown in Fig. 2.2.1. An LED backlight (Photron, Tokyo, Japan) was positioned behind the laser fibre and remained on throughout. The camera was focused on the fibre tip prior to firing. A ruler was attached to the laser fibre to provide an initial calibration picture, after which the ruler was removed to avoid interference with bubble formation — this gave a pixel dimension of 27 µm. The time at which the laser pulse starts in relation to the frames is not known so time $t = 0$ was taken to be the frame prior to that for which vapour is first visible.

The videos were analysed using MATLAB's Image Processing Toolbox to determine the bubble volume at each time-step. The bubble wall was segmented from the images as follows:

- For each bubble video, the first frame is selected and converted to greyscale. An example of this is shown in Fig. 2.2.2a.
- The position of the laser fibre is detected using the `edge` function, selecting the `sobel` algorithm, giving a black and white image with edges marked in white. The fibre edge is dilated by three pixels in all directions using `strel` with the `disk` setting passed to `imdilate`. This step allows the fibre edge to be removed from following frames and the dilation ensures that this removal is robust to small movements of the equipment. The axis of the fibre is approximated by a straight line as marked on Fig. 2.2.2b.
- The subsequent frames of the video are analysed to find the bubble volume at each timestep. Each frame is first converted to greyscale. An example of a frame with a visible bubble is shown in Fig. 2.2.2c.
- The function `edge` is used with the `sobel` algorithm to detect all edges in the frame. This results in a black and white image, with edges marked in white, as in Fig. 2.2.2d.
- The edges of the fibre are removed from the image. For example, Fig. 2.2.2b subtracted from Fig. 2.2.2d gives Fig. 2.2.2e.
- A dilation of two pixels is applied using `strel` with the `disk` setting passed to `imdilate`

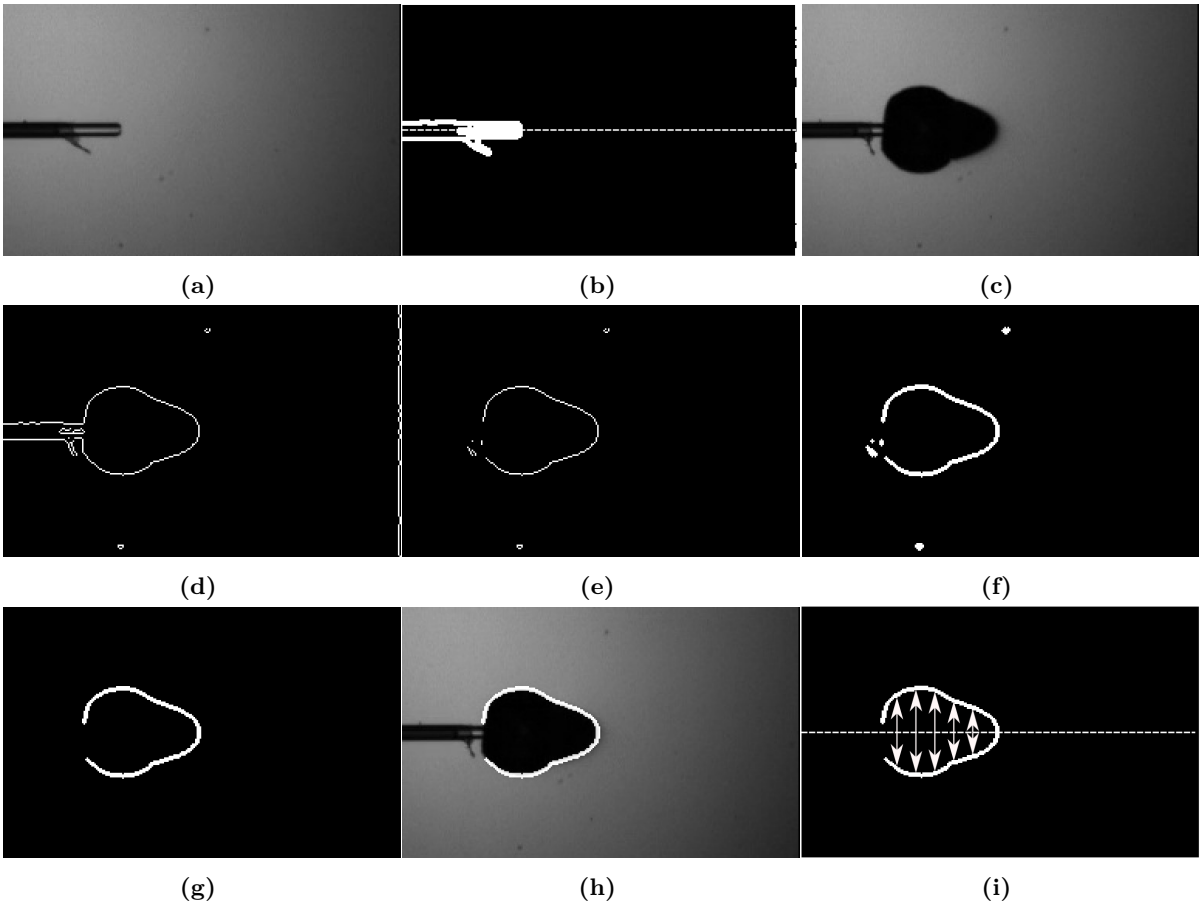


Figure 2.2.2 – Edge detection using Matlab's Image Processing Toolbox. (a) First frame of bubble video showing just laser fibre. (b) Fibre edge is detected in first frame and fibre axis is calculated. (c) Example of frame containing bubble. (d) All edges in image are detected. (e) Fibre edge as found in (b) is removed. (f) Edges are dilated by two pixels to close any small gaps in bubble edge. (g) Regions containing fewer than 100 pixels are removed to avoid any edges from dust or noise in the image. (h) Remaining bubble edge overlaid on original image to compare. (i) Perpendicular distance of bubble edge from fibre axis is found to calculate bubble volume.

to close any small gaps in the detected edge of the bubble. The result of this is shown in Fig. 2.2.2f.

- Erroneous edges are eliminated by employing `bwareaopen` to remove regions containing fewer than 100 pixels. Just the bubble edge remains, as in Fig. 2.2.2g.
- In Fig. 2.2.2h, the detected edge of Fig. 2.2.2g is overlayed onto the original image Fig. 2.2.2c, from which we are satisfied that the edge has been detected to reasonable accuracy.
- Bubble volume is calculated assuming that the bubble is axisymmetric. The volume is approximated by a series of discs one pixel thick, along the axis length, perpendicular to the axis. The disc radius at each pixel along the axis is calculated by finding the perpendicular distance of the bubble edge both above and below the fibre, from which an average is taken. A schematic of this is depicted in Fig. 2.2.2h. The radius is reduced by two pixels to compensate for the previous dilation of the bubble edge. The total bubble volume is the sum of the volume of the discs.

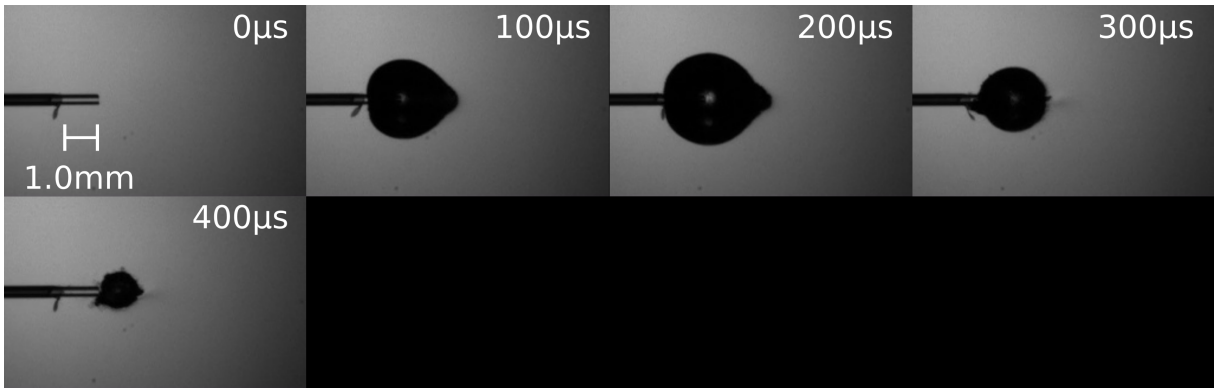
It is assumed that the error in the position of the edge is half of one pixel, 14 µm. As the bubble is taken to be axisymmetric, an error of 14 µm in bubble radius is integrated around the axis and multiplied by the pixel width to give an error in the volume of the bubble. At a radius of 200 µm — the diameter of the laser fibre — the error in volume is 14%. At a radius of 1 mm the error drops to 2.8% and at 2 mm radius the error is 1.4%.

2.2.2 Results

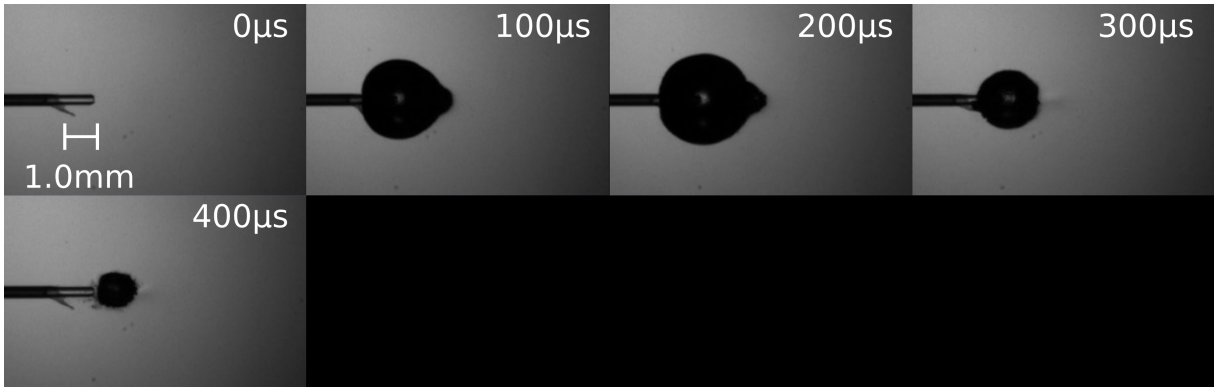
2.2.2.1 Single pulses

Examples of the evolution of laser-induced bubbles captured by high-speed photography for 0.2 J, 1.0 J and 2.0 J single pulses are shown in Fig. 2.2.3, Fig. 2.2.5 and Fig. 2.2.7 respectively, with each showing the cases of short, medium and long pulses. The bubbles formed by the lowest energy 0.2 J pulses have little qualitative difference between short, medium and long, all being relatively spherical. The volume over time for the same bubbles along with the corresponding pulse power over time is plotted in Fig. 2.2.4. Although the pulse shape varies, the power peaks well before the bubble reaches maximum volume in all three cases. The pulse energy is therefore concentrated early in the bubble's expansion, resulting in roughly spherical bubbles of similar sizes with maximum volumes of ~4 mm^3 for the long pulse and ~5 mm^3 for the medium and short pulses. In all cases, maximum volume is reached around 200 µs with the bubble collapsing to a minimum after 300 µs. A bubble rebound is seen at 400 µs, although the mass of vapour during rebound is not contained in a coherent bubble so bubble volume was not estimated after the initial collapse.

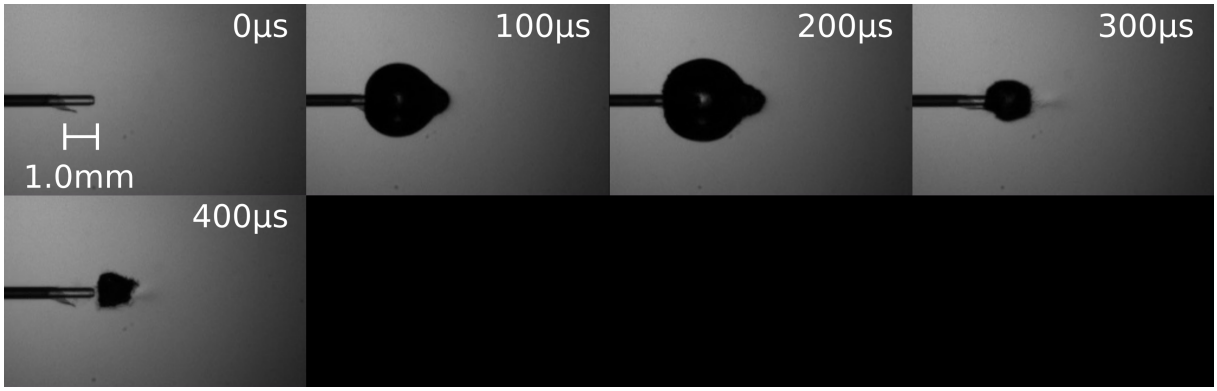
The 1.0 J pulses induce bubbles, shown in Fig. 2.2.5, that are qualitatively different between the cases of short, medium and long; the long pulse creates a longer and narrower



(a)

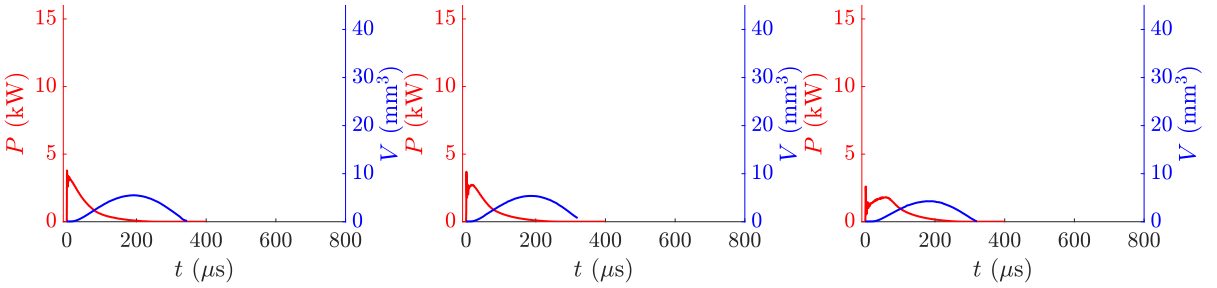


(b)



(c)

Figure 2.2.3 – Bubble induced by a P120 0.2 J (a) short, (b) medium, and (c) long pulse. Some frames are omitted to display the bubble at 100 µs intervals.



(a) **(b)** **(c)**

Figure 2.2.4 – Power over time and resulting bubble volume over time for P120 0.2 J (a) short, (b) medium and (c) long pulses.

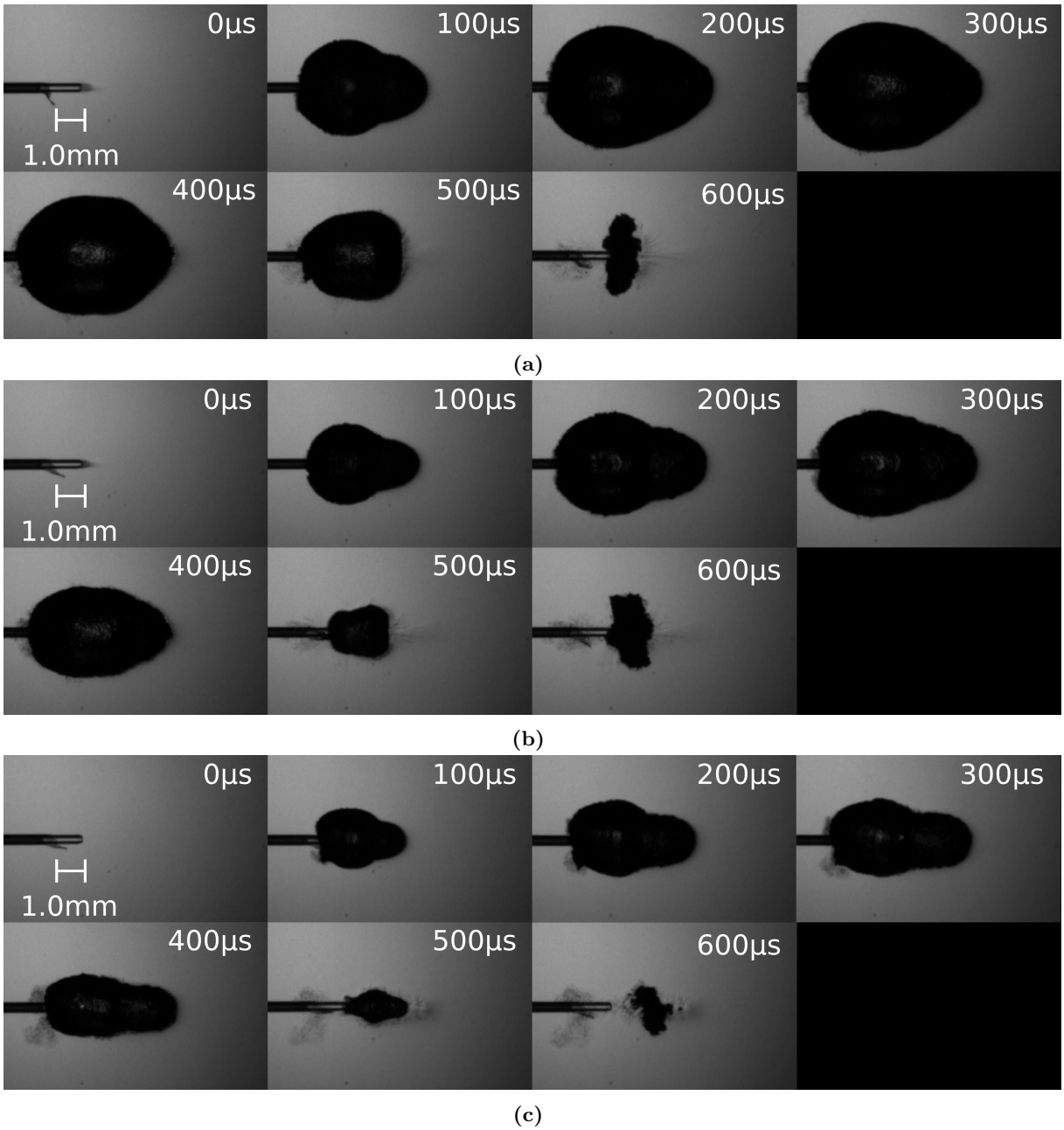


Figure 2.2.5 – Bubble induced by a P120 1.0 J (a) short, (b) medium, and (c) long pulse. Some frames are omitted to display the bubble at 100 µs intervals.

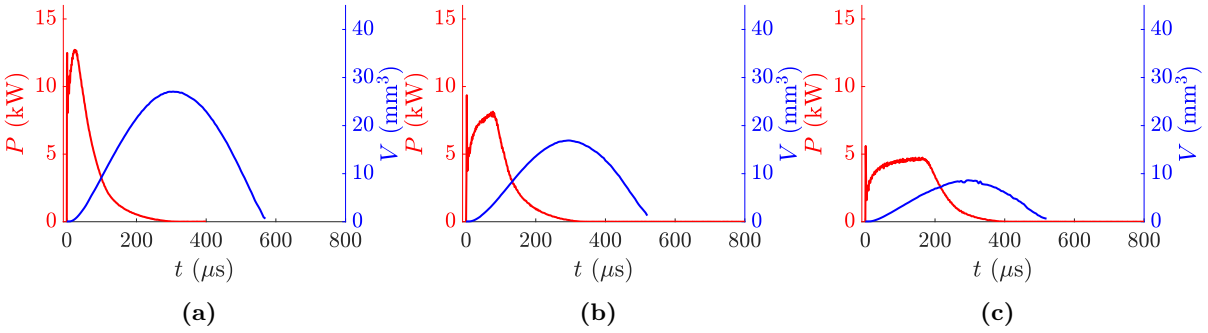
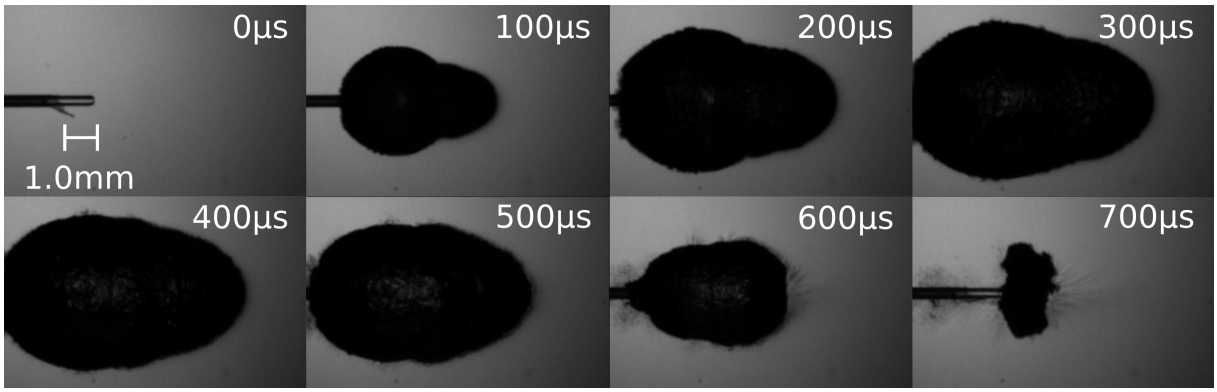
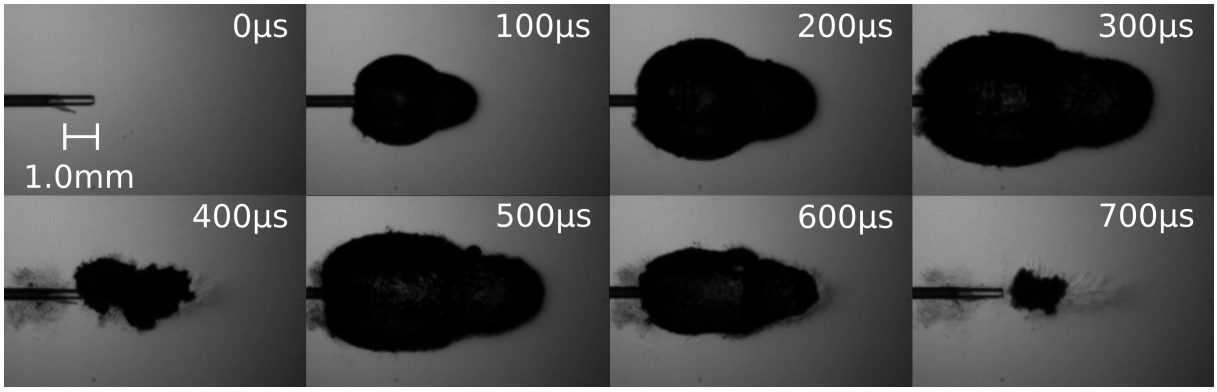


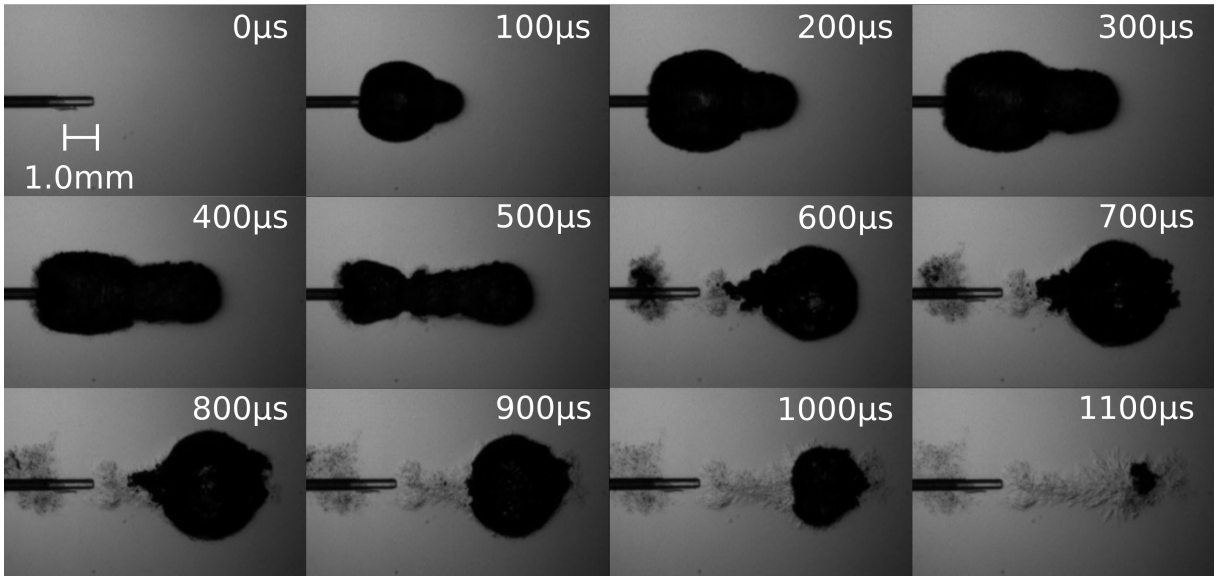
Figure 2.2.6 – Power over time and resulting bubble volume over time for P120 1.0 J (a) short, (b) medium and (c) long pulses.



(a)



(b)



(c)

Figure 2.2.7 – Bubble induced by a P120 2.0 J (a) short, (b) medium, and (c) long pulse. Some frames are omitted to display the bubble at 100 µs intervals.

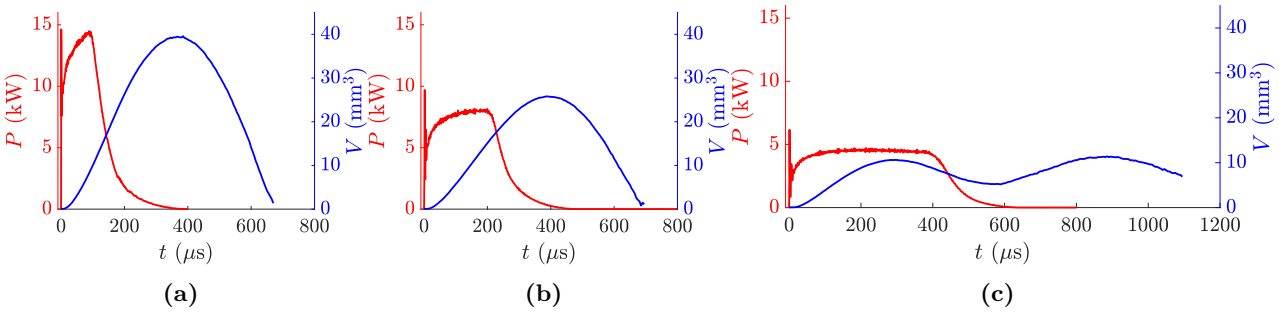


Figure 2.2.8 – Power over time and resulting bubble volume over time for P120 2.0 J (a) short, (b) medium and (c) long pulses.

bubble in comparison to the medium pulse, which is longer and narrower than that of the short pulse. The volume over time for these bubbles is plotted in Fig. 2.2.6, alongside the pulse power over time. The qualitative differences in bubble shape are due to the differences in how the laser energy is temporally distributed. The 1.0 J short pulse, in which the energy is concentrated early in bubble expansion, creates a roughly spherical bubble. The medium pulse induces a slightly elongated bubble; the longer duration of the medium pulse creates an elongation of the bubble due to the Moses effect, as the laser passes freely through the bubble and vaporises liquid on the far side. For the long pulse, the bubble has almost reached maximum size before the laser power begins to drop, forming a highly elongated bubble. Elongation during pulses on this time-scale is expected and has been documented previously [58]. The maximum aspect ratio of the bubbles, a measure for elongation, is discussed further below. In Fig. 2.2.6, it can be seen that the maximum volume of the three bubbles varies greatly: ~30 mm^3 for a short pulse, ~15 mm^3 for a medium pulse and ~10 mm^3 for a long pulse. Although shape and size varies for the three cases, the time-scales of bubble evolution are almost identical: the maximum volume is reached just before 300 µs with the bubble collapsing to a minimum after 500 µs. A rebound is seen in Fig. 2.2.5 at 600 µs but again bubble volume was not estimated after the initial collapse.

The bubbles of the 2.0 J pulses again vary qualitatively between short, medium and long, as shown in Fig. 2.2.7. As with 1.0 J pulses, the medium pulse creates a more elongated bubble in comparison to the short pulse, due to the energy being distributed over a longer time-scale. The volume over time for the same bubbles along with the corresponding pulse power over time is plotted in Fig. 2.2.8. The 2.0 J short pulse delivers energy on a similar time-scale to the 1.0 J medium pulse, shown in Fig. 2.2.6b, and creates a similarly elongated bubble. However, the higher energy of the 2.0 J pulse, in comparison to 1.0 J, causes the bubble to expand to a much larger size with a peak volume of nearly 40 mm^3. Of particular interest is the 2.0 J long pulse, shown in Fig. 2.2.7c and Fig. 2.2.8c, where the pulse duration is long enough that the laser is still delivering energy as the bubble begins to collapse, causing a secondary expansion from 600 µs. This secondary expansion exceeds the volume of the initial expansion and occurs approximately 2 mm from the fibre tip while simultaneously the initial mass of vapour near the bubble tip collapses. This behavior differs from all other single pulse bubbles shown in Fig. 2.2.4,

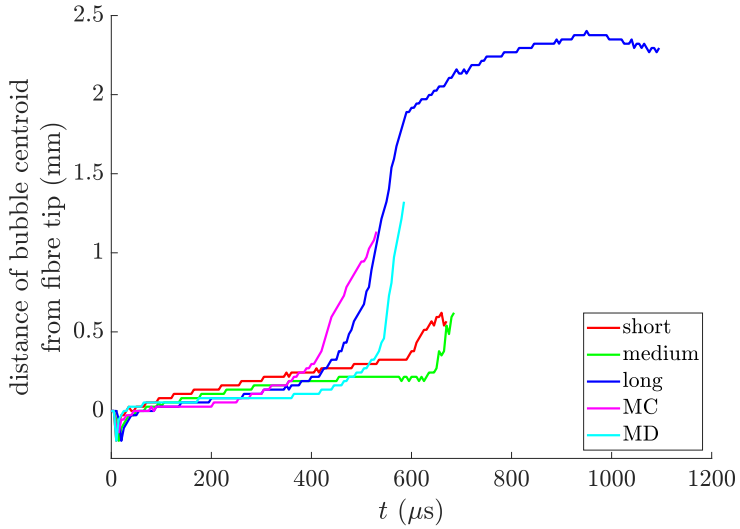


Figure 2.2.9 – Distance of the bubble centroid from the fibre tip, for 2.0 J short, medium, long, MC and MD pulses. Negative values denoting the centroid being to the left of the fibre tip.

Fig. 2.2.6 and Fig. 2.2.8 which remain surrounding or very close to the fibre tip.

In Fig. 2.2.9, the distance of the bubble centroid from the fibre tip is plotted for 2.0 J short, medium, long, MC and MD pulses. The location of the centroid is assumed to align with the fibre axis. With the fibre tip as the origin, the centroid distance is defined to be positive in front of fibre tip and negative behind the fibre tip. The distance of the centroid along the axis is calculated by finding the volume of each disc of the bubble, one pixel thick using the method explained in Sec. 2.2.1. The disc volumes are summed along the axis from left to right until the cumulative volume exceeds half of the total bubble volume; the pixel on the axis at which this occurs is taken to be the location of the centroid. This gives a maximum error in centroid location of 27 µm, the width of one pixel. The centroid is tracked until the first of the following occurs: 1) the bubble collapses to a minimum or 2) the bubble splits into multiple volumes. The distance of the centroid from the fibre tip can be considered as a proxy for the distance at which laser energy is focused; this measure is of interest clinically to determine the optimal distance for kidney stone ablation. In Fig. 2.2.9, we see that for the short and medium pulses, the centroid travels smoothly away from the fibre tip as the bubble grows then moves sharply away during the last stages of collapse to a maximum of approximately 0.5 mm. For the 2.0 J long pulse, the centroid is shifted significantly further from the fibre tip during the formation of the secondary bubble at around 500 µs, reaching a distance of nearly 2.5 mm. This suggests that distributing the pulse energy over a longer time period may be beneficial in delivering laser energy further from the fibre tip. The movement of the bubble centroid for the Moses pulses will be discussed in the following section.

In Fig. 2.2.10a, maximum bubble size, $V_{\max}$, is plotted for all measured single pulses. The error bars mark the uncertainty in pulse energy: legal limits allow a 20% tolerance in energy delivered by clinical laser systems [59]. We observe that the maximum bubble size for a given pulse energy is dependent on pulse type: short, medium or long. In particular, for pulses of

1.2 J and higher, a short pulse results in a peak volume bubble approximately twice as large as that of a medium pulse and approximately four times as large as that of a long pulse. Looking at each pulse type in isolation, short pulses range from a peak volume of approximately 9 mm^3 for a 0.2 J pulse to 40 mm^3 for a 2.0 J pulse. In contrast, the long pulses create bubbles with less variation in size, with V_{max} of approximately 5 mm^3 for a 0.2 J pulse up to 12 mm^3 for 2.0 J. This leads to the conclusion that bubble size is more dependent on peak power than total pulse energy: as noted in Sec. 2.1.2, short pulses vary in peak power whereas long pulses largely all peak at around 5 kW. The medium pulses sit qualitatively between short and long in terms of variation in bubble size with pulse energy — this reflects the fact that the peak power of the medium pulses varies less than that of short pulses but more than that of long pulses.

Fig. 2.2.10b shows the time that maximum volume is reached, $t_{V\max}$, for all single pulses, with error bars again marking the 20% tolerance in pulse energy [59]. This plot confirms that the time-scale of bubble expansion, in most cases, does not vary significantly with pulse type but does increase with pulse energy. However, there are three outliers: the 1.5 J, 1.6 J and 2.0 J long pulses. As seen in Fig. 2.2.8c for the case of 2.0 J, these high energy long pulses cause a double expansion due to their long duration. The 1.8 J long pulse also induces a secondary expansion but the first expansion is larger than the second so it does not appear as an outlier in Fig. 2.2.8c.

The time at which the rightmost edge of the bubble first reaches a distance of 1 mm from the fibre tip is plotted in Fig. 2.2.10c for all measured single pulses. This measure is informative as lithotripsy is ideally performed with the fibre tip 1-2 mm from the kidney stone [16] and once the gap between the fibre and stone has been filled with vapour, subsequent laser energy will pass more efficiently to the kidney stone due to the Moses effect. For a given pulse energy, the time at which 1 mm is reached is shortest for the short pulse and longest for the long pulse. It is reasonable to conclude, therefore, that higher pulse power results in a bubble expanding to 1 mm more quickly. For short pulses, the time to reach 1 mm decreases as pulse energy increases up to 0.8 J, after which there is little variation, remaining around 35 µs. Short pulses of 0.8 J and higher follow the same power over time profile up to approximately 20 µs, as shown in Fig. 2.1.3b, leading to the assumption that it is the power at this short time-scale that determines how quickly the bubble reaches the 1 mm. Similarly, there is little variation in time to reach 1 mm for medium and long pulses of 0.5 J and higher. The 0.2 J and 0.4 J medium and long pulses, which have a lower power than their higher energy counterparts, take around 50% longer to reach 1 mm. In all cases the bubble expands to 1 mm well before it obtains maximum volume.

The maximum bubble aspect ratio for all pulses is plotted in Fig. 2.2.10d, with aspect ratio defined as bubble length divided by bubble width. Bubble length is the distance between the leftmost and rightmost pixel containing vapour and bubble width is the distance between the upper and lower pixel containing vapour; these simple definitions are sufficient for our purposes

as the bubbles are roughly axisymmetric. There is not a clear difference in aspect ratio between short, medium and long pulses for pulses of 0.6 J and less, with all bubbles having a maximum of around 2. This can be explained by the duration of the pulses, seen in Fig. 2.1.3; at these lower energies, the power decays before or around 200 µs for all pulse types. The differences in bubble elongation occur at 0.8 J and higher. At these higher energy settings, the long and medium pulses extend beyond 200 µs whereas the short pulses decay around this time. At 0.8 J and higher, the aspect ratio of the bubbles produced by the short pulses remains around 2, but varies between 2 and 3 for medium pulses. The maximum aspect ratio is highest for long pulses, being between 3 and 5. The 0.4 J long pulse appears as an outlier on Fig. 2.2.10d, due to the duration of this pulse being longer than the higher energy 0.5 J and 0.6 J long pulses, as plotted in Fig. 2.1.3d.

In Fig. 2.2.11, the maximum bubble aspect ratio is plotted against pulse length, where pulse length for single pulses is defined as the time at which the power drops to 10% of its peak. We see a positive correlation between pulse length and aspect ratio up to a pulse length of 400 µs. The correlation between pulse length and aspect ratio is due to the Moses effect: the longer the duration of the pulse, the more the Moses effect is exploited, with energy passing through the bubble causing elongation as liquid on the far side is vaporised. Above 400 µs, there is a negative correlation between pulse length and aspect ratio. For these longest pulses, the bubble dynamics differ from those of the shorter pulses, as shown in Fig. 2.2.7c and discussed above for the case of a 2.0 J long pulse. In these cases a secondary expansion occurs due to laser energy continuing to be delivered as the original mass of vapour collapses.

2.2.2.2 Moses pulses

For the case of the Moses pulses, examples of the induced bubbles are shown in Fig. 2.2.12, Fig. 2.2.14 and Fig. 2.2.16 for 0.2 J, 1.0 J and 2.0 J respectively. The volume over time for the same bubbles along with the corresponding pulse power over time is plotted in Fig. 2.2.13, Fig. 2.2.15 and Fig. 2.2.17 for 0.2 J, 1.0 J and 2.0 J respectively. At the lowest energy 0.2 J, the bubble of the MC pulse appears similar to those of the single pulses up until 200 µs, after which a sideways ‘8’ form develops. This sideways ‘8’ form occurs also between 200 and 300 µs with the higher energy 1.0 J and 2.0 J MC pulses, and is due to the timing of the two pulses. The MC pulses consist of two pulses spaced approximately 200 µs apart, such that the second pulse is delivered before the bubble reaches maximum size, as can be seen in Fig. 2.2.13, Fig. 2.2.15 and Fig. 2.2.17. In contrast to MC, MD delivers the second pulse as the bubble is collapsing. For this reason, the bubble stays roughly spherical on expansion, similar to that of a single short pulse, and the sideways ‘8’ forms as the bubble is collapsing. The effect of the second pulse is imperceptible for 0.2 J MD but more pronounced for the higher energy 1.0 J and 2.0 J MD pulses.

The maximum bubble volume, $V_{\max}$, for all measured Moses pulses is shown in

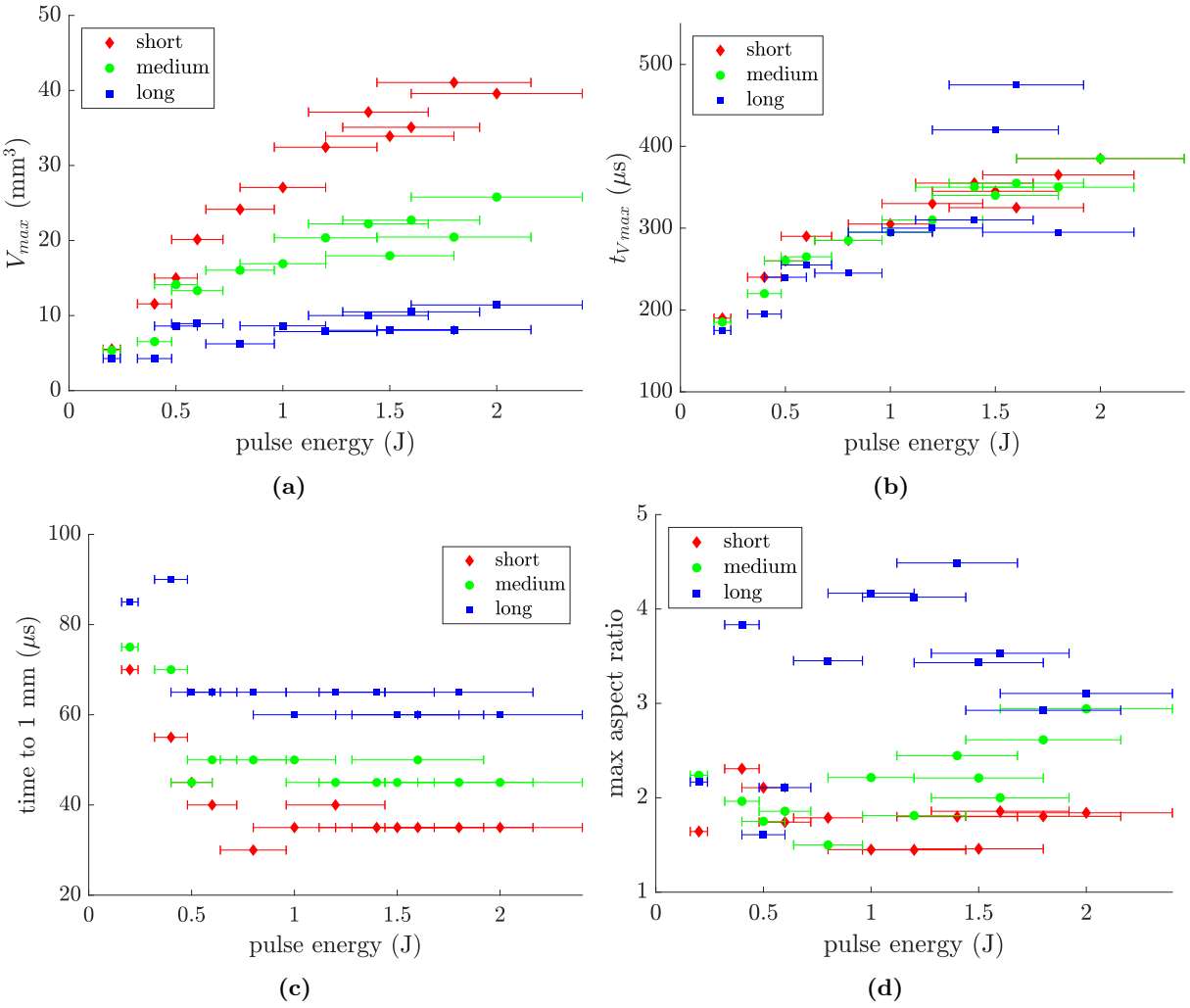


Figure 2.2.10 – (a) Maximum bubble volume for short, medium and long pulses. (b) Time at which maximum volume reached for short, medium and long pulses. (c) Time at which bubble reaches 1 mm from the fibre tip. (d) Maximum bubble aspect radio for short, medium and long pulses. Error bars mark the allowed 20% error in energy delivered by clinical laser systems [59].

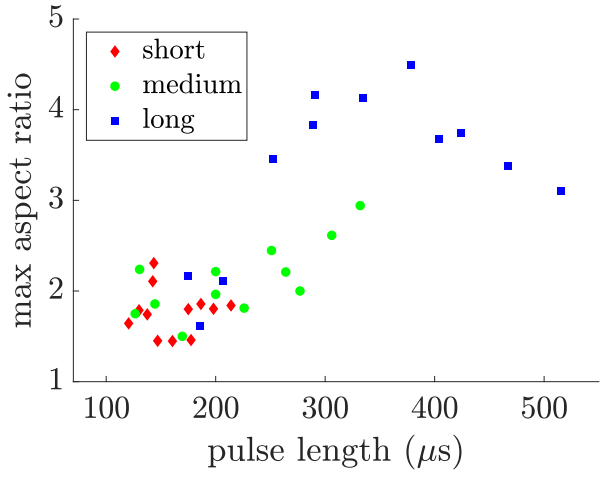


Figure 2.2.11 – Maximum bubble aspect ratio against pulse duration for all measured single pulses.

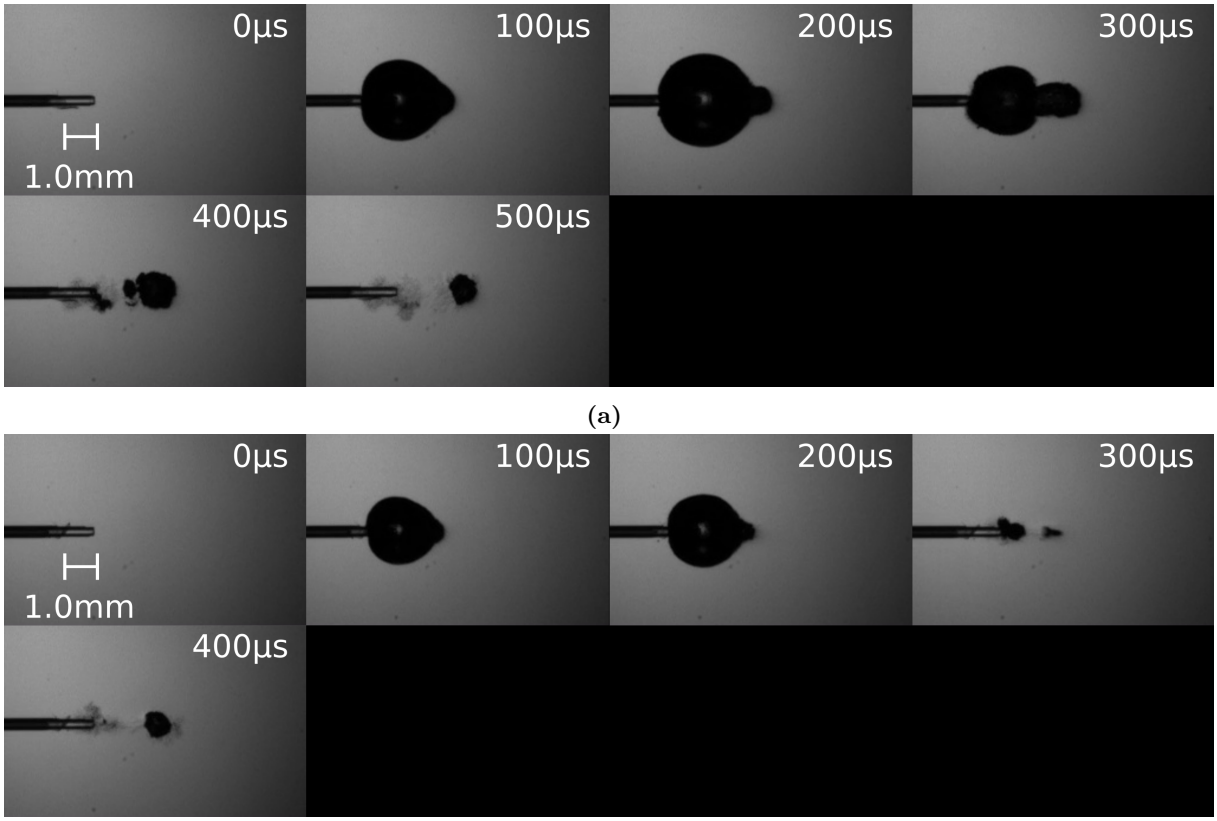


Figure 2.2.12 – Bubble induced by a P120 0.2 J (a) MC and (b) MD pulse. Some frames are omitted to display the bubble at 100 µs intervals.

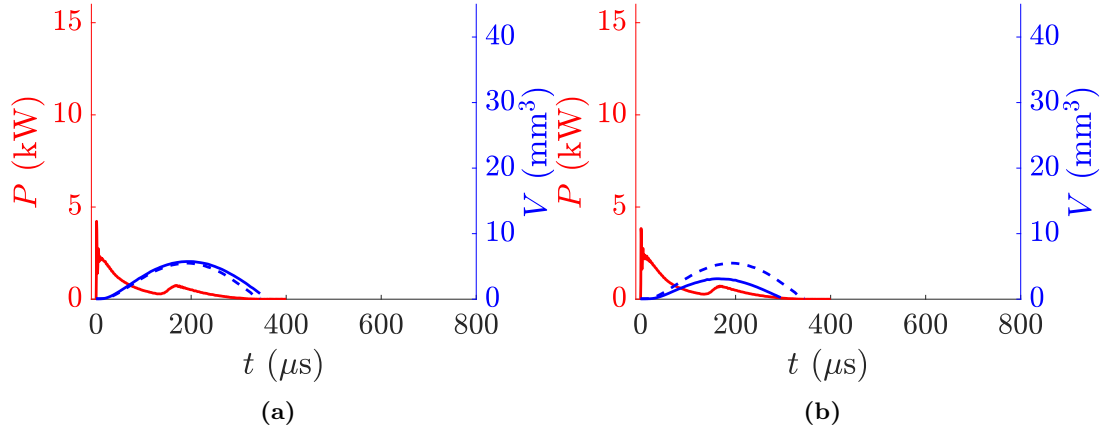


Figure 2.2.13 – Power over time and resulting bubble volume over time for P120 0.2 J (a) MC and (b) MD pulses. The dashed lines mark the bubble volume over time for a P120 0.2 J short pulse.

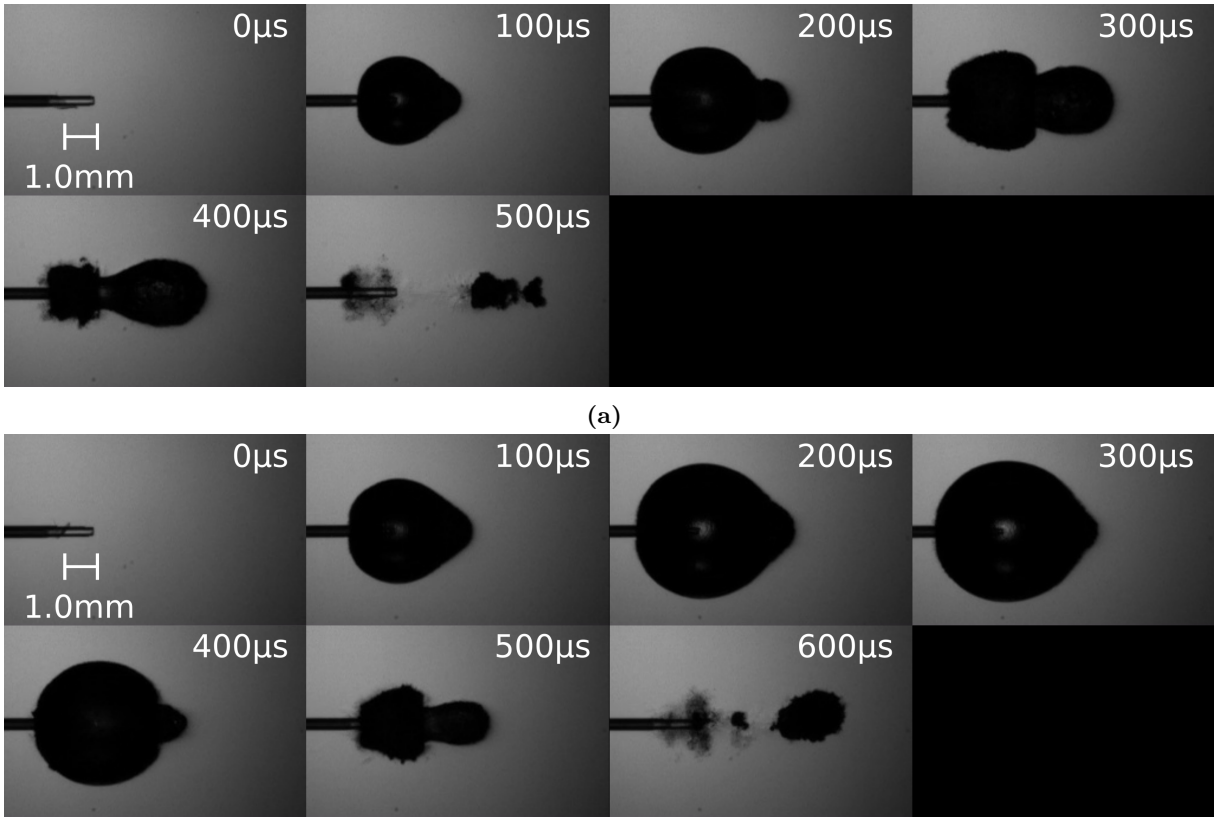


Figure 2.2.14 – Bubble induced by a P120 1.0 J (a) MC and (b) MD pulse. Some frames are omitted to display the bubble at 100 µs intervals.

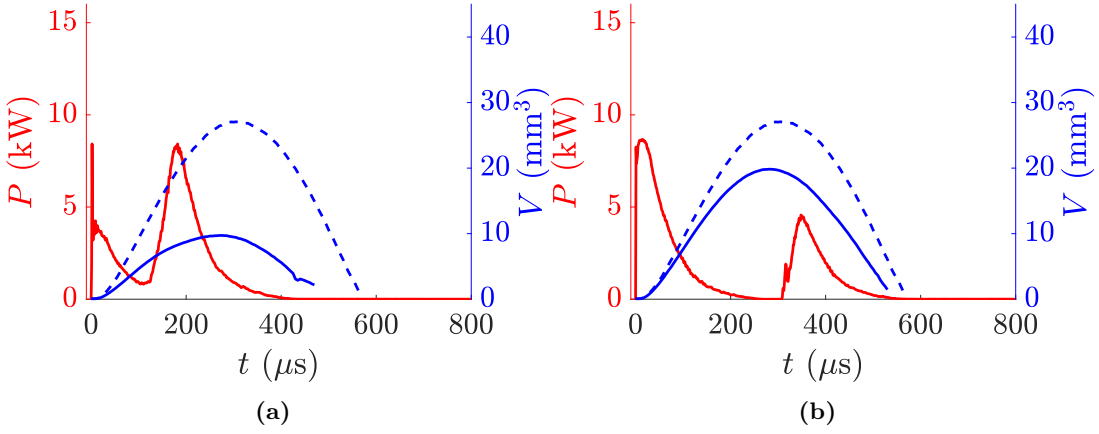
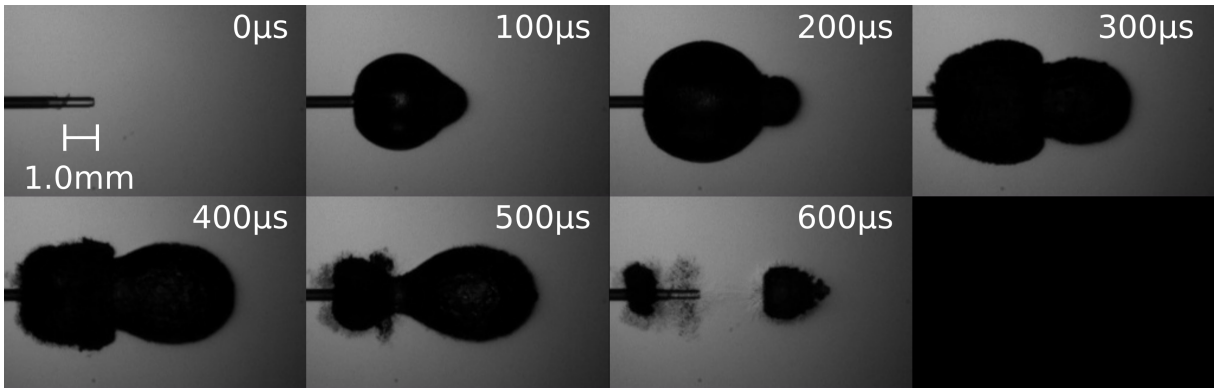
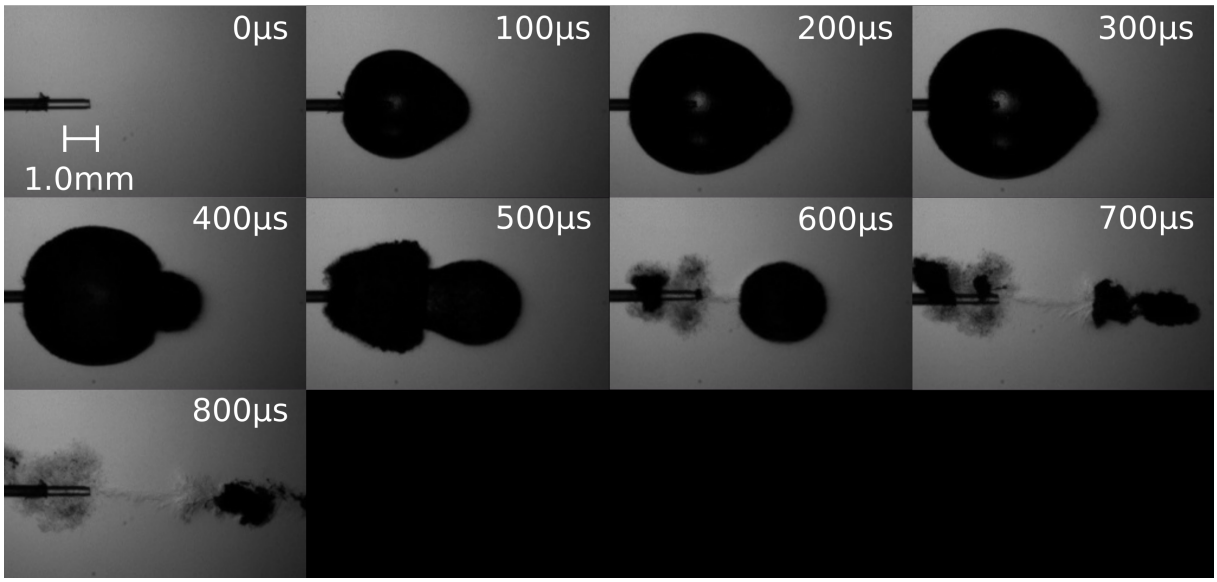


Figure 2.2.15 – Power over time and resulting bubble volume over time for P120 1.0 J (a) MC and (b) MD pulses. The dashed lines mark the bubble volume over time for a P120 1.0 J short pulse.

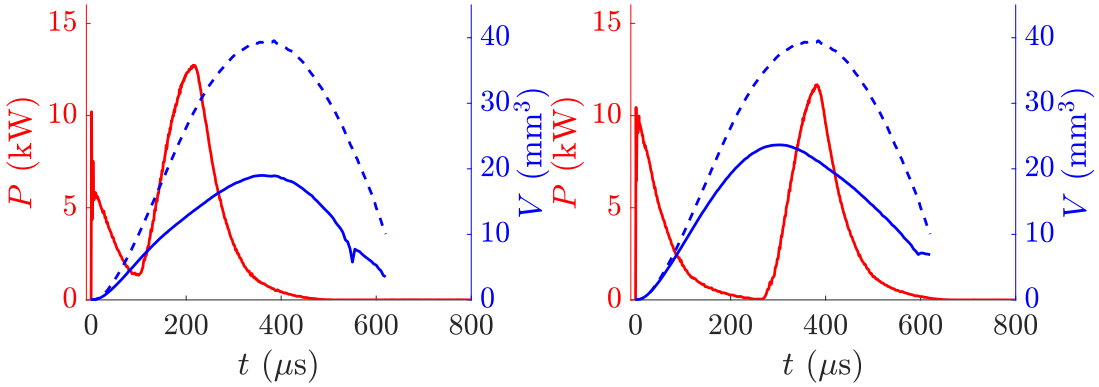


(a)



(b)

Figure 2.2.16 – Bubble induced by a P120 2.0 J (a) MC and (b) MD pulse. Some frames are omitted to display the bubble at 100 µs intervals.



(a) **(b)**

Figure 2.2.17 – Power over time and resulting bubble volume over time for P120 2.0 J (a) MC and (b) MD pulses. The dashed lines mark the bubble volume over time for a P120 2.0 J short pulse.

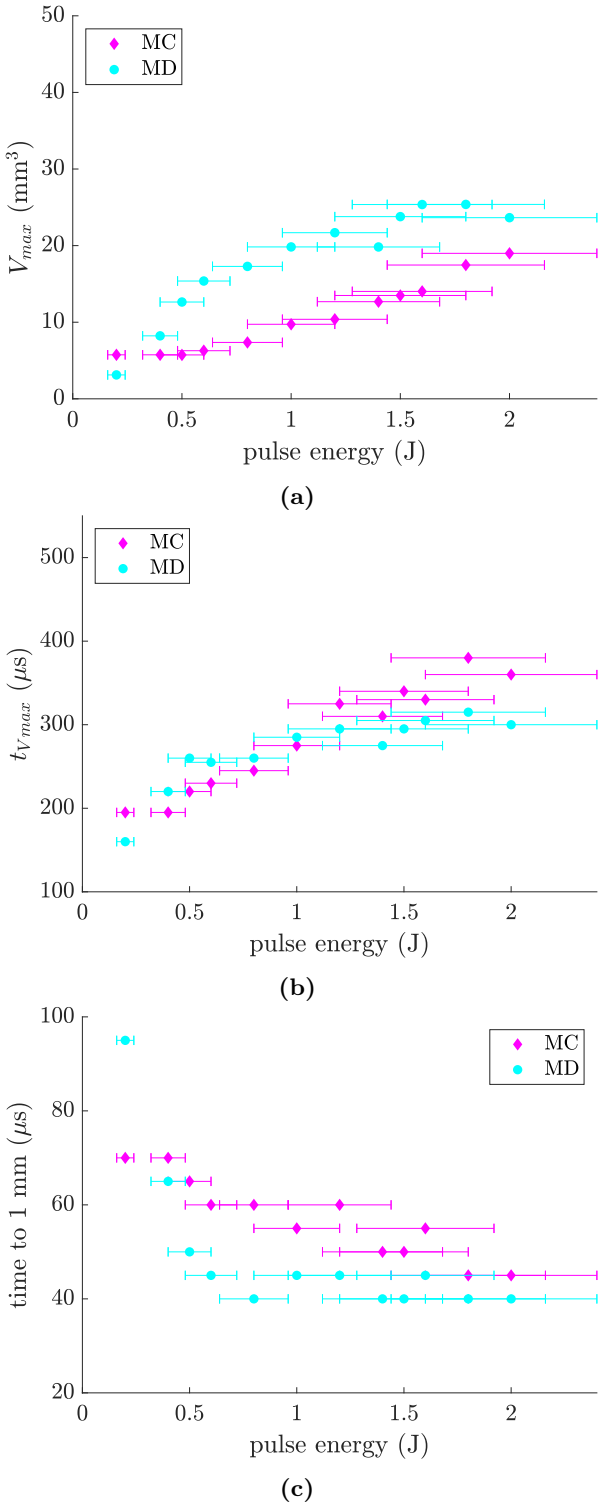


Figure 2.2.18 – (a) Maximum bubble volume for MC and MD pulses. (b) Time at which maximum volume reached for MC and MD pulses. (c) Time at which bubble reaches 1 mm from the fibre tip. Error bars mark the allowed 20% error in energy delivered by clinical laser systems [59].

Fig. 2.2.18a and the time that this volume is reached, $t_{V\max}$, is shown in Fig. 2.2.18b. Both $V_{\max}$ and $t_{V\max}$ increase with pulse energy for both MC and MD. In most cases, a MC pulse produces a smaller bubble than a MD pulse of the same energy. In some cases, the bubbles induced by Moses pulses split into multiple regions of vapour; for this reason, a simple bubble aspect ratio cannot be defined as was done for the single pulses.

In Fig. 2.2.9, the distance of the bubble centroid from the fibre tip is plotted for 2.0 J MC and MD pulses alongside the same energy single pulses. The centroid of the Moses pulses follows a similar trajectory to that of the 2.0 J long pulse, seeing a sharp movement away from the fibre at 400-600 µs.

2.3 Conclusion

Experiments were conducted to measure the optical output and bubble dynamics produced by the P120 laser pulse.

For optical power, it was found that the pulse shapes of the short, medium, long, MC and MD pulses vary qualitatively between each other. Short pulses rise to a peak and then decay, with peak power increasing with total pulse energy. Long pulses rise to a maximum and remain almost at a plateau for some time before falling. The majority of long pulses have a similar peak power of approximately 5 kW, with the exception of 0.2 J and 0.4 J which have a lower peak power of approximately 2 kW. Most medium pulses also reach a plateau but are shorter with a higher peak power than their long pulse counterparts. Moses pulses comprise of two pulses, with the power almost dropping to zero in between. With MC, the peaks of the first and second pulses are approximately 200 µs apart. The two pulses are delivered further apart for MD, at 350-400 µs, with the exception of 0.2 J and 0.4 J for which the second pulse peaks at approximately 200 µs.

For all pulse types, bubble size and duration is correlated to pulse energy but is also dependent on peak power. Short pulses, which vary greatly in peak power, have the greatest variation in maximum bubble size whereas long pulses which have little variation in peak power, vary little in maximum bubble size. This result supports the idea that pulse shape, the temporal distribution of pulse energy plays an important role in bubble dynamics for pulses on this time-scale. The power delivered in the first 20 µs was seen to determine how quickly the bubble wall reaches a distance of 1 mm from the fibre — a typical distance from the kidney stone at which lithotripsy is performed — with higher power causing the bubble to reach this distance more quickly For single pulses of the same energy, the time-scale at which the bubble reaches maximum size varies little between short, medium and long, with the exception of some of the long pulses which have a secondary bubble expansion. These results can be interpreted together to suggest that for a given total energy, a higher power causes a faster expansion but, since the bubble expands further, the time at which peak volume is reached is relatively constant.

For single pulses, the degree of bubble elongation is linked to the time-scale over which the laser energy is delivered. When energy is delivered over a time-scale around 200 µs and less, the bubbles have an aspect ratio of approximately 2. As pulse duration increases, the Moses effect becomes more apparent: energy passes through the bubble, vaporising liquid on far side and causing elongation. The four highest energy long pulses continue to deliver energy even as the bubble begins to collapse, triggering a secondary expansion. A double expansion is also seen in the bubbles of the double Moses pulses. MC delivers the second pulse as the bubble is still expanding, causing a double bubble in a sideways '8' shape on expansion. In contrast, MD delivers the second pulse as the initial bubble is beginning to collapse. For this reason, the bubble induced be MD pulses remain roughly spherical on expansion but forms the sideways '8' shape on collapse. The qualitative differences in bubble shape between different pulse types are subtle at low energies and more pronounced at higher energies.

The trajectory of the bubble centroid was tracked as a proxy for the distance into the fluid at which laser energy can be delivered. Considering the highest energy 2.0 J pulses, the bubble centroid was found to stay within 0.2 mm of the laser fibre for short and medium pulses, until the last stages of collapse at which it shifts sharply to 0.5 mm. The long, MC and MD pulses of 2.0 J, continue to deliver energy past 300 µs, unlike the short and medium pulses, causing secondary expansions and moving the centroid over 1 mm from the fibre.

The data and understanding gained via the experimental work in this chapter motivates the mathematical models presented in the following chapters. We aim to derive models that reflect the experimental results presented here. After such validation, models can be used to generate a bubble from any pulse shape, unlike experimental work in which the pulse shapes are defined by the laser system being used. This freedom in pulse shape allows us to isolate and test the effect of a single parameter, such as peak power, while holding other parameters constant. Through modelling, we can calculate fields that are difficult to measure experimentally, such as pressure and temperature, and understand the physical mechanisms behind expansion of a laser-induced bubble — information that experimental work does not reveal.

Chapter 3

Spherical bubble model

In this chapter, we derive a mathematical model for a laser-induced vapour bubble in liquid using an interface tracking method. With this approach, the liquid and vapour are treated as two distinct regions, each with a set of conservation equations. A third set of equations hold at the vapour-liquid interface and give a mathematical expression for the interface location. The resulting 3D model consists of ten coupled differential equations. The complexity of this system is reduced by assuming spherical symmetry and dropping small terms, leading to a model that can be quickly and easily solved numerically. To capture the evolution of the bubble as laser energy is input into system, we consider a suitable spherically symmetric energy source term, modelling the absorption of the laser energy by the liquid. We do not explicitly consider the complex physics of bubble nucleation but capture the bubble dynamics with a careful specification of the initial conditions. An analysis of the model is presented in the following chapter.

3.1 Nomenclature

b, specific gas constant of vapour

c_p, specific heat capacity at constant pressure

e, internal energy

f, arbitrary field **or** spatial component of laser source term

I, intensity

$\mathcal{I}$, identity matrix

K, thermal conductivity

$\mathcal{K}$, curvature of interface

L, latent heat of vaporisation

$\dot{m}$, mass flux density

$\boldsymbol{n}$, normal to fluid volume surface

P, laser power

$P_{\max}$, peak laser power

p, pressure

$\dot{Q}$, rate of laser energy transferred to liquid

$\boldsymbol{q}$, energy flux

R, bubble radius

r, radial coordinate

S, surface of arbitrary fluid volume

$\boldsymbol{s}$, velocity of fluid volume surface

T, temperature

$T_{\text{vap},\infty}$, vaporisation temperature at far-field pressure

t, time

t^*_{nucl} time at which nucleation occurs

t^*_{vap} time at which liquid reaches vaporisation temperature

$t_{V\max}$, time at which maximum volume is reached

$\mathcal{T}$, viscous stress tensor

$\boldsymbol{u}$, fluid velocity

u, radial speed

V, arbitrary fluid volume **or** bubble volume

$V_{\max}$, maximum bubble volume

$\boldsymbol{x}$, spatial location

Greek symbols

α, fitting parameter

β, fitting parameter

ϵ, small parameter

Θ, reference temperature

λ, dimensionless parameter group

μ, absorption coefficient of laser in liquid

ξ, radial distance from bubble wall

ρ, density

Σ, interface between two fluid volumes

σ, coefficient of surface tension

τ, reference time

Subscripts

l, liquid

R, quantity evaluated at the bubble wall

v, vapour

ij, value of from volume i to volume j

nucl, value at nucleation time

Σ, quantity evaluated at the interface

∞, far-field value

Superscripts

$*$, dimensionless quantitiy

Other notation

overdot, derivative with respect to time

$[\![]\!]$, jump across interface

3.2 3D model

A vapour bubble in liquid is considered to be a region of vapour surrounded by a region of liquid, with an interface across which mass can be transferred as liquid becomes vapour or vice versa. Before considering the specific geometry and parameters of a vapour bubble in liquid, we consider the general case in Sec. 3.2.1 of two arbitrary fluid volumes separated by an interface. We refer to the general model in Sec. 3.2.1 as a 'two-volume' model as, in this case, the two regions can either contain different fluids or be volumes of the same fluid. In Sec. 3.2.2, the general model is used as a framework to derive a 'two-phase' model, in which the two volumes contain the two phases — vapour and gas — of water.

3.2.1 Generalised two-volume fluid model

In this section, we consider a model for two fluid volumes divided by an interface across which mass transfer can occur. This derivation follows the method given by Joseph in *Studies in Applied Mechanics* [60]. Equations marked with a box will form the bubble-specific model in the next section. To obtain equations for conservation of mass, momentum and energy, we first derive a variation of Reynolds transport theorem for a field that is discontinuous at an interface between two volumes but smooth away from this interface.

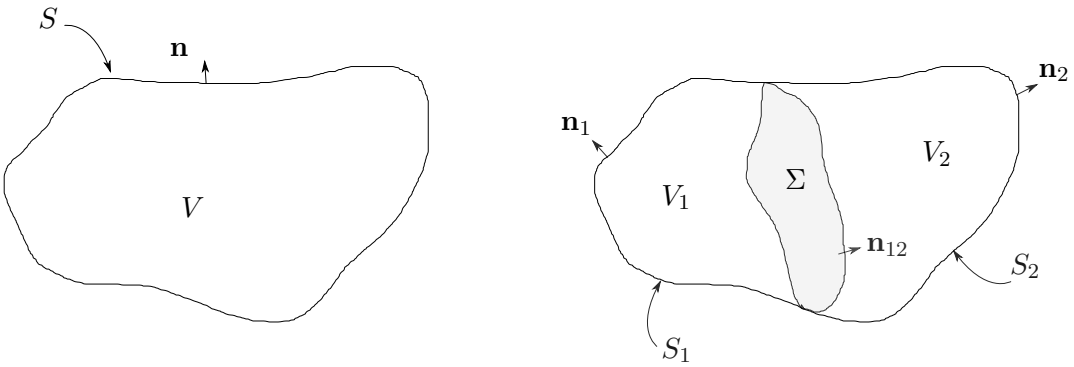


Figure 3.2.1 – (a) A volume V bounded by surface S with outward pointing normal $\boldsymbol{n}$. (b) The volume is divided by an arbitrary interface Σ giving two volumes V_1 and V_2 bounded by surfaces S_1 and S_2 with outward pointing normals $\boldsymbol{n}_1$ and $\boldsymbol{n}_2$ respectively. The interface has normal $\boldsymbol{n}_{12}$, pointing from V_1 into V_2.

Let t be time and $\boldsymbol{x}$ be spatial position. Consider an arbitrary fluid volume $V(t)$, with surface $S(t)$, divided into $V_1(t)$ and $V_2(t)$ by an arbitrary interface $\Sigma(t)$, as in Fig. 3.2.1. Subscripts $i = 1, 2$ denote quantities relating to V_1 and V_2 respectively, while quantities with no subscript relate to the total volume V. The surface of V_i is denoted S_i and has outward pointing normal $\boldsymbol{n}_i$; note that both surfaces $S_1(t)$ and $S_2(t)$ contain the interface Σ. Mass is conserved in V as a whole but mass flux is allowed across Σ. A field $f(\boldsymbol{x}, t)$ in V can have a discontinuity across Σ but is smooth away from the interface. At a point $\boldsymbol{x}$ in V_i, let $\boldsymbol{u}_i(\boldsymbol{x}, t)$ be the fluid velocity. For a point $\boldsymbol{x}$ on the surface S_i let the speed of the surface be $s_i(\boldsymbol{x}, t)$. In each volume, the following holds

$$\frac{\mathrm{D}}{\mathrm{D}t}\int_{V_i} f_i \,\mathrm{d}V = \int_{V_i} \frac{\partial f_i}{\partial t}\,\mathrm{d}V + \int_{S_i} f_i s_i \,\mathrm{d}S. \tag{3.2.1}$$

Away from Σ, the surface moves at the normal fluid velocity at that point, $s_i(\boldsymbol{x}, t) = \boldsymbol{u}_i(\boldsymbol{x}, t)\cdot\boldsymbol{n}_i$. Where S_i coincides with Σ, the speed of the surface is not necessarily equal to the normal fluid velocity due to mass flux across Σ. Therefore on Σ, we set $s_i(\boldsymbol{x}, t) = u_\Sigma(\boldsymbol{x}, t)$, where $u_\Sigma(\boldsymbol{x}, t)$ is the speed of the interface. We can write the last term in Eq. (3.2.1) in terms of $\boldsymbol{u}_i(\boldsymbol{x}, t)$ and $u_\Sigma(\boldsymbol{x}, t)$ as follows

$$\int_{S_i} f_i s_i \mathrm{d}S = \int_{S_i} f_i \boldsymbol{u}_i \cdot \boldsymbol{n}_i \,\mathrm{d}S - \int_\Sigma f_i \boldsymbol{u}_i \cdot \boldsymbol{n}_i \,\mathrm{d}\Sigma + \int_\Sigma f_i u_\Sigma \cdot \boldsymbol{n}_i \,\mathrm{d}\Sigma \tag{3.2.2}$$

$$= \int_{S_i} f_i \boldsymbol{u}_i \cdot \boldsymbol{n}_i \,\mathrm{d}S + \int_\Sigma f_i u_\Sigma - \boldsymbol{u}_i \cdot \boldsymbol{n}_i \,\mathrm{d}\Sigma \tag{3.2.3}$$

$$= \int_{V_i} \boldsymbol{\nabla}\cdot(f_i \boldsymbol{u}_i)\,\mathrm{d}V + \int_\Sigma f_i(u_\Sigma - \boldsymbol{u}_i \cdot \boldsymbol{n}_i)\,\mathrm{d}\Sigma \tag{3.2.4}$$

where the divergence theorem has been applied in the last line. Let v_i be the difference between

the speed of the interface and the normal speed of the fluid at the interface

$$v_i = u_\Sigma - \boldsymbol{u}_i \cdot \boldsymbol{n}_i \tag{3.2.5}$$

where $\boldsymbol{n}_{12}$ is the normal of Σ pointing from V_1 into V_2. Due to the definition of the normal $\boldsymbol{n}_{12}$, on Σ, $\boldsymbol{n}_1 = \boldsymbol{n}_{12}$ and $\boldsymbol{n}_2 = -\boldsymbol{n}_{12}$. We also define the jump of a function across the boundary to be

$$[\![f]\!] = f_1(\boldsymbol{x}, t) - f_2(\boldsymbol{x}, t). \tag{3.2.6}$$

Summing Eq. (3.2.1) over $i = 1, 2$, and using Eq.(3.2.4), Eq.(3.2.5) and Eq.(3.2.6), gives our required identity

$$\frac{\mathrm{D}}{\mathrm{D}t}\int_V f \, \mathrm{d}V = \int_V \left(\frac{\partial f}{\partial t} + \boldsymbol{\nabla}\cdot(f\boldsymbol{u})\right) \, \mathrm{d}V + \int_\Sigma [\![fv]\!] \, \mathrm{d}\Sigma. \tag{3.2.7}$$

This is Reynolds transport theorem with an additional term to account for the discontinuity of a field across Σ.

3.2.1.1 Conservation of mass

Replacing f with ρ in Eq. (3.2.7) leads to

$$\frac{\mathrm{D}}{\mathrm{D}t}\int_V \rho \, \mathrm{d}V = \int_V \left(\frac{\partial \rho}{\partial t} + \boldsymbol{\nabla}\cdot(\rho\boldsymbol{u})\right) \, \mathrm{d}V + \int_\Sigma [\![\rho v]\!] \, \mathrm{d}\Sigma. \tag{3.2.8}$$

Away from the interface, conservation of mass holds

$$\boxed{\frac{\partial \rho}{\partial t} + \boldsymbol{\nabla}\cdot(\rho\boldsymbol{u}) = 0,} \tag{3.2.9}$$

and as specified, mass is conserved over the entire volume V

$$\frac{\mathrm{D}}{\mathrm{D}t}\int_V \rho \, \mathrm{d}V = 0. \tag{3.2.10}$$

The first two terms in Eq.(3.2.8) therefore vanish due to Eq. (3.2.9) and Eq. (3.2.10) leaving

$$\int_\Sigma [\![\rho v]\!] \, \mathrm{d}\Sigma = 0. \tag{3.2.11}$$

Since this holds for any Σ, the integrand must equal zero, which is evaluated to give

$$\boxed{\rho_1 v_1 = -\rho_2 v_2.} \tag{3.2.12}$$

The mass flux per unit area from volume 2 to volume 1 across the interface, referred to as mass flux density, is defined to be

$$\boxed{\dot{m} := \rho_1 v_1} \tag{3.2.13}$$

This equation states that the difference between the speed of the interface and the speed of the fluid at the interface is proportional to the mass flux density at that point.

3.2.1.2 Conservation of momentum

Replacing f with ρf in Eq. (3.2.7), and using again Eq. (3.2.9) and Eq. (3.2.10), gives a second useful identity:

$$\frac{\mathrm{D}}{\mathrm{D}t}\int_V \rho f \,\mathrm{d}V = \int_V \left(\frac{\partial \rho f}{\partial t} + \boldsymbol{\nabla}\cdot(\rho f \boldsymbol{u})\right)\,\mathrm{d}V + \int_\Sigma [\![\rho f v]\!]\,\mathrm{d}\Sigma. \tag{3.2.14}$$

This equation gives the basis to derive the remaining governing equations in the two volumes and across the interface. Replacing f in Eq. (3.2.14) with each component of the velocity $\boldsymbol{u}$ gives three equations that are combined to give the vector equation

$$\frac{\mathrm{D}}{\mathrm{D}t}\int_V \rho \boldsymbol{u} \,\mathrm{d}V = \int_V \left(\frac{\partial \rho \boldsymbol{u}}{\partial t} + \boldsymbol{\nabla}\cdot(\rho \boldsymbol{u}\boldsymbol{u})\right)\,\mathrm{d}V + \int_\Sigma [\![\rho \boldsymbol{u} v]\!]\,\mathrm{d}\Sigma. \tag{3.2.15}$$

A balance of momentum in an arbitrary volume, neglecting the body force due to gravity, is

$$\frac{\mathrm{D}}{\mathrm{D}t}\int_V \rho \boldsymbol{u} \,\mathrm{d}V = \int_S \mathcal{T}\cdot\boldsymbol{n}\,\mathrm{d}S - \int_\Sigma \sigma\mathcal{K}\boldsymbol{n}_{12}\,\mathrm{d}\Sigma, \tag{3.2.16}$$

where $\mathcal{T}$ is the viscous stress tensor, σ is the coefficient of surface tension and $\mathcal{K} = \boldsymbol{\nabla}\cdot\boldsymbol{n}_{12}$ is the local curvature of Σ. The left hand side is replaced using Eq. (3.2.15), to give

$$\int_V \left(\frac{\partial \rho \boldsymbol{u}}{\partial t} + \boldsymbol{\nabla}\cdot(\rho \boldsymbol{u}\boldsymbol{u})\right)\,\mathrm{d}V + \int_\Sigma [\![\rho \boldsymbol{u} v]\!]\,\mathrm{d}\Sigma = \int_S \mathcal{T}\cdot\boldsymbol{n}\,\mathrm{d}S - \int_\Sigma \sigma\mathcal{K}\boldsymbol{n}_{12}\,\mathrm{d}\Sigma. \tag{3.2.17}$$

The second term is simplified using the definition of v, Eq. (3.2.5), conservation of mass at the interface, Eq. (3.2.12), and the definition of $\dot{m}$, Eq. (3.2.13), to give

$$\int_V \left(\frac{\partial \rho \boldsymbol{u}}{\partial t} + \boldsymbol{\nabla}\cdot(\rho \boldsymbol{u}\boldsymbol{u})\right)\,\mathrm{d}V + \int_\Sigma \dot{m}[\![\boldsymbol{u}]\!]\,\mathrm{d}\Sigma = \int_S \mathcal{T}\cdot\boldsymbol{n}\,\mathrm{d}S - \int_\Sigma \sigma\mathcal{K}\boldsymbol{n}_{12}\,\mathrm{d}\Sigma. \tag{3.2.18}$$

The first term on the right hand side can be expanded as

$$\int_S \mathcal{T}\cdot\boldsymbol{n}\,\mathrm{d}S = \int_{S_1} \mathcal{T}\cdot\boldsymbol{n}_1\,\mathrm{d}S + \int_{S_2} \mathcal{T}\cdot\boldsymbol{n}_2\,\mathrm{d}S - \int_\Sigma [\![\mathcal{T}]\!]\cdot\boldsymbol{n}_{12}\,\mathrm{d}\Sigma. \tag{3.2.19}$$

Using Eq. (3.2.19) and the divergence theorem, Eq. (3.2.18) is written as a sum of a volume integral over V and a surface integral over the interface Σ,

$$\int_V \left(\frac{\partial \rho \boldsymbol{u}}{\partial t} + \boldsymbol{\nabla} \cdot (\rho \boldsymbol{u}\boldsymbol{u}) - \boldsymbol{\nabla} \cdot \mathcal{T} \right) \, \mathrm{d}V = - \int_\Sigma (\dot{m} [\![\boldsymbol{u}]\!] + [\![\mathcal{T}]\!] \cdot \boldsymbol{n}_{12} - \sigma \mathcal{K} \boldsymbol{n}_{12}) \, \mathrm{d}\Sigma. \tag{3.2.20}$$

Since this holds for any volume V and interface Σ, both integrands in Eq. (3.2.20) must equal zero, giving the well-known Euler equation in both V_1 and V_2,

$$\boxed{\frac{\partial \rho \boldsymbol{u}}{\partial t} + \boldsymbol{\nabla} \cdot (\rho \boldsymbol{u}\boldsymbol{u}) - \boldsymbol{\nabla} \cdot \mathcal{T} = 0,} \tag{3.2.21}$$

and a stress balance at Σ,

$$\boxed{\dot{m} [\![\boldsymbol{u}]\!] + [\![\mathcal{T}]\!] \cdot \boldsymbol{n}_{12} - \sigma \mathcal{K} \boldsymbol{n}_{12} = 0.} \tag{3.2.22}$$

3.2.1.3 Conservation of energy

Let e be the internal energy and $|\boldsymbol{u}|^2/2$ the kinetic energy of the fluid. Replacing f with $e + |\boldsymbol{u}|^2/2$ in Eq. (3.2.14), we have

$$\begin{aligned} \frac{\mathrm{D}}{\mathrm{D}t} \int_V \rho \left(e + \frac{|\boldsymbol{u}|^2}{2} \right) \, \mathrm{d}V = \int_V \left[\frac{\partial}{\partial t} \left(\rho \left(e + \frac{|\boldsymbol{u}|^2}{2} \right) \right) + \boldsymbol{\nabla} \cdot \left(\rho \boldsymbol{u} \left(e + \frac{|\boldsymbol{u}|^2}{2} \right) \right) \right] \, \mathrm{d}V \\ + \int_\Sigma [\![\rho v \left(e + \frac{|\boldsymbol{u}|^2}{2} \right)]\!] \, \mathrm{d}\Sigma. \end{aligned} \tag{3.2.23}$$

Equation (3.2.9) is used to give

$$\frac{\mathrm{D}}{\mathrm{D}t} \int_V \rho \left(e + \frac{|\boldsymbol{u}|^2}{2} \right) \, \mathrm{d}V = \int_V \rho \frac{\mathrm{D}}{\mathrm{D}t} \left(e + \frac{|\boldsymbol{u}|^2}{2} \right) \, \mathrm{d}V + \int_\Sigma [\![\rho v \left(e + \frac{|\boldsymbol{u}|^2}{2} \right)]\!] \, \mathrm{d}\Sigma. \tag{3.2.24}$$

The rate of change of energy in an arbitrary volume depends on energy flux through the boundary and work done against stresses and surface tension, that is

$$\frac{\mathrm{D}}{\mathrm{D}t} \int_V \rho \left(e + \frac{|\boldsymbol{u}|^2}{2} \right) \, \mathrm{d}V = - \int_S \boldsymbol{q} \cdot \boldsymbol{n} \, \mathrm{d}S + \int_S \boldsymbol{u} \cdot \mathcal{T} \cdot \boldsymbol{n} \, \mathrm{d}S - \int_\Sigma \sigma \mathcal{K} \boldsymbol{u}_\Sigma \cdot \boldsymbol{n}_{12} \, \mathrm{d}\Sigma, \tag{3.2.25}$$

where $\boldsymbol{q}$ is the energy flux. The left hand side is replaced using Eq. (3.2.24) to give

$$\int_V \rho \frac{\mathrm{D}}{\mathrm{D}t} \left(e + \frac{|\boldsymbol{u}|^2}{2} \right) \, \mathrm{d}V + \int_\Sigma [\![\rho v \left(e + \frac{|\boldsymbol{u}|^2}{2} \right)]\!] \, \mathrm{d}\Sigma = - \int_S \boldsymbol{q} \cdot \boldsymbol{n} \, \mathrm{d}S + \int_S \boldsymbol{u} \cdot \mathcal{T} \cdot \boldsymbol{n} \, \mathrm{d}S - \int_\Sigma \sigma \mathcal{K} u_\Sigma \, \mathrm{d}\Sigma. \tag{3.2.26}$$

The second term is simplified using the definition of v, Eq. (3.2.5), conservation of mass at the interface, Eq. (3.2.12), and the definition of $\dot{m}$, Eq. (3.2.13), to give

$$\int_V \rho \frac{\mathrm{D}}{\mathrm{D}t}\left(e+\frac{|\boldsymbol{u}|^2}{2}\right)\,\mathrm{d}V + \int_\Sigma \dot{m}[\![\left(e+\frac{|\boldsymbol{u}|^2}{2}\right)]\!]\,\mathrm{d}\Sigma = -\int_S \boldsymbol{q}\cdot\boldsymbol{n}\,\mathrm{d}S + \int_S \boldsymbol{u}\cdot\mathcal{T}\cdot\boldsymbol{n}\,\mathrm{d}S - \int_\Sigma \sigma\mathcal{K}u_\Sigma\,\mathrm{d}\Sigma. \tag{3.2.27}$$

As in the previous section, the second-to-last term is expanded to give

$$\int_S \boldsymbol{u}\cdot\mathcal{T}\cdot\boldsymbol{n}\,\mathrm{d}S = \int_{S_1} \boldsymbol{u}\cdot\mathcal{T}\cdot\boldsymbol{n}_1\,\mathrm{d}S + \int_{S_2} \boldsymbol{u}\cdot\mathcal{T}\cdot\boldsymbol{n}_2\,\mathrm{d}S - \int_\Sigma \boldsymbol{u}\cdot[\![\mathcal{T}]\!]\cdot\boldsymbol{n}_{12}\,\mathrm{d}\Sigma. \tag{3.2.28}$$

Using Eq. (3.2.28) and the divergence theorem, Eq. (3.2.27) becomes

$$\begin{aligned}&\int_V \left(\rho\frac{\mathrm{D}}{\mathrm{D}t}\left(e+\frac{|\boldsymbol{u}|^2}{2}\right) + \boldsymbol{\nabla}\cdot\boldsymbol{q} - \boldsymbol{\nabla}\cdot\mathcal{T}\cdot\boldsymbol{u}\right)\,\mathrm{d}V \\ &= -\int_\Sigma \left(\dot{m}[\![e+\frac{|\boldsymbol{u}|^2}{2}]\!] - [\![\boldsymbol{q}-\boldsymbol{u}\cdot\mathcal{T}]\!]\cdot\boldsymbol{n}_{12} - \sigma\mathcal{K}u_\Sigma\right)\,\mathrm{d}\Sigma.\end{aligned} \tag{3.2.29}$$

Again, since V and Σ can be any volume and interface, each integrand must equal zero. The first integrand gives conservation of internal and kinetic energy in both V_1 and V_2,

$$\rho\frac{\mathrm{D}}{\mathrm{D}t}\left(e+\frac{|\boldsymbol{u}|^2}{2}\right) + \boldsymbol{\nabla}\cdot\boldsymbol{q} - \boldsymbol{\nabla}\cdot\mathcal{T}\cdot\boldsymbol{u} = 0. \tag{3.2.30}$$

To eliminate kinetic energy, the dot product of $\boldsymbol{u}$ and Eq. (3.2.21) is subtracted from Eq. (3.2.30) to give an equation for internal energy alone

$$\boxed{\rho\frac{\mathrm{D}e}{\mathrm{D}t} + \boldsymbol{\nabla}\cdot\boldsymbol{q} = 0.} \tag{3.2.31}$$

The second integrand of Eq. (3.2.30) gives a balance of energy flux on Σ,

$$\boxed{\dot{m}[\![e+\frac{|\boldsymbol{u}|^2}{2}]\!] - [\![\boldsymbol{q}-\boldsymbol{u}\cdot\mathcal{T}]\!]\cdot\boldsymbol{n}_{12} - \sigma\mathcal{K}u_\Sigma = 0.} \tag{3.2.32}$$

3.2.2 Two-phase bubble model

Using the framework derived in Sec. 3.2.1, we now derive a model of a bubble of water vapour in liquid water under the effect of laser heating. The two volumes described in Sec. 3.2.1 are now taken to be vapour and liquid regions, where subscripts $i = v, l$ denote the vapour and liquid respectively. The single vapour region is entirely surrounded by an infinite region of liquid, as shown in Fig. 3.2.2. The vapour-liquid interface Σ is referred to as the 'bubble wall' and phase change between vapour and liquid occurs only at this interface. Phase change from liquid to vapour is referred to as vaporisation and phase change from vapour to liquid is condensation. The vapour surface corresponds exactly to the interface Σ, with outward pointing normal $\boldsymbol{n}_{vl}$,

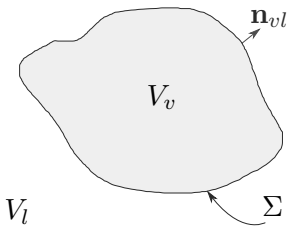


Figure 3.2.2 – A volume of vapour V_v surrounded by a volume of liquid V_l. The liquid region extends to infinity. The vapour-liquid interface Σ has normal $\boldsymbol{n}_{vl}$, pointing from the vapour into the liquid.

while the liquid surface corresponds to the same interface with the opposite normal $-\boldsymbol{n}_{vl}$. There is assumed to be no non-condensable gas or any other contaminants in the fluids. The vapour is taken to be compressible and inviscid while the liquid is incompressible and inviscid. Physical parameters are generally assumed to be constant unless otherwise stated, with values as given in Appendix A.

The aim is to produce a model in which we input the pulse pattern — the time dependent power output of the laser, $P(t)$ — and output the time dependent position of the bubble wall. As the laser is pulsed, energy is added to the system in the form of a source term in the energy equation of the liquid phase. We focus on a holmium laser which emits light at 2.1 µm. At this wavelength, negligible energy is absorbed by water vapour, therefore no source term is necessary in the energy equation of the vapour phase. In the liquid, energy transferred from the laser to the fluid is proportional to the absorption coefficient μ, and the time and space dependent intensity of the light – this is discussed in detail in Sec. 3.3.1. It is assumed that we begin with a microbubble; the initial conditions are discussed further in Sec. 3.3.6, after the model has been reduced to 1D.

Since we assume both the liquid and vapour to be inviscid, the stress tensor within each phase is

$$\mathcal{T} = -p_i \mathcal{I}, \tag{3.2.33}$$

where p_i is pressure and $\mathcal{I}$ is the identity.

In the compressible vapour, conservation of mass and momentum are given by Eq. (3.2.9) and Eq. (3.2.21) respectively

$$\frac{\partial \rho_v}{\partial t} + \boldsymbol{\nabla} \cdot (\boldsymbol{u}_v \rho_v) = 0, \tag{3.2.34}$$

$$\frac{\partial (\rho_v \boldsymbol{u}_v)}{\partial t} + \boldsymbol{\nabla} \cdot (\rho_v \boldsymbol{u}_v \boldsymbol{u}_v) = -\boldsymbol{\nabla} p_v, \tag{3.2.35}$$

with the vapour density given by the ideal gas law

$$\rho_v = \frac{p_v}{bT_v}. \tag{3.2.36}$$

where b is the specific gas constant. The ideal gas law is a commonly used simplification of the relationship between the density, pressure and temperature of a gas. As the liquid is taken to be incompressible, in this region, Eq. (3.2.9) and Eq. (3.2.21) become

$$\boldsymbol{\nabla} \cdot \boldsymbol{u}_l = 0, \tag{3.2.37}$$

$$\frac{\partial \boldsymbol{u}_l}{\partial t} + (\boldsymbol{u}_l \cdot \boldsymbol{\nabla})\boldsymbol{u}_l = -\frac{1}{\rho_l}\boldsymbol{\nabla} p_l. \tag{3.2.38}$$

At the far-field, as $|\boldsymbol{x}| \to \infty$, velocity and pressure satisfy respectively $\boldsymbol{u}_l(\boldsymbol{x}, t) \to \boldsymbol{0}$ and $p_l(\boldsymbol{x}, t) \to p_\infty$, where p_∞ is the far-field pressure, taken to be atmospheric pressure.

Boundary conditions for p_v and $\boldsymbol{u}_v$ are given implicitly by two the interface equations on Σ. At the bubble wall, conservation of mass flux is given by Eq. (3.2.12)

$$\rho_v v_v = -\rho_l v_l. \tag{3.2.39}$$

The stress balance at the interface is given by Eq. (3.2.22)

$$\dot{m}(\boldsymbol{u}_v - \boldsymbol{u}_l) = (p_v - p_l)\boldsymbol{n}_{vl} + \sigma\mathcal{K}\boldsymbol{n}_{vl}. \tag{3.2.40}$$

Physically, Eq. (3.2.40) reflects, on the left hand side, the jump in stresses across the boundary due to vaporisation, and on the right hand side, the jump in stresses due to a difference in pressure across the boundary plus stress due to surface tension.

Within both phases, conservation of internal energy density, Eq. (3.2.31), holds. We rewrite internal energy in terms of temperature using the relationship

$$c_{p,i} = \left(\frac{\partial e_i}{\partial T_i}\right)_p \tag{3.2.41}$$

where $c_{p,i}$ is the specific heat capacity at constant pressure of phase i, and the subscript p on the right hand side denotes that the derivative taken at constant pressure. Local energy flux is also written in terms of temperature as $\boldsymbol{q}_i = -K_i \boldsymbol{\nabla} T_i$, with K_i the thermal conductivity of phase i. Hence, in the vapour, the temperature profile is given by

$$\frac{\partial T_v}{\partial t} + \boldsymbol{u}_v \cdot \boldsymbol{\nabla} T_v = \frac{K_v}{\rho_v c_{p,v}} \nabla^2 T_v. \tag{3.2.42}$$

In the liquid, a source term is added to model the rate of laser energy transferred to the liquid

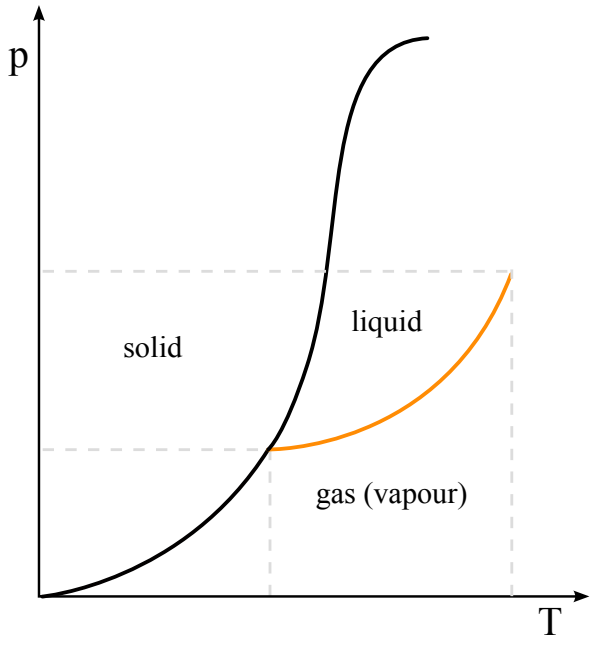


Figure 3.2.3 – Schematic of the phase diagram of water. The fluid at the bubble wall is at vaporisation point so sits on the orange line between the vapour and liquid phases. The Clausius-Clapeyron relation is an approximation of the pressure-temperature relationship along the orange line.

phase, $\dot{Q}(\boldsymbol{x}, t)$, the form of which is detailed in Sec. 3.3.1, giving

$$\frac{\partial T_l}{\partial t} + \boldsymbol{u}_l \cdot \boldsymbol{\nabla} T_l = \frac{K_l}{\rho_l c_{p,l}} \nabla^2 T_l + \frac{\dot{Q}(\boldsymbol{x}, t)}{\rho_l c_{p,l}}, \tag{3.2.43}$$

At the far-field, the liquid temperature decays to body temperature, $T_l \to T_\infty$ as $|\boldsymbol{x}| \to \infty$.

To close the system, three further conditions are specified on the interface. The first condition is continuity of temperature,

$$T_v(\boldsymbol{x}, t) = T_l(\boldsymbol{x}, t). \tag{3.2.44}$$

The second condition is that the vapour-liquid boundary must always be at the point of vaporisation, that is

$$T_v(\boldsymbol{x}, t) = T_{\text{vap}}, \tag{3.2.45}$$

on Σ, where T_{vap} is the pressure-dependent vaporisation temperature. The relationship between pressure and temperature of vaporisation of water is shown by the orange line on the phase diagram of water in Fig. (3.2.3): for a fluid to be at vaporisation point, the pressure and temperature must lie on this line. For a given pressure, one can identify the vaporisation temperature, or conversely, for a given temperature, one can identify the vaporisation pressure. The physical relationship between pressure and temperature of vaporisation is commonly

approximated by the Clausius-Clapeyron relation,

$$\frac{\partial T_{\text{vap}}}{\partial p_v} = \frac{bT_{\text{vap}}^2}{Lp_v}. \tag{3.2.46}$$

The final condition is given by the energy flux equation at the liquid-vapour interface, Eq. (3.2.32). The in internal energy either side of the boundary is expressed in terms of temperature by integrating the relationship given in Eq. (3.2.41). In the liquid this is integrated, assuming $c_{p,l}$ to be constant, to give

$$e_l = c_{p,l}(T_l - T_0) + e_{l,0}. \tag{3.2.47}$$

where T_0 is a reference temperature at which the internal energy is $e_{l,0}$. The vapour phase has an additional constant quantity of internal energy, L, the specific latent heat of vaporisation; latent heat is the quantity of energy required to change liquid to vapour. Therefore, in the vapour, Eq. (3.2.41) is integrated, assuming $c_{p,v}$ to also be constant, to give

$$e_v = c_{p,l}(T_{\text{vap}} - T_0) + e_{l,0} + c_{p,v}(T_v - T_{\text{vap}}) + L, \tag{3.2.48}$$

where T_{vap} is the temperature at which vaporisation occurred. The jump in internal energy at the interface is therefore

$$\begin{aligned} [\![e]\!] &= [c_{p,l}(T_{\text{vap}} - T_0) + e_{l,0} + c_{p,v}(T_v - T_{\text{vap}}) + L] - [c_{p,l}(T_l - T_0) + e_{l,0})] && (3.2.49)\\ &= L, && (3.2.50) \end{aligned}$$

where the last equality uses the fact that $T_v = T_l = T_{\text{vap}}$ at the interface. The energy flux term in Eq. (3.2.32), is written in terms of temperature, $\boldsymbol{q}_i = -K_i \boldsymbol{\nabla} T_i$, such that Eq. (3.2.32) becomes

$$\begin{aligned} \dot{m}L = \dot{m}&\left(\frac{|\boldsymbol{u}_l|^2}{2} - \frac{|\boldsymbol{u}_v|^2}{2}\right) \\ &+ (K_l \boldsymbol{\nabla} T_l - K_v \boldsymbol{\nabla} T_v) \cdot \boldsymbol{n}_{vl} + (p_v \boldsymbol{u}_v - p_l \boldsymbol{u}_l) \cdot \boldsymbol{n}_{vl} + \sigma \mathcal{K} u_\Sigma. \end{aligned} \tag{3.2.51}$$

This equation represents the balance between, on the left hand side, the rate that energy is absorbed as latent heat to vaporise liquid at the boundary and, on the right hand side: the rate that kinetic energy is lost or gained due to vaporisation; the conductive flow of energy on either side of the boundary; the work done against pressure; and the work done to overcome surface tension as the bubble expands. The mass flux density $\dot{m}$ is defined by Eq. (3.2.13),

$$\dot{m} := \rho_v v_v. \tag{3.2.52}$$

When $\dot{m} > 0$, vapour is being produced at the interface and liquid is being lost.

The form of the source term $\dot{Q}$ has not been specified, nor have the initial conditions; both will be determined for the specific case of a spherical bubble in the following section.

3.3 1D spherical bubble model

The 3D bubble model consists of ten coupled differential equations: three in the vapour, Eq. (3.2.34), Eq. (3.2.35) and Eq. (3.2.42) plus a constitutive law, Eq. (3.2.36); three in the liquid, Eq. (3.2.37), Eq. (3.2.38) and Eq. (3.2.43); and four at the vapour-liquid boundary Eq. (3.2.39), Eq. (3.2.40) Eq. (3.2.46) and Eq. (3.2.51). In 3D there is not a straightforward mathematical expression for the bubble wall, which inhabits a 2D surface in 3D space. By taking an assumption of spherical symmetry, the model reduces to 1D and the position of the bubble wall is entirely determined by a single scalar variable, the radius R. The model is reduced further in Sec. 3.3.3 by making the assumption of a diffusion dominated regime in the vapour; the resulting leading order equations can be solved quickly and easily using the method of lines. As discussed in Chapter 2, the P120 short pulses produce bubbles that are approximately spherical while the medium and long pulses produce more elongated bubbles. We therefore hypothesise that for some parameter regimes, a spherical model will give an acceptable prediction for the evolution of the bubble size over time.

In spherical coordinates, the geometry of the system is as shown in Fig. 3.3.1b. As a comparison, a schematic of the physical set-up during lithotripsy is shown alongside in Fig. 3.3.1a. With radial unit vector $\hat{r}$, the bubble is modelled as a region of vapour between $r = 0$ and $r = R(t)$, within a region of liquid from $r = R$ to $r \to \infty$, with a liquid-vapour interface at $r = R(t)$. We assume that no rotational motion occurs so that $\boldsymbol{u} = u\hat{\boldsymbol{r}}$. The speed of the boundary u_Σ now becomes $\dot{R} = \mathrm{d}R/\mathrm{d}t$ where a dot denotes a derivative with respect to time. A subscript R denotes a value evaluated at $r = R$. The governing equations in the spherically-symmetric coordinate system are given here, grouped into liquid equations, vapour equations and boundary equations.

In the liquid region, we have Eq. (3.2.43), Eq. (3.2.38) and Eq. (3.2.37)

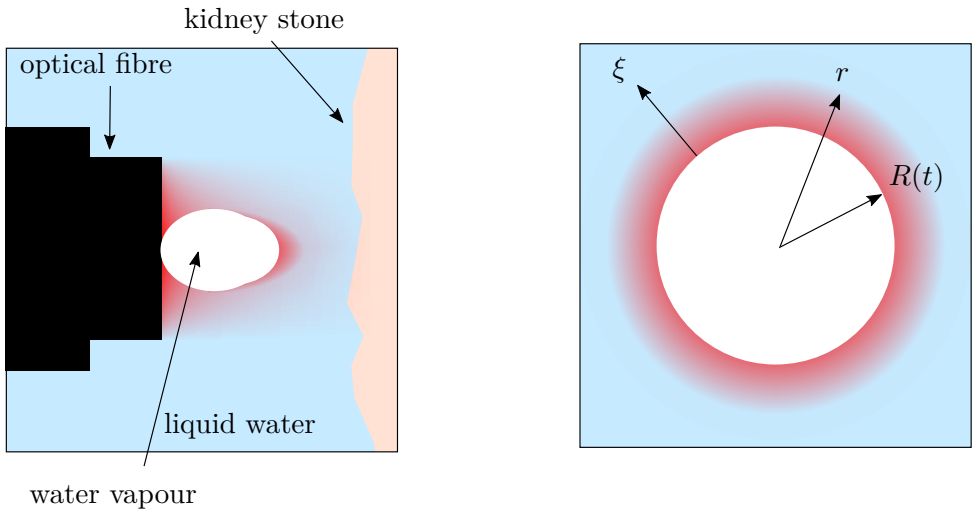
$$\frac{\partial T_l}{\partial t} + u_l \frac{\partial T_l}{\partial r} = \frac{K_l}{\rho_l c_{p,l}} \frac{1}{r^2} \frac{\partial}{\partial r}\left(r^2 \frac{\partial T_l}{\partial r}\right) + \frac{\dot{Q}}{\rho_l c_{p,l}}, \tag{3.3.1}$$

$$\rho_l \left(\frac{\partial u_l}{\partial t} + u_l \frac{\partial u_l}{\partial r}\right) = -\frac{\partial p_l}{\partial r}, \tag{3.3.2}$$

$$\frac{\partial}{\partial r}\left(r^2 u_l\right) = 0. \tag{3.3.3}$$

At the far-field, temperature, velocity and pressure satisfy respectively $T_l \to T_\infty$, $u_l \to 0$ and $p_l \to p_\infty$ as $r \to \infty$, where p_∞ is taken to be atmospheric pressure and T_∞ is body temperature.

The liquid equations can be reduced slightly by integrating Eq. (3.3.3) from the bubble



(a) **(b)**

Figure 3.3.1 – (b) Schematic of the physical system including laser fibre and kidney stone (not to scale). (a) Schematic of the simplified coordinate system of the spherically symmetric model. The variable ξ, which measures radial distance from the bubble wall, is introduced in Section 3.3.5. In both diagrams, the red denotes the region in which laser energy is absorbed by the liquid.

wall at $r = R$ to an arbitrary position $r > R$, which leads to

$$u_l(r,t) = u_{l,R}\frac{R^2}{r^2}. \tag{3.3.4}$$

Using Eq. (3.3.4) in Eq. (3.3.2) and integrating with respect to r from $r = R$ to $r = \infty$ we arrive at an expression for the motion of the bubble wall $\dot{R}$,

$$\rho_l\left(2u_{l,R}\dot{R} + R\frac{\mathrm{d}u_{l,R}}{\mathrm{d}t} - \frac{u_{l,R}^2}{2}\right) = p_{l,R}(t) - p_\infty. \tag{3.3.5}$$

This reduces exactly to the classic Rayleigh-Plesset equation [61] for bubble dynamics, in the case that the liquid at the bubble wall is moving at the same velocity as the boundary itself, $\mathrm{d}u_{l,R}/\mathrm{d}t = \dot{R}$.

In the vapour, we have Eq. (3.2.42), Eq. (3.2.35), Eq. (3.2.34) and Eq. (3.2.36) with spherical symmetry

$$\frac{\partial T_v}{\partial t} + u_v\frac{\partial T_v}{\partial r} = \frac{K_v}{\rho_v c_{p,v}}\frac{1}{r^2}\frac{\partial}{\partial r}\left(r^2\frac{\partial T_v}{\partial r}\right), \tag{3.3.6}$$

$$\rho_v\left(\frac{\partial u_v}{\partial t} + u_v\frac{\partial u_v}{\partial r}\right) = -\frac{\partial p_v}{\partial r}, \tag{3.3.7}$$

$$\frac{\partial \rho_v}{\partial t} + \frac{1}{r^2}\frac{\partial}{\partial r}\left(r^2 u_v \rho_v\right) = 0, \tag{3.3.8}$$

$$\rho_v = \frac{p_v}{bT_v}. \tag{3.3.9}$$

At $r = 0$, we impose the symmetry condition $\partial T_v/\partial r(0,t) = 0$.

At the bubble wall, in spherical coordinates, we have conservation of mass flux Eq. (3.2.39),

$$\rho_v(\dot{R} - u_{v,R}) = -\rho_l(\dot{R} - u_{l,R}), \tag{3.3.10}$$

as well as a stress balance, Eq. (3.2.40), conservation of energy flux, Eq. (3.2.51), and the Clausius-Clapeyron relation, Eq. (3.2.46),

$$\dot{m}(u_{v,R} - u_{l,R}) = p_v - p_l + \frac{2\sigma}{R}, \tag{3.3.11}$$

$$\dot{m}L = \dot{m}\left(\frac{u_{l,R}^2}{2} - \frac{u_{v,R}^2}{2}\right) + \left(K_l \frac{\partial T_l}{\partial r}\Big|_{r=R} - K_v \frac{\partial T_v}{\partial r}\Big|_{r=R}\right) + (u_{v,R}p_{v,R} - u_{l,R}p_{l,R}) + \frac{2\sigma\dot{R}}{R}, \tag{3.3.12}$$

$$\frac{\mathrm{d}T_{v,R}}{\mathrm{d}t} = \frac{bT_{v,R}^2}{Lp_{v,R}} \frac{\mathrm{d}p_{v,R}}{\mathrm{d}t}. \tag{3.3.13}$$

The mass flux density is defined by Eq. (3.2.52)

$$\dot{m} := \rho_v(\dot{R} - u_{v,R}). \tag{3.3.14}$$

We have arrived at a system of ten coupled equations including four partial differential equations (PDEs) five ordinary differential equations (ODEs) and one algebraic equation, for ten unknown variables: $T_l(r,t)$, $T_v(r,t)$, $p_v(r,t)$, $u_v(r,t)$, $\rho_v(r,t)$, $T_{v,R}(t)$, $p_{v,R}(t)$, $u_{v,R}(t)$, $\dot{m}(t)$ and $\dot{R}(t)$. It remains to specify the source term, $\dot{Q}$ in the liquid temperature equation, Eq. (3.3.1).

3.3.1 Laser energy source term

A novel aspect of this model is allowing the laser heating of the liquid to be both time and space dependent. This dependence is modelled via the source term, $\dot{Q}$, in Eq. (3.3.1). The source term is key to the model as it is dependent on the pulse shape, $P(t)$, of the laser; we aim to construct a model such that we input a chosen $P(t)$, simulate the energy transferred to the liquid, and observe the effect on the evolution of a bubble.

Physically, the laser power displays a Gaussian distribution across the fibre tip, and the beam penetrates a roughly cylindrical region of fluid. Negligible laser energy is absorbed by the vapour but energy is absorbed by the liquid, with absorption coefficient μ. The physical constant μ is determined by the wavelength of light and the medium in which it is travelling, in this case liquid water. The rate of energy transferred to the liquid is proportional to the time and space dependent intensity of the light, I, and therefore the source term in the liquid can be written as

$$\dot{Q}(r,R,t) = \mu I(r,R,t). \tag{3.3.15}$$

We allow intensity to be dependent on the bubble radius R as this variable determines the location of the vapour and liquid. Due to the absorption of laser energy by the liquid, the intensity of light decays exponentially with distance into the liquid from the fibre tip, with decay constant μ, as depicted by the red regions in Fig. 3.3.1a.

To maintain the symmetry of the model, the non-spherical input of laser energy to the liquid must be approximated by an appropriate spherically symmetric function, as depicted in Fig. 3.3.1b. Careful consideration is needed to derive a function $I(r, R, t)$ that reflects the key characteristics of the intensity distribution via an appropriate spherically symmetric function. Intensity is modelled as product of two functions, $I = f(r, R)P(t)$, a reasonable assumption since it is dependent on the temporal distribution of laser power and, independently, on spatial position in the liquid.

The form that the spatial function $f(r, R)$ should take is not immediately obvious but we do know its dimension; since P is power, f must have dimension $1/L^2$ where L denotes length, such that $I = f(r, R)P(t)$ has units of intensity. We also require that the rate of energy emitted by the laser is equal to the total rate of energy absorbed by the liquid, that is

$$\int_{V_l} \dot{Q} \, \mathrm{d}V_l = P(t). \tag{3.3.16}$$

With spherical symmetry, this condition can be expressed more simply as

$$4\pi\mu \int_R^\infty r^2 f(r, R)\mathrm{d}r = 1. \tag{3.3.17}$$

A final condition is that we wish to preserve the exponential decay of intensity with distance from the fibre tip into the liquid. A function that satisfies these requirements is

$$f(r, R) = \begin{cases} 0 & r < R \\ \frac{\mathrm{e}^{-\mu(r-R)}}{4\pi(R^2+2R/\mu+2/\mu^2)} & r \geq R. \end{cases} \tag{3.3.18}$$

This can be considered as a point-source emitting light radially from $r = 0$. The numerator $\mathrm{e}^{-\mu(r-R)}$ ensures exponential decay of I with distance from the laser source, with decay only occurring in the liquid, as represented by the red region in Fig. 3.3.1b. This spatial decay can be seen in Fig. 3.3.2, in which $f(r, R)$ is plotted against r for five values of R. The scaling factor in the denominator of f, dependent on R, ensures that Eq. (3.3.17) is satisfied. Due to the R dependent scaling, the spatial peak of intensity drops as the bubble expands. Due to using a spherical function to approximate a non-spherical phenomenon, we expect some discrepancy between the model and the physical system. For this reason, we introduce a constant fitting

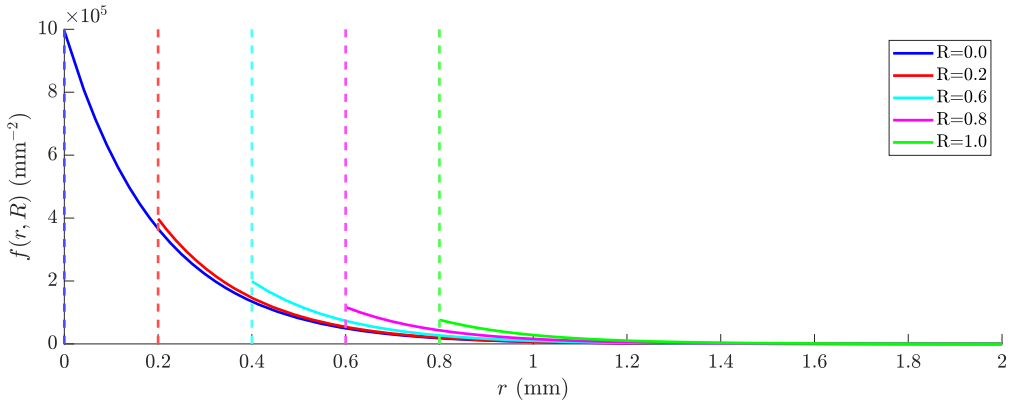


Figure 3.3.2 – The function $f(r, R)$ as given by Eq. (3.3.18) for varying R. The vertical dashed lines mark R for each case.

parameter, α. With the fitting parameter, the source term is

$$\dot{Q}(r, R, t) = \alpha\mu f(r, R)P(t). \tag{3.3.19}$$

The parameter α can be interpreted as the efficiency of optical absorption of the liquid.

3.3.2 Non-dimensionalisation

In this section we non-dimensionalise the model derived above. We denote dimensionless variables and constant with stars. We choose the characteristic length-scale to be the absorption length of the laser, defined as the inverse of the absorption coefficient $1/\mu$, giving $r^* = r\mu$ and $R^* = R\mu$. This is a sensible choice as it is length-scale of the region of liquid heated by the laser. A reference temperature is chosen to be the difference between the far-field liquid temperature, T_∞, and the vaporisation temperature at the far-field pressure, $T_{\text{vap},\infty}$; this reference temperature is denoted $\Theta := T_{\text{vap},\infty} - T_\infty$, giving $T_i^* = T_i/\Theta$ with $i = v, l$ and $T_\infty^* = T_\infty/\Theta$. Pressure is non-dimensionalised with respect to the far-field pressure, giving $p_i^* = p_i/p_\infty$.

We choose the reference time-scale to be $\tau = \sqrt{\rho_l/(p_\infty\mu^2)}$. This time-scale is chosen to balance the left hand side and right hand side of Eq. (3.3.5). This choice of τ gives a dominant balance between the dynamics of the bubble wall and the pressures at the bubble wall; it is the time-scale of a bubble expansion to a dimensional radius of $1/\mu$. With this time-scale, $t^* = t/\tau$ and $u_i^* = u_i\mu\tau$.

Motivated by the ideal gas equation, Eq. (3.3.9), we non-dimensionalise vapour density via $\rho_v^* = \rho_v(\Theta b)/p_\infty$. Liquid density is constant so does not require non-dimensionalisation. Due to the definition Eq. (3.3.10), $\dot{m}$ is non-dimensionalised as $\dot{m}^* = \dot{m}(\mu\Theta b\tau)/p_\infty$. The temporal laser function is non-dimensionalised by identifying the peak power of the pulse, $P_{\max}$, taken to be the highest power emitted from the laser over the duration of one pulse. This non-dimensionalisation leads to to $P^*(t^*) = P(t)/P_{\max}$. The spatial laser component f is non-

Dimensional quantity	Scaling	Dimensional quantity	Scaling
r	$1/\mu$	u_i	$1/(\mu\tau)$
R	$1/\mu$	ρ_v	$p_\infty/(\Theta b)$
p_i	p_∞	$\dot{m}$	$p_\infty/(\mu\Theta b\tau)$
T_i	$\Theta := T_{\mathrm{vap},\infty} - T_\infty$	P	$P_{\max}$
t	$\tau := \sqrt{\rho_l/(p_\infty\mu^2)}$	f	$\mu^2/(4\pi)$

Table 3.3.1 – Non-dimensionalisation of variables.

dimensionalised as $f^*(r^*, R^*) = f(r, R)(4\pi)/\mu^2$, with

$$f^*(r^*, R^*) = \frac{\mathrm{e}^{-(r^*-R^*)}}{((R^*)^2 + 2R^* + 2)}. \tag{3.3.20}$$

The scalings listed above are summarised in Table 3.3.1.

In the dimensionless equations, a number of dimensionless parameter groups are denoted λ_i: these parameter groups remain when the model is reduced in Sec. 3.3.3. Where a term is retained despite being small, the rationale for retaining it is given. The remaining dimensionless parameter groups are marked by square brackets: these parameter groups are dropped in the reduced model.

In the liquid, after non-dimensionalisation, Eq. (3.3.1) becomes

$$\frac{\partial T_l^*}{\partial t^*} + u_l^* \frac{\partial T_l^*}{\partial r^*} = \frac{\lambda_1}{(r^*)^2}\frac{\partial}{\partial r^*}\left((r^*)^2\frac{\partial T_l^*}{\partial r^*}\right) + \lambda_2\alpha f^*(r^*, R^*)P^*(t^*), \tag{3.3.21}$$

where $\lambda_1 = K_l\tau\mu^2/(c_{p,l}\rho_l)$ and $\lambda_2 = P_{\max}\mu^3\tau/(4\pi\Theta\rho_l c_{p,l})$. In the vapour, Eq. (3.3.6), Eq. (3.3.7), Eq. (3.3.8) and Eq. (3.3.9) yield

$$\lambda_T\left(\frac{\partial T_v^*}{\partial t^*} + u_v^*\frac{\partial T_v^*}{\partial r^*}\right) = \frac{1}{\rho_v^*(r^*)^2}\frac{\partial}{\partial r^*}\left((r^*)^2\frac{\partial T_v^*}{\partial r^*}\right), \tag{3.3.22}$$

$$\epsilon_p\rho_v^*\left(\frac{\partial u_v^*}{\partial t^*} + u_v^*\frac{\partial u_v^*}{\partial r^*}\right) = -\frac{\partial p_v^*}{\partial r^*}, \tag{3.3.23}$$

$$\frac{\partial \rho_v^*}{\partial t^*} + \frac{1}{(r^*)^2}\frac{\partial}{\partial r^*}\left((r^*)^2 u_v^*\rho_v^*\right) = 0, \tag{3.3.24}$$

$$\rho_v^* = p_v^*/T_v^*. \tag{3.3.25}$$

where $\lambda_T = c_{p,v}p_\infty/K_v\tau\Theta b\mu^2$ and $\epsilon_p = 1/\Theta b\tau^2\mu^2$, both of which are discussed further in Section 3.3.3.1. The boundary equations, Eq. (3.3.5), Eq. (3.3.10), Eq. (3.3.11), Eq. (3.3.12)

and Eq. (3.3.13) in terms of dimensionless variables are

$$2u^*_{l,R}\dot{R}^* + R^*\frac{\partial u^*_{l,R}}{\partial t^*} - \frac{(u^*_{l,R})^2}{2} = p^*_{l,R} - 1, \tag{3.3.26}$$

$$\left[\frac{p_\infty}{b\Theta\rho_l}\right]\rho^*_{v,R}(\dot{R}^* - u^*_{v,R}) = (\dot{R}^* - u^*_{l,R}), \tag{3.3.27}$$

$$\left[\frac{1}{\Theta b\tau^2\mu^2}\right]\dot{m}^*(u^*_{v,R} - u^*_{l,R}) = p^*_{v,R} - p^*_{l,R} + \frac{\lambda_4}{R^*}, \tag{3.3.28}$$

$$\frac{\mathrm{d}T^*_{v,R}}{\mathrm{d}t^*} = \frac{\lambda_3(T^*_{v,R})^2}{p^*_{v,R}}\frac{\mathrm{d}p^*_{v,R}}{\mathrm{d}t^*}, \tag{3.3.29}$$

where $\lambda_3 = b\Theta/L$ and $\lambda_4 = 2\sigma\mu/p_\infty$. The energy flux Eq. (3.3.12) becomes

$$\dot{m}^* = \left[\frac{1}{2\tau^2 L\mu^2}\right]\dot{m}^*((u^*_{l,R})^2 - (u^*_{v,R})^2) + \lambda_5\lambda_3\frac{\partial T^*_l}{\partial r^*}\Big|_{r^*=R*} - \left[\frac{K_v\Theta\tau\mu^2}{p_\infty}\right]\lambda_3\frac{\partial T^*_v}{\partial r^*}\Big|_{r^*=R^*} + \lambda_3(u^*_{v,R}p^*_{v,R} - u^*_{l,R}p^*_{l,R}) + \lambda_3\lambda_4\frac{\dot{R}^*}{R^*}, \tag{3.3.30}$$

where $\lambda_5 = K_l\Theta\tau\mu^2/p_\infty$. The dimensionless mass flux density derives from Eq. (3.3.14),

$$\dot{m}^* = \rho^*_{v,R}(\dot{R}^* - u^*_{v,R}). \tag{3.3.31}$$

The definitions and interpretations of the dimensionless parameter groups λ_i are given in Table 3.3.2. At the bubble wall we have $T^*_v = T^*_l$ and as $r^* \to \infty$, $p^*_l \to 1$ and $T^*_l \to T_\infty/\Theta$.

3.3.3 Model reduction

The system described above consists of four PDEs and five ODEs for ten unknown variables, with ten dimensionless parameter groups, listed in Table 3.3.2. We anticipate that parameter sizes in the model can be exploited to reduce the vapour equations to ODEs. Specifically, when the two dimensionless parameter groups in Eq. (3.3.22) and Eq. (3.3.23) are sufficiently small, we find that the vapour temperature and pressure can be considered spatially uniform and it follows that the vapour density is also spatially uniform. The vapour velocity is not found to be uniform at leading order but decouples from the other equations such that in the reduced model, only ODEs remain in the vapour region.

The simplification of uniform vapour pressure and temperature leads to a reduction of the interface equations, by which we arrive at the Rayleigh-Plesset equation for the bubble radius and an equation for the vapour temperature that is similar in form to that of Prosperetti et al. [26] — the form of the vapour pressure equation and its physical interpretation is discussed further in Sec. 3.3.4. Therefore, by making as assumption that the parameters in Eq. (3.3.22) and Eq. (3.3.23) are small, we are able to utilise two well-established equations from the bubble modelling literature.

Spatial uniformity of the variables in the vapour facilitates a simple and quick method

Notation	Dimensionless parameter group	Interpretation of ratios	Value
λ_1	$K_l\tau\mu^2/(c_{p,l}\rho_l)$	Time-scale τ to time taken for heat to diffuse in liquid over distance $1/\mu$	1.5×10^{-4}
λ_2	$P_{\max}\mu^3\tau/(4\pi\Theta\rho_l c_{p,l})$	Time-scale τ to time taken for laser to heat liquid by reference temperature Θ	$1 - 10$ for clinically relevant parameters
λ_3	$b\Theta/L$	Energy required to heat liquid by Θ to energy required to vaporise liquid	1.3×10^{-2}
λ_4	$2\sigma\mu/p_\infty$	Force due to surface tension to inertial forces	7.0×10^{-3}
λ_5	$K_l\Theta\tau\mu^2/p_\infty$	Heat flux in liquid over time-scale τ to work done over distance $1/\mu$ per unit surface area of bubble	2.0×10^{-1}
ϵ_p	$1/(\Theta b\tau^2\mu^2)$	Inertial forces to pressure forces	3.4×10^{-3}
λ_T	$c_{p,v}p_\infty/(K_v\tau\Theta b\mu^2)$	Time taken for heat to diffuse in vapour by distance $1/\mu$ to time-scale τ	$\leq \epsilon_p$, see Sec. 3.3.3.1
	$p_\infty/(\Theta b\rho_l)$	Vapour density to liquid density	3.4×10^{-3}
	$1/(2L\tau^2\mu^2)$	Kinetic energy lost in phase change to latent heat gained in phase change	2.1×10^{-5}
	$K_v\Theta\tau\mu^2/p_\infty$	Heat flux in vapour over time-scale τ to work done over distance $1/\mu$ per unit surface area of bubble	7.9×10^{-3}

Table 3.3.2 – Dimensionless parameter groups. Typical values are calculated for water with all parameters as given in Appendix A.

of numerical solution. The system in Sec. 3.3.2 includes a moving boundary at $r = R$, with the vapour equations solved in the region $r \leq R$ and the liquid equations solved in the region $r \geq R$. After eliminating spatial dependence in the vapour, a change of variable to $\xi = r - R$ is applied to the remaining equations, as shown in Sec. 3.3.5, resulting in a time-independent spatial domain.

Throughout the analysis below, we choose to retain terms of size $\lambda_3 = \mathrm{O}(10^{-2})$ and larger in the leading order equations. This choice is to ensure that the right hand side of the Clausius-Clapeyron relation, Eq. (3.3.29) remains non-zero at leading order. Should we allow the the right hand side of Eq. (3.3.29) to be zero, the additional assumption of spatial uniformity would result in a vapour temperature that does not deviate from its initial value. We find from the numerical solutions of the system presented in Chapter 4 that the vapour temperature does vary by an order 1 amount, supporting the choice to retain terms of size $\lambda_3 = \mathrm{O}(10^{-2})$.

The reduction is detailed in the following two sections. Boxes mark equations that, in their leading order form, are included in the final model.

3.3.3.1 Identification of small parameters

The first parameter that we utilise in the model reduction appears on the left hand side of the vapour momentum equation, Eq. (3.3.23),

$$\epsilon_p := \frac{1}{\Theta b \tau^2 \mu^2} = \mathrm{O}(10^{-3}). \tag{3.3.32}$$

This parameter gives the balance between inertial forces and pressure forces in the vapour. The small size of ϵ_p is significant as it indicates that the spatial gradient of the vapour pressure in Eq. (3.3.23) is approximately zero, allowing us to make the assumption of uniform vapour pressure.

The second parameter we utilise appears on the left hand side of Eq. (3.3.22)

$$\lambda_T := \frac{c_{p,v} p_\infty}{K_v \tau \Theta b \mu^2}. \tag{3.3.33}$$

This parameter is significant as it determines the relative dominance of thermal advection and diffusion in the vapour. Analysing Eq. (3.3.22), we identify two different regimes based on the magnitude of λ_T. If $\lambda_T \gg 1$, we have

$$\left(\frac{\partial T_v^*}{\partial t^*} + u_v^* \frac{\partial T_v^*}{\partial r^*} \right) \approx 0, \tag{3.3.34}$$

and the rate of change of vapour temperature is dominated by advection over diffusion. The physical parameter values in our system give $\lambda_T = \mathrm{O}(10^2)$, and therefore advection dominated

temperature. Conversely, if $\lambda_T \ll 1$,

$$\frac{1}{\rho_v^*(r^*)^2}\frac{\partial}{\partial r^*}\left((r^*)^2\frac{\partial T_v^*}{\partial r^*}\right) \approx 0. \tag{3.3.35}$$

This can be integrated subject to the symmetry condition $\partial T_v^*/\partial r(0,t^*) = 0$, to give T_v^* approximately uniform. The case $\lambda_T \ll 1$ corresponds to high diffusivity in the vapour due to either high thermal conductivity or low density, or both.

The assumption of uniform temperature within a vapour bubble is common in the literature. Brennen states from the outset, and without explanation, the assumption of uniform vapour temperature in his model of the expansion of a spherical vapour bubble [62]. Papers by Plesset and Zwick [18], and Plesset and Prosperetti [17] both implicitly assume uniform vapour temperature by neglecting temperature gradients on the vapour side when considering heat flow to the bubble wall. A model of Prosperetti et al. does allow spatial variation in temperature within the bubble but the results display significant gradients only in a thin region at the bubble wall and with these gradients only occurring as the bubble collapses to a minimum size [26]. Zhong et al. assume a priori that a temperature gradient only occurs in a boundary region at the bubble wall and specify this to be of a linear form [53].

We choose to proceed with the assumption of a diffusion dominated regime, which leads to a spatially uniform vapour pressure. Since we choose to retain terms of size $\lambda_3 = \mathrm{O}(10^{-2})$ and larger, for the reason of retaining the right hand side of Eq. (3.3.29), we must put ourselves in the regime $\lambda_T \leq \mathrm{O}(10^{-3})$ to be able to neglect spatial variations in the vapour temperature. For this reason, we set $\lambda_T = \epsilon_T \leq \mathrm{O}(\epsilon_p)$, with $\epsilon_p = \mathrm{O}(10^{-3})$. This choice is supported by the points discussed above. In particular, the reduction facilitated by this regime will leave us with only ODEs in the vapour and, as detailed below, leads to an energy flux balance at the boundary wall very similar to that in the work of Plesset and others [17, 18, 26].

There are two considerations when assessing if uniform vapour temperature is a reasonable model. Firstly, we can check if the temperature within the bubble is, in fact, approximately uniform. Using the second model presented in Chapter 5, which does not have any restrictions on the temperature profile, we can assess if significant temperature gradients do form in the vapour. This will be discussed in Chapter 5. Secondly, if spatial variations of vapour temperature do exist, we can ask if that has a significant effect on the dynamics of the bubble. With a comparison in Chapter 4 between the experimental data and the predictions of the spherical model, we will see a good match in the regime of approximately spherical bubbles, subject to two fitting parameters. With this result we are reassured that the macroscopic bubble dynamics are not sensitive to spatial fluctuations in vapour temperature.

3.3.3.2 Reduction

The model reduction proceeds with the fixed parameter sizes $\epsilon_p = \mathrm{O}(10^{-3})$ and $\epsilon_T \leq \mathrm{O}(\epsilon_p)$, dropping any terms of size ϵ_p or smaller. We do not consider regimes where these parameters take different values. Other parameter values are given in Appendix A.

Dropping small terms and applying the symmetry condition $\partial T_v^*/\partial r(0,t^*) = 0$, Eq. (3.3.22) leads to a uniform vapour temperature at leading order

$$T_v^*(r,t^*) = T_{v,R}^*(t^*). \tag{3.3.36}$$

Physically, Eq. (3.3.36) means that any spatial temperature fluctuations are smoothed out due to the dominating effect of thermal diffusion. Similarly, dropping small terms in Eq. (3.3.23), and applying the boundary condition $p_v^*(R^*) = p_{v,R}^*$, leads to a uniform pressure

$$p_v^*(r^*,t^*) = p_{v,R}(t^*). \tag{3.3.37}$$

We interpret this as the vapour reaching instantaneous mechanical equilibrium at leading order.

The ideal gas law, Eq. (3.3.25), with the expressions above for T_v^* and p_v^* gives a uniform density,

$$\rho_v^* = \rho_{v,R}^*. \tag{3.3.38}$$

With ρ_v^* constant, Eq. (3.3.24) is integrated with resepct to r^* from zero to an arbitrary distance, giving the the vapour speed

$$u_v^* = -\frac{r^*}{3\rho_{v,R}^*}\frac{\mathrm{d}\rho_{v,R}^*}{\mathrm{d}t^*}. \tag{3.3.39}$$

The mass flux density may now be expressed as

$$\dot{m}^* = \rho_{v,R}^*\left(\dot{R}^* + \frac{R^*}{3\rho_{v,R}^*}\frac{\mathrm{d}\rho_{v,R}^*}{\mathrm{d}t^*}\right). \tag{3.3.40}$$

To interpret the meaning of Eq. (3.3.40), we multiply both sides by $4\pi(R^*)^2$ and combine the right hand side into a single derivative, giving

$$4\pi(R^*)^2\dot{m}^* = \frac{\mathrm{d}}{\mathrm{d}t^*}\left(\frac{4\pi(R^*)^3\rho_{v,R}^*}{3}\right). \tag{3.3.41}$$

The left hand side is the total mass flux from liquid to vapour at the bubble wall and the right hand side is the rate of change of mass of vapour, as expected.

Turning our attention to the boundary equations, the left hand side of Eq. (3.3.27) is

of size 10^{-3} and can be dropped, leaving

$$u^*_{l,R} = \dot{R}^*. \tag{3.3.42}$$

This equation tells us that, to a reasonable approximation, the liquid at the bubble wall moves at the speed of the bubble wall. A relationship between the velocity of the bubble wall and the velocity of the vapour at this interface is found by evaluating Eq. (3.3.39) at $r = R$ and using Eq. (3.3.40),

$$u^*_{v,R} = \dot{R}^* - \frac{\dot{m}^*}{\rho^*_{v,R}}. \tag{3.3.43}$$

On the vapour side of the bubble wall, there is a significant difference between the velocities of the vapour and the interface itself due to phase change. The difference in the behavior of the vapour and liquid is due to the large difference in their densities: during phase change, a mass of liquid with negligible volume becomes a non-negligible volume of vapour.

From Eq. (3.3.28), we find that the liquid pressure at the bubble wall is equal to the vapour pressure plus surface tension

$$p^*_{l,R} = p^*_{v,R} + \frac{\lambda_4}{R^*}, \tag{3.3.44}$$

where the $1/R^*$ surface tension term has been retained, despite λ_4 being of order 10^{-3}, to account for cases when $R^* \leq \lambda_4$ and the effect of surface tension becomes important. Due to our choice of initial conditions, as discussed in Sec. 3.3.6, we will have $R^* \leq \lambda_4$ at early times. Equation (3.3.26), using Eq. (3.3.42) and Eq. (3.3.44), can be written as the Rayleigh-Plesset equation,

$$\boxed{R^*\ddot{R}^* + \frac{3}{2}(\dot{R}^*)^2 = p^*_{v,R} - 1 - \frac{\lambda_4}{R^*}.} \tag{3.3.45}$$

The final equation to consider is the boundary energy flux equation, Eq. (3.3.30), repeated here for convenience

$$\left[\frac{1}{2\tau^2 L\mu^2}\right]\dot{m}^*((u^*_{l,R})^2 - (u^*_{v,R})^2) + \lambda_5\lambda_3\frac{\partial T^*_l}{\partial r^*}\Big|_{r^*=R*} - \left[\frac{K_v\Theta\tau\mu^2}{p_\infty}\right]\lambda_3\frac{\partial T^*_v}{\partial r^*}\Big|_{r^*=R^*} + \lambda_3(u^*_{v,R}p^*_{v,R} - u^*_{l,R}p^*_{l,R}) + \lambda_3\lambda_4\frac{\dot{R}^*}{R^*}. \tag{3.3.46}$$

The size of each term is evaluated to find the leading order balance. The left hand side is of order 1, while the first term on the right hand side is of order 10^{-3}, assuming that $u^*_{l,R}$ and $u^*_{v,R}$ remain of order 1. In the second term on the right hand side, although $\lambda_3\lambda_5$ is of order 10^{-3}, we anticipate a boundary layer on the liquid side of the bubble wall, in which case we expect

$\lambda_3\lambda_5 \partial T_l^*/\partial r^*|_{r^*=R^*}$ to be of order 1 or greater. The third term on the right hand side is of order 10^{-3} and we do not expect a boundary layer here due to the vapour temperature being uniform. The fourth term on the right hand side is of order λ_3, which is larger than our small parameter ϵ_p, so this term is retained at leading order. While we do not drop terms of order λ_3 throughout this reduction, in our analysis of the equations, we do acknowledge that they may be small in comparison to terms of order 1. The fifth term is of order 10^{-3} but, as before, we retain this to account for when $R^* \leq \lambda_4$. Hence, Eq. (3.3.30), can be reduced to

$$\dot{m}^* = \lambda_5\lambda_3 \frac{\partial T_l^*}{\partial r^*}\Big|_{r^*=R*} + \lambda_3(u_{v,R}^* p_{v,R}^* - u_{l,R}^* p_{l,R}^*) + \lambda_3\lambda_4 \frac{\dot{R}^*}{R^*}. \tag{3.3.47}$$

The terms that remain on the right hand side are: the conductive flow of energy on the liquid side of the boundary; the work done against pressure; and the work done to overcome surface tension as the bubble expands. The leading order equation does not include terms relating to kinetic energy or the conductive flow of energy on the vapour side of the boundary. Using Eq. (3.3.39), Eq. (3.3.42) and Eq. (3.3.44), to replace $u_{v,R}^*$, $u_{l,R}^*$ and $p_{l,R}^*$ respectively in Eq. (3.3.47), we have

$$\dot{m}^* \left(1 + \frac{\lambda_3 p_{v,R}}{\rho_{v,R}}\right) = \lambda_5\lambda_3 \frac{\partial T_l^*}{\partial r^*}\Big|_{r^*=R*}. \tag{3.3.48}$$

Without the second term on the left hand side, this equation tells us that the energy flux supplied to the bubble wall by the liquid is balanced by the energy flux taken in phase change, which is a common assumption, as discussed further in Sec. 3.3.4 [17, 18, 26]. The second term on the left hand side of Eq. (3.3.48) gives a correction of order λ_3 to this flux balance. Using Eq. (3.3.40) to eliminate, $\dot{m}^*$, Eq. (3.3.47) is written as

$$\left(\rho_{v,R}^* + \lambda_3 p_{v,R}^*\right)\left(\frac{R^*}{3\rho_{v,R}^*}\frac{\mathrm{d}\rho_{v,R}^*}{\mathrm{d}t} + \dot{R}^*\right) = \lambda_3\lambda_5 \frac{\partial T_l^*}{\partial r^*}\Big|_{r^*=R^*}. \tag{3.3.49}$$

The dimensionless Clausius-Clapeyron relation, Eq. (3.3.29), and the ideal gas relation, Eq. (3.3.25), are used to express Eq. (3.3.49) as a differential equation for $p_{v,R}^*$,

$$\boxed{\frac{\mathrm{d}p_{v,R}^*}{\mathrm{d}t^*} = \frac{3}{R^*}\left(1 - \lambda_3 T_{v,R}^*\right)^{-1}\left[\lambda_3\lambda_5\left(1 + \lambda_3 T_{v,R}^*\right)^{-1} T_{v,R}^* \frac{\partial T_l^*}{\partial r^*}\Big|_{r^*=R^*} - p_{v,R}^* \dot{R}^*\right].} \tag{3.3.50}$$

This equation shows that the vapour pressure varies due to two effects. The first of these, expressed by the first term in the square brackets in Eq. (3.3.50), is the inflow of energy to the bubble wall due to the local temperature gradient on the liquid side. This inflow of energy causes phase change from liquid to vapour, increasing the mass of vapour and hence the vapour pressure. The second effect that causes a change in vapour pressure is bubble expansion, with the second term in the square brackets in Eq. (3.3.50) being the velocity of the bubble wall. As the bubble expands, the vapour expands and the pressure drops.

In summary, the reduced model has uniform vapour pressure and temperature, equal to their boundary values, $p_v^* = p_{v,R}^*$, $T_v^* = T_{v,R}^*$. The closed system consists of three ODEs, Eq. (3.3.29), Eq. (3.3.45) and Eq. (3.3.50), plus one PDE, Eq. (3.3.21). These four differential equations are solved to find just four unknown variables: $R^*(t)$, $T_l^*(r,t)$, $T_v^*(t)$ and $p_v^*(t)$. This is much simpler in comparison to the full system described at the start of Sec. 3.3, of four PDEs and five ODEs for ten unknown variables. There are five remaining dimensionless parameter groups, λ_1-λ_5, as given in Table 3.3.2. The simpler form of the reduced model allows for a numerical solution via the method of lines, as detailed in Sec. 3.4.

3.3.4 Alternative derivation of vapour pressure equation

Here we present an alternative derivation of the vapour pressure equation, arriving at a slightly simplified form of Eq. (3.3.50). This derivation provides more insight into the physical meaning of the vapour pressure equation but it will be shown to miss an effect that is captured in Eq. (3.3.50).

Returning to dimensional variables, we take the vapour temperature, pressure and density to be uniform. Considering a balance of energy flux at the bubble wall, it is assumed that conductive heat flow supplies energy to the boundary which is entirely used in phase change of liquid to vapour, with all other energy effects neglected. This assumption is made regularly by Plesset and others [18, 27, 61]. The rate of energy transferred to the boundary from the hot liquid is

$$\dot{Q}_B = 4\pi R^2 K_l \frac{\partial T}{\partial r}\Big|_{r=R}, \tag{3.3.51}$$

and the rate of energy used for the mass flux of liquid to vapour is

$$\dot{Q}_V = 4\pi R^2 L\dot{m}. \tag{3.3.52}$$

With the assumption that all thermal energy supplied to the boundary is used in phase change, we equate Eq. (3.3.51) and Eq. (3.3.52) giving

$$L\dot{m} = K_l \frac{\partial T}{\partial r}\Big|_{r=R}. \tag{3.3.53}$$

This is the dimensional form of Eq. (3.3.48), without the order λ_3 correction. The mass flux can be expressed in terms of the rate of change of mass of the bubble

$$4\pi R^2 \dot{m} = \frac{\mathrm{d}}{\mathrm{d}t}\left(\frac{4\pi}{3} R^3 \rho_v\right), \tag{3.3.54}$$

from which, Eq. (3.3.53) becomes

$$\frac{\mathrm{d}}{\mathrm{d}t}(R^3\rho_v) = \frac{3K_l R^2}{L}\frac{\partial T}{\partial r}\Big|_{r=R}. \tag{3.3.55}$$

Using the ideal gas relation Eq. (3.3.9) to replace ρ_v in Eq. (3.3.55) and expanding the time derivative leads to

$$\frac{p_v}{bT_v}\frac{\mathrm{d}}{\mathrm{d}t}(R^3) + \frac{R^3}{bT_v}\frac{\mathrm{d}p_v}{\mathrm{d}t} - \frac{R^3 p_v}{bT_v^2}\frac{\mathrm{d}T_v}{\mathrm{d}t} = \frac{3R^2K_l}{L}\frac{\partial T}{\partial r}\Big|_{r=R}. \tag{3.3.56}$$

The Clausius-Clapyron relation, Eq. (3.3.13), is used here to eliminate $\mathrm{d}T_v/\mathrm{d}t$ in Eq. (3.3.56), resulting in a differential equation for vapour pressure

$$\frac{\mathrm{d}p_v}{\mathrm{d}t} = \frac{3}{R}\left(1 - \frac{bT_v}{L}\right)^{-1}\left[\frac{bK_l}{L}T_v\frac{\partial T_l}{\partial r}\Big|_{r=R} - p_v\dot{R}\right]. \tag{3.3.57}$$

Non-dimensionalising as in Sec. 3.3.2, Eq. (3.3.57) becomes

$$\frac{\mathrm{d}p_v^*}{\mathrm{d}t^*} = \frac{3}{R^*}\left(1 - \lambda_3 T_v^*\right)^{-1}\left[\lambda_3\lambda_5 T_v^*\frac{\partial T_l^*}{\partial r^*}\Big|_{r^*=R^*} - p_v^*\dot{R}^*\right]. \tag{3.3.58}$$

This equation is also almost identical to Eq. (3.3.50) at leading order in ϵ_p and ϵ_T. The discrepancy between Eq. (3.3.50) and Eq. (3.3.58) comes from neglecting the work done by pressure and surface tension in this alternative derivation whereas the terms relating to these effects were retained in Eq. (3.3.47). Equation (3.3.58) is also similar in form to Eq. (13) of Prosperetti et al. [26] but differs due to their assumptions that the bubble contains non-condensible gas rather than vapour, and that the surrounding liquid is cool. These assumptions mean that Prosperetti et al. neglect mass transfer at the bubble wall. In what follows we employ Eq. (3.3.50).

3.3.5 Model summary and change of variable

It is convenient to rewrite the reduced system in terms of the dimensionless variable $\xi^* = r^* - R^*$, such that position in the liquid is measured from the bubble wall. The change of variable from r^* to ξ^* results in a fixed spatial liquid domain, $0 \leq \xi^* < \infty$, instead of the time dependent domain, $R^*(t^*) \leq r^* < \infty$. A fixed domain makes the numerical scheme for Eq. (3.3.21) simple, as discussed in Sec. 3.4. The remaining differential equations are ODEs in time and are therefore independent of the spatial domain.

In this coordinate system, taking only the leading order terms of the reduced model, we have the Rayleigh-Plesset equation, Eq. (3.3.45), giving the position of the bubble wall

$$R^*\ddot{R}^* + \frac{3}{2}(\dot{R}^*)^2 = p_v^* - 1 - \frac{\lambda_4}{R^*}, \tag{3.3.59}$$

an equation for the vapour pressure, Eq. (3.3.50),

$$\frac{\mathrm{d}p_v^*}{\mathrm{d}t^*} = \frac{3}{R^*}\left(1-\lambda_3 T_v^*\right)^{-1}\left[\lambda_3\lambda_5\left(1+\lambda_3 T_v^*\right)^{-1} T_v^* \frac{\partial T_l^*}{\partial \xi^*}\Big|_{\xi^*=0} - p_v^*\dot{R}^*\right], \tag{3.3.60}$$

the Clausius-Clapeyron relation, Eq. (3.3.29), to give the vapour temperature

$$\frac{\mathrm{d}T_v^*}{\mathrm{d}t^*} = \frac{\lambda_3 (T_v^*)^2}{p_v^*}\frac{\mathrm{d}p_v^*}{\mathrm{d}t^*}, \tag{3.3.61}$$

the liquid temperature equation, Eq. (3.3.21),

$$\frac{\partial T_l^*}{\partial t^*} + \dot{R}^*\frac{\partial T_l^*}{\partial \xi^*}\left(\frac{(R^*)^2}{(\xi^*+R^*)^2}-1\right) = \frac{\lambda_1}{(\xi^*+R^*)^2}\frac{\partial}{\partial \xi^*}\left((\xi^*+R^*)^2\frac{\partial T_l^*}{\partial \xi^*}\right) + \alpha\lambda_2 f^*(\xi^*,R^*)P^*(t^*), \tag{3.3.62}$$

with the function f^*, Eq. (3.3.18), now given by

$$f^*(\xi^*,R^*) = \frac{\mathrm{e}^{-\xi^*}}{((R^*)^2+2R^*+2)}. \tag{3.3.63}$$

At the bubble wall, $\xi^* = 0$, we have continuity of temperature, $T_l^*(0,t^*) = T_v^*$, and as $\xi^* \to \infty$, the liquid temperature and pressure tend to their far field values, $T_l^* \to T_\infty^*$ and $p_l \to 1$.

The final step is to determine the initial conditions, which will be done in the following section.

3.3.6 Initial conditions

While the laser pulse begins at time $t^* = 0$, the mathematical simulation begins a finite time later when a vapour bubble has nucleated. The choice of initial conditions to apply at the time of nucleation and, in fact, the time at which this occurs is not obvious. Laser-induced bubble formation involves complex physics including, in some case, plasma formation [11, 33, 34]. Much existing work on laser-induced bubbles avoids modelling nucleation by focusing on collapse and rebound, beginning with a bubble at maximum size [28, 50, 52, 53]. This approach is not suitable here as the bubble expansion and its dependence on the temporal input of laser energy is of interest. Here we approximate the physical mechanisms of nucleation by specifying conditions at the time of nucleation and the time at which this occurs.

We assume a bubble is nucleated at a time $t^* = t^*_{\mathrm{nucl}}$, with t^*_{nucl} to be determined. We choose the nucleated bubble to be of dimensional radius 1 µm — significantly smaller than the diameter of the laser fibre at approximately 200 µm but significantly larger that a single water molecule at 2.8×10^{-4} µm. This equates to a dimensionless initial bubble size of $R^*_{\mathrm{nucl}} = 5\times10^{-3}$. The choice of initial bubble size is discussed further in Sec. 3.4.4. For simplicity, it is assumed that the bubble is initially stationary, $\dot{R}^*(t^*_{\mathrm{nucl}}) = 0$, and the whole system is at mechanical equilibrium such that vapour pressure equals the far field pressure plus pressure due to surface

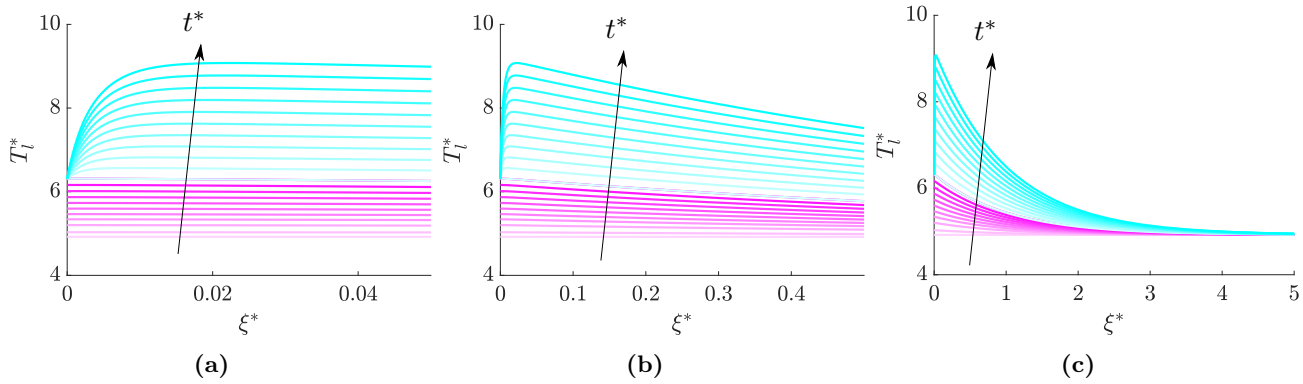


Figure 3.3.3 – Evolution of the temperature profile in the liquid before bubble nucleation at three length-scales. Pink lines mark the first stage of laser heating of the liquid in which the temperature rises to vaporisation temperature. Cyan marks the second stage of heating in which the laser continues to heat the liquid but energy is taken in at $\xi^* = 0$ as latent heat before phase change occurs. The arrow marks the evolution of the temperature profile with time.

tension, $p_v^*(t_{\text{nucl}}^*) = 1 + \lambda_4/R_{\text{nucl}}^*$. The initial temperature of the bubble is the equilibrium vapor temperature corresponding to the initial vapour pressure, $p_v^*(t_{\text{nucl}}^*)$, which we denote $T_v^*(t_{\text{nucl}}^*) = T_{\text{nucl}}^*$. The Clausius-Clapeyron relation gives the relationship between vaporisation pressure and temperature but requires reference values which are determined experimentally; the equilibrium vapour temperature of water at our required initial pressure can be found in standard look-up tables, for example [63].

In summary, at $t^* = t_{\text{nucl}}^*$, we fix

$$R^*(t_{\text{nucl}}^*) = R_{\text{nucl}}^* \qquad = 5.0 \times 10^{-3}, \tag{3.3.64a}$$

$$\dot{R}^*(t_{\text{nucl}}^*) \qquad = 0, \tag{3.3.64b}$$

$$p_v^*(t_{\text{nucl}}^*) \; = 1 + \lambda_4/R_{\text{nucl}}^* = 2.4, \tag{3.3.64c}$$

$$T_v^*(t_{\text{nucl}}^*) = T_{\text{nucl}}^* \qquad = 6.3 \tag{3.3.64d}$$

where t_{nucl}^*, as well as the initial liquid temperature profile $T_l^*(\xi^*, t_{\text{nucl}}^*)$, is found by the two-stage method given below.

Heating stage: $0 < t^* < t_{\text{vap}}^* < t_{\text{nucl}}^*$ The first stage, $0 < t^* < t_{\text{vap}}^*$, sees the liquid heat from ambient temperature, T_∞^*, to the temperature necessary for nucleation to occur, T_{nucl}^*. The heating of the liquid that occurs during this period is reflected by evaluating the liquid temperature equation, Eq. (3.3.62), with $R^* = 0$, uniform initial condition $T_l^*(\xi^*, 0) = T_\infty^*$, symmetry condition $\mathrm{d}T_l^*/\mathrm{d}\xi^*|_{\xi^*=0} = 0$, and far field condition $T_l^*(\xi^*, t^*) \to T_\infty^*$ as $\xi^* \to \infty$. We also drop the fitting parameter α at in this stage, which is equivalent to setting $\alpha = 1$; as there is no bubble and no motion during this stage, we simply model the heating of the liquid due to laser energy. The spatial laser energy source term Eq. (3.3.63) with $R = 0$ is

$$f^*(\xi^*, R^*) = \frac{\mathrm{e}^{-\xi^*}}{2}. \tag{3.3.65}$$

This period is terminated when the temperature reaches T^*_{nucl} at $\xi^* = 0$. The time of termination is denoted t^*_{vap}. The resulting evolution of the liquid temperature profile for $0 \leq t^* \leq t^*_{\text{vap}}$ is plotted in pink in Fig. 3.3.3. At $t^* = t^*_{\text{vap}}$ the liquid is at vaporisation temperature at $\xi^* = 0$ and decays exponentially towards the far-field.

Nucleating stage: $t^*_{\text{vap}} \leq t^* \leq t^*_{\text{nucl}}$ In the second stage, $t^*_{\text{vap}} < 0 < t^*_{\text{nucl}}$, the laser continues to transfer energy to the liquid. At $\xi^* = 0$, where the liquid has reached vaporisation temperature, the liquid must absorb enough additional energy to overcome latent heat in order for vaporisation to occur and a bubble to nucleate. We simulate this process by again solving Eq. (3.3.62) with $T^*_l(\xi^*, t^*) \to T^*_\infty$ as $\xi^* \to \infty$, but with the altered condition at $\xi^* = 0$ of $T^*_l(0, t) = T^*_{\text{nucl}}$. Fixing the temperature of the liquid at $\xi^* = 0$ creates an energy sink, mimicking the energy absorbed by the liquid as latent heat as phase change occurs. In this stage, we take the radius of the bubble to be its nucleation size $R^* = R^*_{\text{nucl}}$, and f^* given by Eq. (3.3.65). Again we neglect the fitting parmeter during this stage by taking $\alpha = 1$. Terminating the temperature equation at $t^* = t^*_{\text{nucl}}$, we obtain $T^*_l(\xi^*, t^*_{\text{nucl}})$, the liquid temperature profile at nucleation time. The evolution of the liquid temperature profile for $t^*_{\text{vap}} < t^* < t^*_{\text{nucl}}$ is plotted in cyan in Fig. 3.3.3. Due to the fixed temperature at $\xi^* = 0$, a sharp positive gradient develops near $\xi^* = 0$, reaching a peak temperature a short distance from the bubble wall. The occurrence of a positive temperature gradient in a thin 'thermal boundary layer' as nucleation occurs is a commonly known phenomenon, as described by Plesset and Prosperetti [17], and Plesset and Zwick [64].

Determining t^*_{nucl} It is left to determine t^*_{nucl}, the time at which nucleation occurs. This would be a straightforward calculation if the energy required for nucleation was known but, since we do not model here the complex physics of bubble nucleation, this quantity is not known. For this reason, t^*_{nucl} is found by a comparison of the model results to the experimental data. Assuming that the time taken to nucleate a bubble is proportional to the time taken to heat the liquid to vaporisation temperature, we set $t^*_{\text{nucl}} = \beta t^*_{\text{vap}}$ where β is a constant. The parameter β is determined, along with the laser intensity scaling factor α, by the method detailed in Sec. 3.4.3. Although we do now know the exact energy required for nucleation, we can find an order of magnitude figure for β, the relative duration of the heating and nucleating stages, by comparing the amount of energy required to raise the temperature of water to vaporisation point to the amount of energy required to change water from liquid to gas. Dimensionally, the energy required to vaporise one kilogram of liquid is the latent heat of vaporisation, L. The heat capacity, $c_{p,l}$, is the energy required to raise one kilogram of water by one degree Kelvin, so $c_{p,l}\Theta$ is the energy to raise one kilogram of water from T_∞ to $T_{\text{vap},\infty}$, approximately the temperature

required for vaporisation. We find

$$\frac{L}{c_{p,l}\Theta} = 9.8, \tag{3.3.66}$$

from which we conclude that approximately ten times the laser energy is required in the nucleating stage than the heating stage. While the laser power may not be the same in the two stages, we estimate $\beta = \mathrm{O}(10)$.

3.4 Numerical method

The system of equations summarised in Sec. 3.3.5 consists of two ODEs in time and two PDEs. Due to the highly non-linear nature of the system, we turn to a numerical method of solution. We solve using the method of lines: the spatial derivatives of the two PDES are discretised via finite difference schemes to give a system of ODEs in time that can be integrated numerically.

3.4.1 Method of lines

The spatial derivatives of T_l^* in Eq. (3.3.62) and Eq. (3.3.60) are replaced with finite difference approximations; the resulting ODEs, along with Eq. (3.3.59) and Eq. (3.3.61), can be numerically integrated with `MATLAB`'s in-built solvers. The spatial domain is discretised into $N+2$ logarithmically spaced points ξ_n^* between 0 and ξ_∞^*, with $n = 0, ..., N+1$. At ξ_n^*, the liquid temperature is denoted $T_n(t) = T_l^*(\xi_n^*, t)$. Logarithmic spacing gives higher resolution near the bubble wall where most of the physics occurs and large temperature gradients are expected, and a coarser mesh at the far-field where the laser heating is negligible.

To discretise Eq. (3.3.62), let $D_{1,n}$ be the discrete form of the first derivative,

$$D_{1,n} \approx \frac{\partial T_l^*}{\partial \xi^*}\Big|_{\xi_n^*} \tag{3.4.1}$$

and $D_{2,n}$ be the discrete form of the higher order derivative in the diffusion term

$$D_{2,n} \approx \left[\frac{1}{(\xi_n^* + R^*)^2}\frac{\partial}{\partial \xi^*}\left((\xi^* + R^*)^2 \frac{\partial T_l^*}{\partial \xi^*}\right)\right]\Big|_{\xi_n^*}. \tag{3.4.2}$$

Equation (3.3.62) is then approximated by

$$\frac{\partial T_n}{\partial t^*} + \dot{R}^* D_{1,n}\left(\frac{(R^*)^2}{(\xi_n^* + R^*)^2} - 1\right) = \lambda_1 D_{2,n} + \alpha\lambda_2 f^*(\xi_n^*, R^*)P^*(t^*). \tag{3.4.3}$$

It is not necessary to solve this equation for $n = 0$ and $n = N + 1$ as boundary conditions are imposed at these points, as shown in Fig. 3.4.1. At the bubble wall, $n = 0$, we set $T_0(t^*) = T_v^*(t^*)$, and at the far-field, $n = N + 1$, we have $T_{N+1}(t^*) = T_\infty^*$. For $n = 1, ..., N$, the first derivative is

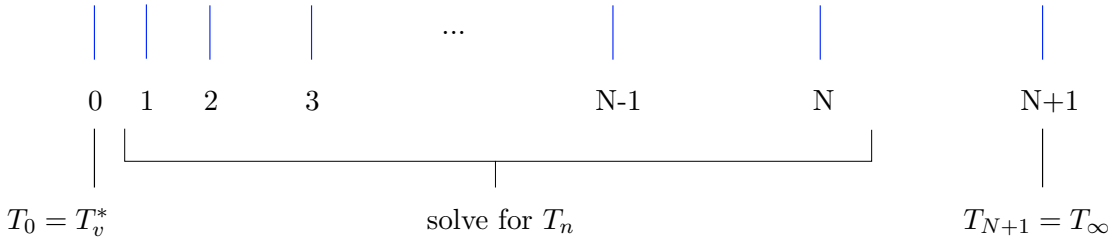


Figure 3.4.1 – Gridpoints in the ξ^* domain. The liquid temperature is calculated at points $n = 1, ..., N$ and boundary conditions are applied at points $n = 0$ and $n = N + 1$.

given by the central difference approximation

$$D_{1,n} = \frac{T_{n+1} + T_{n-1}}{\xi^*_{n+1} - \xi^*_{n-1}}, \tag{3.4.4}$$

and the second derivative, taken from Dew and Walsh [65], is

$$D_{2,n} = \frac{3}{(\xi^*_{n+1/2} + R^*)^3 - (\xi^*_{n-1/2} + R^*)^3} \left[(\xi^*_{n+1/2} + R^*)^2 \left(\frac{T_{n+1} - T_n}{\xi^*_{n+1} - \xi^*_n} \right) - (\xi^*_{n-1/2} + R^*)^2 \left(\frac{T_n - T_{n-1}}{\xi^*_n - \xi^*_{n-1}} \right) \right], \tag{3.4.5}$$

where $\xi^*_{n+1/2} = (\xi^*_{n+1} + \xi^*_n)/2$. This discrete form of the second derivative is chosen as it is found to ensure stability of the numerical solution. Both $D_{1,n}$ and $D_{2,n}$ are second degree accurate [65]. Close to the bubble wall, with the chosen grid parameters the spacing is approximately 10^{-7} giving an accuracy of $\mathrm{O}(10^{-14})$.

A one sided difference equation is used to approximate the ξ^* derivative of T_l^* in the vapour pressure equation, Eq. (3.3.50), giving

$$\frac{\mathrm{d}p_v^*}{\mathrm{d}t^*} = \frac{3}{R^*} \left(\lambda_3 \lambda_5 T_v^* \left(\frac{T_1 - T_0}{\xi_1^*} \right) - p_v^* \dot{R}^* \right). \tag{3.4.6}$$

Although a forward difference approximation is only first degree accurate, with the chosen grid parameters we have $\mathrm{O}(\xi_1^*) = 10^{-7}$ which is acceptably small.

The $N+3$ unknown variables are collected into a vector

$$\boldsymbol{Y} = \begin{bmatrix} p_v \\ T_1 \\ \vdots \\ T_N \\ R \\ \dot{R} \end{bmatrix}. \tag{3.4.7}$$

The full system of differential equations is therefore represented by

$$\dot{\boldsymbol{Y}} = \begin{bmatrix} \frac{3}{R^*}\left(\lambda_3\lambda_5 T_v^*\left(\frac{T_1-T_0}{\xi_1^*}\right) - p_v^*\dot{R}^*\right) \\ \dot{R}^* D_{1,1}\left(1-\frac{(R^*)^2}{(\xi_1^*+R^*)^2}\right) + \lambda_1 D_{2,1} + \alpha\lambda_2 f^*(\xi_1^*, R^*)P^*(t^*) \\ \vdots \\ \dot{R}^* D_{1,N}\left(1-\frac{(R^*)^2}{(\xi_N^*+R^*)^2}\right) + \lambda_1 D_{2,N} + \alpha\lambda_2 f^*(\xi_N^*, R^*)P^*(t^*) \\ \dot{R} \\ (p_v^* - 1 + \frac{\lambda_4}{R^*} - \frac{3}{2}(\dot{R}^*)^2)/R^* \end{bmatrix}, \tag{3.4.8}$$

where $T_{N+1} = T_\infty^*$ and $T_0 = T_v^*$, which can be found from the integral, algebraic form of the Clausius-Clapeyron relation. This algebraic form is found by integrating Eq. (3.3.61) from the initial conditions, $p_v^*(t_{\text{nucl}}^*)$ and $T_v^*(t_{\text{nucl}}^*)$, to an arbitrary p_v^* and T_v^*, giving

$$\frac{1}{T_v^*} = \frac{1}{T_v^*(t_{\text{nucl}}^*)} - \lambda_3 \log\left(p_v^*/p_v^*(t_{\text{nucl}}^*)\right) \tag{3.4.9}$$

$$= \frac{1}{T_v^*(t_{\text{nucl}}^*)} - \lambda_3 \log\left(Y_0/p_v^*(t_{\text{nucl}}^*)\right). \tag{3.4.10}$$

The discrete system is solved using `MATLAB`'s ODE solver for stiff systems, `ODE15s`. We choose $\xi_\infty^* = 10^4$ and $N = 100$; these choices are discussed in Sec. 3.4.4. All physical parameters are as given in Appendix A.

3.4.2 Initial conditions

To solve Eq. (3.4.8), the initial value of $\boldsymbol{Y}$ is set as

$$\boldsymbol{Y}(t^*_{\text{nucl}}) = \begin{bmatrix} p_v(t^*_{\text{nucl}}) \\ T_1(t^*_{\text{nucl}}) \\ \vdots \\ T_N(t^*_{\text{nucl}}) \\ R(t^*_{\text{nucl}}) \\ \dot{R}(t^*_{\text{nucl}}) \end{bmatrix}. \tag{3.4.11}$$

where $T_1(t^*_{\text{nucl}})$ to $T_N(t^*_{\text{nucl}})$ must be calculated and the other values are known, as explained in Sec. 3.3.6. The value of $T_v(t^*_{\text{nucl}})$ is also known, as given in Sec. 3.3.6, allowing Eq. (3.4.10) to be solved. The values $T_1(t^*_{\text{nucl}})$ to $T_N(t^*_{\text{nucl}})$ are found by solving the liquid temperature for the heating and vaporisation stages, as follows.

Heating stage: $0 < t^* < t^*_{\text{vap}}$ The ODE

$$\dot{\tilde{\boldsymbol{Y}}} = \begin{bmatrix} \dot{R}^* D_{1,1} \left(1 - \frac{(R^*)^2}{(\xi^*_1 + R^*)^2}\right) + \lambda_1 D_{2,1} + \lambda_2 e^{-\xi^*} P^*(t^*)/2 \\ \vdots \\ \dot{R}^* D_{1,N} \left(1 - \frac{(R^*)^2}{(\xi^*_N + R^*)^2}\right) + \lambda_1 D_{2,N} + \lambda_2 e^{-\xi^*} P^*(t^*)/2 \end{bmatrix}, \tag{3.4.12}$$

is solved, where

$$\tilde{\boldsymbol{Y}} = \begin{bmatrix} T_1 \\ \vdots \\ T_N \end{bmatrix}, \tag{3.4.13}$$

subject to the boundary conditions $T_0 = T_1$ and $T_{N+1} = T^*_\infty$, and the initial condition

$$\tilde{\boldsymbol{Y}}(0) = \begin{bmatrix} T^*_\infty \\ \vdots \\ T^*_\infty \end{bmatrix}. \tag{3.4.14}$$

The integration is terminated when $T_0 = T^*_{\text{nucl}}$ and this time is denoted t^*_{vap}.

Nucleating stage: $t^*_{\mathrm{vap}} \leq t^* \leq t^*_{\mathrm{nucl}}$ The same equation

$$\dot{\tilde{\boldsymbol{Y}}} = \begin{bmatrix} \dot{R}^* D_{1,1}\left(1 - \frac{(R^*)^2}{(\xi_1^* + R^*)^2}\right) + \lambda_1 D_{2,1} + \lambda_2 e^{-\xi^*} P^*(t^*)/2 \\ \vdots \\ \dot{R}^* D_{1,N}\left(1 - \frac{(R^*)^2}{(\xi_N^* + R^*)^2}\right) + \lambda_1 D_{2,N} + \lambda_2 e^{-\xi^*} P^*(t^*)/2 \end{bmatrix}, \tag{3.4.15}$$

is solved subject to the altered boundary conditions $T_0 = T^*_{\mathrm{nucl}}$ and $T_{N+1} = T^*_\infty$, and the initial condition

$$\tilde{\boldsymbol{Y}}(t^*_{\mathrm{vap}}) = \begin{bmatrix} T_1(t^*_{\mathrm{vap}}) \\ \vdots \\ T_N(t^*_{\mathrm{vap}}) \end{bmatrix}, \tag{3.4.16}$$

which is the terminal condition of the previous step. We terminate the integration at $t^*_{\mathrm{nucl}} = \beta t^*_{\mathrm{vap}}$. The terminal values are inserted into the initial condition for the full bubble simulation $\boldsymbol{Y}(t^*_{\mathrm{nucl}})$.

3.4.3 Fitting to experimental data

The two unknown parameters α and β are found by fitting the model to experimental data. The dimensionless bubble radius over time $R^*(t^*)$, is converted to dimensional volume, $V(t)$, to allow a comparison to the bubble volume over time determined experimentally as detailed in Chapter 2. The free parameters α and β are used to fit to the data of the P120 short pulses, minimising the normalised error

$$E_{V\max} = \sqrt{\sum_{j=1}^{M} (V_{\max,m,j} - V_{\max,d,j})^2} \,/ (M \max_j(V_{\max,d,j})), \tag{3.4.17}$$

where M is the number the short pulse energy settings used experimentally, j indexes these settings, with $j \in \{0.2, 0.4, 0.5, 0.6, 0.8, 1.0, 1.2, 1.4, 1.5, 1.6, 1.8, 2.0\}$, and $V_{\max,j}$ is the maximum volume of the resulting bubble, with $V_{\max,d,j}$ as given by the data and $V_{\max,m,j}$ as given by the model. An example of the values $V_{\max,d,j}$ and $V_{\max,m,j}$ for pulse energy $j = 1.0$ is shown in Fig. 3.4.2a. A parameter sweep over α and β is shown in Fig. 3.4.2b and Fig. 3.4.2c, from which we choose $\alpha = 0.2$, $\beta = 2.7$. We also observe the error in the time that maximum volume is reached, $t_{V\max}$

$$E_{tV\max} = \sqrt{\sum_{j=1}^{M} (t_{V\max,m,j} - t_{V\max,d,j})^2} \,/ (M \max_j(t_{V\max,d,j})), \tag{3.4.18}$$

where again $t_{V\max,d,j}$ and $t_{V\max,m,j}$ are as calculated using the data and model respectively for the pulse energy j. Again, an example of $t_{V\max,d,j}$ and $t_{V\max,m,j}$ for pulse energy $j = 1.0$ is

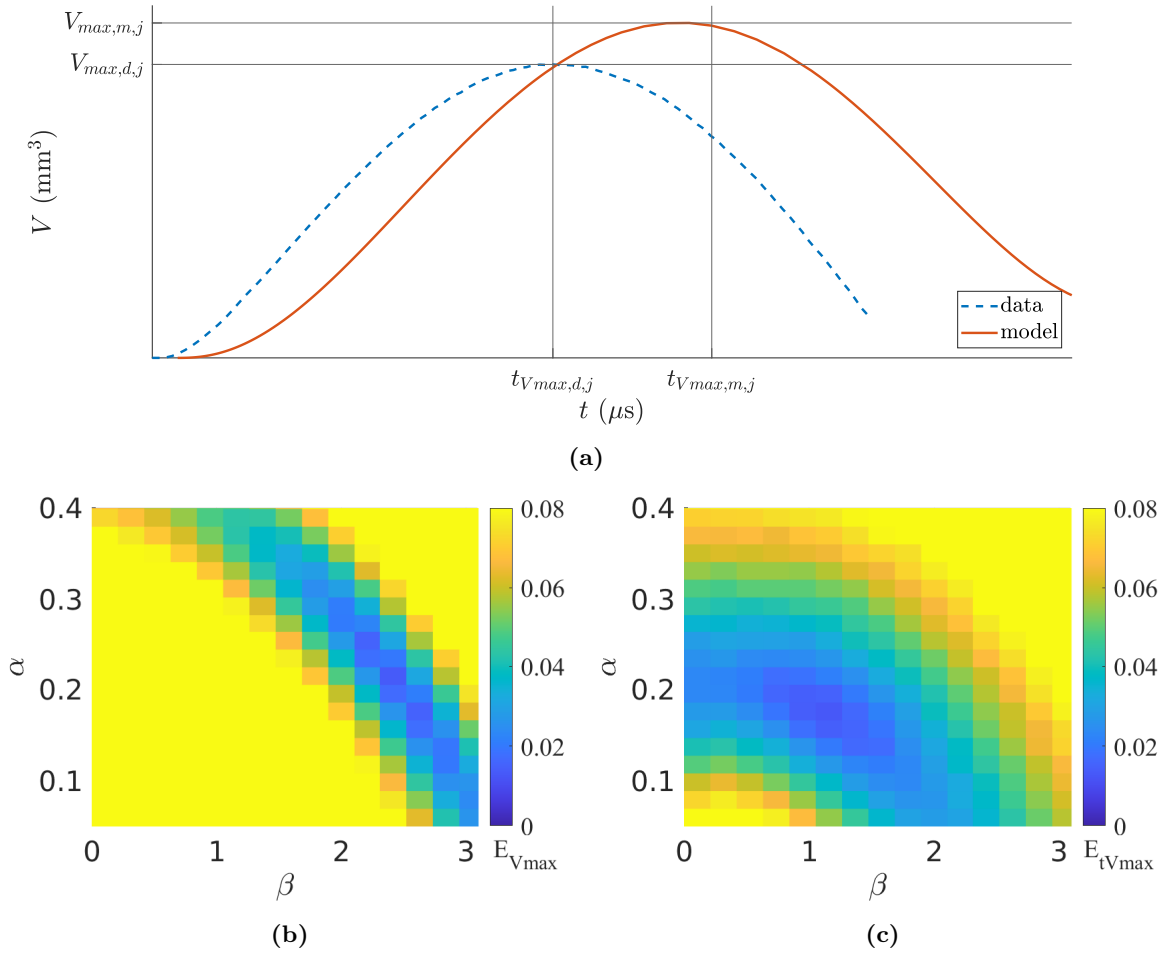


Figure 3.4.2 – (a) Bubble volume over time for the example of $j = 1.0$, as determined by the model and from the data. Maximum volume $V_{\max}$ and time at which this volume is reached t_{Vmax} is marked for both the model prediction and the data. (b) and (c) The effect of changing parameters α and β on the error between the model and data, with $E_{V\max}$ the error in maximum bubble volume over all P120 short pulses and $E_{tV\max}$ the error in the time of maximum volume. Optimal values are $\alpha = 0.2$ and $\beta = 2.7$.

shown in Fig. 3.4.2a.

3.4.4 Sensitivity to parameter values

We now test the sensitivity of the model against the parameters chosen for the initial condition and numerical grid, namely R^*_{nucl}, ξ^*_∞ and N.

The size of the initial nucleated bubble, as explained in Sec. 3.3.6, was chosen to be significantly smaller than the diameter of the laser fibre giving the upper bound $R^*_{\mathrm{nucl}} \ll 5\times10^{-1}$. In Fig. 3.4.3, we plot bubble radius over time and the liquid temperature profile at time of nucleation for three bubble nucleation sizes that satisfy this constraint. For $R^*_{\mathrm{nucl}} = 5 \times 10^{-2}$ and $R^*_{\mathrm{nucl}} = 5\times10^{-3}$, there is little variation between the two cases, with only a 3% difference in peak bubble size and a 4% difference in peak liquid temperature at nucleation time. For these reasons $R^*_{\mathrm{nucl}} = 5 \times 10^{-3}$ is a satisfactory choice.

The numerical grid is chosen to be sufficiently large such that the bubble dynamics are

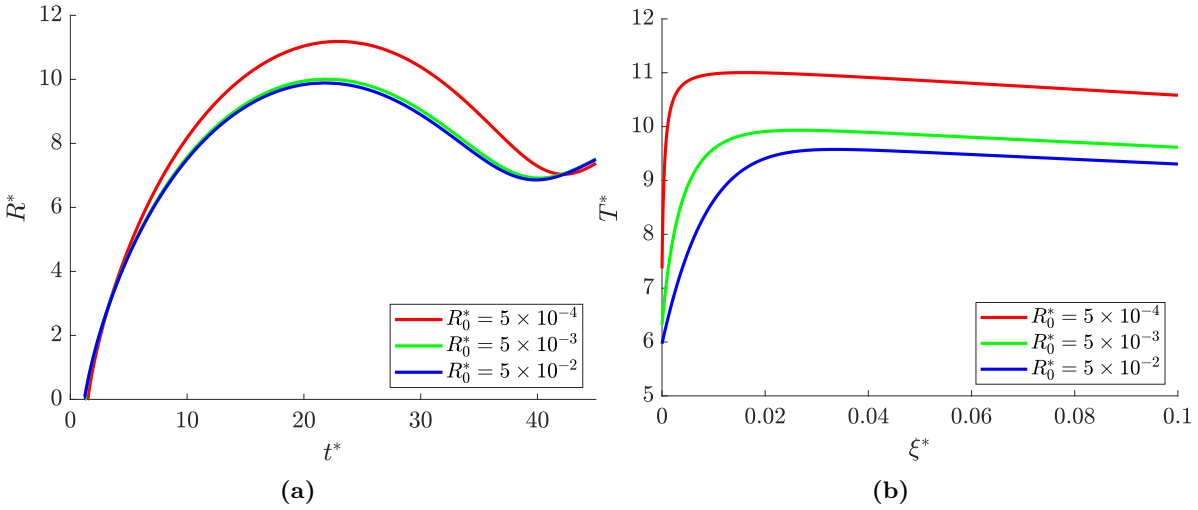


Figure 3.4.3 – (a) Dimensional bubble radius over time for three values of the dimensionless initial bubble size R^*_{nucl}. (b) Dimensional temperature profile at time of bubble nucleation for three values of R^*_{nucl}, plotted at a length-scale such that the temperature gradient at $\xi = 0$ is visible.

not affected by the far field boundary and the laser heating is acceptably close to zero at ξ^*_∞. In Fig. 3.4.4 the bubble radius over time and the liquid temperature profile at time of nucleation are plotted for four values of ξ^*_∞. There is an almost imperceptible difference between the four cases so any value within this range is considered to be acceptable.

Finally, considering the number of grid points N in the discretisation of the domain, we require the temperature profile to be sufficiently accurate at $\xi^* = 0$. For three values of N, Figs. 3.4.5a and b show the bubble radius over time and the liquid temperature profile at time of nucleation. Figure 3.4.5c shows the relative error in liquid temperature at time of nucleation near the bubble wall for various N, with relative error measured compared to the previous value of N. Figure 3.4.5d shows the run time of the numerical solution for various N. Choosing $N = 100$ is a good compromise between error and solve time, with a sufficiently low relative error of 0.001 and a run time of approximately 5s.

3.5 Viscous Effects

It is common in the literature to model the effect of liquid viscosity by including an additional term in the Rayleigh-Plesset equation [24, 31, 62]. However in the model derived in this chapter the liquid was assumed to be inviscid for simplicity. In this section, we asses whether neglecting liquid viscosity was a reasonable simplification.

In dimensional form, the Rayleigh-Plesset equation with a viscous term is widely given as

$$R\ddot{R} + \frac{3}{2}(\dot{R})^2 = \frac{1}{\rho_l}(p_{v,R} - p_\infty) - \frac{2\sigma}{\rho_l R} - \frac{4\eta\dot{R}}{\rho_l R}, \tag{3.5.1}$$

where η is the dynamic viscosity of the liquid surrounding the bubble [24, 31, 62].

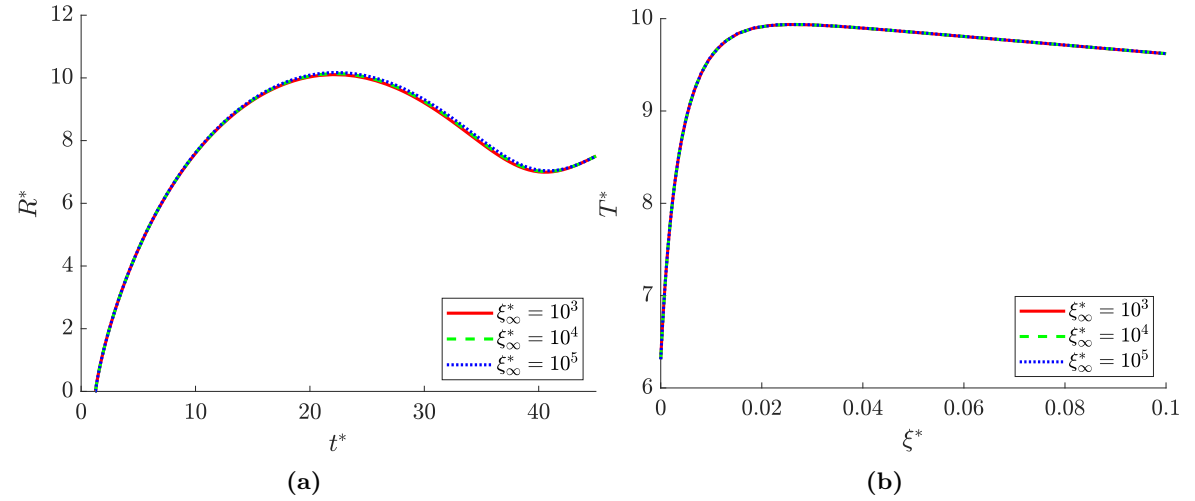


Figure 3.4.4 – (a) Dimensional bubble radius over time for three values of ξ^*_∞. All lines sit so close together than they cannot be distinguished. (b) Dimensional temperature profile at time of bubble nucleation for three values of ξ^*_∞, plotted at a length-scale such that the temperature gradient at $r^* = 0$ is visible.

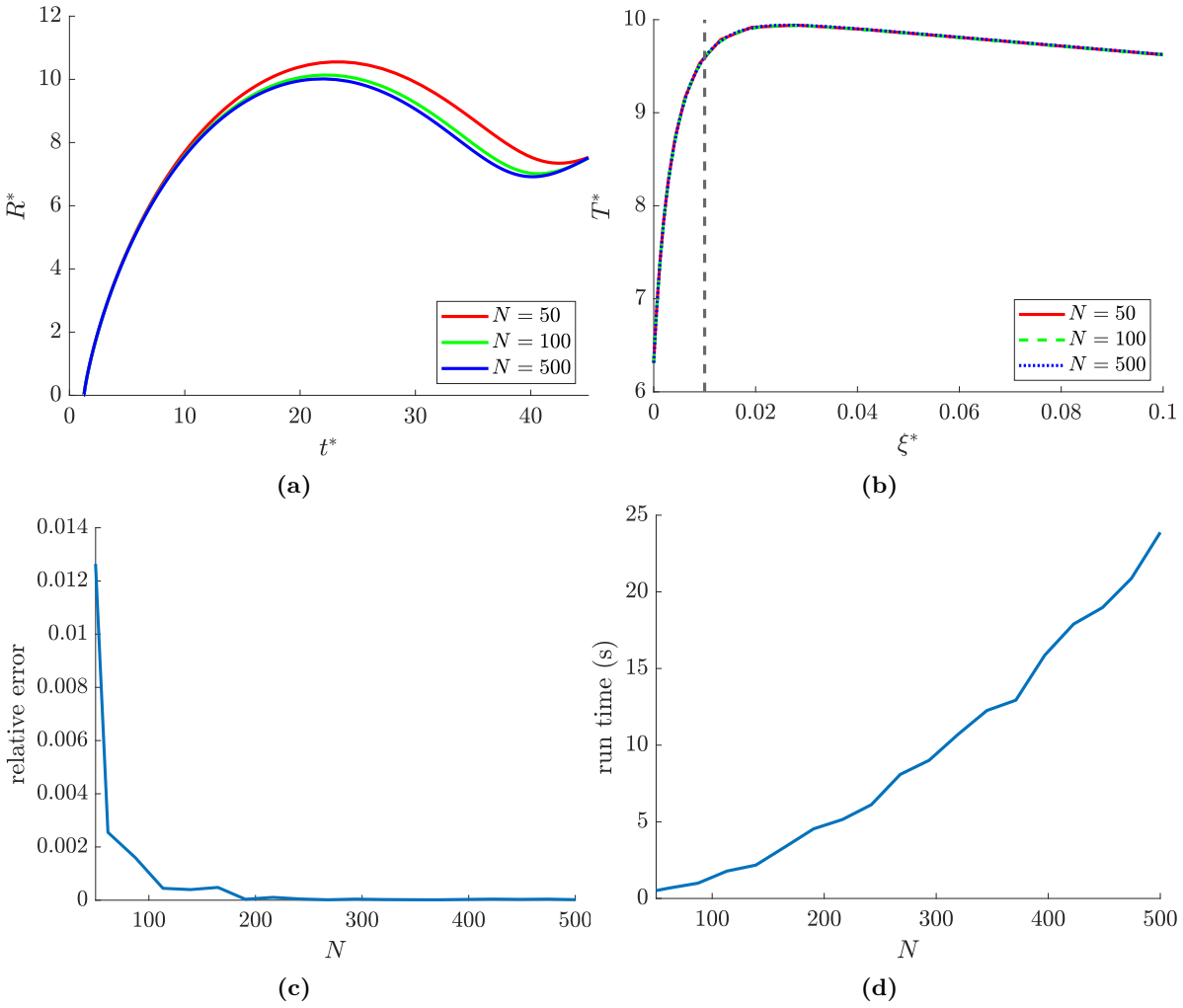


Figure 3.4.5 – (a) Dimensional bubble radius over time for three values of N. (b) Dimensional temperature profile at time of bubble nucleation for three values of N, plotted at a length-scale such that the temperature gradient at $\xi = 0$ is visible. (c) Relative error in T_l at time of nucleation, calculated at the value of ξ marked by the dashed line in (b). (d) Dependency on N of run time for numerical solution.

Non-dimensionalising as in Sec. 3.3.2, this becomes

$$R^*\ddot{R}^* + \frac{3}{2}(\dot{R}^*)^2 = p^*_{v,R} - 1 - \frac{\lambda_4}{R^*} - \underbrace{\left[\frac{4\eta\tau^2\mu^2}{\rho_l}\right]\frac{\dot{R}^*}{R^*}}_{\text{IV}}. \tag{3.5.2}$$

The form of the Rayleigh-Plesset equation used in the spherical model, Eq. (3.3.45), does not include term IV and is repeated here for convenience

$$\underbrace{R^*\ddot{R}^* + \frac{3}{2}(\dot{R}^*)^2}_{\text{I}} = \underbrace{p^*_{v,R} - 1}_{\text{II}} - \underbrace{\frac{\lambda_4}{R^*}}_{\text{III}}. \tag{3.5.3}$$

The left hand side of Eq. (3.5.3) is denoted term I. Term II is the pressure difference between the bubble wall and the far field, and term III is the effect of surface tension. The magnitudes of terms I-IV are plotted in Fig. 3.5.1 for the case of a laser pulse that emits a constant 15 kW for 100 µs. These pulse parameters are comparable to those of a P120 short pulse, as shown in Fig. 2.1.3a. Terms I-III are found by solving the spherical model in Sec. 3.3.5 and term IV is calculated with the resulting R^* and $\dot{R}^*$, taking $\eta = 6.9 \times 10^{-4}$ Pa s. In Fig. 3.5.1a, we see that initially terms II and III, the pressure and surface tension terms, are of similar size so both contribute to term I, while term IV is at least an order of magnitude smaller. As the bubble expands, term III drops, leaving term II to dominate the bubble motion. Term IV remains at least an order of magnitude smaller than the most dominant term. In Fig. 3.5.1b, we see the behaviour at the timescale at which the bubble will reach its largest volume. At this timescale, term I is almost exactly equal to term II and terms III and IV are negligibly small.

From this brief analysis, we conclude that neglecting liquid viscosity is a reasonable assumption for our modelling purposes; the surface tension term in the Rayleigh-Plesset has been shown to be negligibly small in comparison to the dominant terms.

3.6 Conclusion

We began by developing governing equations for a 3D vapour bubble in liquid, based on the framework derived by Joseph [60]. This consisted of six PDEs and four ODEs plus the ideal gas relation. Although this provided an understandable model of conservation equations, to allow a simple method of numerical solution, the equations were simplified by assuming spherical symmetry and spatially uniform vapour pressure and temperature at leading order. These assumptions facilitated a reduction of the model. After dropping negligible terms, we found that the rate of energy taken in phase change is balanced by conductive heat flow from the liquid, work done against pressure and work done against surface tension, with other effects being negligible. With this balance of energy flux, we showed how the vapour pressure equation differs compared to using the standard method which neglects work done against pressure and

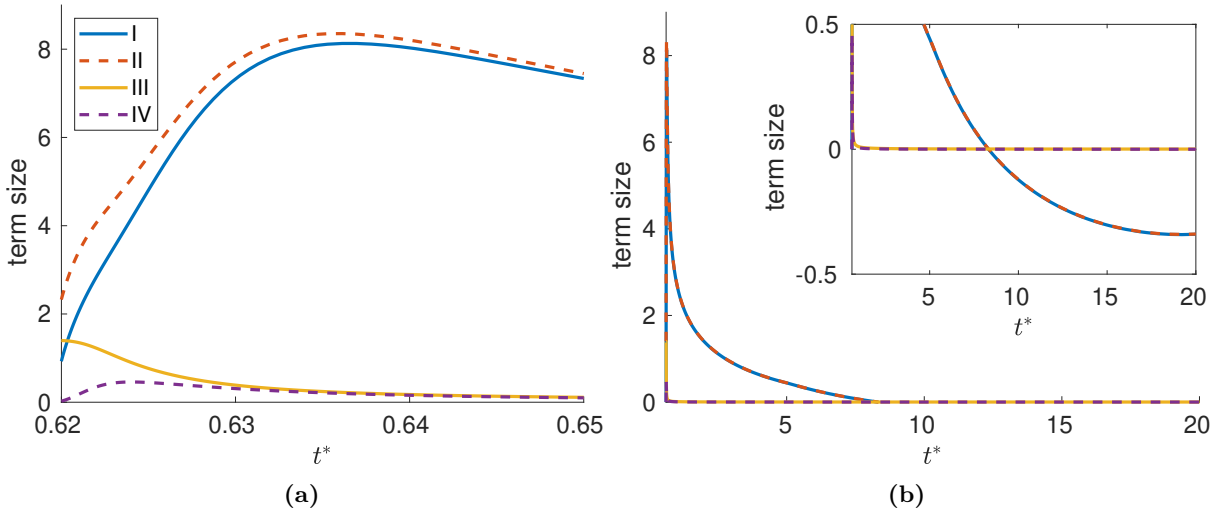


Figure 3.5.1 – Magnitude of terms I-IV of Eq (3.5.2) for the case of a rectangular last pulse that emits 15 kW for 100 µs at two timescales.

surface tension [18, 27, 61].

The reduced 1D model consists of just one PDE, a temperature equation in the liquid, and two ODEs, the Rayleigh-Plesset equation and an equation for the vapour pressure, plus the Clausius-Clapeyron, which is rewritten as an algebraic expression for the vapour temperature. A laser energy source term was derived, reflecting the key physical characteristics via a spherically symmetric function. Careful consideration was given to the conditions to apply at the time of bubble nucleation. These conditions were found by simulating the time between the laser pulse starting and a bubble nucleating in two stages: the first being the heating of the liquid from body temperature to the temperature necessary for nucleation, after which the second stage approximates the continuing absorption of laser energy by the liquid to overcome latent heat for phase change to occur. We assumed that after this second stage, a bubble is nucleated and the full mathematical model starts at this time. The numerical solution was implemented using the method of lines, with integration in time carried out using `MATLAB` solver `ODE15s`. The two unknown model parameters were found by fitting the model to the experimental data for the P120 short pulses.

In the following chapter we analyse the spherical model, comparing to the experimental data for all P120 single pulses. The model is utilised to reveal the underlying physics behind bubble expansion and to explore the dependence of the bubble dynamics on the pulse parameters.

Chapter 4

Numerical and analytical studies of spherical bubble model

In this chapter, we study the spherical model derived in Chapter 3. In Sec. 4.2, results of the model are compared to the experimental data presented in Chapter 2. This comparison allows us to determine the conditions under which the model does and does not give a good reflection of the physical system. In Sec. 4.3, the behavior of the bubble at three time-scales is analysed by studying the dominant terms in the governing equations. In the final section in this chapter, Sec. 4.4, we input a variety of rectangular pulses into the model to test the effect of pulse power, duration and energy on bubble size and duration.

4.1 Nomenclature

$\dot{m}$, mass flux density

P, laser power

$P_{\max}$, peak laser power

p, pressure

R, bubble radius

$R_{\max}$, maximum bubble volume

T, temperature

$T_{\text{vap},\infty}$, vaporisation temperature at far-field pressure

$T_{l,b}$, liquid temperature in boundary layer

t, time

t_p, pulse duration

t^*_{nucl} time at which nucleation occurs

t^*_{vap} time at which liquid reaches vaporisation temperature

$t_{V\max}$, time at which maximum volume is reached

$t_{R\max}$, time at which maximum radius is reached

$V_{\max}$, maximum bubble volume

Greek symbols

α, fitting parameter

β, fitting parameter

ϵ, small parameter

Θ, reference temperature

λ, dimensionless parameter group

μ, absorption coefficient

ξ, radial distance from bubble wall

ρ, density

τ, reference time

Subscripts

l, liquid

v, vapour

nucl value at nucleation time

∞, far-field value

Superscripts

$*$, dimensionless quantity

(1), quantity rescaled for expansion stage 1

(2), quantity rescaled for expansion stage 1

(3), quantity rescaled for expansion stage 1

Other notation

overdot, derivative with respect to time

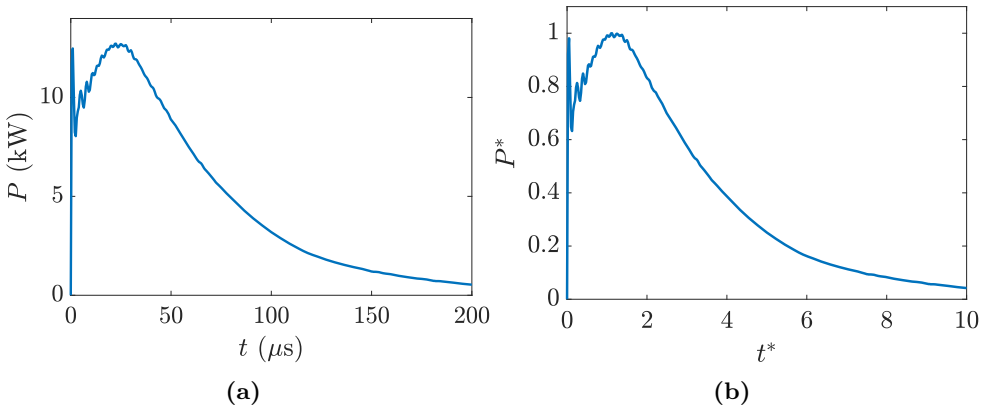


Figure 4.2.1 – An example of the time dependent power of a P120 1.0 J short pulse. The pulse is shown (a) dimensionally as $P(t)$ and (b) non-dimensionally as $P^*(t^*)$.

4.2 Model and data comparison

To compare the model results to the experimental data presented in Chapter 2, we simulate the bubbles resulting from the P120 short, medium and long single pulses. To achieve this, the power of the laser, $P(t)$, is taken to be the experimentally determined power of the required pulse. An example of this for the case of the P120 1.0 J short pulse is shown in Fig. 4.2.1. The full range of P120 single pulses are plotted in Fig. 2.1.3. In this section, all results are presented in dimensional variables to allow a direct comparison between the model predictions and experimental data.

In Fig. 4.2.2, the maximum bubble volume, $V_{\max}$, and the time that this volume is reached, $t_{V,\max}$, are plotted, as given by the data and the model. The top row of Fig. 4.2.2 shows the cases of the short pulses, the middle row shows medium pulses and the bottom row shows long pulses.

As detailed in Sec. 3.4, the model parameters were fitted to $V_{\max}$ of the P120 short pulses, resulting in $\alpha = 0.2$ and $\beta = 2.7$. Figure 4.2.2a, shows the data to which the model was fitted and we see a good fit with just two parameters. In Fig. 4.2.2b, we see that the model gives the correct correlation between pulse energy and duration for short pulses, but overestimates $t_{V,\max}$ by approximately 20%. For the case of a 1.0 J short pulse, Fig. 4.2.3 shows V and $\mathrm{d}V/\mathrm{d}t$ over time as given by the data and the model. This plot makes clear the reason for discrepancy in $t_{V,\max}$ between the model and data: the model displays a more gentle initial acceleration, $\mathrm{d}^2V/\mathrm{d}t^2$, than the physical bubble and so takes longer to reach the same volume. However, aside from a temporal shift, the model gives V and $\mathrm{d}V/\mathrm{d}t$ profiles that are qualitatively similar to the data. The model does not give a strictly monotonic relationship between pulse energy and both $V_{\max}$ and $t_{V,\max}$. For example, the model predicts $V_{\max}$ to be lower for a 1.5 J short pulse than for a 1.4 J short pulse. This non-monotonicity is due to using real P120 pulse data as the input $P(t)$ and is reflected in the experimental data; the reason for this is that the distribution of energy varies between pulses so it is possible that, in some cases, a higher energy pulse may

produce a smaller bubble.

As shown in Figures 4.2.2c and 4.2.2d, for medium pulses, the model overshoots the data by around 50% for both $V_{\max}$ and t_{Vmax} but does predict the correlation between these variables and pulse energy.

Not surprisingly, the model agrees less well for long pulses since these bubbles are highly elongated. It is encouraging, however, that the relationship between pulse energy and bubble size is correctly reflected; the peak power of these pulses varies very little, therefore bubble size varies little, as discussed in Sec. 2.2.2.1. However, the current model cannot account for the secondary bubble created by the 1.6, 1.8 and 2.0 J long pulses.

Overall, the model gives accurate results for pulses of duration less than 200 µs, the length of the P120 short pulses, which produce approximately spherical bubbles. The P120 medium pulses have a duration up to 400 µs and the long pulses up to 500 µs, producing elongated bubbles which are less well predicted by the model. However, even for highly elongated bubbles, the model gives a correct order of magnitude prediction for size and duration of bubble and captures the correlation of bubble dynamics with pulse energy and shape.

4.3 Stages of expansion

The behaviour of the system is analysed at different time-scales to probe the mechanisms of bubble expansion. This work shows a key benefit of mathematical modelling alongside experimental work for improving lithotripsy. Analysing the model provides an understanding of the complex physics of an expanding laser-induced bubble. Motivated by the numerical solutions of the mathematical model, three time-scales are identified. We look at the dominant terms in the governing equations during these three stages of expansion which reveals the physical effects driving expansion. An asymptotic reduction of the model is made when it is possible and beneficial. In this section, we return to using dimensionless variables.

We present the dimesionless spherical model derived in the previous chapter again here for convenience:

$$R^*\ddot{R}^* + \frac{3}{2}(\dot{R}^*)^2 = p_v^* - 1 + \frac{\lambda_4}{R^*}, \tag{4.3.1a}$$

$$\frac{\mathrm{d}p_v^*}{\mathrm{d}t^*} = \frac{3}{R^*}\left(1-\lambda_3 T_v^*\right)^{-1}\left[\lambda_3\lambda_5\left(1+\lambda_3 T_v^*\right)^{-1} T_v^* \frac{\partial T_l^*}{\partial \xi^*}\Big|_{\xi^*=0} - p_v^*\dot{R}^*\right], \tag{4.3.1b}$$

$$\frac{\mathrm{d}T_v^*}{\mathrm{d}t^*} = \frac{\lambda_3 (T_v^*)^2}{p_v^*}\frac{\mathrm{d}p_v^*}{\mathrm{d}t^*}, \tag{4.3.1c}$$

$$\frac{\partial T_l^*}{\partial t^*} + \dot{R}^*\frac{\partial T_l^*}{\partial \xi^*}\left(\frac{(R^*)^2}{(\xi^*+R^*)^2} - 1\right) = \frac{\lambda_1}{(\xi^*+R^*)^2}\frac{\partial}{\partial \xi^*}\left((\xi^*+R^*)^2\frac{\partial T_l^*}{\partial \xi^*}\right) + \alpha\lambda_2 f^*(\xi^*, R^*)P^*(t^*), \tag{4.3.1d}$$

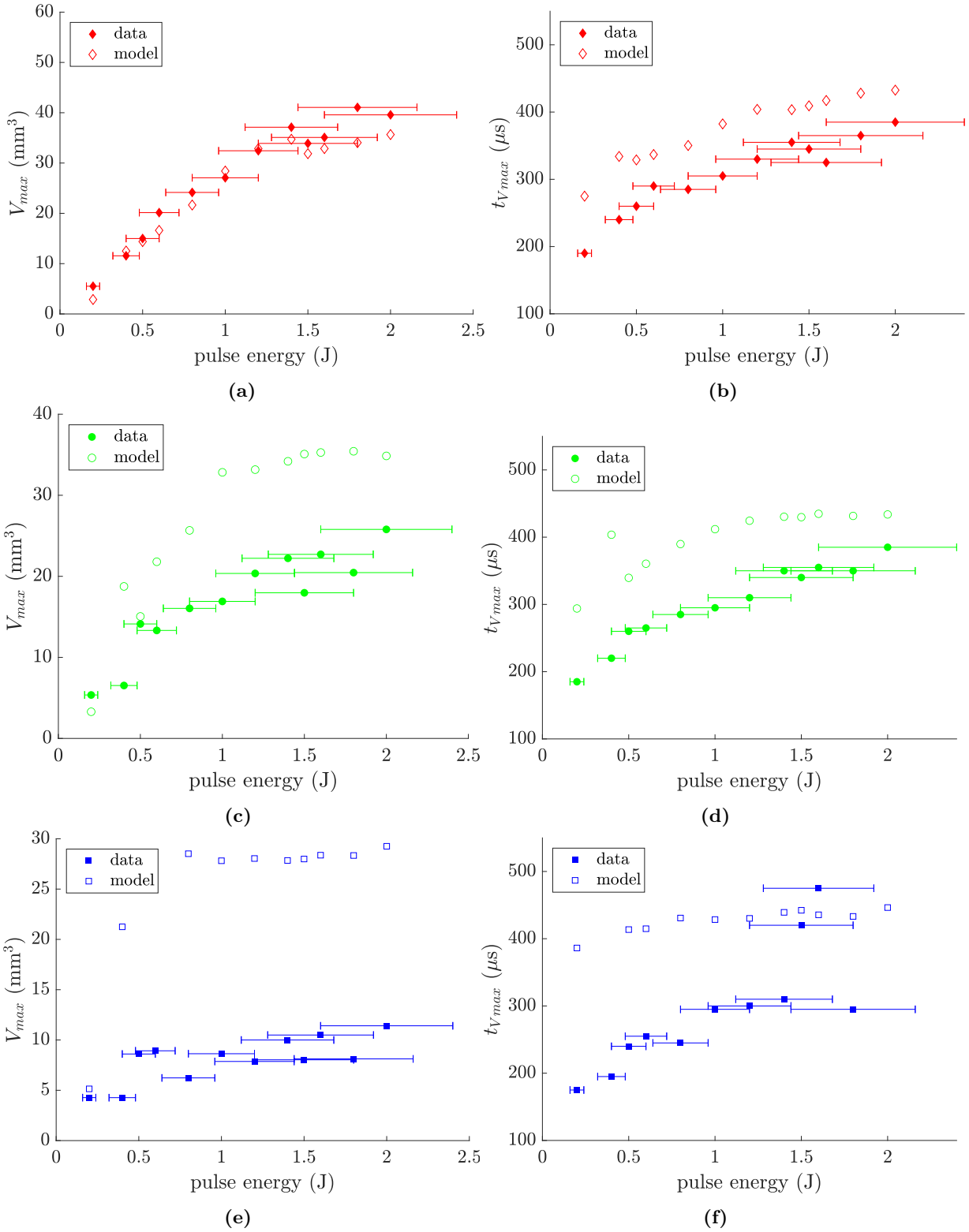


Figure 4.2.2 – Maximum bubble volume, $V_{\max}$ and time at which maximum volume reached, t_{Vmax} as determined experimentally and numerically for P120 (a and b) short pulses, (c and d) medium pulses and (e and f) long pulses.

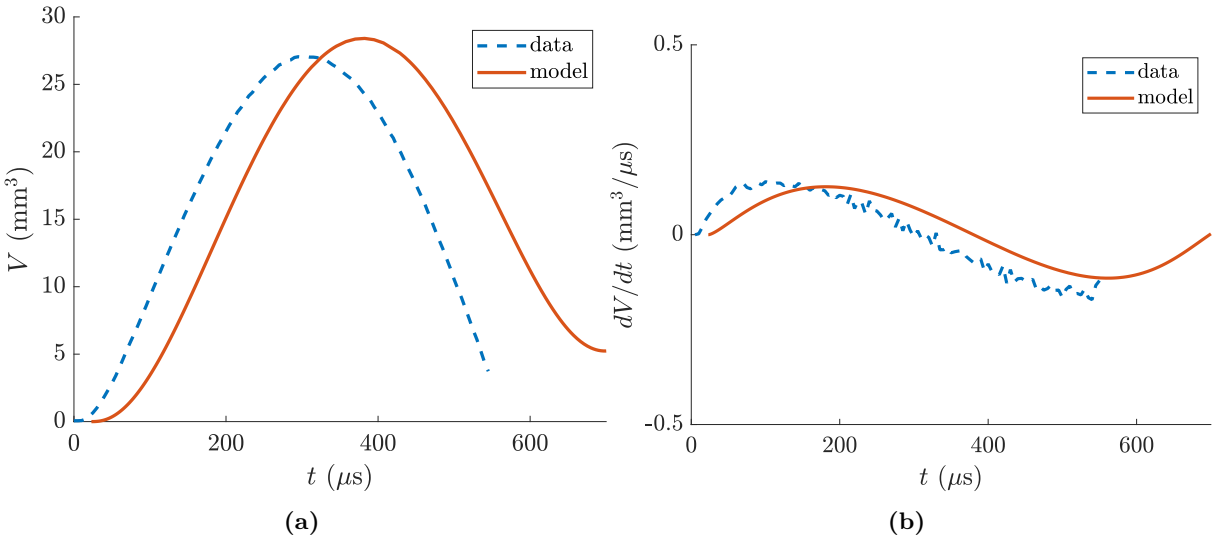


Figure 4.2.3 – (a) bubble volume and (b) rate of change of bubble volume for a P120 1.0 J short pulse, as determined experimentally and numerically.

with

$$f^*(\xi^*, R^*) = \frac{\mathrm{e}^{-\xi^*}}{((R^*)^2 + 2R^* + 2)}, \tag{4.3.2}$$

and $P^*(t^*)$ specified for the relevant pulse.

At the bubble wall, $\xi^* = 0$, we have continuity of temperature, $T_l^*(0, t^*) = T_v^*$, and as $\xi^* \to \infty$, the liquid temperature tends to its far field value, $T_l^* \to T_\infty^*$.

The initial conditions are, at $t^* = t_{\text{nucl}}^*$

$$R^*(t_{\text{nucl}}^*) = R_{\text{nucl}}^* \qquad = 5.0 \times 10^{-3}, \tag{4.3.3a}$$

$$\dot{R}^*(t_{\text{nucl}}^*) \qquad = 0, \tag{4.3.3b}$$

$$p_v^*(t_{\text{nucl}}^*) \; = 1 + \lambda_4 / R_{\text{nucl}}^* = 2.4, \tag{4.3.3c}$$

$$T_v^*(t_{\text{nucl}}^*) = T_{\text{nucl}}^* \qquad = 6.3, \tag{4.3.3d}$$

where t_{nucl}^* and the initial liquid temperature profile $T_l^*(t_{\text{nucl}}^*)$ are found by the method given in Sec. 3.3.6.

The variables R^* and $\dot{R}^*$ are plotted in Fig. 4.3.1a and the variables p_v^* and T_v^* are plotted in Fig. 4.3.1b at three time-scales for the example of a P120 1.0 J short pulse. The function $P^*(t^*)$ for this pulse is the same as that in Fig. 4.2.1b. The liquid temperature gradient at the bubble wall is shown in Fig. 4.3.1c at the same three time-scales as in Fig. 4.3.1a and Fig. 4.3.1b. Three snapshots of the liquid temperature profile are plotted in Fig. 4.3.1d at the times marked by the corresponding vertical dashed, dotted, and dash-dotted lines in Fig. 4.3.1a, Fig. 4.3.1b and Fig. 4.3.1c. The numerical solution for the P120 1.0 J short pulse is displayed here as an example but we expect the analysis in this section to hold for any pulse.

From the numerical results, we can identify different behavior at different time-scales.

Parameter	Value	Parameter	Value
λ_1	1.5×10^{-4}	α	1.0 before nucleation
λ_2	$O(1-10)$	α	0.2 after nucleation
λ_3	1.3×10^{-2}	T^*_∞	4.9
λ_4	7.0×10^{-3}	T^*_{nucl}	6.3
λ_5	2.0×10^{-1}	R^*_{nucl}	5.0×10^{-3}

Table 4.3.1 – Relevant parameter values.

For this pulse, the bubble nucleates at $t^* = 1.315$. At the time of the vertical dotted line at $t^* = 1.318$, the liquid temperature has a steep positive gradient at the bubble wall, as shown in Fig. 4.3.1c and by the dotted line in Fig. 4.3.1d. This temperature gradient facilitates heat flow to the bubble wall causing a rise in vapour pressure and temperature, visible in Fig. 4.3.1b. The higher pressure within the bubble causes an outward acceleration of the bubble wall, as shown in Fig. 4.3.1a.

The time $t^* = 2$ is marked by the vertical dashed lines in Fig. 4.3.1. The liquid temperature at $t^* = 2$, marked by the dashed line in Fig. 4.3.1d, is illustrative of the form of the temperature profile at a second time-scale. There is a much reduced temperature gradient at the bubble wall, dropping by an order of magnitude in comparison to $t^* = 1.318$. This lower gradient means that energy is still flowing to the bubble wall but at a reduced rate. Furthermore, as we can see in Fig. 4.3.1b and Fig. 4.3.1a, the vapour pressure and temperature drop but the bubble continues to expand.

At the time-scale of the dash-dotted line at $t^* = 10$, we can see in Fig. 4.3.1c that the liquid temperature gradient at the bubble wall has dropped by another order of magnitude in comparison to the previous stage. The vapour pressure drops close to 1, the far-field value, visible in Fig. 4.3.1b. In Fig. 4.3.1a, we see that this significant drop in pressure causes slowing of the bubble expansion until the bubble reaches maximum size.

In the following three sections, we probe the governing equations to understand the reasons for the behavior described above and determine how the time-scales for these three stages of expansion depend on the system parameters.

4.3.1 Stage 1: acceleration

In the first stage of bubble expansion, the pressure increases, causing the initially stationary bubble wall to accelerate outwards. The vapour pressure at nucleation is set such that the bubble is at equilibrium, so just an order 1 increase in vapour pressure triggers outwards acceleration of the bubble wall. We determine the time-scale τ_1 over which the pressure increases and the bubble begins to expand. We also determine how this time-scale depends on the power of the laser.

This initial behavior is understood by examining the vapour pressure equation,

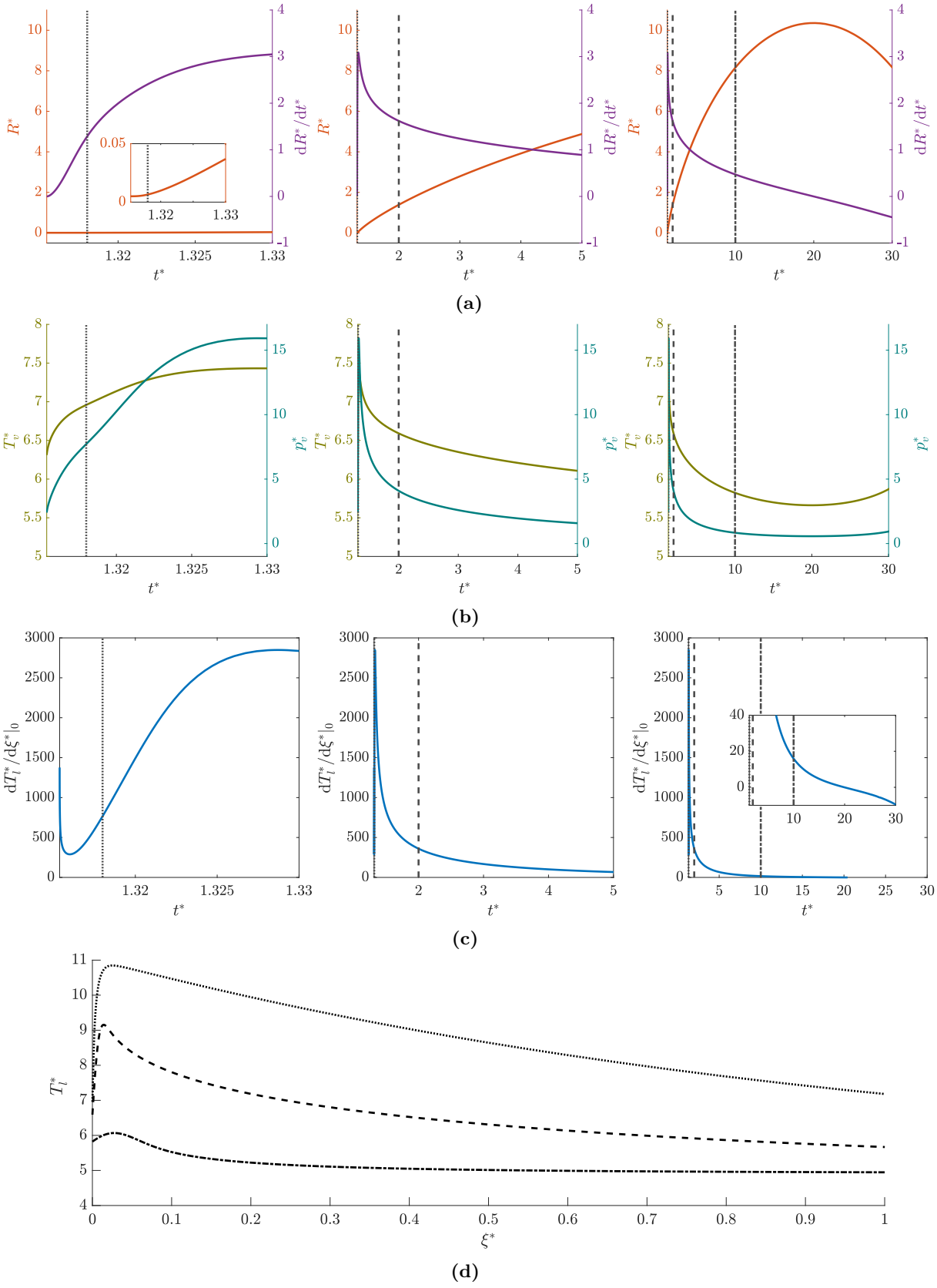


Figure 4.3.1 – Plots of (a) bubble radius and velocity and (b) vapour temperature and pressure over three time-scales, each beginning at $t^* = t^*_{\mathrm{nucl}} = 1.315$, for the case of a P120 1.0 J short pulse. (c) Liquid temperature gradient at the bubble wall for the same three time-scales as (a) and (b). (d) The liquid temperature profile at the three times marked by the corresponding dashed, dotted and dash-dotted vertical lines in (a) and (b). For this pulse, $\lambda_2 = 10.6$, $t^*_{\mathrm{nucl}} = 1.313$ and other parameter values are as given in Table 4.3.1.

Eq. (4.3.1b). In this equation, we rescale time by the as-yet-unknown time-scale τ_1, giving $t^{(1)} = (t^* - t^*_{\rm nucl})/\tau_1$, where a supercript (1) denotes a variable rescaled in this stage. The bubble remains small in this stage so we rescale to the initial bubble size and let $R^{(1)} = R^*/R^*_{\rm nucl}$. The vapour pressure equation is then

$$\frac{1}{\tau_1}\frac{{\rm d}p_v^*}{{\rm d}t^{(1)}} = \frac{3}{R^{(1)}}\left(1-\lambda_3 T_v^*\right)^{-1}\left[\frac{\lambda_3\lambda_5}{R^*_{\rm nucl}}\left(1+\lambda_3 T_v^*\right)^{-1} T_v^*\frac{\partial T_l^*}{\partial \xi^*}\Big|_{\xi^*=0} - \frac{1}{\tau_1}p_v^*\frac{{\rm d}R^{(1)}}{{\rm d}t^{(1)}}\right]. \tag{4.3.4}$$

Assuming $t^{(1)}$ and $R^{(1)}$ are of order 1, the left hand side of this equation is of order $1/\tau_1$, as is the second term in the square brackets. Bubble expansion is initiated by the first term in the square brackets — an increase in pressure is driven by the gradient of the liquid temperature at the bubble wall — so we evaluate the magnitude of this term when the bubble nucleates. Assuming that T_v^* is of order 1, and other relevant parameter values are as given in Table 4.3.1, it remains to evaluate the magnitude of the liquid temperature gradient at the bubble wall.

4.3.1.1 Magnitude of temperature gradient

To determine the magnitude of the temperature gradient at the bubble wall at the early time-scale τ_1, we find an approximate analytic solution to the liquid temperature profile at $t^* = t^*_{\rm nucl}$ when the bubble nucleates. As detailed in Sec. 3.3.6, there are two stages simulated before the bubble nucleates: the 'heating stage' for $0 < t^* < t^*_{\rm vap}$, and the 'nucleating stage' $t^*_{\rm vap} \le t^* \le t^*_{\rm nucl}$.

The liquid temperature satisfies Eq. (4.3.1d). During the heating stage we have no bubble, $R = 0$, and no flow, $\dot{R} = 0$. Therefore the advection term of Eq. (4.3.1d) is zero and we have

$$\frac{\partial T_l^*}{\partial t^*} = \frac{\lambda_1}{(\xi^*)^2}\frac{\partial}{\partial \xi^*}\left((\xi^*)^2\frac{\partial T_l^*}{\partial \xi^*}\right) + \alpha\lambda_2 f^*(\xi^*,0)P^*(t^*), \tag{4.3.5}$$

In the heating stage, we also neglect the diffusion term; since the diffusion term is of size $\lambda_1 = 1.5\times10^{-4}$ and the laser heating term is of size $\lambda_2 = {\rm O}(1-10)$, we assume that heating occurs on a time-scale too short for diffusion to be significant. Neglecting diffusion and with f as given by Eq. (4.3.2), $\alpha = 1$ and $R^* = 0$, as specified for the heating stage, Eq. (4.3.5) becomes

$$\frac{\partial T_l^*}{\partial t^*} = \frac{\lambda_2 e^{-\xi^*}}{2}P^*(t^*). \tag{4.3.6}$$

Obtaining an approximate analytic expression for the liquid temperature at the end of the heating stage can be deduced from inspection of this equation. The liquid is heated from a uniform temperature of T^*_∞ until it reaches $T^*_{\rm nucl}$ at $\xi^* = 0$. Therefore, the temperature profile

at $t^* = t^*_{\text{vap}}$ is approximately

$$T^*_l(\xi^*, t^*_{\text{vap}}) = (T^*_{\text{nucl}} - T^*_\infty)e^{-\xi^*} + T^*_\infty. \tag{4.3.7}$$

We make a further simplification that the laser is at peak power for the duration of the heating stage, that is $P^*(t^*) = 1$. This simplification will allow us to easily approximate the duration of the heating phase, t^*_{vap}. The parameter λ_2 is the ratio of the reference time-scale τ to the time taken for the laser to heat the liquid approximately from body temperature to vaporisation temperature. It follows that the dimensionless time for the liquid to heat to vaporisation temperature is $t^*_{\text{vap}} \approx 1/\lambda_2$.

Finding an analytic expression for the liquid temperature in the nucleating stage takes a little more work. In this stage, we have a small region of vapour at the origin of fixed size R^*_{nucl}. The liquid temperature again satisfies Eq. (4.3.1d) without advection as the fluid is stationary. In contrast to the heating phase, in this stage we do not assume diffusion to be negligible. The numerical results of the temperature profile during the nucleation stage, as plotted in Fig. 3.3.3b, reveal a boundary layer in which we anticipate diffusion is significant. However, Eq. (4.3.1d) can be simplified somewhat by again taking $\alpha = 1$, the laser to be at maximum power for the duration of the nucleating stage, $P^*(t^*) = 1$, and approximating Eq. (4.3.2) as

$$f^*(\xi^*, R^*_{\text{nucl}}) = f^*(\xi^*, 0) = \frac{e^{-\xi^*}}{2}, \tag{4.3.8}$$

a reasonable assumption since $R^*_{\text{nucl}} \ll 1$. With these approximations, Eq. (4.3.1d) is

$$\frac{\partial T^*_l}{\partial t^*} = \frac{\lambda_1}{(\xi^* + R^*)^2}\frac{\partial}{\partial \xi^*}\left((\xi^* + R^*)^2 \frac{\partial T^*_l}{\partial \xi^*}\right) + \frac{\lambda_2}{2}e^{-\xi^*}. \tag{4.3.9}$$

We solve this equation in a shifted time $\hat{t} = t^* - t^*_{\text{vap}}$. The initial condition is given by Eq. (4.3.7). At $\xi^* = 0$ the temperature is fixed at $T^*_l(R^*_{\text{nucl}}, \hat{t}) = T^*_{\text{nucl}}$, and as $\xi^* \to \infty$, $T^*_l(\xi^*, \hat{t}) \to T^*_\infty$. Equation (4.3.9) is of a convenient form to be solved by a Laplace transform. We use Mathematica to conduct a Laplace transform of Eq. (4.3.9), find solution to the resulting ODE, and conduct an inverse Laplace transform. The resulting solution for the liquid temperature

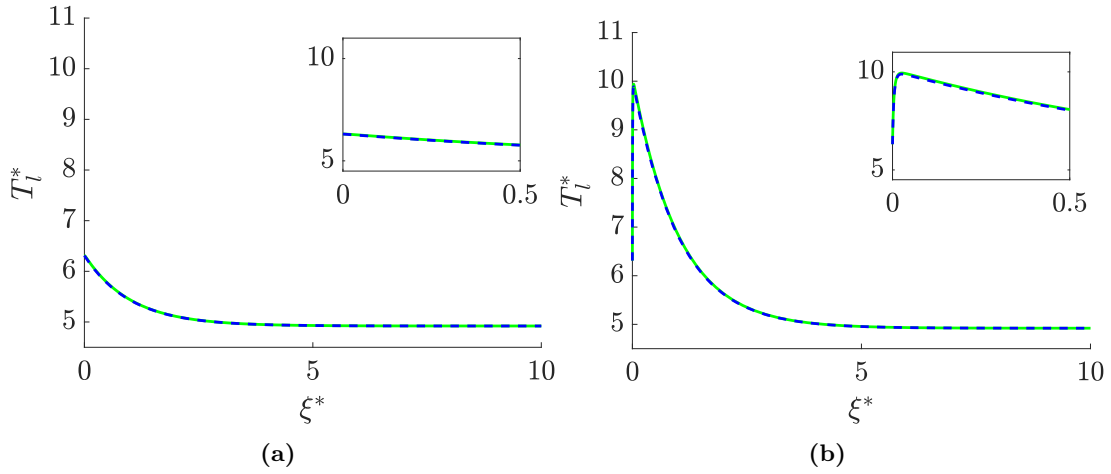


Figure 4.3.2 – Numerical solution (solid green line) and analytic approximation (dashed blue line) for T_l^* for the case of constant power laser, $P^*(t^*) = 1$ and $\lambda_2 = 13$ at (a) $t^* = t^*_{\text{vap}}$ and (b) $t^* = t^*_{\text{nucl}}$. Inserts show a region close to $\xi^* = 0$.

during the nucleation stage is found to be

$$
\begin{aligned}
T_l^*(\xi^*, \hat{t}) = T_\infty^* + \frac{\lambda_2}{2\lambda_1(\xi^* + R_{\text{nucl}})} \Bigg[& e^{-\xi^*} \Bigg\{ -2 - \xi^* - R_{\text{nucl}} \\
& + e^{\lambda_1 \hat{t}} \left(2 + \left(\xi^* + R_{\text{nucl}} - 2\lambda_1 \hat{t} \right) \left(1 + \frac{2\lambda_1 (T^*_{\text{nucl}} - T^*_\infty)}{\lambda_2} \right) \right) \Bigg\} \\
& + \left(2 + R^*_{\text{nucl}} + \frac{2\lambda_1 R^*_{\text{nucl}} (T^*_{\text{nucl}} - T^*_\infty)}{\lambda_2} \right) \operatorname{erfc} \left(\frac{\xi^*}{2\sqrt{\lambda_1 \hat{t}}} \right) \\
& + e^{-\xi^* + \lambda_1 \hat{t}} \left\{ -1 + \left(-\frac{\xi^* + R_{\text{nucl}}}{2} + \lambda_1 \hat{t} \right) \left(1 + \frac{2\lambda_1 (T^*_{\text{nucl}} - T^*_\infty)}{\lambda_2} \right) \right\} \operatorname{erfc} \left(\frac{\xi^* - 2\lambda_1 \hat{t}}{2\sqrt{\lambda_1 \hat{t}}} \right) \\
& + e^{\xi^* + \lambda_1 \hat{t}} \left\{ -1 + \left(\frac{\xi^* + R_{\text{nucl}}}{2} - R^*_{\text{nucl}} + \lambda_1 \hat{t} \right) \left(1 + \frac{2\lambda_1 (T^*_{\text{nucl}} - T^*_\infty)}{\lambda_2} \right) \right\} \operatorname{erfc} \left(\frac{\xi^* + 2\lambda_1 \hat{t}}{2\sqrt{\lambda_1 \hat{t}}} \right) \Bigg].
\end{aligned}
\tag{4.3.10}
$$

The analytic solution for the liquid temperature is shown in Fig. 4.3.2 alongside the numerical solution found by the method in Sec. 3.4 for the case of constant power laser, $P^*(t^*) = 1$, and $\lambda_2 = 13$. Figure 4.3.2a shows the temperature profile at $t^* = t^*_{\text{vap}}$ and Fig. 4.3.2b shows the temperature profile at $t^* = t^*_{\text{nucl}}$. The two solutions agree very well. In Fig. 4.3.3, the analytic solution is shown alongside the numerical solution for the case of a P120 1.0 J short pulse. In this case the analytic approximation overestimates the liquid temperature at $t^* = t^*_{\text{nucl}}$ because of the simplification that the laser is at peak power at all times. The agreement is still close enough to allow us to determine the time-scale τ_1 for pulses with non-constant power.

However, is it the gradient of $T_l^*(\xi^*, \hat{t})$ at the bubble wall that is of interest, so we take

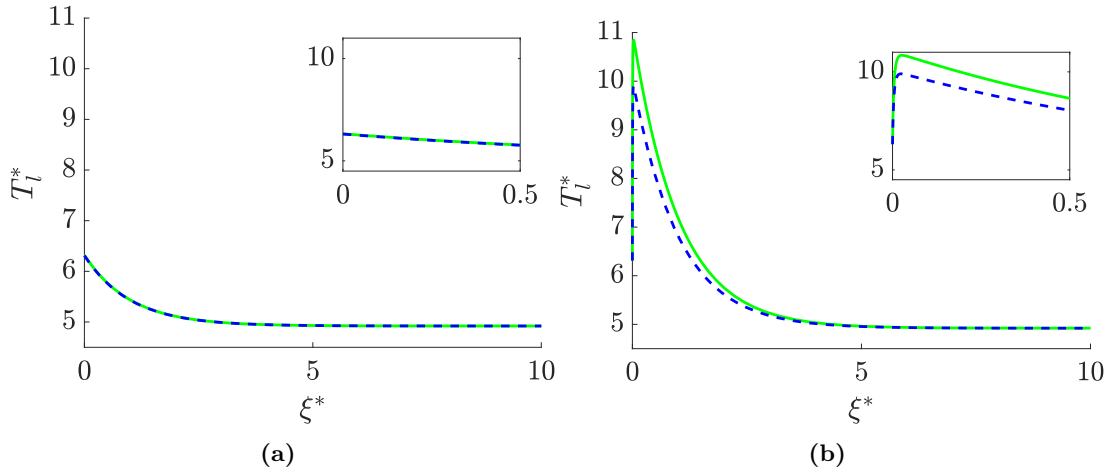


Figure 4.3.3 – Numerical solution (solid green line) and analytic approximation (dashed blue line) for T_l^* for the case of a P120 1.0 J short pulse at (a) $t^* = t^*_{\text{vap}}$ and (b) $t^* = t^*_{\text{nucl}}$. Inserts show a region close to $\xi^* = 0$.

the derivative of Eq. (4.3.10) with respect to ξ^* and evaluate at $\xi^* = 0$ to give

$$\begin{aligned}\left.\frac{\partial T_l^*(\xi^*,\hat{t})}{\partial \xi^*}\right|_{\xi^*=0} &= -\frac{T^*_{\text{nucl}} - T^*_\infty}{R^*_{\text{nucl}}} + \frac{\lambda_2}{\lambda_1 R^*_{\text{nucl}}}\Bigg[1 + R^*_{\text{nucl}} \\ &\quad - \sqrt{\frac{\lambda_1}{\pi t}}\left(2t + \frac{4\lambda_1 t(T^*_{\text{nucl}} - T^*_\infty)}{\lambda_2}\right) \\ &\quad + e^{\lambda_1 t}\left\{-2 + (1 - R^*_{\text{nucl}} + 2\lambda_1 t)\left(1 + \frac{2\lambda_1(T^*_{\text{nucl}} - T^*_\infty)}{\lambda_2}\right)\right\}\operatorname{erfc}\left(\sqrt{\lambda_1 t}\right)\Bigg].\end{aligned} \tag{4.3.11}$$

The duration of the nucleation stage is βt^*_{vap}, where $\beta = 2.7$, found from the fitting conducted in Sec. 3.4.3. Therefore, the bubble nucleates at time $\hat{t} = t^*_{\text{nucl}} - t^*_{\text{vap}} = 2.7 t^*_{\text{vap}} \approx 2.7/\lambda_2$. The gradient of the liquid temperature at the bubble wall as the bubble nucleates is therefore denoted

$$DT(\lambda_2) = \left.\frac{\partial T_l^*(\xi^*,\hat{t})}{\partial \xi^*}\right|_{\substack{\xi^*=0 \\ \hat{t}=2.7/\lambda_2}}, \tag{4.3.12}$$

where the derivative is given by the analytic expression in Eq. (4.3.11).

4.3.1.2 Time-scale of acceleration

We now use the results of the previous section to determine the time-scale on which the bubble pressure increases and the bubble wall accelerates. Returning to the rescaled vapour pressure equation, Eq. (4.3.4), we evaluate the size of the first term in the square brackets. With $\lambda_3 = \text{O}(10^{-2})$, and assuming $R^{(1)}$ and T_v^* are of order 1, this term is of size

$$\frac{\lambda_3\lambda_5}{R^*_{\text{nucl}}}\frac{3}{R^{(1)}\left(1 - (\lambda_3 T_v^*)^2\right)}T_v^*\left.\frac{\partial T_l^*}{\partial \xi^*}\right|_{\xi^*=0} = \text{O}\left(\frac{\lambda_3\lambda_5}{R^*_{\text{nucl}}}DT(\lambda_2)\right). \tag{4.3.13}$$

$P_{\max}$ (kW)	λ_2	τ_1	τ_3	ϵ_R
0.5	4.2×10^{-1}	2.7×10^{-3}	-	-
1	8.3×10^{-1}	2.5×10^{-3}	1.1	0.90
5	4.2	2.1×10^{-3}	3.2	0.31
10	8.3	1.8×10^{-3}	5.2	0.20
50	42	1.3×10^{-3}	15	0.066

Table 4.3.2 – Dimensionless parameter λ_2, time-scales τ_1 and τ_3, and parameter ϵ_R for a range of dimensional peak laser powers. The time-scale τ_1 is defined and explained in Sec. 4.3.1. The time-scale τ_3 and parameter ϵ_R are defined and explained in Sec. 4.3.3. Peak power of the P120 laser pulses lies between 1 kW and 15 kW but values outside this range are given for interest. No values of τ_3 and ϵ_R are given for the case $P_{\max} = 0.5$ kW as the definition of these parameters breaks down at this low power, as explained in Sec. 4.3.3.

From Eq. (4.3.4), we see that τ_1 is the inverse of the magnitude of this term,

$$\tau_1 = \frac{R^*_{\text{nucl}}}{\lambda_3 \lambda_5 DT(\lambda_2)}. \tag{4.3.14}$$

The time-scale τ_1 is dependent on the dimensionless parameter λ_2 which varies with the peak power of the laser. The other parameter values are given in Table 4.3.1. For laser pulses within clinically relevant parameters, $1 \leq \lambda_2 \leq 10$ and for this range of λ_2, we find $\tau_1 = \mathrm{O}(10^{-3})$.

The Rayleigh-Plesset equation, Eq. (4.3.1a), with the rescaled variables, is

$$\left(\frac{R^*_{\text{nucl}}}{\tau_1}\right)^2 \left(R^{(1)} \frac{\mathrm{d}^2 R^{(1)}}{\mathrm{d}(t^{(1)})^2} + \frac{3}{2} \left(\frac{\mathrm{d}^2 R^{(1)}}{\mathrm{d}(t^{(1)})^2} \right)^2 \right) = \left(p^*_v - 1 - \frac{\lambda_4}{R^*_{\text{nucl}} R^{(1)}} \right). \tag{4.3.15}$$

The terms $\left(R^*_{\text{nucl}}/\tau_1\right)^2$ and $\lambda_4/R^*_{\text{nucl}}$ are both approximately of order 1. The initial vapour pressure is chosen such that the bubble is at equilibrium and the right hand side is zero. To see an order 1 bubble velocity, the right hand side of Eq. (4.3.15) must become order 1, which is obtained by an order 1 increase in vapour pressure. This increase in vapour pressure overcomes the effect of surface tension to allow the bubble to expand. The time-scale of the pressure increase is exactly the time-scale τ_1 that we have found.

In Table 4.3.2, τ_1 is given for a range of peak laser power values, including values outside the clinically relevant range. The time-scale of this stage decreases with λ_2 but does not vary considerably. This is confirmed by studying the numerical results for these laser powers, as in Fig. 4.3.4. In all cases, the vapour pressure increases on similar time-scales, although the magnitude of the increase varies with λ_2. Similarly for all cases, the bubble accelerates on similar time-scales but the acceleration is greater for higher power pulses.

4.3.2 Stage 2: continued laser driven expansion

As detailed in stage 1, expansion is initially triggered by the positive temperature gradient in the liquid that occurs at the bubble wall during nucleation. During the next stage,

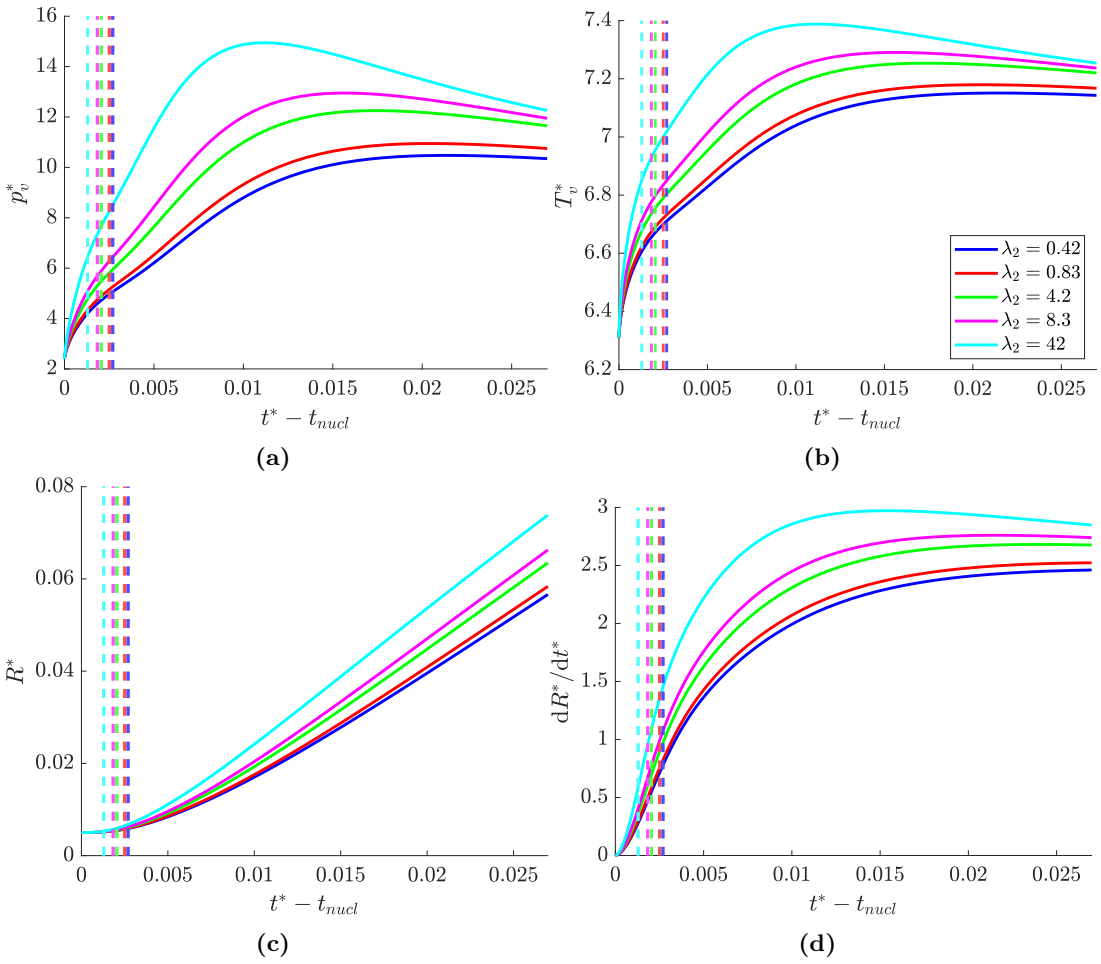


Figure 4.3.4 – (a) Vapour pressure, (b) vapour temperature, (c) bubble radius and (d) bubble velocity over time for four laser powers. In all cases $P^*(t^*) = 1$. The vertical dashed lines mark τ_1 for each case.

the positive temperature gradient persists and expansion continues due to ongoing input of laser energy to the liquid. We determine the dominant physics during this mid stage of bubble expansion, considering order 1 time-scales. The time-scale τ was chosen to balance the Rayleigh-Plesset equation, based on the absorption length of the laser, $1/\mu$, as detailed in Sec. 3.3.2. For this reason, the bubble reaches a dimensionless radius of order 1 on a dimensionless order 1 time-scale. At this time- and length-scale, the Rayleigh-Plesset equation remains in its original form

$$R^*\ddot{R}^* + \frac{3}{2}(\dot{R}^*)^2 = p_v^* - 1 + \frac{\lambda_4}{R^*}. \tag{4.3.16}$$

The final term, the surface tension term, is of order $\lambda_4 = 7 \times 10^{-3}$; during this stage the bubble expands relatively unimpeded by surface tension.

At an order 1 time-scale, the liquid is heating at a maximum rate of $\alpha\lambda_2$, the magnitude of the laser source term. Letting a superscript (2) denote variables rescaled in stage 2, liquid temperature is rescaled from its original form in Eqs. (4.3.1), to

$$T_l^{(2)} = (T_l^* - T_{\text{nucl}}^*))/(\alpha\lambda_2). \tag{4.3.17}$$

Equation (4.3.1d) then becomes

$$\frac{\partial T_l^{(2)}}{\partial t^*} + \frac{\mathrm{d}R^*}{\mathrm{d}t^*}\frac{\partial T_l^{(2)}}{\partial \xi^*}\left(\left(\frac{R^*}{\xi^*+R^*}\right)^2 - 1\right) = \frac{\lambda_1}{(\xi^*+R^*)^2}\frac{\partial}{\partial \xi^*}\left((\xi^*+R^*)^2\frac{\partial T_l^{(2)}}{\partial \xi^*}\right) + f^*(\xi^*, R^*)P^*(t^*), \tag{4.3.18}$$

with

$$f^*(\xi^*, R^*) = \frac{\mathrm{e}^{-\xi^*}}{((R^*)^2 + 2R^* + 2)}. \tag{4.3.19}$$

In this equation, all terms are of order 1 except the diffusion term, the first term on the right hand side, which is of order $\lambda_1 = 1.5 \times 10^{-4}$; the rate of change of temperature is dominated by advection and the input of laser energy while diffusion has little effect. However, we expect diffusion to be significant in an inner region as the numerical results suggest a steep temperature gradient at the bubble wall persists at this time-scale. A boundary layer at the bubble wall is also identified in the work of Plesset in [61], in which he states that heat flow to the bubble wall occurs primarily in a region in the liquid with thickness equal to the time dependent diffusion length. The diffusion length is given dimensionally as $\sqrt{D_l t}$, where $D_l = K_l/(c_{p,l}\rho_l)$ is the thermal diffusivity of the liquid [61]. In our dimensionless system, the diffusion length at this order 1 time-scale is $\sqrt{\lambda_1}$. The dimensionless parameter $\lambda_1 = K_l\tau\mu^2/(c_{p,l}\rho_l)$ is the ratio of the time-scale τ — on which time was non-dimensionalised in Chapter 3 — to the diffusion time-

scale. In the inner region, the length-scale is therefore $\xi^{(2)} = \xi^*/\sqrt{\lambda_1}$ and we denote the liquid temperature in this boundary region $T^{(2)}_{l,b}$. The inner liquid temperature equation is therefore

$$\begin{aligned}\frac{\partial T^{(2)}_{l,b}}{\partial t^*} + \frac{1}{\sqrt{\lambda_1}}\frac{\mathrm{d}R^*}{\mathrm{d}t^*}\frac{\partial T^{(2)}_{l,b}}{\partial \xi^{(2)}}\left(\left(\frac{R^*}{\sqrt{\lambda_1}\xi^{(2)} + R^*}\right)^2 - 1\right) \\ = (\sqrt{\lambda_1}\xi^{(2)} + R^*)^{-2}\frac{\partial}{\partial \xi^{(2)}}\left((\sqrt{\lambda_1}\xi^{(2)} + R^*)^2\frac{\partial T^{(2)}_{l,b}}{\partial \xi^{(2)}}\right) \\ + f^*(\sqrt{\lambda_1}\xi^{(2)}, R^*)P^*(t^*),\end{aligned} \tag{4.3.20}$$

with

$$f^*(\sqrt{\lambda_1}\xi^{(2)}, R^*) = \frac{\mathrm{e}^{-\sqrt{\lambda_1}\xi^{(2)}}}{((R^*)^2 + 2R^* + 2)}. \tag{4.3.21}$$

We verify that the second term of Eq.(4.3.20) is of order 1 by making the expansion

$$\frac{1}{\sqrt{\lambda_1}}\left(\left(\frac{R^*}{\sqrt{\lambda_1}\xi^{(2)} + R^*}\right)^2 - 1\right) = \frac{1}{\sqrt{\lambda_1}}\left(\left(1 - \frac{2\sqrt{\lambda_1}\xi^{(2)}}{R^*} + \mathrm{O}(\lambda_1)\right) - 1\right) \tag{4.3.22}$$

$$= \frac{2\xi^{(2)}}{R^*} + \mathrm{O}(\sqrt{\lambda_1}). \tag{4.3.23}$$

Equation (4.3.20) for the temperature in the boundary layer is solved subject to

$$T^{(2)}_{l,b}(0, t^*) = (T^*_v(t^*) - T^*_{\mathrm{vap}})/(\alpha\lambda_2), \tag{4.3.24}$$

at the bubble wall and the matching condition

$$T^{(2)}_{l,b}(\xi^{(2)}, t^*) \to T^{(2)}_l(0, t^*), \tag{4.3.25}$$

as $\xi^{(2)} \to \infty$.

Equation (4.3.1b) under the rescaled variables is

$$\frac{\mathrm{d}p^*_v}{\mathrm{d}t^*} = \frac{3}{R^*}(1 - \lambda_3 T^*_v)^{-1}\left[\frac{\alpha\lambda_2\lambda_3\lambda_5}{\sqrt{\lambda_1}}(1 + \lambda_3 T^*_v)^{-1}T^*_v\frac{\partial T^{(2)}_{l,b}}{\partial \xi^{(2)}}\Big|_{\xi^{(2)}=0} - p^*_v\dot{R}^*\right]. \tag{4.3.26}$$

The term of the left hand side and the second term in the square brackets on the right hand side are both of order 1. For a clinically relevant range of laser powers, the first term in the square brackets lies between $\mathrm{O}(10^{-2})$ and $\mathrm{O}(1)$. The relative impact on the rate of change of vapour pressure from the laser heating in comparison to vapour expansion during this phase is therefore dependent on the laser power. Equation (4.3.1c) remains unchanged under the rescaled variables.

In this stage, there is no benefit in a formal reduction of the model as we have identified

only two small terms: the surface tension term in the Rayleigh-Plesset equation and the diffusion term of the liquid temperature in the outer region. However, we have identified a boundary layer at the bubble wall in which the diffusion term is of order 1. Of particular interest is Eq. (4.3.26); during this stage, the vapour pressure depends both on influx of energy from the liquid and bubble expansion. The relative dominance of these effects is dependent on the temperature gradient at the bubble wall, which is sustained by laser heating of the liquid. The balance of the two effects determines the rate of change of vapour pressure at this time-scale, which in turn affects bubble expansion via (4.3.16). In the next stage, this balance changes and the bubble moves into a different regime.

4.3.3 Stage 3: deceleration

In this stage, the bubble decelerates until reaching maximum size. In the previous stage, continued expansion was driven by laser heating; it follows that for the deceleration stage we seek a time-scale, τ_3, at which the laser is no longer dominant in the dynamics of the bubble.

The spatio-temporal intensity of the laser is $\alpha P^*(t^*)f^*(\xi^*, R^*)$, which, due to non-dimensionalisation, is bounded between 0 and $\alpha = 0.2$. The spatial part of the laser intensity, Eq. (4.3.2) is

$$f^*(\xi^*, R^*) = \frac{\mathrm{e}^{-\xi^*}}{((R^*)^2 + 2R^* + 2)}. \tag{4.3.27}$$

This function decreases as R^* increases: as the bubble expands, the laser power is distributed over a larger area. For a yet-to-be-determined small parameter $\epsilon_R \ll 1$, when $1/R^* = \mathrm{O}(\epsilon_R)$ we have

$$f^*(\xi^*, R^*) = \mathrm{O}(\epsilon_R^2), \tag{4.3.28}$$

and the intensity is $\alpha P^*(t^*)f^*(\xi^*, R^*) = \mathrm{O}(\alpha\epsilon_R^2)$. The Rayleigh-Plesset equation, Eq. (4.3.1a), gives the time-scale at which this bubble size is reached: assuming that the vapour pressure remains at order 1 and therefore that the left hand side of Eq. (4.3.1a) is also of order 1, we conclude that $R^* = \mathrm{O}(1/\epsilon_R)$ occurs at a time-scale $\tau_3 = \mathrm{O}(1/\epsilon_R)$.

Variables rescaled in stage 3 are denoted with a superscript (3). Time and bubble size are rescaled on ϵ_R from their original form in Eqs.(4.3.1), giving $t^{(3)} = (t^* - t^*_{\mathrm{nucl}})\epsilon_R$ and $R^{(3)} = \epsilon_R R^*$. The rescaled dimensionless Rayleigh-Plesset equation, Eq. (4.3.1a), is therefore

$$R^{(3)}\frac{\mathrm{d}^2R^{(3)}}{\mathrm{d}(t^{(3)})^2} + \frac{3}{2}\left(\frac{\mathrm{d}^2R^{(3)}}{\mathrm{d}(t^{(3)})^2}\right)^2 = p_v^* - 1 - \frac{\lambda_4\epsilon_R}{R^{(3)}}. \tag{4.3.29}$$

As in the previous stage, the change in temperature in the liquid is related to the time-scale $\tau_3 = 1/\epsilon_R$, and the magnitude of the laser source term $\alpha\lambda_2\epsilon_R^2$, so liquid temperature is rescaled

to

$$T_l^{(3)} = (T_l^* - T_{\rm nucl}^*)\epsilon_R/(\epsilon_R^2\alpha\lambda_2) \tag{4.3.30}$$

$$= (T_l^* - T_{\rm nucl}^*)/(\epsilon_R\alpha\lambda_2). \tag{4.3.31}$$

The Clausius-Clapeyron relation, Eq. (4.3.1c) remains unchanged

$$\frac{{\rm d}T_v^*}{{\rm d}t^{(3)}} = \frac{\lambda_3(T_v^*)^2}{p_v^*}\frac{{\rm d}p_v^*}{{\rm d}t^{(3)}}. \tag{4.3.32}$$

The liquid temperature equation, Eq. (4.3.1d), becomes

$$\frac{\partial T_l^{(3)}}{\partial t^{(3)}} + \frac{1}{\epsilon_R}\frac{{\rm d}R^{(3)}}{{\rm d}t^{(3)}}\frac{\partial T_l^{(3)}}{\partial \xi^*}\left(\left(\frac{R^{(3)}}{\epsilon_R\xi^* + R^{(3)}}\right)^2 - 1\right) = \frac{\lambda_1}{\epsilon_R(\epsilon_R\xi^* + R^{(3)})^2}\frac{\partial}{\partial\xi^*}\left((\epsilon_R\xi^* + R^{(3)})^2\frac{\partial T_l^{(3)}}{\partial\xi^*}\right) + \frac{{\rm e}^{-\xi^*}}{((R^{(3)})^2 + 2\epsilon_R R^{(3)} + 2\epsilon_R^2)}. \tag{4.3.33}$$

The numerical results in Fig 4.3.1d suggest that the boundary layer has lowered and spread at the time-scale of the third stage. However, we assume that a temperature gradient of some magnitude remains in a boundary layer at the bubble wall. The length-scale in this region is again the diffusion length $\xi^{(3)} = \xi/\sqrt{\lambda_1\tau_3} = \xi\sqrt{\epsilon_R/\lambda_1}$. The liquid temperature in this region is denoted $T_{l,b}^{(3)}$ and is given by

$$\frac{\partial T_{l,b}^{(3)}}{\partial t^{(3)}} + \frac{1}{\sqrt{\lambda_1\epsilon_R}}\frac{{\rm d}R^{(3)}}{{\rm d}t^{(3)}}\frac{\partial T_{l,b}^{(3)}}{\partial \xi^{(3)}}\left(\left(\frac{R^{(3)}}{\sqrt{\lambda_1\epsilon_R}\xi^{(3)} + R^{(3)}}\right)^2 - 1\right)$$
$$= (\sqrt{\lambda_1\epsilon_R}\xi^{(3)} + R^{(3)})^{-2}\frac{\partial}{\partial\xi^{(3)}}\left((\sqrt{\lambda_1\epsilon_R}\xi^{(3)} + R^{(3)})^2\frac{\partial T_{l,b}^{(3)}}{\partial\xi^{(3)}}\right)$$
$$+ \frac{{\rm e}^{-\sqrt{\lambda_1/\epsilon_R}\xi^{(3)}}}{((R^{(3)})^2 + 2\epsilon_R R^{(3)} + 2\epsilon_R^2)}. \tag{4.3.34}$$

Equation (4.3.34) for the temperature in the boundary layer is solved subject to

$$T_{l,b}^{(3)}(0, t^{(3)}) = (T_v^*(t^{(3)}) - T_{\rm vap}^*)/(\epsilon_R\alpha\lambda_2). \tag{4.3.35}$$

at the bubble wall and the matching condition

$$T_{l,b}^{(3)}(\xi^{(3)}, t^{(3)}) \to T_l^{(3)}(0, t^{(3)}), \tag{4.3.36}$$

as $\xi^{(3)} \to \infty$.

Finally, the vapour pressure equation, Eq. (4.3.1b), with the rescaled variables is

$$\frac{\mathrm{d}p_v^*}{\mathrm{d}t^{(3)}} = \frac{3}{R^{(3)}}\left(1-\lambda_3 T_v^*\right)^{-1}\left[\alpha\lambda_2\lambda_3\lambda_5\sqrt{\frac{\epsilon_R^3}{\lambda_1}}\left(1+\lambda_3 T_v^*\right)^{-1} T_v^*\frac{\partial T_{l,b}^{(3)}}{\partial \xi^{(3)}}\Big|_{\xi^{(3)}=0} - p_v^*\frac{\mathrm{d}R^{(3)}}{\mathrm{d}t^{(3)}}\right]. \quad (4.3.37)$$

As with the previous two stages, the balance of the terms in the vapour pressure equation is key to the bubble dynamics in this stage. In this case, this equation allows us to determine the size of the small parameter ϵ_R which tells us the time-scale of this stage, $\tau_3 = 1/\epsilon_R$. In particular, we look for ϵ_R such that the first term in the square brackets is small enough that the flow of heat to the bubble wall can be considered negligible. In the last stage we determined that the size of this term lay between 10^{-2} and 1, so we now seek ϵ_R such that this term is less than or equal to 10^{-3}, that is

$$\alpha\lambda_2\lambda_3\lambda_5\sqrt{\frac{\epsilon_R^3}{\lambda_1}} \leq 10^{-3}. \quad (4.3.38)$$

Requiring terms to be of order 10^{-3} or smaller to be considered negligible is consistent with the reduction in the previous chapter.

For a clinically relevant range of laser powers, we have $\lambda_2 = \mathrm{O}(1-10)$. The values of ϵ_R and τ_3 are given in Table 4.3.2 for this range of λ_2 as well as for values outside of this range. For the case $\lambda_2 = 0.42$, no values of ϵ_R and τ_3 can be found as it is not possible to satisfy both Eq. (4.3.38) and $\epsilon_R \ll 1$. For the case $\lambda_2 = 0.82$, which is at the lower end of the clinically relevant range, ϵ_R is only a little less that 1 and we see that the time-scales of stages 2 and 3 are very close, with stage 2 occurring on a time-scale of 1 and in this case $\tau_3 = 1.1$. We therefore conclude that for $\lambda_2 = \mathrm{O}(1)$, stages 2 are 3 may not be distinct. For the reduction in the following section we focus on the mid to high end of the clinically relevant range with $\lambda_2 = \mathrm{O}(10)$.

4.3.3.1 Reduced equations

In this stage, a formal reduction of the model is carried out. We find that the system reduces significantly and we can interpret the remaining equations to understand the physics at this stage. Taking $\lambda_2 = \mathrm{O}(10)$, we find $\epsilon_R = \mathrm{O}(0.1)$ and $\tau_3 = \mathrm{O}(10)$. With these values, we identify and define small parameters in the rescaled equations, Eqs.(4.3.29)-(4.3.37) to be

$$\epsilon_1 = \lambda_4\epsilon_R \qquad = \mathrm{O}(10^{-3}), \quad (4.3.39a)$$

$$\epsilon_2 = \alpha\lambda_2\lambda_3\lambda_5\sqrt{\epsilon_R^3/\lambda_1} = \mathrm{O}(10^{-3}). \quad (4.3.39b)$$

A further small parameter is defined in anticipation that it will appear in the reduced equations

$$\epsilon_3 = \lambda_3^2 = \mathrm{O}(10^{-4}). \quad (4.3.40)$$

We take an asymptotic expansion of all variables in the small parameters ϵ_1, ϵ_2, and ϵ_3. In the Rayleigh-Plesset equation, Eq. (4.3.29), at leading order the surface tension term is neglected but the other terms remain, giving

$$R^{(3)}\frac{\mathrm{d}^2R^{(3)}}{\mathrm{d}(t^{(3)})^2}+\frac{3}{2}\left(\frac{\mathrm{d}^2R^{(3)}}{\mathrm{d}(t^{(3)})^2}\right)^2=p_v^*-1+\mathrm{O}(\epsilon_1,\epsilon_2,\epsilon_3). \tag{4.3.41}$$

The Clausius-Clapeyron relation, Eq. (4.3.32) remains unchanged at leading order,

$$\frac{\mathrm{d}T_v^*}{\mathrm{d}t^{(3)}}=\frac{\lambda_3(T_v^*)^2}{p_v^*}\frac{\mathrm{d}p_v^*}{\mathrm{d}t^{(3)}}+\mathrm{O}(\epsilon_1,\epsilon_2,\epsilon_3). \tag{4.3.42}$$

The vapour pressure equation, Eq. (4.3.1b), is

$$\frac{\mathrm{d}p_v^*}{\mathrm{d}t^{(3)}}=-\frac{3p_v^*}{R^{(3)}\left(1-\lambda_3T_v^*\right)}\frac{\mathrm{d}R^{(3)}}{\mathrm{d}t^{(3)}}+\mathrm{O}(\epsilon_1,\epsilon_2,\epsilon_3). \tag{4.3.43}$$

which can be further expanded as

$$\frac{\mathrm{d}p_v^*}{\mathrm{d}t^{(3)}}=-\frac{3p_v^*}{R^{(3)}}\frac{\mathrm{d}R^{(3)}}{\mathrm{d}t^{(3)}}\left(1+\lambda_3T_v^*\right)+\mathrm{O}(\epsilon_1,\epsilon_2,\epsilon_3). \tag{4.3.44}$$

We observe that at leading order, these three equations — Eq. (4.3.41), Eq. (4.3.42) and Eq. (4.3.42) — decouple from the liquid temperature, T_l^*. The magnitude of the liquid temperature and boundary layer at this stage gave us the size of the temperature gradient term in Eq. (4.3.37), which provided the condition on ϵ_R given by Eq. (4.3.38). However, in the reduced sytem it is not neccesary to solve for the liquid temperature to determine the dynamics of the bubble. We therefore drop Eq. (4.3.33) and Eq. (4.3.34).

In summary, at leading order in stage 3 the bubble dynamics are determined by just three equations,

$$R^{(3)}\frac{\mathrm{d}^2R^{(3)}}{\mathrm{d}(t^{(3)})^2}+\frac{3}{2}\left(\frac{\mathrm{d}^2R^{(3)}}{\mathrm{d}(t^{(3)})^2}\right)^2=p_v^*-1, \tag{4.3.45a}$$

$$\frac{\mathrm{d}T_v^*}{\mathrm{d}t^{(3)}}=\frac{\lambda_3(T_v^*)^2}{p_v^*}\frac{\mathrm{d}p_v^*}{\mathrm{d}t^{(3)}}, \tag{4.3.45b}$$

$$\frac{\mathrm{d}p_v^*}{\mathrm{d}t^{(3)}}=-\frac{3p_v^*}{R^{(3)}}\frac{\mathrm{d}R^{(3)}}{\mathrm{d}t^{(3)}}\left(1+\lambda_3T_v^*\right). \tag{4.3.45c}$$

The solution of the reduced system begins at $t^*=\tau_3+t^*_{\mathrm{nucl}}$ which, in the rescaled time

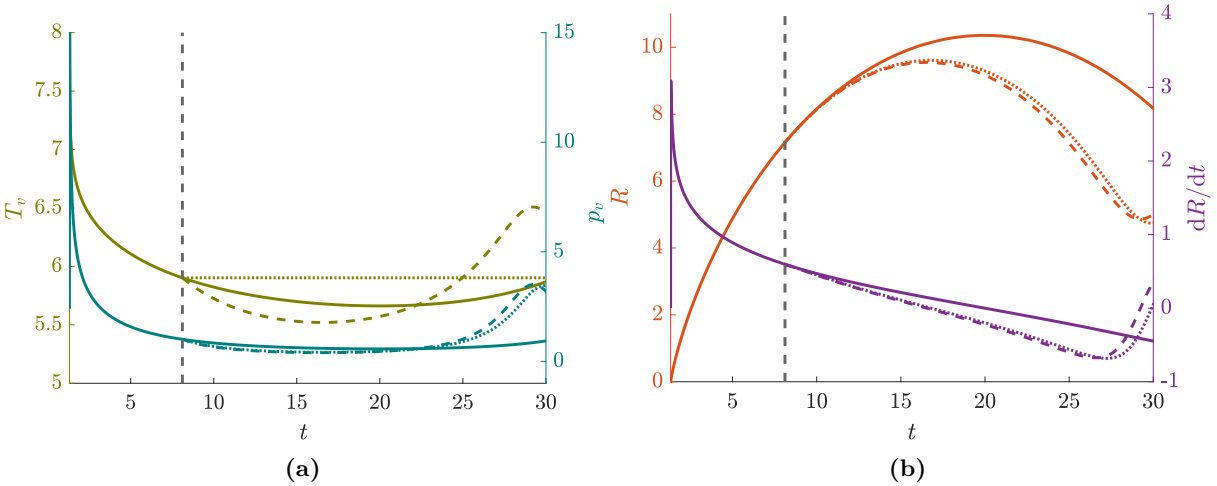


Figure 4.3.5 – (a) Vapour temperature and vapour pressure and (b) bubble radius and velocity for a P120 1.0 J short pulse. Solid lines mark the full numerical solution, dashed lines show the solution of the leading order equations for stage 3, Eqs.(4.3.45), for $t^* > \tau_3 + t_{\text{nucl}} = 8.1$. Dotted lines show the case that p_v^* is given by Eq. (4.3.47), and the bubble expands isothermally. The vertical dashed line marks $t^* = \tau_3 = 10$

of this stage, is $t^{(3)} = 1$. The initial conditions applied at $t^{(3)} = 1$ are

$$p_v^*(t^{(3)} = 1) = p_v^*(t^* = \tau_3 + t_{\text{nucl}}^*), \tag{4.3.46a}$$

$$T_v^*(t^{(3)} = 1) = T_v^*(t^* = \tau_3 + t_{\text{nucl}}^*), \tag{4.3.46b}$$

$$R^{(3)}(t^{(3)} = 1) = \epsilon_R R^*(t^* = \tau_3 + t_{\text{nucl}}^*), \tag{4.3.46c}$$

$$\tag{4.3.46d}$$

where $p_v^*(t^* = \tau_3 + t_{\text{nucl}}^*)$, $T_v^*(t^* = \tau_3 + t_{\text{nucl}}^*)$ and $R^*(t^* = \tau_3 + t_{\text{nucl}}^*)$ are given by the numerical solution of the full system, Eqs.(4.3.1).

4.3.3.2 Analysis of stage 3

The significant difference between this stage and the previous one is the vapour pressure equation, Eq. (4.3.45). In this stage, the temperature gradient term does not contribute at leading order and therefore the vapour cools and the bubble expands to its maximum size under momentum.

The full numerical solution is plotted alongside the solution of the leading order equations for $t^* \geq \tau_3 + t_{\text{nucl}}$ in Fig. 4.3.5, for the case of a P120 1.0 J short pulse. For this pulse, $\lambda_2 = 13$ and $\tau_3 + t_{\text{nucl}} = 8.1$. The reduced equations give a reasonable approximation to the full model although underestimate bubble size. This underestimation comes from neglecting any heatflow from the liquid to the vapour.

Although we have so far retained terms larger than $\mathrm{O}(10^{-3})$, it is interesting to analyse the behavior of Eq. (4.3.44) without the $\lambda_3 = \mathrm{O}(10^{-2})$ term; keeping just the largest two terms,

this equation is written as

$$\frac{\mathrm{d}p_v^*}{\mathrm{d}t^{(3)}} = -\frac{3p_v^*}{R^{(3)}}\frac{\mathrm{d}R^{(3)}}{\mathrm{d}t^{(3)}}, \tag{4.3.47}$$

which can be directly integrated to

$$p_v^* = -\left(\frac{C}{R^{(3)}}\right)^3, \tag{4.3.48}$$

where C is an integration constant. This is the equation for isothermal expansion of a fixed mass of gas, in which pressure and volume are inversely proportional. The expansion at this stage is therefore close to isothermal and we expect little mass flux between liquid and vapour. The magnitude of mass flux is evaluated by returning to its definition, Eq. (3.3.31), and using the expression for vapour velocity Eq. (3.3.39), evaluated at the bubble wall, giving

$$\begin{aligned}\dot{m}^* &= \rho_v(\dot{R}^* - u_{v,R}^*) \\ &= \frac{p_v^*\dot{R}^*}{T_v^*} + \frac{R^*}{3}\frac{\mathrm{d}}{\mathrm{d}t^*}\left(\frac{p_v^*}{T_v^*}\right),\end{aligned} \tag{4.3.49}$$

where we have used the ideal gas relationship $\rho_v^* = p_v^*/T_v^*$. The Clausius-Clapeyron relationship, Eq. (4.3.1c), is used to write the temperature derivative in terms of pressure,

$$\begin{aligned}\dot{m}^* &= \frac{p_v^*\dot{R}^*}{T_v^*} + \frac{R^*}{3}\frac{\mathrm{d}p_v^*}{\mathrm{d}t^*}\left(\frac{1}{T_v^*} - \lambda_3\right), \\ &= \frac{p_v^*}{T_v^*}\frac{\mathrm{d}R^{(3)}}{\mathrm{d}t^{(3)}} + \frac{R^{(3)}}{3}\frac{\mathrm{d}p_v^*}{\mathrm{d}t^{(3)}}\left(\frac{1}{T_v^*} - \lambda_3\right),\end{aligned} \tag{4.3.50}$$

where time and bubble size have been rescaled in the last line, leaving the form of the equation unchanged. The pressure derivative is now written in terms of $R^{(3)}$ using Eq. (4.3.43), with the λ_3 term included,

$$\begin{aligned}\dot{m}^* &= \frac{p_v^*}{T_v^*}\frac{\mathrm{d}R^{(3)}}{\mathrm{d}t^{(3)}} - p_v^*\frac{\mathrm{d}R^{(3)}}{\mathrm{d}t^{(3)}}\left(1 + 2\lambda_3 T_v^*\right)\left(\frac{1}{T_v^*} - \lambda_3\right), \\ &= \lambda_3 p_v^*\frac{\mathrm{d}R^{(3)}}{\mathrm{d}t^{(3)}} + \mathrm{O}(\epsilon_3).\end{aligned} \tag{4.3.51}$$

From this equation we see that the mass flux of liquid to vapour is of order $\lambda_3 = \mathrm{O}(10^{-2})$ and becomes negative as the bubble collapses.

The case of isothermal expansion is plotted in Fig. 4.3.5 alongside the full model and the leading order equations. In the isothermal case the vapour pressure is given by Eq. (4.3.47) and the vapour temperature remains at a constant value from $t^* = \tau_3 + t_{\mathrm{nucl}}^*$, for the duration of stage 3. The isothermal case gives very close agreement to the leading order stage 3 model for vapour pressure, bubble size and bubble velocity, confirming that variations in vapour temperature are small and have little effect on the bubble dynamics at this time-scale.

4.3.4 Discussion

We have uncovered and analysed three stages of bubble expansion: acceleration; laser driven expansion; and deceleration. It was found that the vapour pressure equation, Eq. (4.3.1b), is key to understanding and determining the behavior at the different stages. The first term on the right hand side of this equation is the increase in vapour pressure due to the flow of heat to the bubble wall. Finding the relative size of this term is fundamental to understanding the bubble dynamics because increased vapour pressure drives bubble expansion. In stage 1, the time-scale of bubble acceleration, τ_1, was determined by finding the time-scale on which the heat conduction term becomes order 1. This time-scale was found to be dependent on the laser power but varies very little for the range of clinically relevant powers. In stage 2, we considered an order 1 time-scale and found that the size of the heat conduction term in the vapour pressure equation is dependent on the power of the laser. In both of these stages, a formal reduction of the system was not beneficial as very few terms could be dropped. This suggests that, at these time-scales, there is a complicated balance of physics. In stage 3 we sought a time-scale, τ_3, at which the heat conduction term of the vapour pressure equation is small. The time-scale of this stage, as with the first stage, is dependent on the power of the laser. As the conduction of heat from the liquid to the bubble is considered negligible in this stage, a reduction of the system sees the liquid and vapour equations decouple. The bubble's trajectory after this point is driven by momentum and residual heat.

4.4 Pulse exploration

In this section, we explore the effect on the bubble of pulse power, duration, and energy. We use the simple case of a rectangular pulse in which the laser is at maximum power for the duration of the pulse. We present the results in dimensional form in this section; since the non-dimensionalisation of the pusle power, $P(t)$, depends on the peak power of the laser, we cannot compare the dimensionless form of this function when varying the peak power.

4.4.1 Varying pulse power

We first vary the pulse power, $P_{\max}$, from 1 kW to 10 kW while keeping pulse duration, t_p, constant at 100 µs. This results in the pulse energy ranging from 0.1 J to 1.0 J. These pulses are plotted in Fig. 4.4.1a with the resulting bubble radii over time shown in Fig. 4.4.1b in the corresponding colour. Although not visible at the scale of this plot, all bubbles begin at size $R = 10^{-3}$ mm, as specified in Sec. 3.3.6.

The insert in Fig. 4.4.1b shows the bubble produced by the lowest power pulse, which delivers 0.1 J of energy in total; the energy delivered is enough to nucleate a bubble but not enough to cause expansion and the bubble just collapses from its initial size. For the remaining

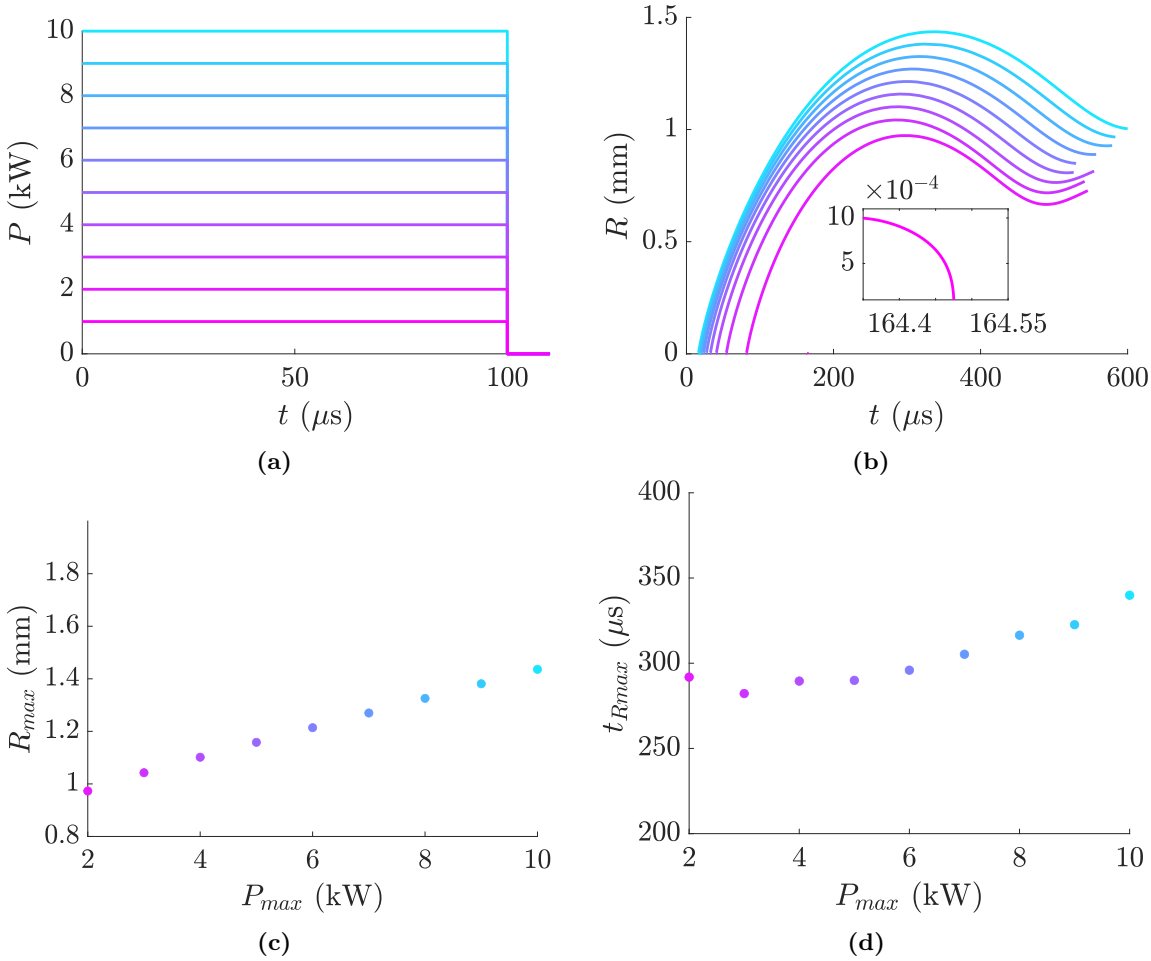


Figure 4.4.1 – (a) Laser pulses used in the simulations discussed in Sec. 4.4.1 and (b) the resulting bubble radii over time plotted in the corresponding colour. The insert in (b) shows the bubble of the lowest power pulse collapsing immediately after nucleation. (c) Maximum bubble radius and (d) time of maximum bubble radius plotted against pulse power for the pulses shown in (a).

pulses, the maximum bubble radius, $R_{\max}$, and the time that this radius is reached, $t_{R\max}$, are plotted against $P_{\max}$ in Fig. 4.4.1c and Fig. 4.4.1d respectively. We see that pulse power correlates approximately linearly with maximum bubble size.

Looking at the time at which the plots begin on Fig. 4.4.1b, we see that the higher the power, the quicker the bubble nucleates. The difference in nucleation time is due to the liquid heating more quickly when the laser power is higher. However after nucleation, the bubble takes longer to reach maximum size for higher power pulses due to expanding to a larger radius. The combination of decreasing nucleation time but increasing expansion time as the power is increased results in a non monotonic relationship in Fig. 4.4.1d between $P_{\max}$ and $t_{R\max}$. However, for pulses with $P_{\max} \geq 5$ kW, the difference in nucleation time is less significant and therefore there is a positive correlation between $P_{\max}$ and $t_{R\max}$.

4.4.2 Varying pulse duration

Next, we keep $P_{\max}$ constant at 10 kW and vary t_p from 10 µs to 100 µs. As in the previous section, the energy of these pulses ranges from 0.1 J to 1.0 J. The pulses are plotted

in Fig. 4.4.2a and the resulting bubble radii over time are plotted in Fig. 4.4.2b. The insert in Fig. 4.4.2b displays the bubble of the shortest pulse. Similarly to the lowest power pulse in Fig. 4.4.1, this bubble collapses immediately after nucleation due to the pulse energy being too low to drive expansion. For the remaining bubbles, $R_{\max}$ and $t_{R\max}$ are plotted against t_p in Fig. 4.4.2c and Fig. 4.4.2d respectively.

The peak power is the same for all pulses in this case so the bubbles all nucleate at the time same. In Fig. 4.4.2c and Fig. 4.4.2d, we see that both $R_{\max}$ and $t_{R\max}$ increase with t_p. The relationship between t_p and $R_{\max}$ appears not to be linear, with the gradient of the curve in Fig. 4.4.2c decreasing as the pulses increase in length. This is due to the form of the source term derived in Sec. 3.3.1. In particular, the spatial part of the source term,

$$f(\xi, R) = \frac{\mathrm{e}^{-\mu\xi}}{4\pi(R^2 + 2R/\mu + 2/\mu^2)}, \tag{4.4.1}$$

tends to zero as R becomes large. For this reason, as discussed in detail in Sec. 4.3.3, the laser heating of the liquid becomes negligible after a certain point in the bubble's expansion even if the laser is still at peak power.

4.4.3 Varying pulse duration and power

In this final study, t_p is varied from 10 µs to 100 µs but the pulse energy is kept constant at 1.0 J. This results in $P_{\max} = 1.0/t_p$ varying from 100 kW to 10 kW. The pulses are plotted in Fig. 4.4.3a and the resulting bubble radii over time are plotted in Fig. 4.4.3b. The variables $R_{\max}$ and $t_{R\max}$ are plotted against t_p in Fig. 4.4.3c and Fig. 4.4.3d respectively, and against $P_{\max}$ in Fig. 4.4.3e and Fig. 4.4.3f respectively.

As the pulse duration increases, $R_{\max}$ decreases, as seen in Fig. 4.4.3c. This is due to the power being lower as the pulse gets longer; in Fig. 4.4.3c the positive but non-linear relationship between $P_{\max}$ and $R_{\max}$ is clear. The time taken for the bubble to reach maximum size, $t_{\max}$, is approximately constant with varying t_p, and consequently also approximately constant with varying $P_{\max}$. This reflects the behavior seen experimentally and shown in Fig. 2.2.10a and Fig. 2.2.10b. The experimental results show that, for a given pulse energy, changing the duration of the pulse does not result in a significant change in the time taken for the bubble to reach maximum size, $t_{V\max}$, but does affect the maximum bubble volume $V_{\max}$. Both the experimental results and the model agree that delivering the energy as a shorter, higher-power pulse results in a larger bubble. In Fig. 4.4.3b, we can see that the nucleation time varies, which is due to the variation in pulse power. However, the difference in nucleation time between these bubbles is small compared to the time-scale of bubble expansion.

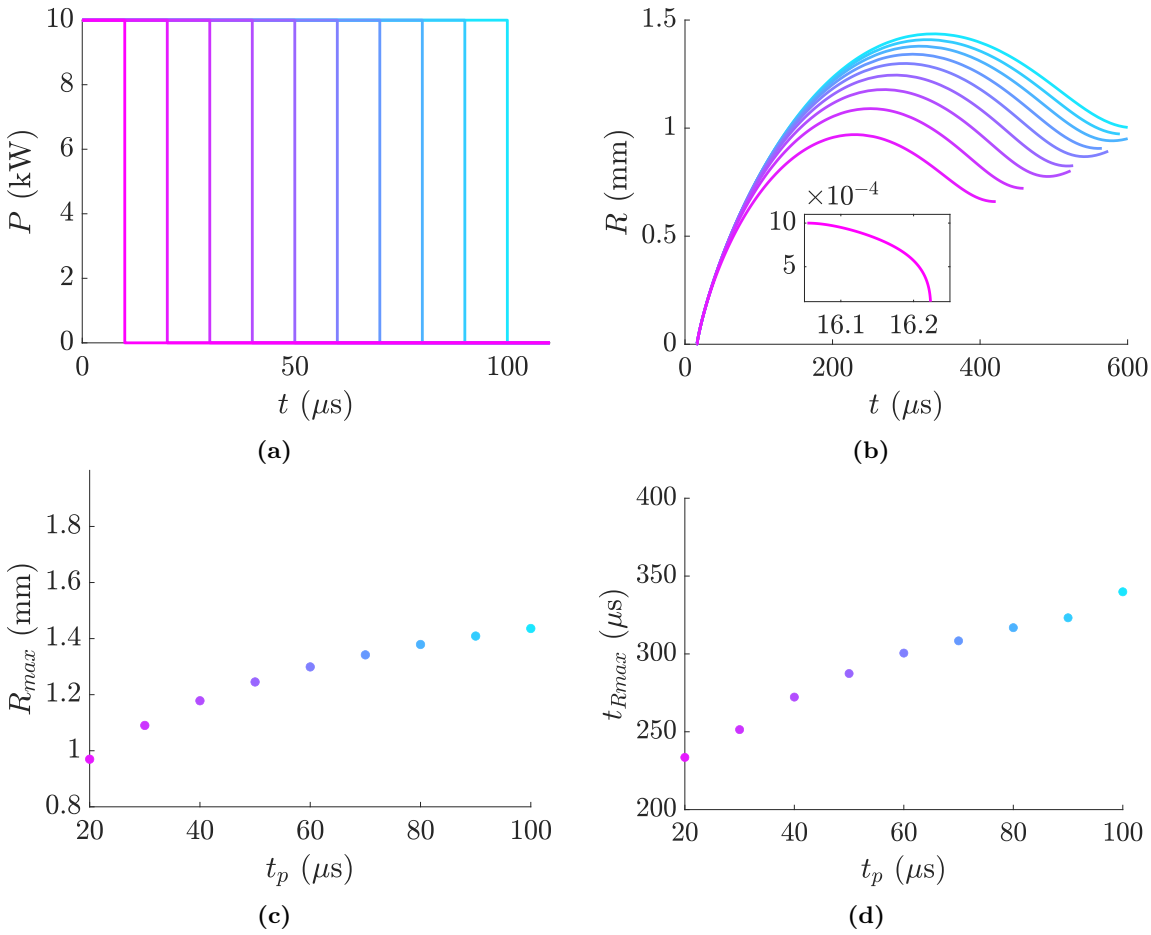


Figure 4.4.2 – (a) Laser pulses used in the simulations discussed in Sec. 4.4.2 and (b) the resulting bubble radii over time plotted in the corresponding colour. The insert in (b) shows the bubble of the lowest power pulse collapsing immediately after nucleation. (c) Maximum bubble radius and (d) time of maximum bubble radius plotted against pulse duration for the pulses shown in (a).

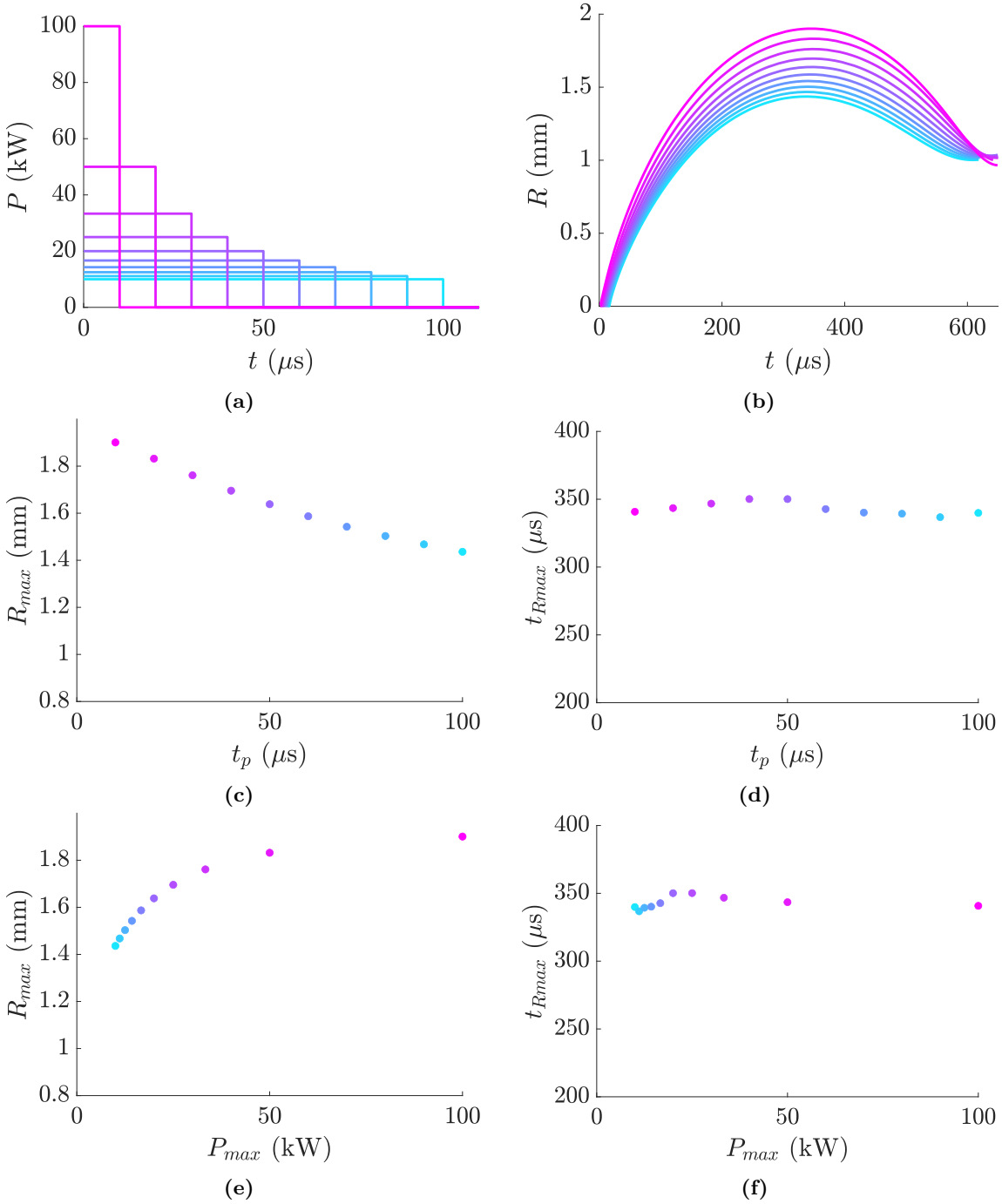


Figure 4.4.3 – (a) Laser pulses used in the simulations discussed in Sec. 4.4.3 and (b) the resulting bubble radii over time plotted in the corresponding colour. The insert in (b) shows the bubble of the lowest power pulse collapsing immediately after nucleation. (c) Maximum bubble radius and (d) time of maximum bubble radius plotted against pulse duration for the pulses shown in (a). (e) Maximum bubble radius and (f) time of maximum bubble radius plotted against pulse power for the pulses shown in (a).

4.4.4 Discussion

The results in Sec. 4.4.1 and Sec. 4.4.2, imply that bubble size increases as pulse energy increases. This relationship is true whether the energy increase is due to extending the pulse duration or increasing the pulse power. However, after a certain point, increasing the pulse length has a less notable effect on bubble size due to the form of the laser energy source term. In Sec. 4.4.3, we saw that for a given amount of energy, a larger bubble can be produced by delivering the energy over a shorter time.

The time of bubble expansion, $t_{R\max}$, is approximately constant across the pulses in Sec. 4.4.3, in which pulse energy was held constant. This leads to the conclusion that the time of expansion is closely tied to total pulse energy. This interpretation is supported by the positive correlation between pulse energy and $t_{R\max}$ in Sec. 4.4.1 and Sec. 4.4.2. The exception to this correlation is when the pulse power is below about 5 kW and the nucleation time is no longer negligible in comparison to $t_{R\max}$.

4.5 Conclusion

In this chapter we have shown the information and understanding about laser-induced bubbles that can be gained from the spherical model. The model gives good quantitative results for laser pulses shorter than about 200 µs, for which the bubbles are approximately spherical. For pulses longer than 200 µs, which produce highly elongated bubbles, the model yields reasonable order-of-magnitude results and qualitatively reflects the correlation between pulse energy and both bubble size and duration.

Probing the governing equations gives insight into the bubble dynamics at different time-scales. At the first stage of expansion, we found that the bubble accelerates from stationary on a dimensionless time-scale of $O(10^{-3})$ for all clinically relevant pulse powers. During the mid stage of expansion we saw a balance between vapour pressure increasing due to continued laser heating and vapour pressure dropping due to bubble expansion. The pulse power affects the relative sizes of these two effects which determines the bubble acceleration or deceleration at this time-scale. In the last stage of expansion, which occurs on a dimensionless time-scale of $O(10)$, the effect of the laser is negligible and the bubble equations decouple from the liquid temperature. The bubble expands under momentum but decelerates until reaching maximum size.

The simplicity of the model and numerical scheme allow solutions to be obtained within a few seconds. Due to the speed of the numerical solution, it is easy and cheap to vary pulse parameters and determine their effect on the bubble. As a simple example, a range of rectangular pulses were tested. It was found that pulse energy was the most important factor for both bubble size and bubble duration but that the distribution of the energy also had an effect on bubble size. These tests could be taken further to explore different pulse shapes.

There are certainly limitations to a spherical model. In particular, this model cannot reflect the shape of the elongated bubbles seen experimentally and cannot incorporate the solid boundaries of the laser fibre and stone. Furthermore, the spherically symmetric source term does not distribute the laser energy in the same way as the approximately-linear laser beam. To address these limitations, another modelling approach using a computational model in an axisymmetric geometry is presented in the following chapter.

Chapter 5

Axisymmetric bubble model

Although the spherical model can provide information and understanding about bubble dynamics, it is beneficial to move to a model that can handle an axisymmetric domain, more accurately reflecting the geometry of the laser fibre, bubble and stone. In particular, we wish to capture the elongated shape of the laser-induced bubbles seen experimentally. It is possible to use an interface tracking method — as used for the spherical model — in two or three dimensions, but analytically expressing the location of the vapour-liquid boundary becomes non-trivial. For this reason, we instead choose an interface capturing approach for the axisymmetric model.

The specific interface capturing model used here is the volume of fluid (VOF) method, which is commonly used for multi-phase flows in which the two or more fluids are immicisble. In this method, the spatial domain is divided into cells and a phase fraction parameter denotes the volume fraction of each fluid contained within each cell. The phase fraction may also be referred to as a 'phase field' or 'colour function'. In the case of a two-phase flow, the phase fraction is equal to 1 if the cell contains only fluid 1, and equal to 0 if the cell only contains fluid 2. In interface capturing methods, the location of the interface between phases is not explicitly tracked from one time-step to the next but is reconstructed at each time-step. Various methods of interface reconstruction exist; in the VOF method, the location of the interface between the two fluids is determined by finding the cells in which the phase fraction lies above 0 and below 1, as depicted in Fig. 5.0.1. Properties of the interface, such as curvature, become functions of the phase field.

With the flexibility given by the geometry of the axisymmetric model, we can gain information that could not be provided by the spherical model. Primarily, we aim to use this model to simulate bubbles that display the elongated shape seen experimentally. In particular, we want to reflect the dependence between pulse shape, bubble shape and bubble size. Once the correct qualitative behavior has been established, we can simulate a range of pulses that would not be possible experimentally and observe their effect on the bubble dynamics. Additionally, the axisymmetric geometry will allow us to test the effect of a solid, insulated boundary perpendicular to the laser fibre, in the position that a kidney stone would sit. We aim to observe physical properties at this boundary, including pressure, velocity and temperature. In lithotripsy treatment, the pressure, velocity and temperature at the kidney stone will determine factors such as the rate of stone breaking and the occurrence of retropulsion. While a solid, insulated boundary is not an accurate kidney stone model, we aim to gain an initial understanding of how a boundary near a bubble would be affected and show how the model could be utilised further for lithotripsy optimisation. The axisymmetric model and method of solution are detailed in Sec. 5.2, and numerical results of the model are presented in Sec. 5.3.

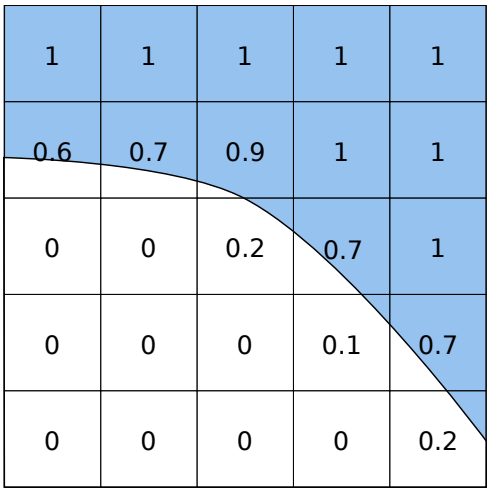


Figure 5.0.1 – Example values of the phase field of a two-phase flow. The phase fraction, α, only takes values away from 0 or 1 in cells containing the interface between the two fluids

5.0.1 OpenFOAM

The model presented in the following section is implemented using the computational fluid dynamics C++ package OpenFOAM 9. OpenFOAM uses a numerical method of solution called the finite volume method (FVM). We describe the FVM briefly in Sec. 5.2.6.1. Many solvers exist in OpenFOAM, each of which solves a pre-determined set of governing equations. However, being open source, it is possible to build custom solvers or adapt existing ones. There are a range of boundary conditions from which to choose while the domain and initial conditions are set by the user. OpenFOAM is commonly used to solve multi-phase VOF models and has been utilised previously for modelling bubbles [46, 48, 52, 66].

OpenFOAM 9 includes the functionality to include phase-change in a VOF model via the compressibleInterFoam solver. This solver is described as a "solver for 2 compressible, non-isothermal immiscible fluids using a VOF (volume of fluid) phase fraction based interface capturing approach, with optional mesh motion and mesh topology changes including adaptive re-meshing" [67]. The governing equations solved by compressibleInterFoam are given in 5.2.1. An explanation and derivation of the governing equations for this solver are not given in the OpenFOAM documentation. However, we have, as far as possible, investigated the equations and boundary conditions to ensure that the solver is consistent and relevant to our model.

We adapt compressibleInterFoam in two ways to model laser-induced bubbles. Firstly, we introduce a custom source term to the energy equation to model the transfer of laser energy to the fluid. Secondly, we implement a temperature-based model for phase change, described in Sec. 5.2.2, as opposed to one of the three pre-programmed, pressure-based phase change models in compressibleInterFoam. Pressure-based phase change occurs when a liquid is cool but a pressure drop triggers vaporisation and bubble nucleation. Temperature-based phase change occurs when the liquid pressure remains near or above atmospheric pressure and phase change is triggered by a rise in temperature.

5.1 Nomenclature

b, specific gas constant of vapour **or** distance between fibre tip and right hand domain boundary

c, half of domain dimension in z-direction

c_V, specific heat capacity at constant volume

D, thermal diffusivity

F, arbitrary field

K, thermal conductivity

k, kinetic energy

l_f, length of laser fibre

$\dot{M}$, mass transfer per unit volume

$\boldsymbol{n}$, normal vector

$\boldsymbol{u}_S$, normal vector to boundary S

P, laser power

p, pressure

r_f, radius of laser fibre

$\dot{Q}$, heat source in liquid due to laser

$\boldsymbol{u}$, velocity

S, right hand domain boundary

T, temperature

T_{vap}, vaporisation temperature

t, time

V, bubble volume

$\boldsymbol{x}$, tangent vector

$\boldsymbol{x}$, spatial location

Greek symbols

α, phase fraction of liquid

β_e, evaporation tuning parameter

β_c, condensation tuning parameter

δ, small distance

θ_d, angle of wedge domain

μ, absorption coefficient of laser in liquid

ρ, density

σ, coefficient of surface tension

τ, viscous stress tensor

Subscripts

l, liquid

v, vapour

∞, far-field value

5.2 Model

5.2.1 Governing equations

The volume of fluid (VOF) method is characterised by solving one set of equations that hold across both phases, with physical parameters averaged over the two phases [45–47]. The domain is divided into cells on which discretised versions of the governing equations are solved for pressure, p, temperature, T, velocity, $\boldsymbol{u}$ and the phase field α, as discussed in Sec. 5.2.6. The VOF method assumes that the phases are immiscible: a hard boundary between the liquid and vapour exists, although only the approximate location of this boundary is determined. Since the fluids are immiscible, only one is present at any location, therefore only one value of pressure,

temperature and velocity exist at any location. In cells containing the interface between phases, a volume average of each field value is obtained. The VOF approach contrasts to the two-phase models of Drew [41] and Zein et al. [43] in which the fluids are miscible and each has a separate pressure, temperature and velocity field.

Equations are given here in the form used in compressibleInterFoam, which can be found in the source code [68, 69]. A derivation of the equations is not given in the OpenFOAM documentation but we do find a derivation of the phase fraction and momentum equations in a paper by Shi et al [49]. Shi et al. developed a custom, two-phase OpenFOAM solver independently to the compressibleInterFoam solver, which uses largely the same governing equations, differing only in the form of the energy equation [49]. We therefore we follow the derivation of the phase fraction and momentum equations presented by Shi et al. [49]. OpenFOAM uses dimensional units so all quantities are given here dimensionally.

The phase fraction, α, gives the volume fraction of liquid in each cell. Since there are only two phases, the volume fraction of vapour is $1-\alpha$. Each phase satisfies conservation of mass

$$\frac{\partial}{\partial t}(\alpha\rho_l) + \boldsymbol{\nabla}\cdot(\alpha\rho_l\boldsymbol{u}) = \dot{M}, \tag{5.2.1}$$

$$\frac{\partial}{\partial t}((1-\alpha)\rho_v) + \boldsymbol{\nabla}\cdot((1-\alpha)\rho_v\boldsymbol{u}) = -\dot{M}, \tag{5.2.2}$$

where $\dot{M}$ is the rate of phase change from vapour to liquid per unit volume, referred to as volumetric mass flux or just 'mass flux' [49]. This definition of mass flux differs in two ways from the $\dot{m}$ defined and used in Chapter 3. Firstly, $\dot{m}$ is defined as the phase change per unit surface area of the bubble wall while $\dot{M}$ is defined per unit volume of the fluid. Secondly, positive $\dot{m}$ denotes phase change from liquid to vapour and negative denotes vapour to liquid whereas the sign of $\dot{M}$ is defined the opposite way; this definition of $\dot{M}$ is the convention in OpenFOAM.

The two conservation of mass equations, Eq. (5.2.1) and Eq. (5.2.2) are summed to give conservation of mass across both phases [49]

$$\frac{\partial\rho}{\partial t} + \boldsymbol{\nabla}\cdot(\rho\boldsymbol{u}) = 0, \tag{5.2.3}$$

where ρ is the volume averaged density,

$$\rho = \alpha\rho_l + (1-\alpha)\rho_v. \tag{5.2.4}$$

Equation (5.2.3) is preferable to Eq. (5.2.1) and Eq. (5.2.2), as it expresses conservation of mass across both phases and does not depend on mass flux. The variable α has been eliminated from Eq. (5.2.3) but an equation for the evolution of α is derived from Eq. (5.2.1) and Eq. (5.2.2) below. We take the liquid phase to be incompressible and the vapour density to be given by the

ideal gas equation

$$\rho_v = p/bT, \tag{5.2.5}$$

where b is the specific gas constant of the vapour.

The derivatives in Eq. (5.2.1) and Eq. (5.2.2) are expanded to

$$\frac{\partial \alpha}{\partial t} + \boldsymbol{\nabla} \cdot (\alpha \boldsymbol{u}) = -\frac{\alpha}{\rho_l}\frac{\mathrm{D}\rho_l}{\mathrm{D}t} + \frac{\dot{M}}{\rho_l}, \tag{5.2.6}$$

$$-\frac{\partial \alpha}{\partial t} + \boldsymbol{\nabla} \cdot ((1-\alpha) \boldsymbol{u}) = -\frac{(1-\alpha)}{\rho_v}\frac{\mathrm{D}\rho_v}{\mathrm{D}t} - \frac{\dot{M}}{\rho_v}. \tag{5.2.7}$$

We take $(1-\alpha)$ times Eq. (5.2.6) minus α times Eq. (5.2.7) to obtain a governing equation for the phase fraction [49]

$$\frac{\partial \alpha}{\partial t} + \boldsymbol{\nabla} \cdot (\alpha \boldsymbol{u}) = \alpha(1-\alpha)\left(\frac{1}{\rho_v}\frac{\mathrm{D}\rho_v}{\mathrm{D}t} - \frac{1}{\rho_l}\frac{\mathrm{D}\rho_l}{\mathrm{D}t}\right) + \alpha \boldsymbol{\nabla} \cdot \boldsymbol{u} + \dot{M}\left(\frac{1}{\rho_l} - \alpha\left(\frac{1}{\rho_l} - \frac{1}{\rho_v}\right)\right). \tag{5.2.8}$$

Equation (5.2.8), rather than Eq. (5.2.1) and Eq. (5.2.2), is solved for α as this form of the source term due to mass flux is more beneficial for numerical stability. The source term, the final term in Eq. (5.2.8), is split into a positive part and a negative part; positive and negative source terms are discretised in different ways in OpenFOAM to aid the stability of the solution.

The momentum equation is

$$\frac{\partial}{\partial t}(\rho \boldsymbol{u}) + \boldsymbol{\nabla} \cdot (\rho \boldsymbol{u}\boldsymbol{u}) = -\boldsymbol{\nabla} p + \boldsymbol{\nabla} \cdot \tau + \boldsymbol{f}_\sigma, \tag{5.2.9}$$

where τ is the viscous stress tensor and $\boldsymbol{f}_\sigma$ is stress due to surface tension. Acceleration due to gravity is neglected for simplicity. The viscous stress tensor takes the usual form

$$\tau_{ij} = \zeta(\boldsymbol{\nabla} \cdot \boldsymbol{u})\delta_{ij} + \eta\left(\frac{\partial u_i}{\partial x_j} + \frac{\partial u_j}{\partial x_i}\right) \tag{5.2.10}$$

where ζ is the bulk viscosity, η is the dynamic viscosity. Without f_σ, Eq. (5.2.9) is the standard Navier-Stokes equation for a single phase flow. This equation is applied to a two phase flow by replacing the density, dynamic viscosity and bulk viscosity with their volume averaged values and including the surface tension term, $\boldsymbol{f}_\sigma$. The stress due to surface tension is calculated as a function of the phase field

$$\boldsymbol{f}_\sigma = -\sigma \boldsymbol{\nabla} \cdot \left(\frac{\boldsymbol{\nabla}\alpha}{|\boldsymbol{\nabla}\alpha|}\right)\boldsymbol{\nabla}\alpha, \tag{5.2.11}$$

where σ is the coefficient of surface tension, and $-\boldsymbol{\nabla} \cdot (\boldsymbol{\nabla}\alpha/|\boldsymbol{\nabla}\alpha|)$ is the curvature of the liquid-vapour interface [49]. OpenFOAM uses an adjusted pressure $p_{rgh} = p - \rho(\boldsymbol{g} \cdot \boldsymbol{x})$, where $\boldsymbol{g}$ is acceleration due to gravity and $\boldsymbol{x}$ is the spatial location [70]. However, as we have taken $\boldsymbol{g} = \boldsymbol{0}$,

we have $p_{rgh} = p$ and the form of Eq. (5.2.9) does not change.

Finally, we have an energy equation

$$\frac{\partial}{\partial t}(\rho T) + \boldsymbol{\nabla} \cdot (\rho \boldsymbol{u} T) + \frac{1}{c_V}\left[\frac{\partial}{\partial t}(\rho k) + \boldsymbol{\nabla} \cdot (\rho \boldsymbol{u} k) + \boldsymbol{\nabla} \cdot (\boldsymbol{u} p)\right] = \boldsymbol{\nabla} \cdot (D \boldsymbol{\nabla} T) + \dot{Q}, \tag{5.2.12}$$

where $k = |\boldsymbol{u}|^2/2$ is kinetic energy, $\dot{Q}$ is a source term, D is the thermal diffusivity and c_V is the heat capacity at constant volume. For a single phase compressible flow, the form of Eq. (5.2.12) is standard, under the assumption of constant c_V and defining $D = K/c_V$, where K is thermal conductivity. Replacing the physical parameters ρ, $1/c_V$ and D with volume averaged parameters, Eq. (5.2.12) becomes an equation for the two phase flow. The heat capacity is averaged with respect to its inverse

$$\frac{1}{c_V} = \frac{\alpha}{c_{V,l}} + \frac{1-\alpha}{c_{V,v}}, \tag{5.2.13}$$

where the heat capacity of each phase is assumed to be constant. The volume averaged thermal diffusivity is

$$D = \frac{\alpha K_l}{c_{V,l}} + \frac{(1-\alpha)K_v}{c_{V,v}}. \tag{5.2.14}$$

Equation (5.2.12) does not include a term to model the latent heat used or released during phase change. The inclusion of a source or sink term for latent heat would be a beneficial addition to this equation to ensure conservation of energy is correctly modelled. It is likely that the temperatures reached using this model will be artificially high without accounting for the loss of energy to the latent heat of vaporisation.

To summarise, Eq. (5.2.3), Eq. (5.2.8), Eq. (5.2.9) and Eq. (5.2.12) are solved for four unknown variables: $\boldsymbol{u}$, α, p and T. The density ρ is given by Eq. (5.2.4) and Eq. (5.2.5), and the mass flux $\dot{M}$ is given by the model in the following section. Initial conditions are required for the four variables $\boldsymbol{u}$, α, p and T and are specified in Sec. 5.2.3. The definition of the domain and boundary conditions is given in Sec. 5.2.4.

5.2.2 Phase change

Many models exist for phase change in a VOF framework. The compressibleInterFoam solver in OpenFOAM 9 includes three phase change models, all of which are pressure-based [68, 69] — phase change is triggered by a pressure drop below a critical value. We require a temperature-based model — phase change is triggered by a temperature rise above a critical value. We choose the Lee model for phase change due to its simplicity and ease of numerical implementation [49, 71].

In this model, the mass flux is defined as: the mass of vapour, $(1-\alpha)\rho_v$, times the rate of production of liquid from vapour, $\dot{M}^+$, plus the the mass of liquid, $\alpha\rho_l$, times the rate of loss

of liquid to vapour, $\dot{M}^-$, where only one of $\dot{M}^+$ and $\dot{M}^-$ are non-zero at any time. That is,

$$\dot{M} = (1-\alpha)\rho_v \dot{M}^+ + \alpha\rho_l \dot{M}^-. \tag{5.2.15}$$

We assume that phase change occurs at a fixed temperature, $T_{\text{vap}} = 373$ K, the boiling temperature of water at atmospheric pressure. Vapour below this temperature will change phase to liquid and liquid above this temperature will change phase to vapour. This differs from the spherical model which used a variable pressure-dependent vaporisation temperature, with the relationship given by the Clausius-Clapeyron relation, as discussed in Sec. 3.2.2.

The rate of phase change of vapour to liquid per unit mass is dependent on the difference between T and T_{vap},

$$\dot{M}^+ = -\beta_c \min(T - T_{\text{vap}}, 0), \tag{5.2.16}$$

where β_c is a condensation tuning parameter. If $T \geq T_{\text{vap}}$, $\dot{M}^+ = 0$ and condensation of vapour to liquid does not occur. If $T < T_{\text{vap}}$, $\dot{M}^+ > 0$ and liquid is produced by condensation. Similarly,

$$\dot{M}^- = -\beta_e \max(T - T_{\text{vap}}, 0), \tag{5.2.17}$$

where β_e is an evaporation (vaporisation) tuning parameter. If $T \leq T_{\text{vap}}$, $\dot{M}^- = 0$ and vaporisation of liquid to vapour does not occur. If $T > T_{\text{vap}}$, $\dot{M}^- < 0$ and liquid is lost to vaporisation.

Although studies exist on the effect of varying β_c and β_e [72], these constants are generally tuned manually for a particular simulation [46, 49, 71]. Values are typically in the range $0.1 - 10^7$ s^{-1} and are chosen to be sufficiently small to ensure numerical convergence of the solution but high enough to ensure that the temperature at the vapour-liquid interface does not deviate significantly from $T = T_{\text{vap}}$ [49, 71]. Constants β_c and β_e are selected via a trial and error method, taking the largest values at which numerical convergence is obtained. We take $\beta_c = 1.0$ s^{-1} and $\beta_e = 2.0$ s^{-1} unless otherwise stated.

5.2.3 Initial conditions

Unless otherwise stated, initial conditions are set to be

$$\alpha(\boldsymbol{x}, 0) = 1, \tag{5.2.18}$$

$$p(\boldsymbol{x}, 0) = p_\infty, \tag{5.2.19}$$

$$T(\boldsymbol{x}, 0) = T_\infty, \tag{5.2.20}$$

$$\boldsymbol{u}(\boldsymbol{x}, 0) = \boldsymbol{0} \text{ m s}^{-1}, \tag{5.2.21}$$

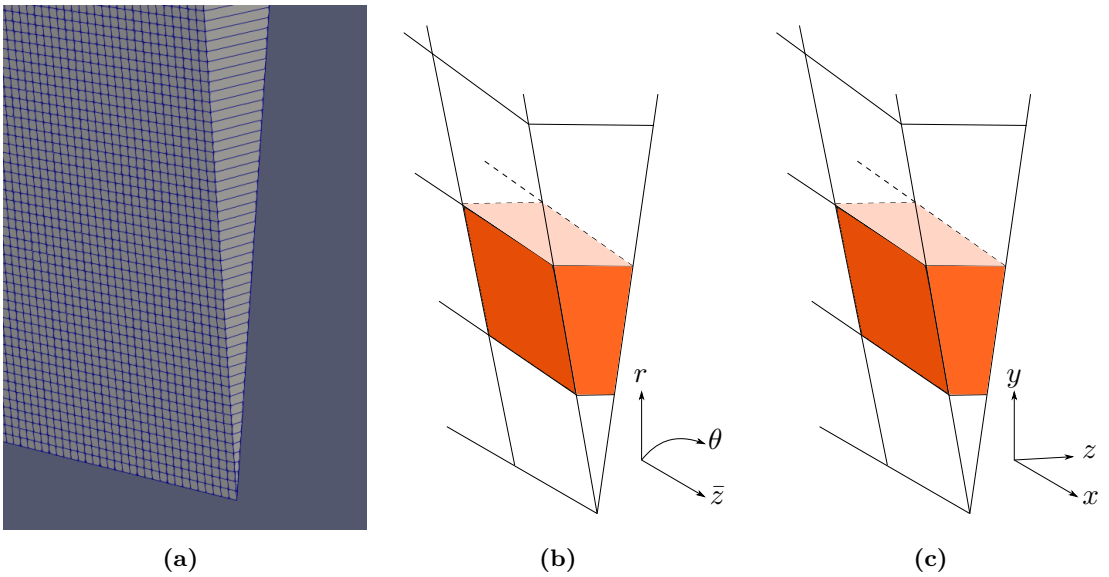


Figure 5.2.1 – (a) A side on view of an axisymmetric 'wedge' shaped grid. (b) A close-up of one cell in the wedge shaped grid; in cylindrical coordinates, the wedge axis is aligned with the $\hat{z}$-axis and the flow is symmetric about the θ-axis.(c) To solve in OpenFOAM, The wedge shaped grid is placed in Cartesian coordinates, with the axis of symmetry aligned with the x-axis.

where $T_\infty = 300$ K, body temperature, and $p_\infty = 10^5$ Pa, atmospheric pressure. This is equivalent to the domain containing only stationary liquid at body temperature and atmospheric pressure.

5.2.4 Domain and boundary conditions

The geometry of the laser fibre and bubble is approximately axisymmetric so can be approximated by a 2D domain. OpenFOAM solves all models in 3D Cartesian coordinates but lower dimension problems can be simulated by defining an appropriate domain and boundary conditions. In particular, axisymmetric models are handled in OpenFOAM by using a wedge shaped domain as shown in Fig. 5.2.1 [73]. In cylindrical coordinates, $(r, \theta, \hat{z})$, the wedge axis is aligned with the $\hat{z}$-direction and is one cell thick in the θ-direction, as shown in Fig. 5.2.1b. Periodic conditions are applied on the front and back planes of the wedge; this theoretically allows θ-direction flow but in practise the flow remains 2D in the r-$\hat{z}$ plane [74]. The same wedge is shown in Cartesian coordinates in Fig. 5.2.1c – following OpenFOAM convention, the wedge axis is aligned with the x-axis in Cartesian coordinates and the 2D flow is in the x-y plane. For the remainder of the chapter we take the position and velocity to be 2D, that is $\boldsymbol{x} = (x, y)$ and $\boldsymbol{u} = (u, v)$.

The fluid domain in the x-y plane is as shown by the blue region in Fig. 5.2.2a. The side of the wedge is shown in Fig. 5.2.3a. The laser fibre, marked in black in Fig. 5.2.2a, is positioned at the bottom left of the domain with its tip at $x = 0$ and its axis aligned with $y = 0$. The fibre radius, r_f, is set to be 0.1 mm, typical of the fibres used in lithotripsy. The values of a, b, c and l_f will be given for each simulation, choosing a and c such that $\theta_d < 5°$ [73]. The cell

size is 0.01 mm in both the x- and y- directions. This cell size along with the domain dimensions determine the number of cell in each direction.

In Fig. 5.2.2b and Fig. 5.2.3b, the type of boundary on each side of the domain is shown, and details of the conditions applied at each type of boundary are given below. The inward pointing normal at the boundaries is denoted $\boldsymbol{n}$ and the tangent $\boldsymbol{t}$. The fibre forms two solid boundaries at the bottom left of the domain. At the left-hand and top edges, the fluid is allowed to exit or enter the domain depending on the direction of the flow; these are labelled entrainment boundaries. The right hand edge is labelled S and is chosen to be either a solid boundary or an entrainment boundary, depending on the simulation. The inward pointing normal to S is denoted $\boldsymbol{n}_S$. The bottom edge of the domain is the axis of symmetry so only symmetry conditions are applied here. The front and back of the domain are 'wedge' boundaries, on which periodic conditions are applied. We will now specify the conditions applied on solid and entrainment boundaries.

5.2.4.1 Solid boundary condition

At a solid boundary, we apply a no-slip condition on the velocity

$$\boldsymbol{u}(\boldsymbol{x}, t) = \boldsymbol{0} \text{ m s}^{-1}. \tag{5.2.22}$$

The laser fibre, stone and other solid boundaries generally take in thermal energy, acting as heat sinks. Heat flux at a boundary can be modelled as

$$K\boldsymbol{n} \cdot \boldsymbol{\nabla} T(\boldsymbol{x}, t) = K_b \boldsymbol{n} \cdot \boldsymbol{\nabla} T_b(\boldsymbol{x}, t), \tag{5.2.23}$$

where $\boldsymbol{n}$ is the normal to the boundary and K_b and T_b are the thermal conductivity and temperature respectively of the solid material. For simplicity, we take $K_b = 0$, and the boundary condition on T becomes

$$\boldsymbol{n} \cdot \boldsymbol{\nabla} T(\boldsymbol{x}, t) = 0 \text{ K m}^{-1}. \tag{5.2.24}$$

This is equivalent to a thermally insulated boundary.

Finally, where the liquid-vapour interface meets a solid boundary, a fixed contact angle of ϕ is imposed. The contact angle depends on the material of the boundary, which has not been specified, and the temperature of the liquid water and water vapour [75]. At a hydrophobic surface, the contact angle will be greater $\pi/2$ and at a hydrophilic surface, the contact angle will be less than $\pi/2$. As the material of the boundary is as yet unknown a contact angle of $\phi = \pi/2$ is chosen for the simulations in this chapter.

5.2.4.2 Entrainment boundary condition

In OpenFOAM, on boundaries at which both outflow and inflow may occur and where inflow velocity is not known, it is common to apply a combination of conditions called entrainment boundary conditions [76]. Outflow corresponds to negative normal velocity, considering an inward pointing normal, while inflow corresponds to positive normal velocity. A different set of conditions are applied depending on whether there is inflow of outflow. The direction of the flow, and therefore the boundary conditions, are determined at each timestep for each cell on an entrainment boundary.

When there is outflow, the conditions act like far-field conditions and assume the flow is fully-developed. These conditions are

$$p = p_\infty, \tag{5.2.25}$$

$$(\boldsymbol{n} \cdot \boldsymbol{\nabla})\boldsymbol{u} = \boldsymbol{0} \text{ m s}^{-1} \tag{5.2.26}$$

$$\boldsymbol{n} \cdot \boldsymbol{\nabla} T = 0 \text{ K m}^{-1}, \tag{5.2.27}$$

$$\boldsymbol{n} \cdot \boldsymbol{\nabla} \alpha = 0 \text{ m}^{-1}. \tag{5.2.28}$$

When there is inflow, it is assumed that some properties of the flow are known, in particular, we assume that fluid entering is at body temperature and in liquid phase,

$$T = T_\infty, \tag{5.2.29}$$

$$\alpha = 1. \tag{5.2.30}$$

The pressure is adjusted from the far-field pressure to account for the flow of fluid away from the boundary; this adjustment aids stability of the solution [76, 77]. The pressure at the boundary is therefore given by [78]

$$p = p_\infty - \frac{1}{2}\rho|\boldsymbol{u}|^2. \tag{5.2.31}$$

The tangential component of the velocity is taken to be zero,

$$\boldsymbol{u} \cdot \boldsymbol{t} = 0 \text{ m s}^{-1}, \tag{5.2.32}$$

where $\boldsymbol{t}$ is the tangent to the boundary. The normal velocity is not known and allowed to adjust with the pressure, with the condition

$$(\boldsymbol{n} \cdot \boldsymbol{\nabla})(\boldsymbol{u} \cdot \boldsymbol{n}) = 0 \text{ m s}^{-1}. \tag{5.2.33}$$

In summary, for inflow the conditions are

$$p = p_\infty - \frac{1}{2}\rho|\boldsymbol{u}|^2, \tag{5.2.34}$$

$$\boldsymbol{u} \cdot \boldsymbol{t} = 0 \text{ m s}^{-1}, \tag{5.2.35}$$

$$(\boldsymbol{n} \cdot \boldsymbol{\nabla})(\boldsymbol{u} \cdot \boldsymbol{n}) = 0 \text{ m s}^{-1}, \tag{5.2.36}$$

$$T = T_\infty, \tag{5.2.37}$$

$$\alpha = 1. \tag{5.2.38}$$

5.2.5 Laser energy source term

As explained in the derivation of the spherical model, the rate of energy transferred to the liquid is proportional to the time and space dependent intensity of the light, I. However, the definition of $\dot{Q}$ in this model differs from that in Chapter 3, as here it includes the heat capacity of the liquid, $c_{V,l}$. The source term in this case is

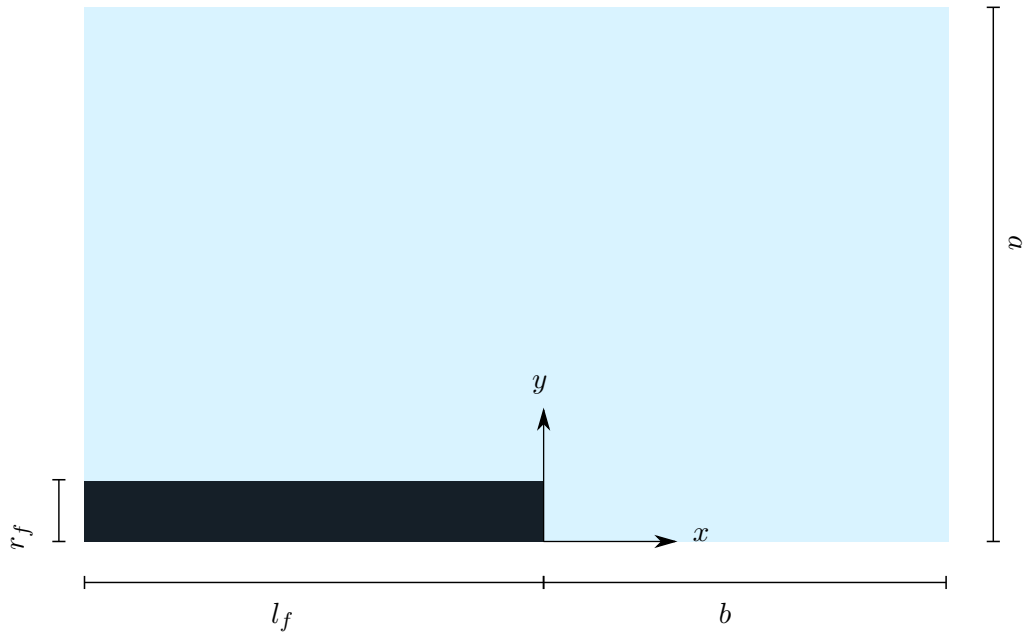
$$\dot{Q}(\boldsymbol{x}, \alpha, t) = \frac{\alpha\mu}{c_{V,l}} I(\boldsymbol{x}, \alpha, t), \tag{5.2.39}$$

where μ is the absorption coefficient of the laser in the liquid. The variable α here is the phase fraction and is included because the laser energy is absorbed only by the liquid phase, assuming that the absorption of laser energy by the vapour is negligible. This differs from Eq. (3.3.19) in the spherical model, in which α was a fitting parameter. The liquid heat capacity, $c_{V,l}$ is used rather than the mixture heat capacity as the source term acts only in the liquid.

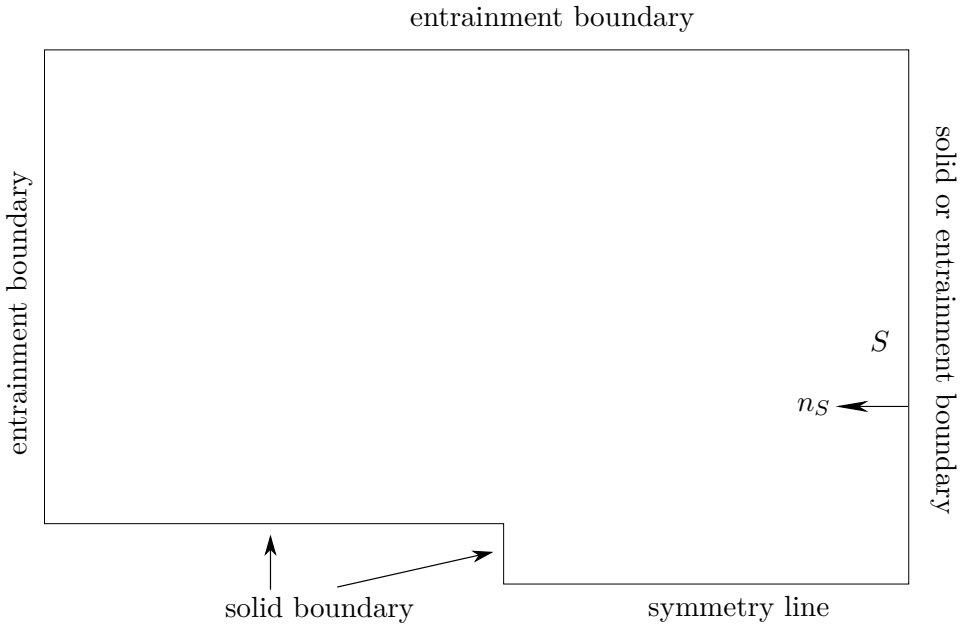
The form of the intensity function in this model differs that in Chapter 3 as we are now not restricted to spherical symmetry. With an axisymmetric source term, we can closely reflect the spatial distribution of liquid heating by the laser. With the domain as shown in Fig. 5.2.2a, the laser shines to the right from $x = 0$, in the region $y \leq r_f$. Therefore, for $y > r_f$, the intensity of light is zero and $\dot{Q} = 0$. In the region $y \leq r_f$ the intensity is decomposed into spatial and temporal functions $I(r, \alpha, t) = P(t)f(\boldsymbol{x}, \alpha)$, and therefore

$$\dot{Q}(\boldsymbol{x}, \alpha, t) = \frac{\alpha\mu}{c_{V,l}} f(\boldsymbol{x}, \alpha)P(t). \tag{5.2.40}$$

The temporal component is the time dependent power output of the laser, $P(t)$. The spatial component, $f(\boldsymbol{x}, \alpha)$, models two physical properties of the laser light. The first of these properties is a Gaussian distribution of intensity across the diameter of the fibre tip. This Gaussian distribution of intensity, with variance taken to be equal to the fibre radius, is modelled by the



(a)



(b)

Figure 5.2.2 – Domain geometry and boundaries in the x-y plane. The boundary on the right hand side of the domain is labelled S, with inward pointing normal $\boldsymbol{n}_S$, and will be specified as a solid or entrainment boundary for each simulation.

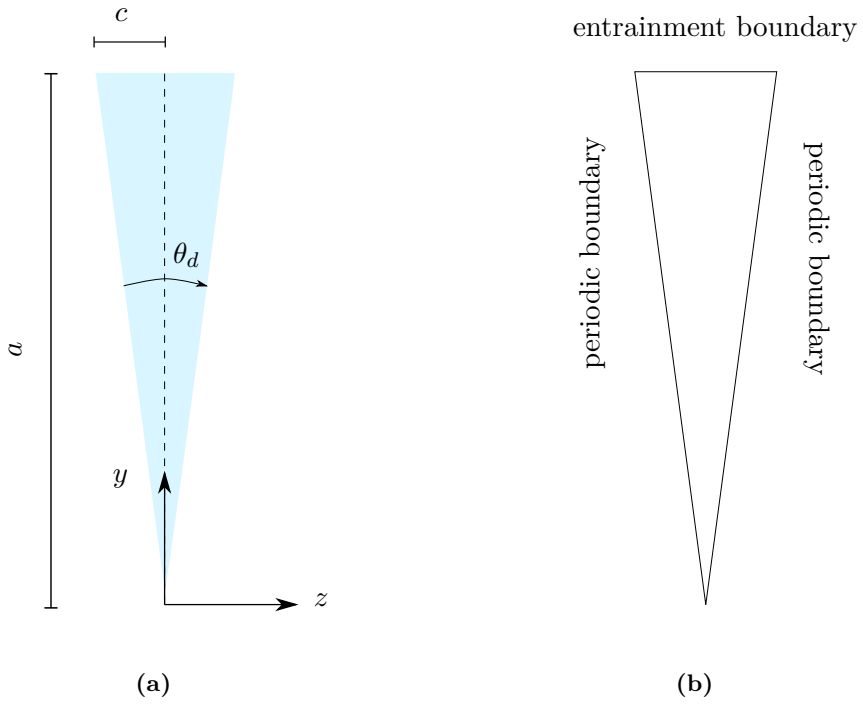


Figure 5.2.3 – Domain geometry and boundaries in the y-z plane.

term

$$\frac{A}{r_f\sqrt{2\pi}}\exp\left(-\frac{1}{2}\left(y/r_f\right)^2\right), \tag{5.2.41}$$

where A is the normalisation constant and

$$A^{-1} = \frac{\sqrt{2\pi}}{r_f}\int_0^{r_f} r\,\exp\left(-\frac{1}{2}\left(y/r_f\right)^2\right)\mathrm{d}y \tag{5.2.42}$$

$$= \sqrt{2\pi}\,r_f(1-\exp(-1/2)). \tag{5.2.43}$$

The second property of the light is an exponential decay of intensity with distance in the x-direction from the fibre tip, with decay occurring only in the liquid. The exponential decay, with decay constant μ, is modelled by the term

$$\exp\left(-\mu\int_0^x \alpha(\boldsymbol{x})\mathrm{d}x\right). \tag{5.2.44}$$

Therefore the spatial function is

$$f(\boldsymbol{x},\alpha) = \frac{A}{r_f\sqrt{2\pi}}\exp\left(-\frac{1}{2}\left(y/r_f\right)^2\right)\exp\left(-\mu\int_0^x \alpha(\boldsymbol{x})\mathrm{d}x\right). \tag{5.2.45}$$

In summary, the laser source term is defined as

$$\dot{Q}(\boldsymbol{x},\alpha,t)=\begin{cases}0 & \text{if } y>r_f\\ \frac{\alpha\mu}{c_{V,l}}P(t)\frac{A}{r_f\sqrt{2\pi}}\exp\left(-\frac{1}{2}\left(y/r_f\right)^2\right)\exp\left(-\mu\int_0^x\alpha(\boldsymbol{x})\mathrm{d}x\right) & \text{if } y\leq r_f.\end{cases} \tag{5.2.46}$$

This source term completes the mathematical model. The following section briefly outlines the numerical scheme employed by OpenFOAM to solve the model.

5.2.6 Numerical method

5.2.6.1 Finite volume method

The finite volume method (FVM) is a technique for solving systems of partial differential equations. In the FVM, the domain is split into convex cell volumes V_P with centroids P. The values of all variables are stored at the cell centroids. For a quantity F, a general transport equation takes the form

$$\frac{\partial\rho F}{\partial t}+\boldsymbol{\nabla}\cdot(\rho\boldsymbol{u}F)-\boldsymbol{\nabla}\cdot(\rho\Gamma_F\boldsymbol{\nabla}F)=S_F(F). \tag{5.2.47}$$

The first term is the time derivative, the second is the convection or advection term, the third is the diffusion term with diffusive coefficient Γ_F and the final term is a source term. This is the form that our governing equations — Eq. (5.2.3), Eq. (5.2.8), Eq. (5.2.9) and Eq. (5.2.12) — take. The governing equations are integrated over the cell volume to give

$$\int_{V_p}\frac{\partial\rho F}{\partial t}\mathrm{d}V+\int_{V_p}\boldsymbol{\nabla}\cdot(\rho\boldsymbol{u}F)\mathrm{d}V-\int_{V_p}\boldsymbol{\nabla}\cdot(\rho\Gamma_F\boldsymbol{\nabla}F)\mathrm{d}V=\int_{V_p}S_F(F)\mathrm{d}V. \tag{5.2.48}$$

The divergence theorem is used to convert the advection and diffusion terms to surface integrals, giving

$$\int_{V_p}\frac{\partial\rho F}{\partial t}\mathrm{d}V+\int_{\partial V_p}(\rho\boldsymbol{u}F)\cdot\mathrm{d}\boldsymbol{S}-\int_{\partial V_p}(\rho\Gamma_F\boldsymbol{\nabla}F)\cdot\mathrm{d}\boldsymbol{S}=\int_{V_p}S_F(F)\mathrm{d}V. \tag{5.2.49}$$

The source term is formulated as a discrete source at the cell centre. Volume integrals are found by multiplying the integrand, as evaluated at the cell centroid, by the cell volume. Various schemes exist for approximating the surface integrals but they generally involve taking the value of the integrand at the centre of each cell face, multiplying by the surface area of the face, and summing over the faces. As variables are stored at cell centres, interpolation schemes are necessary to give the value at the face centres. Many schemes also exists for stepping in time. A comprehensive introduction to FVM is given on the OpenFOAM Wiki website [79].

Parameter	Default value	Parameter	Default value
cell size	0.01 mm	T_∞	300 K
c	0.01 mm	p_∞	10^5 Pa
r_f	0.1 mm	$\alpha(\boldsymbol{x}, 0)$	1
β_e	1.0 s^{-1}	$p(\boldsymbol{x}, 0)$	10^5 Pa
β_c	2.0 s^{-1}	$T(\boldsymbol{x}, 0)$	300 K
T_{vap}	373 K	$\boldsymbol{u}(\boldsymbol{x}, 0)$	$\mathbf{0}$ m s^{-1}

Table 5.2.1 – Default parameter values for simulations in Sec. 5.3. When the default values are not used, this is stated in the text.

5.2.6.2 OpenFOAM solution method

In OpenFOAM, the solution at each timestep is found using an iterative loop. In the case of compressibleInterFoam, the method used is called the PIMPLE loop, an overview of which can be found on the CFD Direct website [80]. In brief, the process is:

1. The energy equation, Eq. (5.2.12), is solved, using values from the previous time-step to give an updated temperature field.
2. The updated temperature field is used to solve Eq. (5.2.8), giving the new phase field.
3. The new pressure and velocity fields are are determined in a combined, iterative sub-loop called a PISO (Pressure Implicit with Splitting of Operators) loop [80–85]. In brief, the PISO loop process is
   (a) Using the pressure values from the previous timestep, the momentum equation, Eq. (5.2.9), is solved to give a predicted solution for the velocity field.
   (b) Equation (5.2.3) and Eq. (5.2.9) are combined to give an equation for pressure.
   (c) The pressure equation is solved using the predicted velocity field.
   (d) The velocity field is updated using the new pressure field.

The outer PIMPLE loop — steps 1-3 — and the inner PISO loop — steps (a)-(d) — are iterated to obtain the temperature, phase fraction, pressure and velocity fields. The number of iterations of each loop is specified by the user. Details of the PIMPLE and PISO algorithms are given on the Open CFD and OpenFOAM Wiki websites [80–82, 84].

5.3 Results

The simulations presented in this section are an illustration of the way in which the model can be utilised. These simple examples will enable us to gain preliminary insight into how the laser, bubble and boundaries interact. The first simulation considers the simple case of a small, nucleated bubble expanding without laser heating and phase change, with a solid boundary placed at different distances from the laser fibre. Here, we will demonstrate how the domain geometry affects both the bubble and the solid boundaries. In the second example, laser

heating and phase change are introduced and the behavior of the bubble is evaluated under three different pulse shapes. In this case, S is an entrainment boundary. Comparing the results of this simulation to the experimental observations, we ensure that the model has the correct qualitative behavior. In the final simulation, we look at the effect of splitting the pulse energy into a number of small 'micropulses'. With this simulation we explore a range of pulses and pulse packets that would not be possible experimentally due to the limitations of the laser systems. We run this simulation with S as an entrinment boundary and again as a solid boundary.

The default values for all parameters are given in Table 5.2.1. In all cases, the default timestep is 5×10^{-7} s but we enable the adjustable time step in OpenFOAM. The adjustable time step increases or decreases the time step where appropriate or necessary while ensuring the Courant number remains below the selected value of 0.5. All other parameters are as given in Appendix A.

5.3.1 Fibre-boundary distance

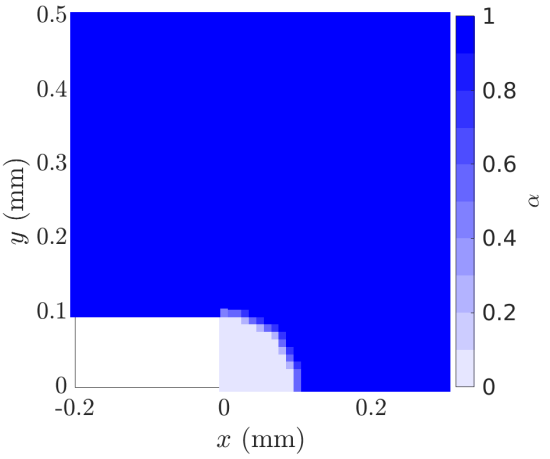
We study the fluid dynamics when the laser fibre is placed at different distances perpendicular to a thermally insulated boundary. This is simulated by setting the S to be a solid boundary and varying the parameter b, as defined in Fig. 5.2.2. This is an example of how the model can be utilised to explore the effect of the geometry on the fluid and the effect of the fluid on the solid boundaries.

We set $l_f = 2.0$ mm, $a = 1.0$ mm, $c = 0.01$ mm and consider three values of b: 2.0 mm, 1.0 mm and 0.5 mm. We begin at $t = 0$ with a region of vapour under high pressure at the fibre tip. The initial conditions on α, T and p are as shown in Fig. 5.3.1 and Fig. 5.3.2, while $\boldsymbol{u}(\boldsymbol{x}, 0) = \mathbf{0}$ m s^{-1}. These initial conditions approximate the scenario that the liquid has been heated by the laser to $T = T_{\text{vap}} = 373$ K, nucleating a hemi-spherical bubble at the fibre tip. The bubble has radius equal to the radius of the fibre tip. Within the bubble we set $\alpha = 0$ and $T = 373$ K. We choose the initial pressure of the bubble to be $p = 2 \times 10^6$ Pa, 20 times atmospheric pressure — this value is approximately the peak vapour pressure produced by the spherical model, for example, in Fig. 4.3.1b. Outside of the bubble, $\alpha = 1$, $p = 10^5$ Pa and the temperature is

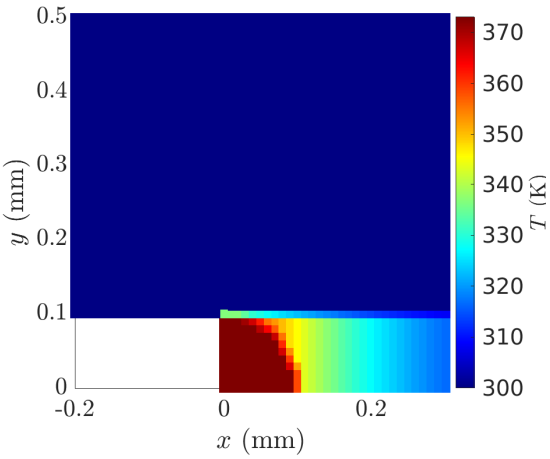
$$T(\boldsymbol{x}, 0) = \begin{cases} T_\infty + (T_{\text{vap}} - T_\infty)e^{-x} & \text{if } y \leq r_f \\ T_\infty & \text{if } y > r_f. \end{cases} \tag{5.3.1}$$

In this simple case, we consider no laser heating or phase change for $t \geq 0$, which is equivalent to setting $P(t \geq 0) = 0$ kW, $\beta_e = 0$ s^{-1} and $\beta_c = 0$ s^{-1}.

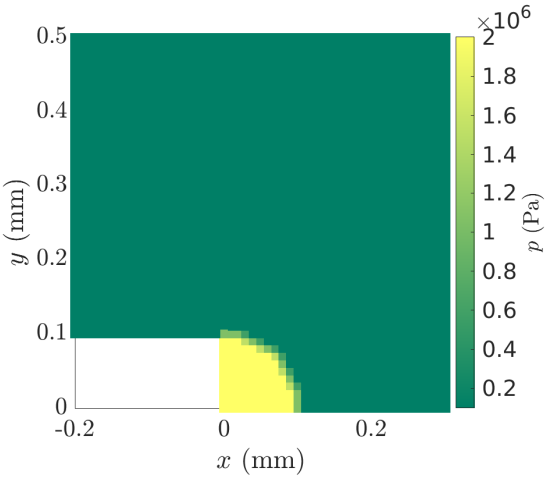
The evolution of the bubble is shown in Fig. 5.3.3 for case the of $b = 2.0$ mm and in Fig. 5.3.4 for case of $b = 0.5$ mm. Most notable about these plots is the form of the bubble as it collapses, displayed in more detail in Fig. 5.3.5 for the case of $b = 0.5$ mm. During collapse, the bubble breaks into a jet of liquid directed towards S; as can be seen by the direction of the flow



(a)

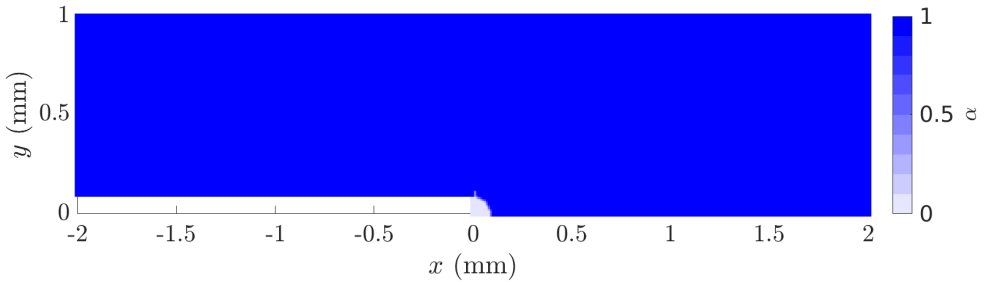


(b)

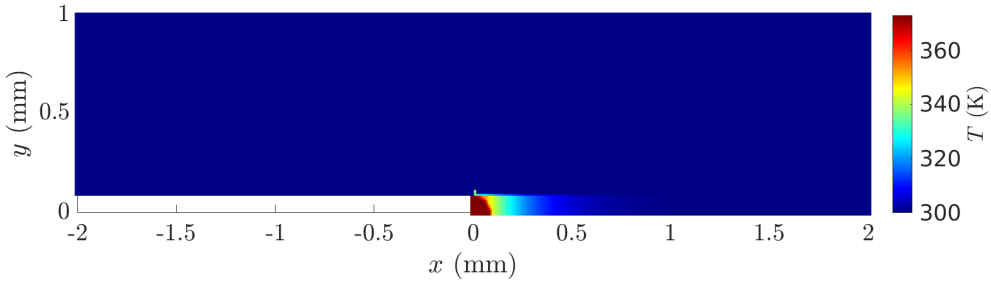


(c)

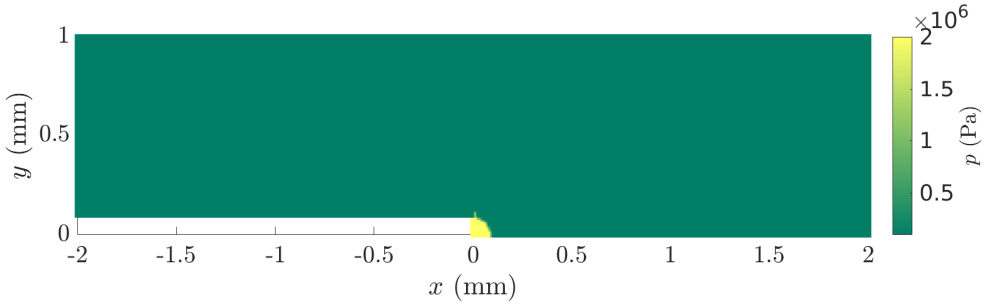
Figure 5.3.1 – Initial conditions on α, T and p for the simulations in Sec. 5.3.1 for the case $b = 2.0$ mm, showing a region close to the fibre trip. The full domain is shown in Fig. 5.3.2.



(a)



(b)



(c)

Figure 5.3.2 – Initial conditions on α, T and p for the simulations in Sec. 5.3.1 for the case $b = 2.0$ mm, showing the full domain. A region close to the fibre tip is shown in Fig. 5.3.1.

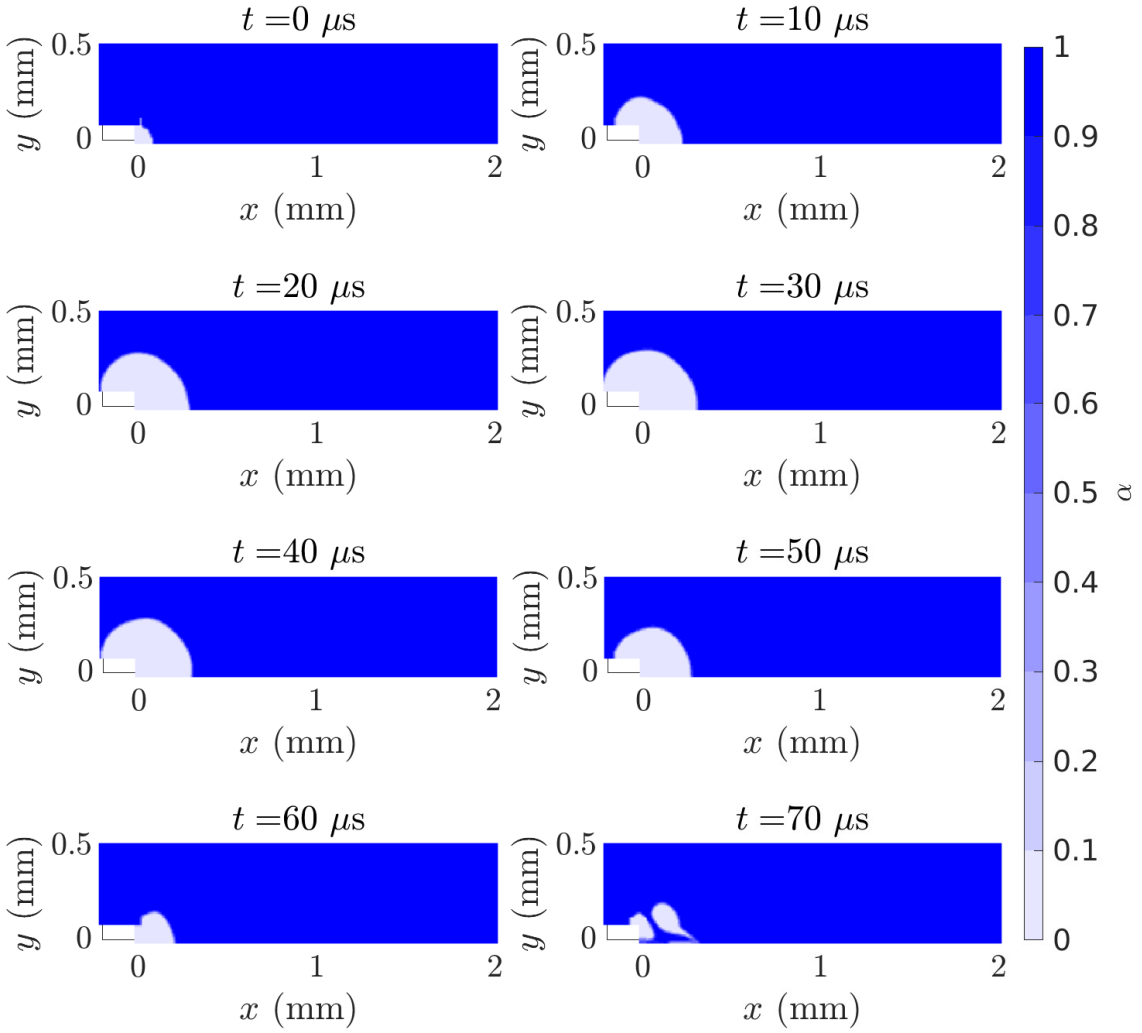


Figure 5.3.3 – Evolution of α for the simulation detailed in Sec. 5.3.1 with $b = 2.0$ mm.

near the axis as shown in Fig. 5.3.5. This liquid jet is a known phenomenon that occurs when bubbles collapse near a solid boundary and has been studied extensively both mathematically and experimentally [13, 14, 40]. The form of the bubble in this case is different to that generally presented in the literature, for example by Plesset and Chapman [13], in which the jet forms along the central axis. In our case, due to the additional solid boundary of the laser fibre, the jet initially forms at the edge of the fibre, as shown in the first panel of Fig. 5.3.5, and flows towards the axis. However, the observation remains the same that a liquid jet towards a solid surface occurs during bubble collapse.

The liquid jet is known to produce high pressures, due to the so-called water hammer effect. We define the maximum pressure on S to be

$$p_{\max}(t) = \max_{y} \{p(x = b, y, t)\} . \tag{5.3.2}$$

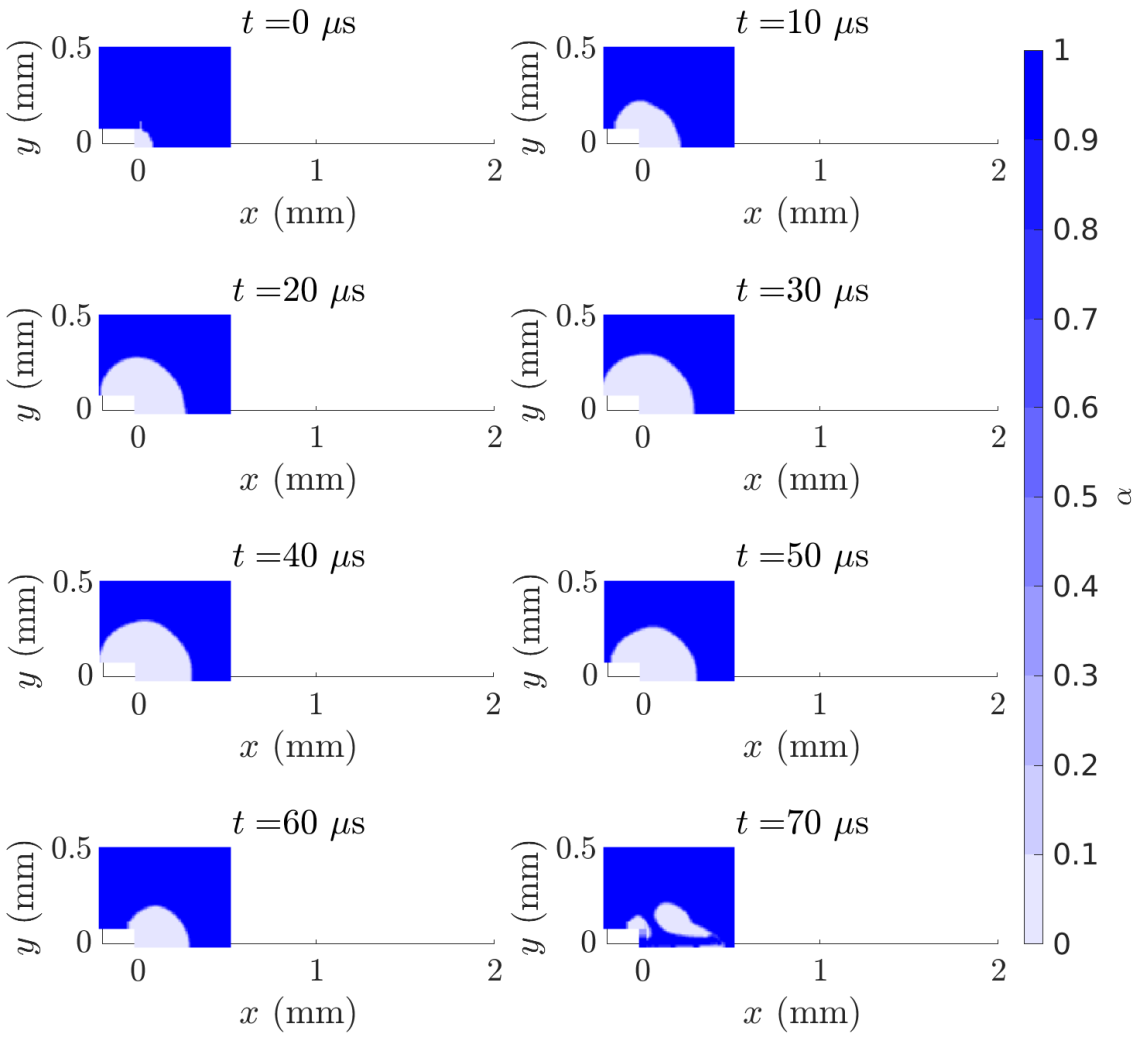
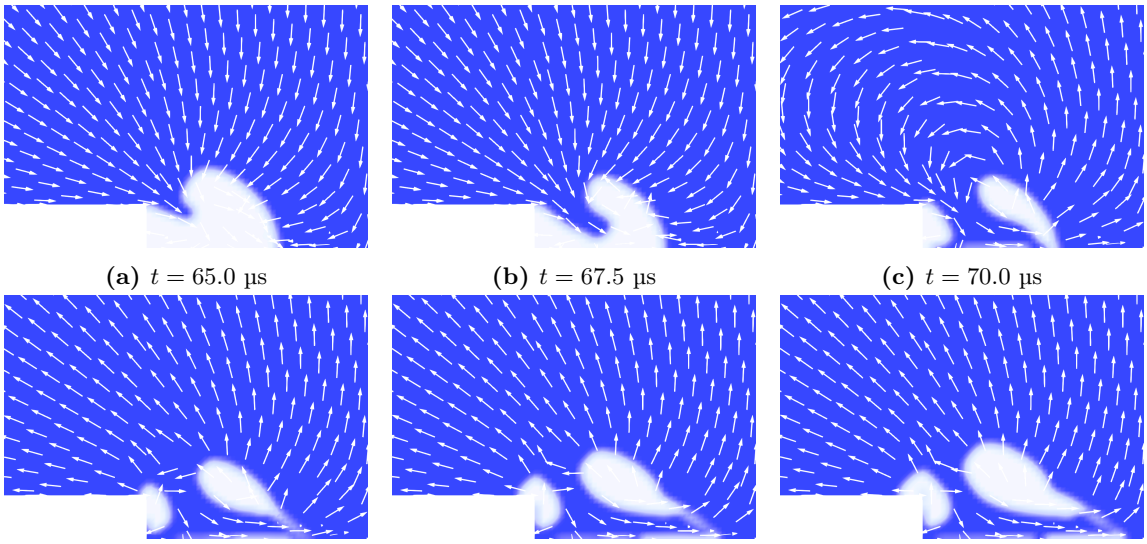


Figure 5.3.4 – Evolution of α for the simulation detailed in Sec. 5.3.1 with $b = 0.5$ mm.



(a) $t = 65.0$ µs **(b)** $t = 67.5$ µs **(c)** $t = 70.0$ µs

(d) $t = 72.5$ µs **(e)** $t = 75.0$ µs **(f)** $t = 77.5$ µs

Figure 5.3.5 – Direction of fluid flow during bubble collapse for the simulation detailed in Sec. 5.3.1 with $b = 0.5$ mm. The formation of a jet of liquid directed towards the boundary can be seen, which penetrates the bubble at approximately 70.0 µs.

For the three values of b, $p_{\max}(t)$ is plotted in Fig. 5.3.6a. We see that one pressure spike occurs very close to $t = 0$ µs, as the bubble first begins expansion; this is due to initiating the bubble as a high pressure region of vapour. Another spike occurs in all cases between 60 and 70 µs. For the case of $b = 0.5$ mm, the second spike occurs at 70 µs and a snapshot of the bubble at this time is shown in Fig. 5.3.6b; we see that the liquid jet has just penetrated the front edge of the bubble and is the cause of the pressure spike at this time. The peak of both spikes is approximately twice as high for $b = 1.0$ mm in comparison to $b = 2.0$ mm, and twice as high again for $b = 0.5$ mm.

We also measure the axial velocity at S during expansion and collapse. This measure is taken at $y = 0$ mm and at a distance $\delta = 0.01$ mm from S, since at the boundary itself we have the condition $\boldsymbol{u} = \mathbf{0}$ m s^{-1}. The axial velocity near S is therefore defined to be

$$u_a(t) = -\boldsymbol{n}_S \cdot \boldsymbol{u}(x = b - \delta, y = 0 \text{ mm}, t). \tag{5.3.3}$$

This results in $u_a(t)$ positive if the flow is towards S and negative if it is away from S. For the three values of b, $u_a(t)$ is plotted in Fig. 5.3.6c, with the same plot on a smaller vertical scale shown in Fig. 5.3.6d. It is clear that much higher velocities occur near the boundary when $d = 0.5$ mm, than for $d = 1.0$ mm or $d = 2.0$ mm. For $b = 2.0$ mm, u_a appears to be negligible, suggesting that the fluid at the boundary is far enough from the fibre to be relatively undisturbed by the bubble. For $b = 1.0$ mm, there is a flow of fluid towards S during bubble expansion then away from S as the bubble begins to collapse. During the last stages of collapse the fluid again moves towards S. The velocity is the same order of magnitude for these three stages of the flow, with $|u_a(t)| = \mathrm{O}(10^{-2})$ m s^{-1}. Similarly for $b = 0.5$ mm, there is a flow of

fluid towards S during expansion and away from S during the early stages of collapse. We see that $u_a(t)$ is a similar order of magnitude in both of these stages, $|u_a(t)| = \mathrm{O}(0.1)$ m s^{-1}, an order of magnitude larger than for the case $b = 1.0$ mm. The flow of liquid towards S during the last stages of collapse is an order of magnitude larger again, rising to approximately 6 m s^{-1}. In this case, from the snapshot in Fig. 5.3.6b, we see that the change in direction of $u_a(t)$ during bubble collapse is due to the liquid jet penetrating the front of the bubble, allowing flow towards S. The effect of the liquid jet is felt most strongly on S in the case $b = 0.5$ mm, due to the reduced distance between the boundary and bubble.

The results in Fig. 5.3.7 show how the boundary is affected as the parameter b is varied. To ascertain if the flow itself varies with b, we again measure pressure and velocity but at a fixed distance of 0.5 mm from the fibre. We define a new measure of pressure to be

$$p_{0.5}(t) = p(x = 0.5 \text{ mm}, y = 0 \text{ mm}, t). \tag{5.3.4}$$

This is plotted in Fig. 5.3.7a, for the three values of b. The pressure spikes during bubble expansion and collapse are of the same order of magnitude in all three cases, although the peak pressure of both spikes is higher for smaller b. This result suggests that moving the boundary closer to the fibre increases the pressures generated in the fluid. Similarly, a new measure of axial velocity is defined at a distance $x = 0.5 - \delta$ mm from the fibre

$$u_{0.5}(t) = -\boldsymbol{n}_S \cdot \boldsymbol{u}(x = (0.5 - \delta) \text{ mm}, y = 0 \text{ mm}, t). \tag{5.3.5}$$

As with the definition of $u_a(t)$, $u_{0.5}(t)$ is measured a small distance $\delta = 0.01$ mm from $x = 0.5$ mm. This x value is chosen because the velocity at $x = 0.5$ mm is fixed at $\boldsymbol{u} = \boldsymbol{0}$ m s^{-1} due to the no-slip condition in the case that the boundary is located at $b = 0.5$ mm. For the three values of b, $u_{0.5}(t)$ is plotted in Fig. 5.3.7b. The result is very similar for $b = 1.0$ mm and $b = 2.0$ mm. During bubble expansion and early collapse, $|u_{0.5}(t)|$ for the case of $b = 0.5$ mm is at least an order of magnitude smaller than the other two cases. The presence of the boundary at $b = 0.5$ mm has the effect of slowing the flow whereas a boundary further away at $b = 1.0$ mm or $b = 2.0$ mm does not have this effect. However, at approximately $t = 80$ µs, at which time a jet of liquid towards the boundary has formed, $u_{0.5}(t)$ is almost as large in the case of $b = 0.5$ mm as in the other two cases. The presence of the boundary at $b = 0.5$ mm is not enough to slow the flow when the liquid jet reaches $x = 0.5 - \delta$ mm.

We have shown that pressure and velocity felt at the boundary S are dependent on the fibre-boundary distance. Furthermore, the flow itself is altered as the boundary is brought closer to the fibre. The simulation presented in this section could be extended by coupling the model to a kidney stone model via the boundary conditions on S. The measures of pressure and axial velocity described in this section begin to show the effect of varying fibre-stone distance,

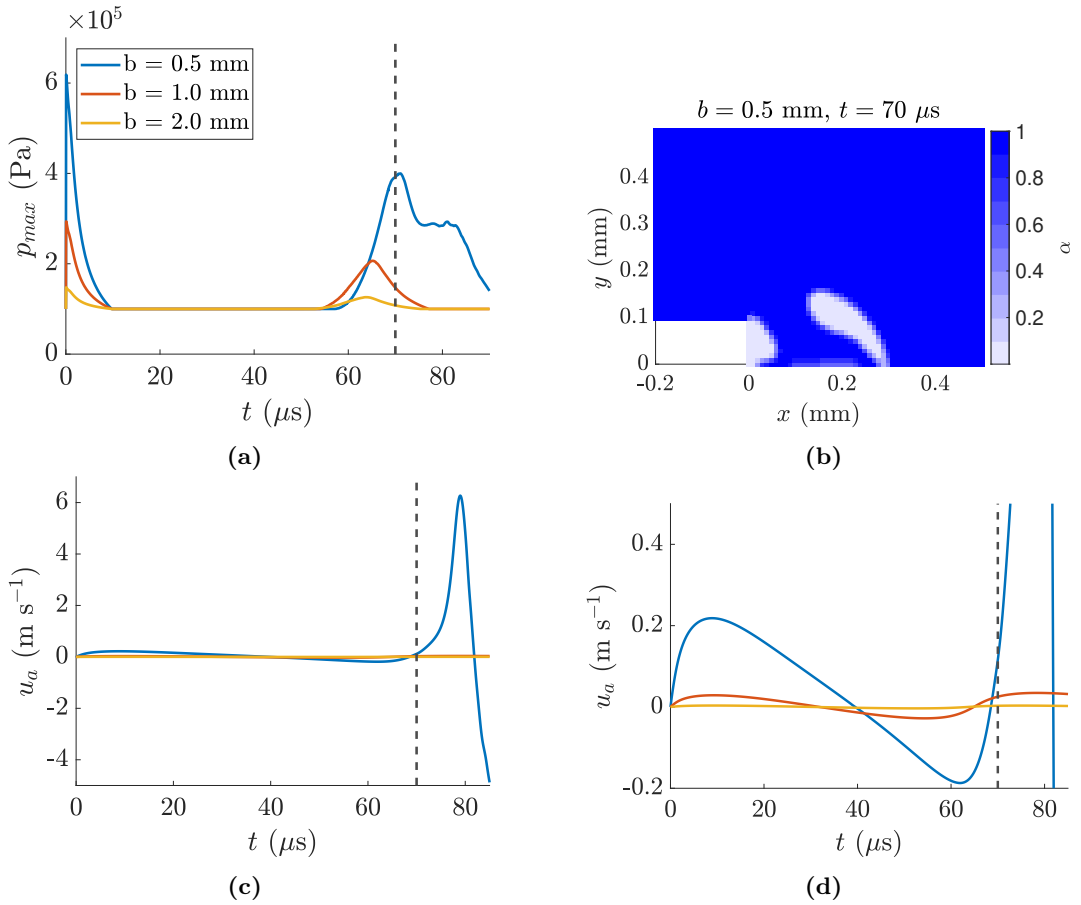


Figure 5.3.6 – (a) Maximum pressure on S, $p_{\max}(t)$, for three values of b. The vertical dashed line marks the time of the snapshot shown in (b). (b) A snapshot of the bubble at $t = 70$ µs for the case $b = 0.5$ mm. (c) Axial velocity at a distance $\delta = 0.01$ mm from S, $u_a(t)$, for three values of b with a smaller scale shown in (d), with the vertical dashed line in both marking the time of the snapshot shown in (b).

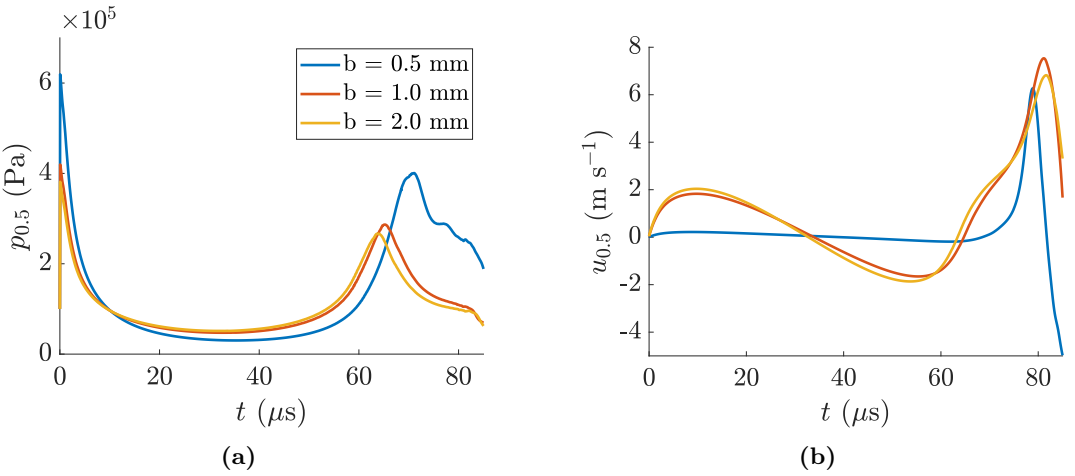
and, coupled to a stone model, have the potential to model stone breaking and retropulsion.

5.3.2 Single pulse

In this section, we introduce laser heating of the fluid due to a single pulse, exploring the effect of pulse shape on bubble shape and size. We revert to the uniform initial conditions given in Sec. 5.2.3. With these initial conditions, for $t > 0$ we allow the liquid to heat from T_∞ due to the effect of the laser. When T_{vap} is reached, phase change will occur and a bubble will nucleate. With this model we therefore do not need to begin with a nucleated bubble, as was done in the previous section and in the spherical model in Chapters 3 and 4.

We set $l_f = 0.5$ mm, $a = 1.0$ mm, $b = 1.5$ mm and $c = 0.01$ mm. We introduce phase change, with $\beta_e = 2.0$ s^{-1} and $\beta_c = 1.0$ s^{-1}. In contrast to the last section, here we set S to be an entrainment boundary, allowing flow in and out. This choice is made as we wish to understand how the bubble size and shape changes as the pulse shape changes, so it is preferable for the bubble to be unimpeded by a solid boundary at S.

Reflecting the qualitative form of the P120 short pulses, as shown in Fig. 2.1.3, the



(a) **(b)**

Figure 5.3.7 – (a) Pressure at $x = 0.5$ mm and $y = 0$ mm for three values of b. (b) Axial velocity at $x = 0.5 - \delta$ mm and $y = 0$ mm, for three values of b.

power of the pulse used in this simulation is modelled by a polynomial rise followed by an exponential decay, as shown in Fig. 5.3.8. This pulse is a P120 2.0 J short pulse with the power scaled by 0.05 and the time scaled by 0.1. The power of the pulse is reduced in comparison to the P120 2.0 J short pulse to remain in a regime in which the numerical solution converges. The resulting pulse has a total energy of 0.01 J. The duration of the pulse is scaled such that the power-time proportions of the pulse remain similar to the original pulse, albeit not identical. The evolution of the fluid temperature is shown in Fig. 5.3.9a and the resulting bubble is shown in Fig. 5.3.9b and the times of the plots are marked by the vertical dashed line in Fig. 5.3.8. At around 10 µs, the temperature is high enough for the liquid to change phase and we see the first signs of vapour. The laser continues to heat the liquid and the the bubble grows, as seen at 20 µs in Fig. 5.3.9b. From around 30 µs, the laser power drops-off but the hot vapour continues to expand. The bubble becomes rounded but slightly elongated along the x-axis, qualitatively mirroring the forms of the bubbles seen experimentally in Fig. 2.2.5. The bubble is shown up to its peak size at 60 µs. After this point, the bubble does not collapse as much as we would expect from experimental observations, but remains close to maximum size. The possible reasons for this are discussed in Sec. 5.4. For this reason, we only plot the bubble until maximum volume is reached.

Samples of the variables α, T and p, taken along the axis $x = 0$ are plotted in Fig. 5.3.10. The times of these plots correspond to the middle five temperature field and phase field snapshots in Fig. 5.3.9. The vertical dotted line marks the length of the bubble at each time. Bubble length is measured along the x-axis and is taken to be the rightmost cell containing at least 80% vapour, or in which $\alpha \leq 0.2$. In Fig. 5.3.10c we see a high pressure region form as liquid begins to change phase. The pressure region moves away from the laser fibre as the bubble expands as seen in Fig. 5.3.10f. It is informative to study the pressure and temperature fields within the bubble to assess the validity of the assumption in the spherical model of these fields being spatially uniform. From the pressure plots in Fig. 5.3.10, we consider the approximation of a uniform

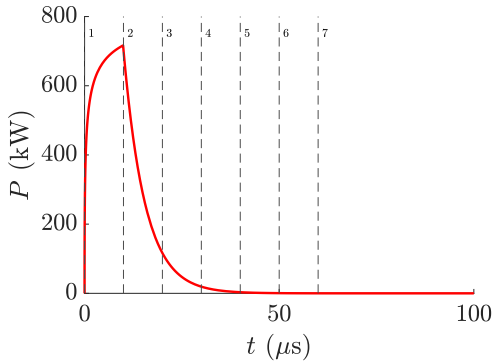


Figure 5.3.8 – Power for a single pulse used in the simulation detailed in Sec. 5.3.2. Evolution of T and α resulting from this pulse are shown in Fig. 5.3.9, at the times marked by the dashed lines.

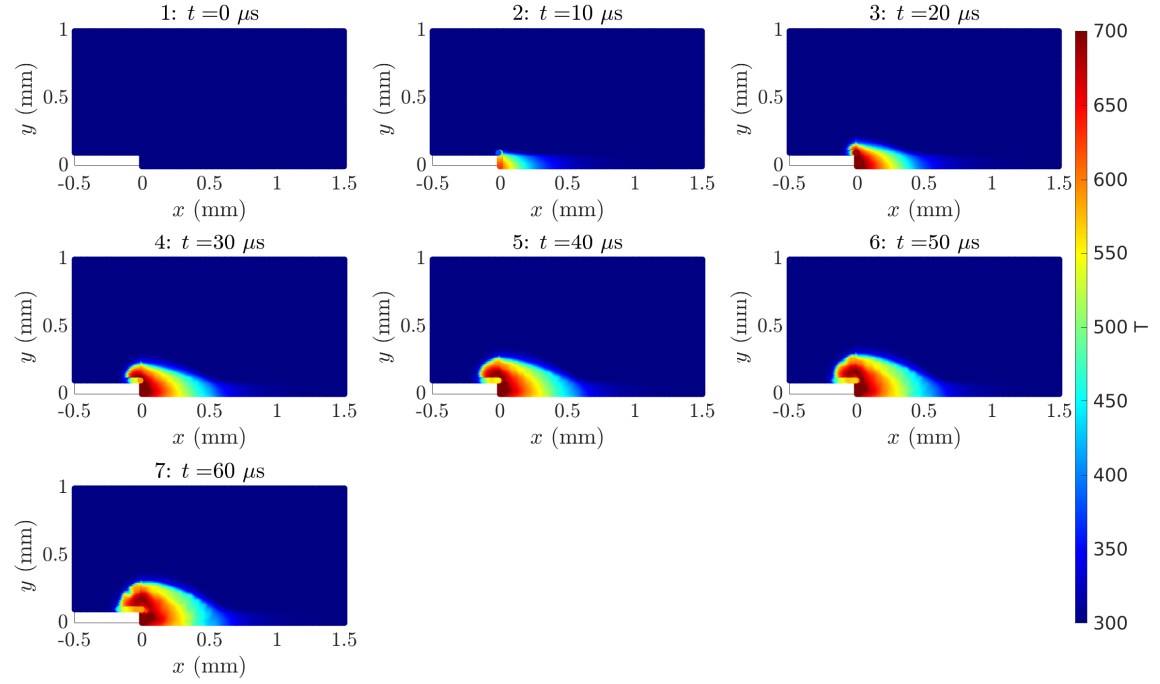
pressure field in the bubble to be reasonable, although pressure gradients can be seen near the liquid-vapour interface, particularly noticeable in Fig. 5.3.10f. Looking at the temperature plots in Fig. 5.3.10, uniform temperature within the bubble does not appear to be a good assumption. At all times plotted, we see a negative temperature gradient from the centre of the bubble towards the liquid-vapour interface.

To explore how the form of the bubble varies as the pulse shape changes, we repeat the simulation above for three pulses of same energy, 0.01 J, but with different shape. The power over time for the three pulses is plotted in Fig. 5.3.11a; the red, green and blue pulses are scaled down versions of the P120 short, medium and long pulses respectively, as shown in Fig. 2.1.3. Again, the power is scaled by 0.05 and the time is scaled by 0.1 in comparison to the P120 pulses. For the three pulses in Fig. 5.3.11a, the bubble volume, length and width are plotted in Fig. 5.3.11b, Fig. 5.3.11c and Fig. 5.3.11d respectively in the corresponding colours. Bubble volume is calculated as the vapour volume summed over all cells, multiplied by the number of wedges around the axis. This can be written as

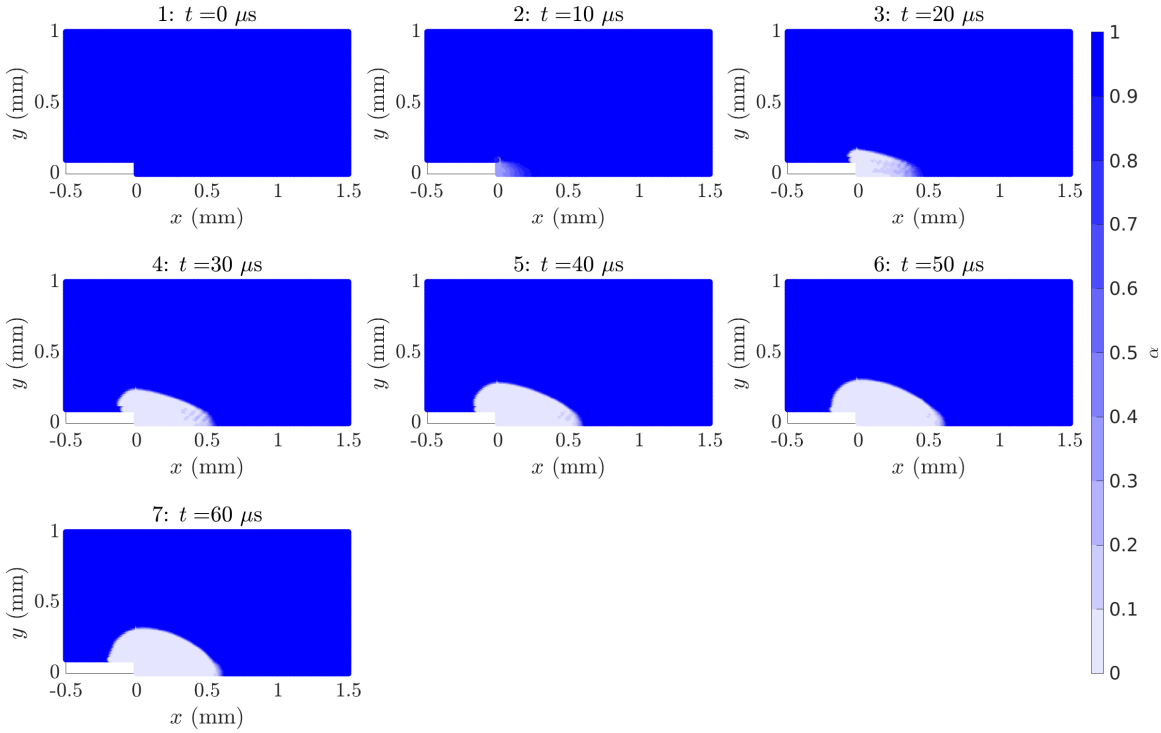
$$V = \frac{2\pi}{\theta_d} \sum_p (1 - \alpha) V_p, \tag{5.3.6}$$

where p is a cell, V_p is the cell volume, and θ_d is the angle of the domain wedge at the x-axis, as shown in Fig. 5.2.3a. As above, Bubble length is measured at the x-axis and is taken to be the rightmost cell in which $\alpha \leq 0.2$. This definition only holds when the bubble remains as a single mass of vapour around the fibre tip so we cease measurement as the bubble begins to collapse. Bubble width is measured along the y-axis where the fibre tip is located as we anticipate the widest point to occur along this axis. Similarly to length, bubble width is defined as the uppermost cell with $\alpha \leq 0.2$. Since bubble width is measured at the fibre tip, measurements only begin once the bubble is wider than the laser fibre, causing the discontinuity in the plots in Fig. 5.3.11d.

In Fig. 5.3.11 we see that the red pulse creates a bubble which grows most quickly and reaches the largest volume and width. There is little difference in peak volume and width between



(a)



(b)

Figure 5.3.9 – Evolution of (a) T and (b) α resulting from the pulse plotted in Fig. 5.3.8. The times of these snapshots correspond to the dashed lines in Fig. 5.3.8 and Fig. 5.3.11b. Other details of the simulation are given in Sec. 5.3.2.

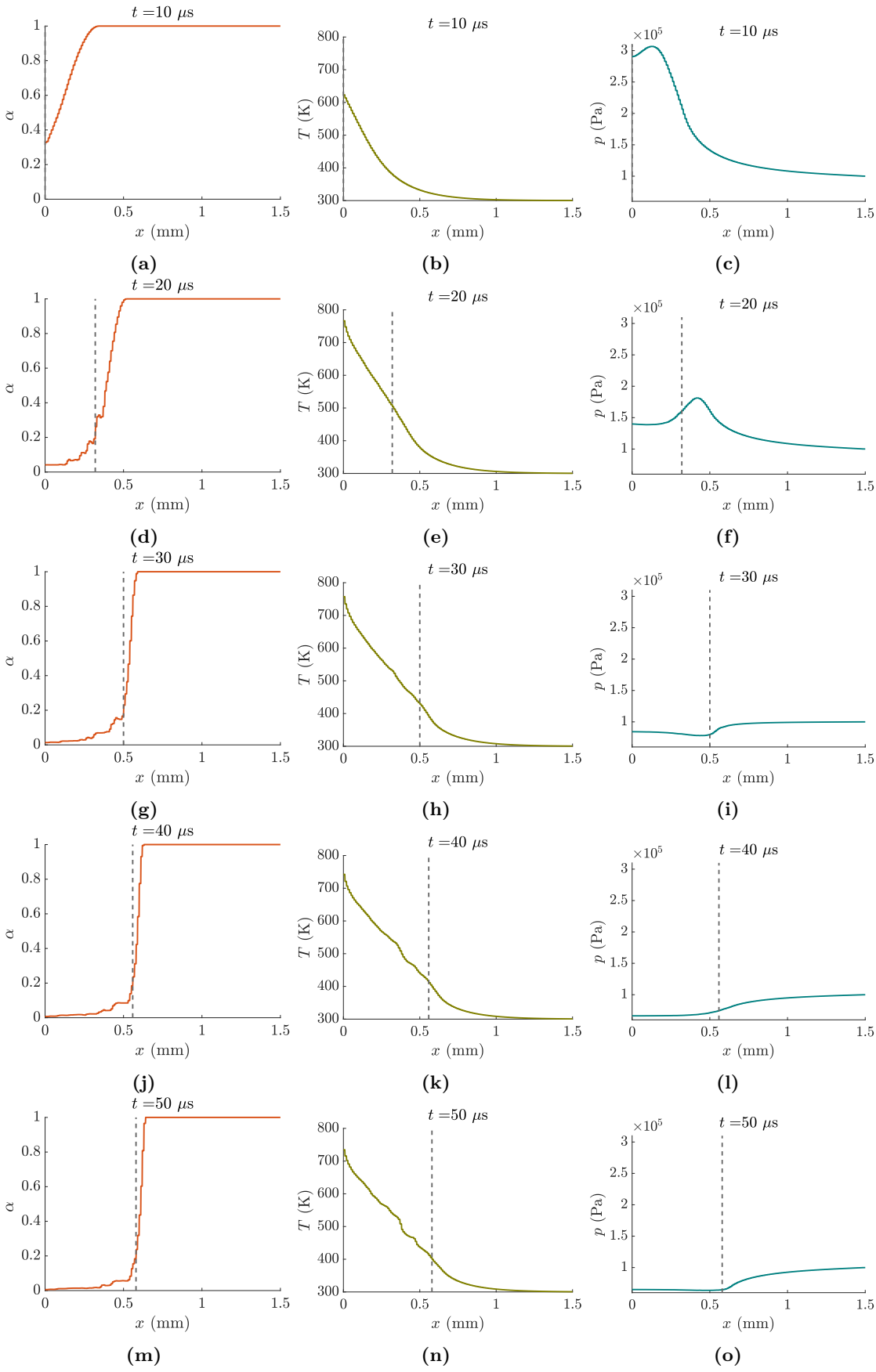


Figure 5.3.10 – Samples of α, T and p taken along the axis $x = 0$, for the case of the bubble produced by the pulse in Fig. 5.3.8. The vertical dashed line marks the length of the bubble at that time.

the green and blue pulses but the blue bubble grows more slowly. Conversely, the blue pulse creates the longest bubble, with the bubbles of the red and green pulses being approximately the same length. All three bubbles are shown at their longest point in Fig. 5.3.12. The time at which the bubble reaches its longest point is approximately 50 µs, 60 µs and 80 µs for the red, green and blue pulses respectively. As a comparison, the bubbles produced by the P120 2.0 J short, medium and long pulses are shown at their longest point in Fig. 5.3.13. These bubble reach their longest point at approximately 300 µs, 400 µs and 500 µs for the short, medium and long pulses respectively. The length-scale and the time-scale of the bubbles in Fig. 5.3.12 would not be expected to match those in Fig. 5.3.13 as they were produced by different pulses. However, the form of these bubbles produced by the model follows a similar pattern to those of the P120 2.0 J pulses: the shortest pulse creates the widest but shortest bubble while the longest pulse creates the narrowest and longest bubble. Furthermore, in both the model and experiment, the longer the duration of the pulse, the longer the bubble takes to reach maximum length.

With the knowledge that the model qualitatively reflects the experimental results, in particular the dependence between pulse shape and bubble shape, we move on to testing pulses that may not be easy to produce experimentally. In the following section, we split an amount of energy into different numbers of micropulses and study the effect on the bubble.

5.3.3 Pulse packet

In this section, we study the effect on the bubble of splitting the pulse energy into a number of small pulses. This study is motivated by the laser systems developed in the last decade for lithotripsy that deliver 'packets' of micropulses [6, 8]. Packets consist of number of short pulses delivered in quick succession with a specified packet repetition frequency. The P120 double Moses pulses, shown in Fig. 2.1.4, are one example of multiple pulses delivered close together, while other laser systems can deliver packets of three or more pulses [6, 8]. The mathematical model allows us to move beyond the pulses that can be produced by current laser systems and exactly control the distribution of energy in a pulse in a way that would not be possible physically. The knowledge gained from this type of study could go on to inform the way that lasers are designed.

The parameters for this simulation remain the same as the previous one. We again begin with the uniform initial conditions given in Sec. 5.2.3 and set $l_f = 0.5$ mm, $a = 1.0$ mm, $b = 1.5$ mm, $c = 0.01$ mm, $\beta_e = 2.0$ s^{-1} and $\beta_c = 1.0$ s^{-1} and S remains an entrainment boundary.

We begin with a 0.1 J rectangular pulse which we split into 5, 10 and 20 rectangular micropulses with a 5 µs space between. The power over time for all four cases is plotted in Fig. 5.3.14. The volume, length and width — as defined in Sec. 5.3.2 — of the resulting bubbles

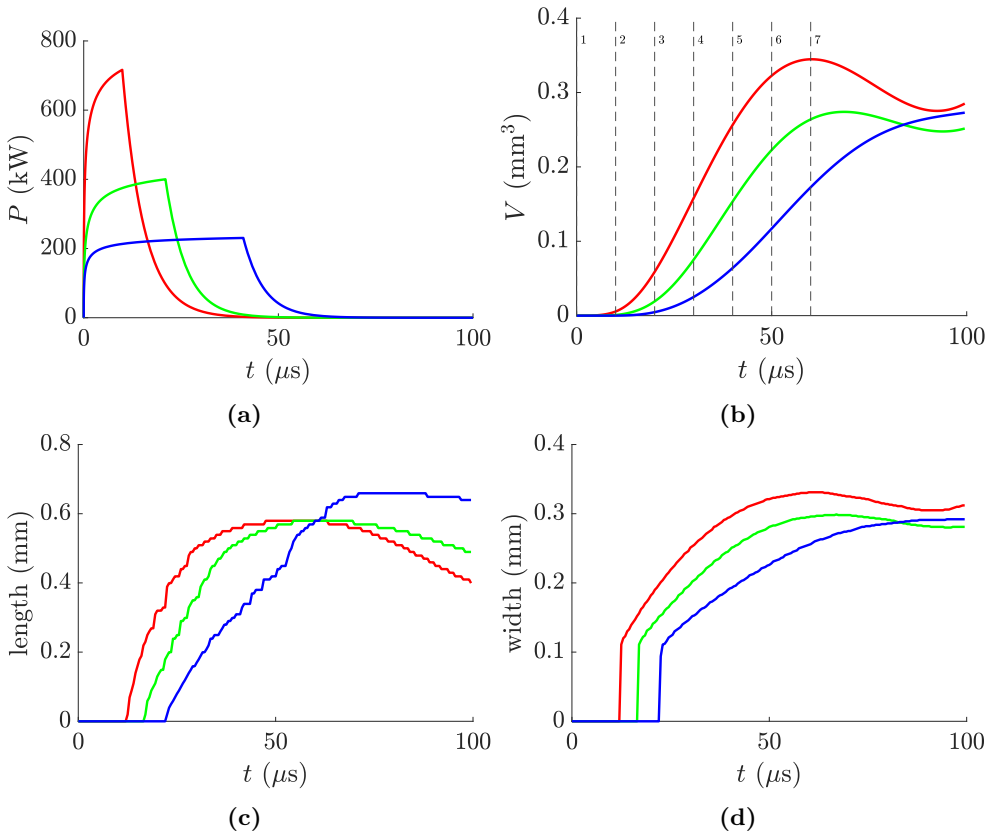


Figure 5.3.11 – (a) Power over time for three pulses used in the simulation detailed in Sec. 5.3.2. The resulting bubble (a) volume, (b) length and (c) width from the pulses in (a) is plotted in the corresponding colour. The dashed lines in (c) correspond to the times of the images in Fig. 5.3.9, which show the case of the red pulse.

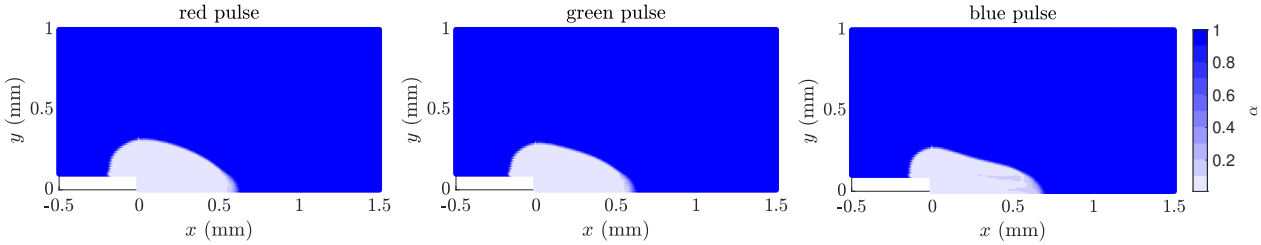


Figure 5.3.12 – The bubbles resulting from the pulses plotted in Fig. 5.3.11a shown at the time of maximum length.

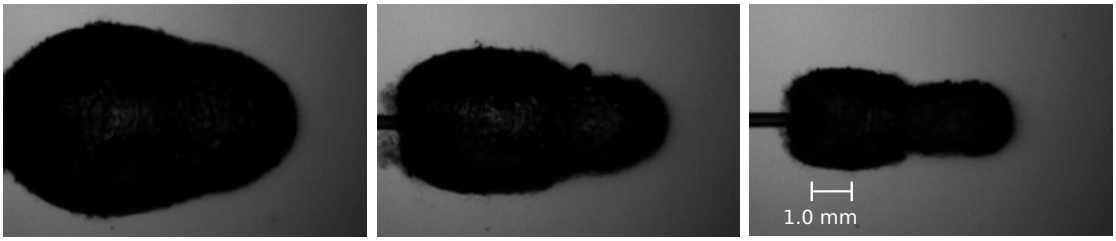


Figure 5.3.13 – The bubbles resulting from a P120 2.0 J (a) short, (b) medium and (c) long pulse, shown at the time of maximum length.

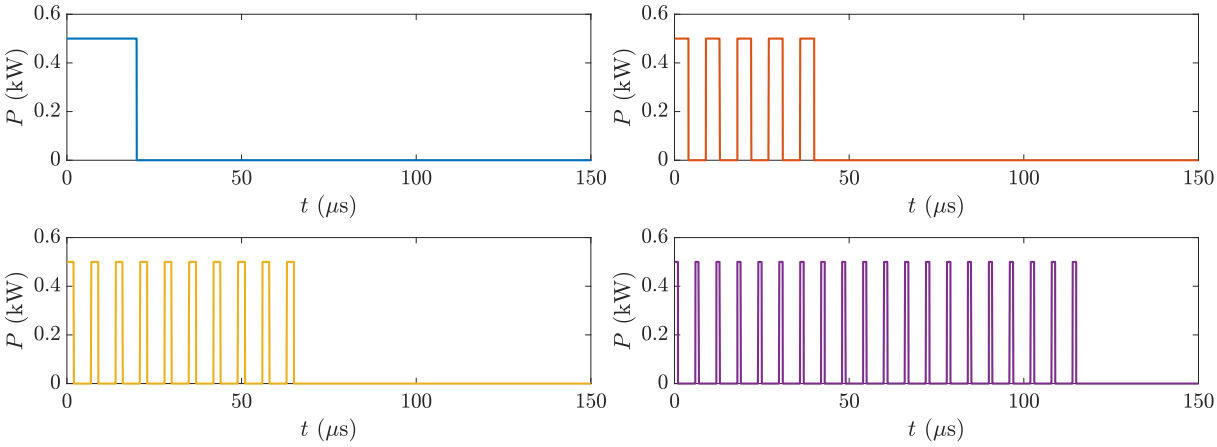


Figure 5.3.14 – Power over time for pulse packets used in the simulation detailed in Sec. 5.3.3.

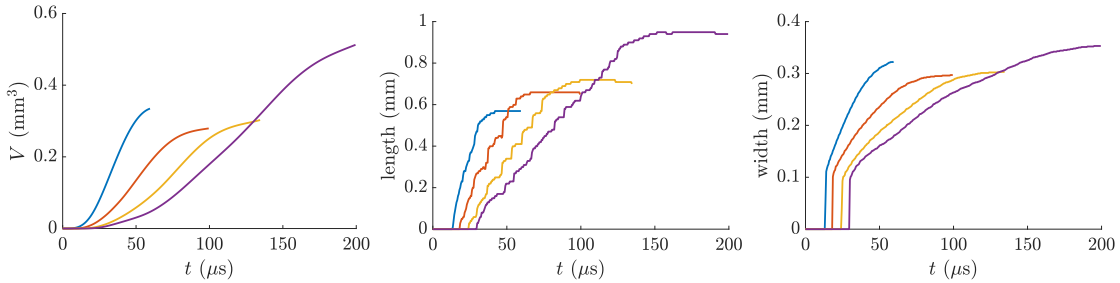


Figure 5.3.15 – (a) Bubble volume, (b) length and (c) width caused by the pulse packets shown in Fig. 5.3.14 in the corresponding colour. In this case S is an entrainment boundary.

are plotted in Fig. 5.3.15 in the corresponding colours. There is a clear correlation between the number of micropulses and the length of the bubble, which is expected due to the Moses effect. The time between the micropulses allows some expansion to occur, meaning that the energy of the subsequent micropulse passes a further distance from the fibre, heating and vaporising the liquid at the front edge of the bubble. There is a less clear correlation between number of micropulses and bubble volume or bubble width, although the bubble produced by the 20 pulse packet stands out with a noticeably larger volume and width.

5.3.4 Pulse packet with boundary

We run the simulations described in Sec. 5.3.3 again under the same conditions except for setting $b = 1.0$ and changing S to be a solid boundary. By doing this, we effectively introduce a thermally insulated wall at a distance of 1.0 mm from the fibre tip. This is done to investigate if the number of micropulses affects the temperatures generated on a solid boundary. We found above that the length of the bubble is correlated with number of micropulses and we hypothesise that via the Moses effect, a longer bubble will allow thermal energy to travel further, creating higher temperatures on the boundary.

The bubbles resulting from each of the four pulse packets for the case of S being a solid boundary are shown at their maximum length in Fig. 5.3.16. We plot the bubble length

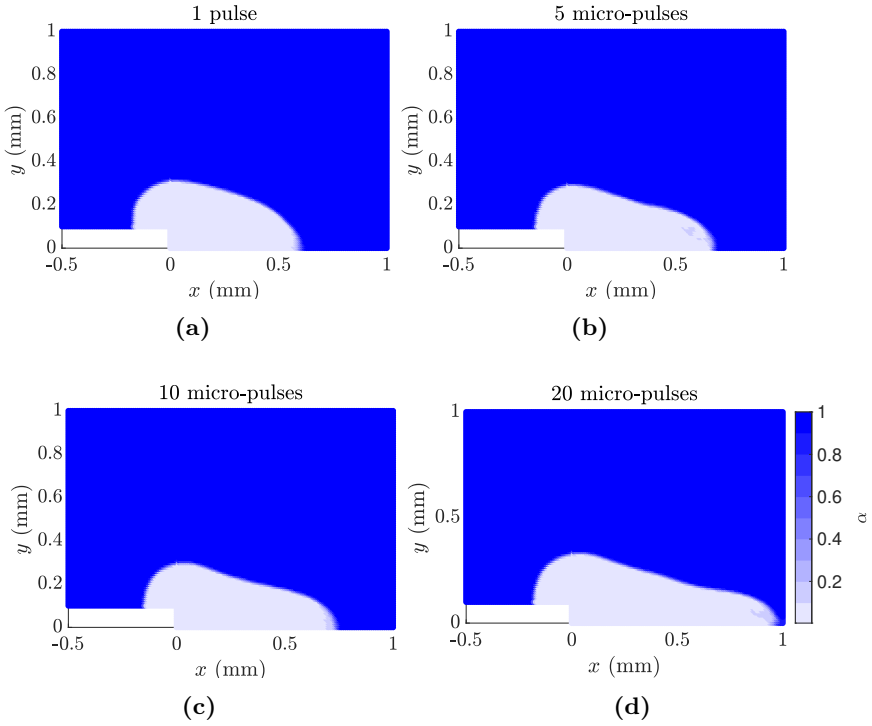


Figure 5.3.16 – The bubbles resulting from the pulses plotted in Fig. 5.3.14 shown at the time of maximum length. In these simulations, a solid boundary is located at $x = 1$ mm.

over time in Fig. 5.3.17a. This plot appears almost identical to Fig. 5.3.15b, suggesting that at 1.0 mm, the boundary does not significantly affect the bubble expansion. We also measure the maximum temperature on S over time, defining this temperature to be

$$T_{\max}(t) = \max_{y} \{T(x = b, y, t)\} . \tag{5.3.7}$$

For the four cases, $T_{\max}$ is plotted in Fig. 5.3.17b and we find that the peak temperature at the boundary is correlated to the number of micropulses, as predicted. The peak temperature on the boundary lies between 300 K and 320 K for the cases of 1, 5 and 10 pulses but rises up to approximately 380 K for the case of 20 pulses. The reason for the significantly higher temperature in the case of 20 pulses can be seen in Fig. 5.3.16. The bubble of the 20 pulse packet extends almost to $x = 1.0$ mm, creating a path for the laser energy to pass to the boundary. In the other three cases, there is at least 0.5 mm of liquid between the bubble and the boundary which absorbs some of the laser energy.

The work in this section forms a starting point for future investigations into pulse packets. We studied here just the number of micropulses in a packet but one could vary many other parameters.

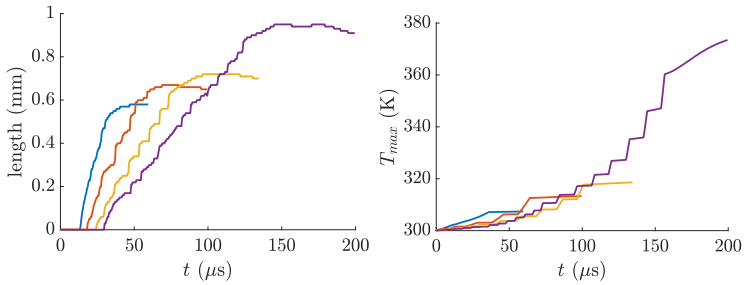


Figure 5.3.17 – (a) Bubble length and (c) $T_{\max}$ caused by the pulse packets shown in Fig. 5.3.14 in the corresponding colour. In this case S is a solid boundary.

5.4 Conclusion

In this chapter, we presented an interface capturing approach to bubble modelling, using a VOF method. The numerical solutions are relatively slow — taking a few minutes as opposed to a few seconds for the spherical model — due to the extra dimension as well as the modelling method. However, this model has a number of advantages over the spherical one. Primarily, the axisymmetric geometry closely reflects the reality of the fibre-bubble-stone geometry. The axisymmetry allows a reasonably faithful representation of the distribution of laser intensity within the fluid, which in turn gives a realistic pattern of fluid temperature and vapour formation, producing the elongated bubble form seen experimentally.

There are a number of limitations to the current model, although many of these could be overcome with further investigation. The first of these limitations is the upper-bound on the rate of phase change to maintain numerical convergence, which resulted in the low values of β_c and β_e and the scaled-down pulse powers in comparison to the P120 pulses. The simulated bubbles qualitatively reflected the bubbles seen experimentally but did not expand as quickly or as large due to the limited rate of phase change. This model also did not predict the collapse of the bubbles that, in the experimental observations, occurred on the same timescale as expansion. Bubble collapse occurs due to low pressure in the vapour when a bubble rapidly expands. It is likely that these low pressures did not occur in our simulations as the expansion was too gentle. This means that violent bubble collapse did not occur.

Another reason that the experimental and simulated bubbles may initially expand at different rates is due to the model neglecting the physics of laser-induced bubble nucleation. In the simulations that considered laser heating, Sec. 5.3.2 and Sec. 5.3.3, we began with a uniform, cool liquid. Nucleation occured in the simulation due the the effect of boiling. However, laser-induced bubble nucleation is known to be a complicated physical process that initiates explosive expansion.

A further problem with the numerical solutions is the region in which the phase fraction takes values larger than 0 and smaller than 1. The form of the governing equations of a VOF model relies on the assumption that the fluids are immiscible. Therefore a hard boundary exists

between the two phases and there should only be one numerical cell between a region that is $\alpha = 0$ and one that is $\alpha = 1$, as shown in Fig. 5.0.1. However, in the simulations that include phase change, for example that shown in Fig. 5.3.9b, there is a wide region at the front of the bubble in which $0 < \alpha < 1$. There are number of ways that this could be addressed, some of which are discussed in Section 6.2.

Two physical effects are neglected from the model in this chapter and could be included to improve the accuracy of the simulations. Firstly, the energy equation used by compressibleInterFoam does not account for the latent heat used or released when vaporisation or condensation occur. An additional source term could be introduced to Eq. (5.2.12) to model this energy change due to phase change and would be an interesting extension of the capabilities of this model. Secondly, the model in this chapter assumes that vaporisation occurs at a constant temperature whereas, in reality, the vaporisation temperature is pressure dependent, as discussed in the derivation of the interface tracking model in Sec. 3.2.2.

The results in Sec. 5.3 give some initial insight into the interaction of the laser, bubble and boundaries. These results show the potential for VOF modelling in optimising the lithotripsy process. After making some of the improvements discussed above, the model could be validated against both standard problems — for example, a linear Stefan problem [47] — and the experimental data presented in Chapter 2. A validated axisymmetric model would both support and reduce the need for experimental work. As we demonstrated, both the geometry and pulses can be manipulated to predict and understand the effect of the laser parameters and other variables. An obvious next step is to couple this fluid model to a kidney stone model, through which it could be determined how the pressures, velocities and temperatures generated by the laser and bubble result in stone breaking and retropulsion.

Chapter 6

Conclusion

The primary aim of this work was to develop an understanding of how the dynamics of a laser-induced bubble depend on the pulse shape, ultimately to inform the design and use of lasers for lithotripsy treatment of kidney stones. To achieve this, we derived two different models for a laser-induced vapour bubble as a function of a time dependent laser pulse. An initial understanding of the relationship between pulse parameters and bubble dynamics was obtained by generating and analysing experimental data. The mathematical models were also validated through comparison with these experimental results.

The experimental work was presented in Chapter 2. We recorded the pulse shapes of the P120 laser for all three single pulse types — short, medium and long — and the optical output of the laser was measured over a range of parameters. For a single short pulse, the peak power increased with the energy setting, ranging from 2 to 15 kW, while the pulse length varied only a little, from 200 to 300 µs. In contrast, the medium and long pulses varied more in length: 200 to 400 µs for medium and 200 to 500 µs for long. Apart from the lowest two energy settings, the medium pulses all had a similar peak power of approximately 8 kW and the long all had a similar peak power of approximately 5 kW. These results informed the pulse parameter ranges used in the models. High speed photography was used to record the bubbles produced by the same P120 pulses. We found that the short pulses produced approximately spherical bubbles with an aspect ratio of 2 or less. For medium and long pulses, which have a longer duration, the bubbles became more elongated with an aspect ratio up to 3 for medium and nearly 5 for long. As expected, pulse power correlated to both bubble size and time to maximum size.

Two models for a laser-induced vapour bubble in water were derived using two different approaches. Both models included the effects of phase change associated with vaporisation and condensation of the water. Unlike existing published work on laser-induced bubbles, it was necessary for us to model the effect of laser heating past the point of bubble nucleation. We achieved this by including a spatiotemporal heat source in the liquid region. The time dependence of the laser-induced fluid heating was an important aspect in modelling the bubbles that occur in lithotripsy because temporal distribution of the pulse energy is known to affect the size, shape and duration of the bubbles. Spatial dependence was also necessary as the localised laser heating causes spatial variations in liquid temperature, which results in localised phase change.

In Chapter 3, we presented a model for a spherically symmetric bubble using an interface tracking method. The model was first derived in 3D for the general case of two arbitrary fluid volumes, then reduced to 1D for the specific case of a spherical vapour bubble in liquid. With a further reduction, based on the assumption of a spatially uniform vapour pressure and temperature, we arrived at the commonly used Rayleigh-Plesset equation coupled to three further differential equations. Using this model, it was numerically straightforward and quick to investigate different pulse parameters and how they affected the bubble dynamics. In Chapter 4, we simulated bubbles produced by rectangular laser pulses with varying pulse

length, power and total energy. The power of the pulse determined the nucleation time of the bubble, with higher power pulses taking less time to heat the liquid and nucleate a bubble. We found that higher pulse energy results in a larger bubble and, in most cases, a bubble that takes longer to reach maximum volume. When varying pulse duration but with the pulse energy held constant, a bigger bubble was produced when the energy was concentrated into a shorter, higher power pulse, although there was little variation in the time taken to reach maximum size.

Chapter 4 included a mathematical analysis of the spherical model; studying the terms in the governing equations, we revealed the dominating physical effects at different stages of bubble expansion. Firstly, we looked at the time-scale on which the bubble accelerates from its initial size. This is the time-scale at which the pressure increases by an order 1 amount, overcoming surface tension and enabling expansion. The time-scale of this stage is not found to vary significantly across the clinically relevant range of pulse powers. Secondly, we looked at the behaviour on a dimensionless order 1 time-scale. At this time-scale, there is a balance of the vapour pressure being driven up by vaporisation of molecules at the boundary due to an the influx of laser energy, and the vapour pressure dropping due to bubble expansion. Finally, during the last stage of expansion, the bubble grows big enough that the effect of laser is negligible. This can be interpreted as the laser energy passing through the bubble and its immediate surroundings without significant absorption. The time-scale at which this final stage occurs is found to be dependent on the peak power of the laser. At this time-scale, the liquid temperature equation decouples from the vapour equations and the bubble is primarily expanding to maximum size under momentum. We found that this last stage of expansion is close to isothermal.

To tackle some of the limitations of the spherical model, we presented a second, axisymmetric model in Chapter 5. This model used an interface capturing approach called the volume of fluid (VOF) method. The computational fluid dynamics package OpenFOAM was utilised for this model as it has inbuilt phase change capabilities within the compressibleInterFoam solver that could be adapted for our system. We changed the phase change model from a pressure-based one to the temperature-based Lee model [49, 86]. The Lee model was simple to implement and reflects the physical relationship between the temperature of the fluid and the rate of phase change. A custom source term was added to the solver to model the effect of the laser. Using this model we ran three sets of simulations. Firstly, we studied the expansion and collapse of an initially high pressure vapour region, without the effect of laser heating and phase change but with a solid, insulated boundary in the position of a kidney stone. From this simulation, we showed that pressures and velocities on a solid boundary increase as the distance between the fibre and boundary is reduced. Secondly, now including laser heating and phase change, we simulated the bubbles produced by scaled down versions of P120 short, medium and long pulses. The results qualitatively reflected the bubbles seen experimentally. Finally, we studied the effect of splitting a laser pulse into a number of

micropulses. We found that splitting the energy into a greater number of smaller pulses resulted in a longer bubble, due to the Moses effect. When repeating this last simulation with a solid boundary 1 mm from the fibre, the longer bubble caused higher temperatures at the boundary.

The features and strengths of the two models are summarised in Table 6.0.1, and discussed in detail in the following section.

6.1 Model comparison

A comparison of the key features of the two models is summarised in Table. 6.0.1, and we will discuss each one in detail.

Modelling approach: The first model took the simplified case a spherical bubble, which lends itself to an interface tracking method. Interface tracking gives the exact location of the boundary, which is given by a single parameter in the case of 1D. Interface tracking can be utilised for 2D and 3D multi-phase modelling but the representation of the interface becomes complicated. When moving to axisymmetry for the second model, the interface capturing VOF method was an obvious choice as it has been employed previously in bubble modelling and, in particular, in laser-induced bubble modelling [46, 52]. With interface capturing methods, the exact location of the interface is not known and the interface is susceptible to numerical diffusion. However, these methods can handle more complex interface geometries as well as bubble breakup or multiple bubbles. As we showed in Sec. 5.3.1, solid, insulated boundaries can be introduced into the axisymmetric model, in place of the fibre and stone, to see how both the flow and boundaries are affected. It is not possible to introduce boundaries into the spherical model due to the inherent symmetry of the problem.

Ease of interpretation and solution: The spherical form meant that the reduced model was based around the Rayleigh-Plesset equation, which is well understood and interpretable. With just one spatial dimension, the equations were solved using the easily implemented method of lines. The simulations ran in just a few seconds, allowing us to quickly test and compare the impact of different laser pulses. The equations for the second model were not as straightforward to interpret, primarily as there is no explicit expression for the position of the bubble boundary. The asymmetric simulations also took longer to run that the spherical case, on the order of a few minutes, meaning it was less easy to analyse a wide range of laser parameters. The axisymmetric model could be extended to a fully 3D model, should asymmetric boundaries, for example, be of interest. The governing equations of this model are formulated in 3D so just a change of domain and boundary conditions in OpenFOAM would be necessary to move to 3D. However, the additional dimension would increase the computational time significantly.

	Spherical model	**Axisymmetric model**
Method	Interface tracking	Interface capturing
Interpretation of governing equations	Simple	Not simple
Solid boundaries	Not possible	Can be included
Spatial dependence of laser heating	Spherically symmetric	Linear (physically accurate)
Solution time on a standard laptop	Seconds	Minutes
Vapour pressure	Spatially uniform	Spatially dependent
Vapour temperature	Spatially uniform	Spatially dependent
Temperature of vaporisation	Pressure dependent based on Clausius-Clapeyron relation	Constant
Initial conditions	Approximate bubble nucleation	Uniform and cool
Rate of phase change	Scaled by fitting parameter α	Limited to ensure numerical convergence
Validation and fitting	Yes	No
Quantitative accuracy	Yes	No
Qualitative accuracy	No	Yes
Application to other lasers	Possible but adaptations to model necessary	Yes

Table 6.0.1 – An overview of the differences between the spherical model presented in Chapter 3 and the axisymmetric model presented in Chapter 5.

Vapour temperature and pressure: The simple form of the spherical model was dependent on the vapour pressure and temperature being spatially uniform within the bubble. From the size of the dimensionless parameter groups in Eq. (3.3.22) and Eq. (3.3.23), we know that spatial uniformity is a reasonable assumption for the vapour pressure but not necessarily for the vapour temperature. The axisymmetric model, however, does not place any restrictions on the vapour pressure and temperature and in the solutions of this model we do observe order 1 variations in temperature within the bubble, as shown in Fig. 5.3.9a. There are two considerations. Firstly, do leading order temperature gradients in the vapour exist? The bubble modelling of Prosperetti et al. shows significant temperature gradients only near the bubble wall and only as the bubble collapses to a minimum volume [26]. Secondly, do any leading order spatial temperature variations affect the bubble dynamics? Further modelling and investigation may be needed to confidently answer this but we can compare the spherical model, which neglects spatial temperature gradiaents, to the experimental data. We saw in Sec. 4.2 that the spherical model does recover the correct size and rate of expansion for bubbles that are approximately spherical, albeit after fitting to the data.

Laser heating source term: The inherent symmetry of the spherical model dictated the form of the laser source term. The function derived in Sec. 3.3.1 does reflect some of the key features of the laser and recovers the correct correlations between pulse parameters and bubble size and duration. However this spherical function could not accurately reflect the linear form of the path of the laser light. The axisymmetric form of the source term in the second model allowed us to represent the spatial variation of the laser intensity accurately, with a Gaussian distribution radially from the centre of fibre tip and with exponential decay along the axis away from the fibre tip, with heating and decay only in the liquid. This form gave localised heating and vaporisation at the front edge of the bubble, as observed experimentally.

Fitting and validation: Both models included two tuning parameters. In the spherical model, α adjusted the intensity of the laser, necessary due to approximating the laser heating as a spherically symmetric function, and β gave the nucleation time of the bubble. The maximum bubble size produced by the P120 short pulses was used to fit α and β to the experimental data. After fitting, the spherical model was found to give good predictions in the regime that the bubbles have an aspect ratio of two or less. We therefore have confidence in the predictions of this model for pulses that decay at approximately 200 µs, in which case the bubbles remain approximately spherical. For the medium and long pulses, which mostly have a duration longer than 200 µs, the spherical model does not give accurate quantitative results. This is not surprising since these pulses produce highly elongated bubbles that cannot be represented by spherical equations. However the spherical model does give the correct order of magnitude for bubble size and duration and the correct correlation between pulse energy and

both bubble size and duration for medium and long pulses. The spherical model could therefore be used to give a preliminary understanding about the effect on the bubble of a given pulse parameter, even for pulses longer than 200 µs.

The axisymmetric model was able to qualitatively capture the elongated shape that was observed experimentally. The parameters β_e and β_c in the axisymmetric model were used to control the rates of vaporisation and condensation respectively. It was necessary to choose sufficiently low values for these two parameters to ensure numerical convergence. For the same reason, it was necessary to scale down the pulse power in comparison to the P120 pulses. Due to the choice of β_e, β_c and pulse power, the axisymmetric model could not be directly compared to the experimental data and would not be expected to give results of the correct order of magnitude. This model has therefore not been fitted or validated against the data. However, unlike the spherical model, the axisymmetric model recovered the qualitative differences of the bubbles when the pulse energy was distributed differently. In particular, this model reflected the increased length and reduced width of the bubble when the energy is distributed over a longer period.

Initial conditions: The choice of initial conditions may be another factor in the discrepancy between the axisymmetric model and the experimental observations. In the simulations in Sec. 5.3.2 and Sec. 5.3.3, the model was initiated with a uniform, cool liquid, after which a bubble formed when the liquid became hot enough for phase change to occur. However, laser-induced bubble nucleation is thought to be more complicated than just simple phase change due to vaporisation, often including plasma formation, which triggers rapid, explosive expansion. We did not see the rate of expansion in the simulations that we would expect. The explosive expansion after bubble nucleation creates low pressure as the bubble reaches maximum size, causing subsequent bubble collapse. The collapse could therefore also not be accurately simulated in this model as low pressures were not generated, as discussed in Section 5.3.2. However, in the simulation shown in Section 5.3.1, which began with a bubble at high pressure, we did see explosive expansion and collapse. This suggests that a reconsideration of the initial conditions could help to improve this model. In contrast, the spherical model had carefully considered initial conditions to approximate bubble nucleation. The results of this model did show expansion and collapse on an accurate time and length scale.

Temperature of vaporisation: In the axisymmetric model, we made the simplification of a constant vaporisation temperature — the temperature at which phase change occurs — whereas in reality, the vaporisation temperature is pressure dependent. In the spherical model, the relationship between the vaporisation pressure and temperature was approximated by the commonly used Clausius-Clapeyron relation, with the bubble uniformly at vaporisation point.

Although the Clausius-Clapeyron relation is still a simplification of the physical relationship between vaporisation pressure and temperature, it is more accurate than setting a constant vaporisation temperature. We see from the numerical results of the spherical model that the vapour temperature varies by about 2 dimensionless units, which is approximately 120 K. A constant vaporisation temperature is therefore not considered to be a good assumption.

Application to other lasers: Both models considered only the P120 laser system. The type of laser, in this case holmium, determines the wavelength of light emitted and therefore the absorption coefficient, μ. Thulium lasers are beginning to be developed and used more recently in lithotripsy [6], so it would be beneficial to have a model that could be applied to different laser types. Simulating different lasers using the axisymmetric model would be as simple as changing the beam profile and the value of μ, provided that absorption in the vapour remains negligible. Should there be significant absorption in the vapour, the source term in the axisymmetric model could be adapted to use a volume averaged absorption coefficient. The spherical model could also, in theory, also be adapted by changing μ, provided absorption in the vapour remains negligible. However the non-dimensionalisation of this model is dependent on the absorption length $1/\mu$ so changing this parameter could invalidate the reduction of the model presented in Sec. 3.3.3. Furthermore, a change in μ would likely change the interpretation of the physical behavior as determined in Sec. 4.3.

6.2 Future work

Despite its simplifications, significant insight was gained from the spherical model. A mathematical analysis of the equations provided an understanding of the physics of laser-induced bubble expansion that has not been shown in the literature previously. This model could be utilised further by exploring a wider range of pulses shapes, rather than just rectangular pulses as was done in Sec. 4.4. Due to the quick run-time of the numerical solution, this model would be a useful tool for performing optimisation of laser parameters.

The axisymmetric model showed the potential of the VOF method in bubble modelling for kidney stone treatment, particularly as it can reflect the elongated bubble shapes seen. However, further development, fitting and validation is required before we can be confident that the model reflects the physical reality. Firstly, investigation is needed to overcome the limited rate of phase change required to ensure a stable solution; this limit to the rate of phase change is discussed in the literature but without resolution [49, 71]. Secondly, since the fluids are assumed to be immiscible, there should only be a narrow region one cell thick containing both liquid and vapour, however the numerical results show a wide region at the bubble wall where both fluids exist. This issue may be overcome by increasing the rate of phase change such that all the liquid in one cell is vaporised before the next cell becomes hot enough for vaporisation to occur. Other

possible approaches include: increasing the artificial compression of the boundary region, which is already implemented by OpenFOAM; 'snapping' α to 0 or 1 if the value is within a specified tolerance; or implementing a phase change model that acts only at the vapour-liquid interface. Thirdly, initial conditions could be derived, similar to those in the spherical mode, that trigger the explosive expansion seen experimentally. Fourthly, the model assumes that vaporisation occurs at a constant temperature whereas, in reality, the vaporisation temperature is pressure dependent. As with the spherical model, the Clausius-Clapeyron relation or an alternative could easily be introduced to give a pressure dependent vaporisation temperature. Finally, an important physical effect has been neglected in this model: the energy equation does not account for the latent heat used or released when vaporisation or condensation occur. In any further use of this model, an additional source term should be introduced to the energy equation model this energy change due to phase change. As well as being necessary to give accurate temperatures and rate of phase change, this source term may also overcome the first two issues in this list: the need for an artificial limit to phase change to ensure stability; and the unphysically wide region in which both liquid and vapour exist.

After making some of the improvements discussed above, fitting and validation should be performed. The model could be validated against both standard problems — for example, a linear Stefan problem [47] — and the experimental data presented in Chapter 2. Once validated, there is a lot of potential for aiding lithotripsy treatment. The pulses and packets studied in Chapter 5 are only a small sample of those that could be simulated. The pulse shapes can be varied infinitely as well as, amongst other things: the spacing between micropulses; the distribution of energy across the micropulses; and the peak power and duration of each micropulse.

It would be beneficial to couple this model to other models to simulate and optimise the whole process of lithotripsy. For example, the conditions on a solid boundary could be coupled to a thermomechanical stone model and the background flow could be coupled to a model of flow within the kidney such as that of Williams et al. [87].

References

[1] Nicole L. Miller and James E. Lingeman. Management of kidney stones. *British Medical Journal*, 334(7591):468–472, 2007. ISSN 09598146. doi: 10.1136/bmj.39113.480185.80.

[2] Hendrik Heers and Benjamin W. Turney. Trends in urological stone disease: a 5-year update of hospital episode statistics. *BJU International*, 118(5):785–789, 2016. ISSN 1464410X. doi: 10.1111/bju.13520.

[3] Harry W. Herr. 'Crushing the stone': A brief history of lithotripsy, the first minimally invasive surgery. *BJU International*, 102(4):432–435, 2008. ISSN 14644096. doi: 10.1111/j.1464-410X.2008.07639.x.

[4] Harry Reynolds. *Mathematical modelling of unsteady flows during ureteroscopy*. PhD thesis, University of Oxford, 2019.

[5] Jessica G. Williams. *Mathematical modelling of fluid flows during –ureteroscopic kidney stone removal*. PhD thesis, University of Oxford, 2019. URL `https://ora.ox.ac.uk/objects/uuid:c57503bf-e705-41ee-b0af-23176e3cfe19`.

[6] Peter Kronenberg and Bhaskar Somani. Advances in lasers for the treatment of stones—a systematic review. *Current Urology Reports*, 19(6), 2018. ISSN 15346285. doi: 10.1007/s11934-018-0807-y.

[7] Luke A. Hardy, Joshua D. Kennedy, Christopher R. Wilson, Pierce B. Irby, and Nathaniel M. Fried. Analysis of thulium fiber laser induced bubble dynamics for ablation of kidney stones. *Journal of Biophotonics*, 10(10):1240–1249, 2017. ISSN 18640648. doi: 10.1002/jbio.201600010.

[8] Peter Kronenberg and Olivier Traxer. MP22-13 burst laser lithotripsy – a novel lithotripsy mode. *Journal of Urology*, 195(4S):e258, 2016. ISSN 0022-5347. doi: 10.1016/j.juro.2016.02.701. URL `http://dx.doi.org/10.1016/j.juro.2016.02.701`.

[9] Kristian M. Black, Ali H. Aldoukhi, and Khurshid R. Ghani. A users guide to holmium laser lithotripsy settings in the modern era. *Frontiers in Surgery*, 6:1–3, 2019. ISSN 2296875X. doi: 10.3389/fsurg.2019.00048.

[10] Eugenio Ventimiglia and Olivier Traxer. What is Moses effect: A historical perspective. *Journal of Endourology*, 33(5):353–357, 2019. ISSN 1557900X. doi: 10.1089/end.2019.0012.

[11] Ayaka Tamura, Ayumu Matsumoto, Kazuhiro Fukami, Naoya Nishi, and Tetsuo Sakka. Simultaneous observation of nascent plasma and bubble induced by laser ablation in water

with various pulse durations. *Journal of Applied Physics*, 117(17), 2015. ISSN 10897550. doi: 10.1063/1.4919729.

[12] S. Sh Rekhviashvili. Single-bubble sonoluminescence model. *Technical Physics Letters*, 34 (12):1072–1074, 2008. ISSN 10637850. doi: 10.1134/S1063785008120250.

[13] Milton S. Plesset and Richard B. Chapman. Collapse of an initially spherical vapour cavity in the neighbourhood of a solid boundary. *Journal of Fluid Mechanics*, 47(2):283–290, 1971. ISSN 14697645. doi: 10.1017/S0022112071001058.

[14] J. R. Blake and D. C. Gibson. Cavitation Bubbles Near Boundaries. *Annual Review of Fluid Mechanics*, 19:99–123, 1987. ISSN 00664189. doi: 10.1146/annurev.fluid.19.1.99.

[15] Outi Supponen, Danail Obreschkow, Philippe Kobel, and Mohamed Farhat. Detailed jet dynamics in a collapsing bubble. *Journal of Physics: Conference Series*, 656(1):1–5, 2015. ISSN 17426596. doi: 10.1088/1742-6596/656/1/012038.

[16] Ali H. Aldoukhi, William W. Roberts, Timothy L. Hall, and Khurshid R. Ghani. Watch your distance: The role of laser fiber working distance on fragmentation when altering pulse width or modulation. *Journal of Endourology*, 33(2):120–126, 2019. ISSN 1557900X. doi: 10.1089/end.2018.0572.

[17] Milton S. Plesset and Andrea Prosperetti. Bubble dynamics and cavitation erosion. *Annual Review of Fluid Mechanics*, pages 145–185, 1977.

[18] M. S. Plesset and S. A. Zwick. The growth of vapor bubbles in superheated liquids. *Journal of Applied Physics*, 25(4):493–500, 1954. ISSN 00218979. doi: 10.1063/1.1721668.

[19] Lord Rayleigh. VIII. On the pressure developed in a liquid during the collapse of a spherical cavity . *The London, Edinburgh, and Dublin Philosophical Magazine and Journal of Science*, 34(200):94–98, 1917. ISSN 1941-5982. doi: 10.1080/14786440808635681.

[20] A. Lezzi. Bubble dynamics in a compressible liquid. Part 1. First-order theory. *Journal of Fluid Mechanics*, 168:457–478, 1986. ISSN 14697645. doi: 10.1017/S0022112086000460.

[21] A. Prosperetti and A. Lezzi. Bubble dynamics in a compressible liquid. Part 2. Second-order theory. *Journal of Fluid Mechanics*, 185:289–321, 1987. ISSN 14697645. doi: 10.1017/S0022112087003185.

[22] Joseph B. Keller and Michael Miksis. Bubble oscillations of large amplitude. *Journal of the Acoustical Society of America*, 68(2):628–633, 1980. ISSN NA. doi: 10.1121/1.384720.

[23] Nikolay A. Kudryashov and Dmitry I. Sinelshchikov. Analytical solutions of the Rayleigh equation for empty and gas-filled bubble. *Journal of Physics A: Mathematical and Theoretical*, 47(40):1–12, 2014. ISSN 17518121. doi: 10.1088/1751-8113/47/40/405202.

[24] Ali F. Abu-Bakr and Aly M. Abourabia. The Cole-Hopf transformation for solving Rayleigh-Plesset equation in bubble dynamics. *Advances in Modelling and Analysis A*, 55(2):82–87, 2018. ISSN 12585769. doi: 10.18280/ama_a.550207.

[25] H. G. Flynn. Cavitation dynamics. i. a mathematical formulation. *Journal of the Acoustical Society of America*, 57(6):1379–1396, 1975. ISSN NA. doi: 10.1121/1.380624.

[26] Andrea Prosperetti, Lawrence A. Crum, and Kerry W. Commander. Nonlinear bubble dynamics. *Journal of the Acoustical Society of America*, 83(2):502–514, 1988. ISSN NA. doi: 10.1121/1.396145.

[27] Y. Hao and A. Prosperetti. The dynamics of vapor bubbles in acoustic pressure fields. *Physics of Fluids*, 11(8):2008–2019, 1999. ISSN 10706631. doi: 10.1063/1.870064.

[28] I. Akhatov, O. Lindau, A. Topolnikov, R. Mettin, N. Vakhitova, and W. Lauterborn. Collapse and rebound of a laser-induced cavitation bubble. *Physics of Fluids*, 13(10): 2805–2819, 2001. ISSN 10706631. doi: 10.1063/1.1401810.

[29] Alexander A. Doinikov, Paul S. Sheeran, Ayache Bouakaz, and Paul A. Dayton. Vaporization dynamics of volatile perfluorocarbon droplets: A theoretical model and in vitro validation. *Medical Physics*, 41(10):1–10, 2014. ISSN 24734209. doi: 10.1118/1.4894804.

[30] Matthieu Guédra and François Coulouvrat. A model for acoustic vaporization of encapsulated droplets. *The Journal of the Acoustical Society of America*, 138(6):3656–3667, 2015. ISSN 0001-4966. doi: 10.1121/1.4937747.

[31] Wafaa Soliman, Tetsutaro Nakano, Noriharu Takada, and Koichi Sasaki. Modification of Rayleigh-Plesset theory for reproducing dynamics of cavitation bubbles in liquid-phase laser ablation. *Japanese Journal of Applied Physics*, 49(11), 2010. ISSN 00214922. doi: 10.1143/JJAP.49.116202.

[32] A. De Bonis, M. Sansone, L. D'Alessio, A. Galasso, A. Santagata, and R. Teghil. Dynamics of laser-induced bubble and nanoparticles generation during ultra-short laser ablation of Pd in liquid. *Journal of Physics D: Applied Physics*, 46(44), 2013. ISSN 00223727. doi: 10.1088/0022-3727/46/44/445301.

[33] G. Sinibaldi, A. Occhicone, F. Alves Pereira, D. Caprini, L. Marino, F. Michelotti, and C. M. Casciola. Laser induced cavitation: Plasma generation and breakdown shockwave. *Physics of Fluids*, 31(10), 2019. ISSN 10897666. doi: 10.1063/1.5119794. URL `https://doi.org/10.1063/1.5119794`.

[34] Ki Taek Byun and Ho Young Kwak. A Model of laser-induced cavitation. *Japanese Journal of Applied Physics, Part 1: Regular Papers and Short Notes and Review Papers*, 43(2):621–630, 2004. ISSN 00214922. doi: 10.1143/JJAP.43.621.

[35] Sheguang Zhang and James H. Duncan. On the nonspherical collapse and rebound of a cavitation bubble. *Physics of Fluids*, 6(7):2352–2362, 1994. ISSN 10706631. doi: 10.1063/1.868185.

[36] R. P. Tong. A new approach to modelling an unsteady free surface in boundary integral methods with application to bubble-structure interactions. *Mathematics and Computers in Simulation*, 44(4):415–426, 1997. ISSN 03784754. doi: 10.1016/s0378-4754(97)00067-0.

[37] E. Klaseboer, K. C. Hung, C. Wang, C. W. Wang, B. C. Khoo, P. Boyce, S. Debono, and Herve Charlier. Experimental and numerical investigation of the dynamics of an underwater

explosion bubble near a resilient/rigid structure. *Journal of Fluid Mechanics*, 537:387–413, 2005. ISSN 00221120. doi: 10.1017/S0022112005005306.

[38] J. R. Blake. The Kelvin impulse: application to cavitation bubble dynamics. *The Journal of the Australian Mathematical Society. Series B. Applied Mathematics*, 30(2):127–146, 1988. ISSN 0334-2700. doi: 10.1017/s0334270000006111.

[39] John R. Blake, David M. Leppinen, and Qianxi Wang. Cavitation and bubble dynamics: The Kelvin impulse and its applications. *Interface Focus*, 5(5):1–15, 2015. ISSN 20428901. doi: 10.1098/rsfs.2015.0017.

[40] Outi Supponen, Danail Obreschkow, Marc Tinguely, Philippe Kobel, Nicolas Dorsaz, and Mohamed Farhat. Scaling laws for jets of single cavitation bubbles. *Journal of Fluid Mechanics*, 802:263–293, 2016. ISSN 14697645. doi: 10.1017/jfm.2016.463.

[41] D A Drew. Mathematical modeling of two-phase flow. *Annual Review of Fluid Mechanics*, 1983.

[42] Richard Saurel and Rémi Abgrall. A multiphase godunov method for compressible multifluid and multiphase flows. *Journal of Computational Physics*, 150(2):425–467, 1999. ISSN 00219991. doi: 10.1006/jcph.1999.6187.

[43] Ali Zein, Maren Hantke, and Gerald Warnecke. Modeling phase transition for compressible two-phase flows applied to metastable liquids. *Journal of Computational Physics*, 229(8): 2964–2998, 2010. ISSN 10902716. doi: 10.1016/j.jcp.2009.12.026. URL `http://dx.doi.org/10.1016/j.jcp.2009.12.026`.

[44] Ali Zein, Maren Hantke, and Gerald Warnecke. On the modeling and simulation of a laser-induced cavitation bubble. *International Journal for Numerical Methods in Fluids*, 73(2): 172–203, 2013. ISSN 02712091. doi: 10.1002/fld.3796.

[45] Grétar Tryggvason, Ruben Scardovelli, and Stéphane Zaleski. the volume-of-fluid method. In *Direct numerical simulations of gas-liquid multiphase flows*, chapter 5, pages 95–132. Cambridge University Press, Cambridge, 2011.

[46] Mahdi Nabil and Alexander S. Rattner. interThermalPhaseChangeFoam—A framework for two-phase flow simulations with thermally driven phase change. *SoftwareX*, 5:216–226, 2016. ISSN 23527110. doi: 10.1016/j.softx.2016.10.002. URL `http://dx.doi.org/10.1016/j.softx.2016.10.002`.

[47] Nima Samkhaniani and MohamadReza Ansari. A VOF method to phase change modeling. *Proceedings of 1st Iranian Conference on Heat and Mass Transfer-ICHMT2012*, 2(October): 1–9, 2012.

[48] Christiane Lechner, Max Koch, Werner Lauterborn, and Robert Mettin. Pressure and tension waves from bubble collapse near a solid boundary: A numerical approach. *The Journal of the Acoustical Society of America*, 142(6):3649–3659, 2017. ISSN 0001-4966. doi: 10.1121/1.5017619. URL `http://dx.doi.org/10.1121/1.5017619`.

[49] Xiaojun Shi, Kai Zheng, and Bangtao Yin. Numerical method for gas-liquid two-phase flow with phase change heat transfer considering compressibility using OpenFOAM. *International Journal of Thermal Sciences*, 188(May 2022):108195, 2023. ISSN 12900729. doi: 10.1016/j.ijthermalsci.2023.108195. URL `https://doi.org/10.1016/j.ijthermalsci.2023.108195`.

[50] Siegfried Müller, Mathieu Bachmann, Dennis Kröninger, Thomas Kurz, and Philippe Helluy. Comparison and validation of compressible flow simulations of laser-induced cavitation bubbles. *Computers and Fluids*, 38(9):1850–1862, 2009. ISSN 00457930. doi: 10.1016/j.compfluid.2009.04.004.

[51] Hemant J. Sagar and Ould el Moctar. Numerical simulation of a laser-induced cavitation bubble near a solid boundary considering phase change. *Ship Technology Research*, 65(3): 163–179, 2018. ISSN 20567111. doi: 10.1080/09377255.2018.1473235.

[52] Max Koch, Christiane Lechner, Fabian Reuter, Karsten Köhler, Robert Mettin, and Werner Lauterborn. Numerical modeling of laser generated cavitation bubbles with the finite volume and volume of fluid method, using OpenFOAM. *Computers and Fluids*, 126:71–90, 2016. ISSN 00457930. doi: 10.1016/j.compfluid.2015.11.008.

[53] Xiaoxu Zhong, Javad Eshraghi, Pavlos Vlachos, Sadegh Dabiri, and Arezoo M. Ardekani. A model for a laser-induced cavitation bubble. *International Journal of Multiphase Flow*, 132:103433, nov 2020. ISSN 03019322. doi: 10.1016/j.ijmultiphaseflow.2020.103433.

[54] P. Koukouvinis, M. Gavaises, O. Supponen, and M. Farhat. Numerical simulation of a collapsing bubble subject to gravity. *Physics of Fluids*, 28(3), 2016. ISSN 10897666. doi: 10.1063/1.4944561. URL `http://dx.doi.org/10.1063/1.4944561`.

[55] Xuning Zhao, Wentao Ma, Junqin Chen, Gaoming Xiang, Pei Zhong, and Kevin Wang. Long-pulse laser-induced cavitation: A race between advection and phase transition. pages 1–36, 2023. URL `http://arxiv.org/abs/2308.11866`.

[56] Mostafa M. Elhilali, Shadie Badaan, Ahmed Ibrahim, and Sero Andonian. Use of the Moses technology to improve holmium laser lithotripsy outcomes: A preclinical study. *Journal of Endourology*, 31(6):598–604, 2017. ISSN 1557900X. doi: 10.1089/end.2017.0050.

[57] Eugenio Ventimiglia, Steeve Doizi, Anastasiya Kovalenko, Viktoria Andreeva, and Olivier Traxer. Effect of temporal pulse shape on urinary stone phantom retropulsion rate and ablation efficiency using holmium:YAG and super-pulse thulium fibre lasers. *BJU International*, 126(1):159–167, 2020. ISSN 1464410X. doi: 10.1111/bju.15079.

[58] Milad Mohammadzadeh, Julian Martinez Mercado, and Claus Dieter Ohl. Bubble dynamics in laser lithotripsy. *Journal of Physics: Conference Series*, 656(1):8–12, 2015. ISSN 17426596. doi: 10.1088/1742-6596/656/1/012004.

[59] British Standards Institute. BS EN IEC 60601-2-22:2020 Medical electrical equipment. Particular requirements for basic safety and essential performance of surgical, cosmetic,

therapeutic and diagnostic laser equipment, 2020. URL https://bsol.bsigroup.com/PdfViewer/Viewer?pid=000000000030329829.

[60] Daniel D. Joseph. Equations of Motion. In *Studies in Applied Mechanics*, volume 28, chapter 3, pages 225–232. Springer-Verlag, New York; London, 1992. doi: 10.1016/B978-0-444-98700-6.50019-6.

[61] M. S. Plesset. Physical effects in cavitation and boiling. *Symposium on Naval Hydrodynamics (1st : 1956 : Washington, D.C.)*, pages 297–317, 1957.

[62] Christopher Earls Brennen. Cavitation and bubble dynamics. In *Cavitation and bubble dynamics*, chapter 2. Cambridge University Press, Cambridge, 2003. ISBN 0195094093.

[63] William M. Haynes, David R. Lide, and Thomas J. Bruno, editors. *CRC handbook of chemistry and physics*, volume 268. CRC Press, Boca Raton, Florida, 97 edition, 1992. doi: 10.1016/0022-2860(92)85083-s.

[64] M. S. Plesset and S. A. Zwick. A nonsteady heat diffusion problem with spherical symmetry. *Journal of Applied Physics*, 23(1):95–98, 1952. ISSN 00218979. doi: 10.1063/1.1701985.

[65] P. M. Dew and J. E. Walsh. A set of library routines for solving parabolic equations in one space variable. *ACM Transactions on Mathematical Software (TOMS)*, 7(3):295–314, 1981. ISSN 15577295. doi: 10.1145/355958.355962.

[66] Sang Joon Ahn and Oh Joon Kwon. Numerical investigation of cavitating flows for marine propulsors using an unstructured mesh technique. *International Journal of Heat and Fluid Flow*, 43:259–267, 2013. ISSN 0142727X. doi: 10.1016/j.ijheatfluidflow.2013.05.007. URL http://dx.doi.org/10.1016/j.ijheatfluidflow.2013.05.007.

[67] The OpenFOAM Foundation. compressibleInterFoam.C File Reference, 2021. URL https://cpp.openfoam.org/v9/compressibleInterFoam{_}8C.html{#}details.

[68] The OpenFOAM Foundation. OpenFOAM v9. source code, 2021. URL https://openfoam.org/.

[69] The OpenFOAM Foundation. OpenFOAM dev: C++ Source Code Guide, 2022. URL https://cpp.openfoam.org/dev/.

[70] OpenCFD Ltd. Hydrostatic pressure effects, 2018. URL https://www.openfoam.com/documentation/guides/latest/doc/guide-applications-solvers-variable-transform-p-rgh.html.

[71] Z. Yang, X. F. Peng, and P. Ye. Numerical and experimental investigation of two phase flow during boiling in a coiled tube. *International Journal of Heat and Mass Transfer*, 51 (5-6):1003–1016, 2008. ISSN 00179310. doi: 10.1016/j.ijheatmasstransfer.2007.05.025.

[72] Yuanwei Cao and Rafael Macián-Juan. Numerical investigation of vapor bubble condensation in subcooled quiescent water. *Nuclear Engineering and Design*, 388(December 2021), 2022. ISSN 00295493. doi: 10.1016/j.nucengdes.2021.111621.

[73] Boundaries. URL https://www.openfoam.com/documentation/user-guide/4-mesh-generation-and-conversion/4.2-boundaries.

[74] Openfoam. Standard boundary conditions, 2016. URL http://www.openfoam.com/documentation/user-guide/standard-boundaryconditions.php.

[75] Zhang Shi, Yi Zhang, Mingchao Liu, Dorian A.H. Hanaor, and Yixiang Gan. Dynamic contact angle hysteresis in liquid bridges. *Colloids and Surfaces A: Physicochemical and Engineering Aspects*, 555(April):365–371, 2018. ISSN 18734359. doi: 10.1016/j.colsurfa.2018.07.004. URL https://doi.org/10.1016/j.colsurfa.2018.07.004.

[76] Chris Greenshields. Derived boundary conditions, 2023. URL https://doc.cfd.direct/openfoam/user-guide-v11/derived-boundary-conditions.

[77] Chris Greenshields and Henry Weller. Total pressure condition, 2022. URL https://doc.cfd.direct/notes/cfd-general-principles/total-pressure-conditions.

[78] OpenCFD Ltd. prghTotalPressure, 2023. URL https://doc.openfoam.com/2306/tools/processing/boundary-conditions/rtm/derived/general/prghTotalPressure/.

[79] Joel Guerrero. Crash introduction to the FVM, 2019. URL https://wiki.openfoam.com/Theory{_}by{_}Joel{_}Guerrero.

[80] OpenCFD Ltd. The PIMPLE algorithm in OpenFOAM, 2018. URL https://openfoamwiki.net/index.php/OpenFOAM{_}guide/The{_}PIMPLE{_}algorithm{_}in{_}OpenFOAM.

[81] Chris Greenshields and Henry Weller. The PIMPLE algorithm, 2022. URL https://doc.cfd.direct/notes/cfd-general-principles/the-pimple-algorithm{#}x153-20100021.

[82] Chris Greenshields and Henry Weller. Transient solution, 2022. URL https://doc.cfd.direct/notes/cfd-general-principles/transient-solution{#}x150-19700019.

[83] Chris Greenshields and Henry Weller. Steady-state solution, 2022. URL https://doc.cfd.direct/notes/cfd-general-principles/steady-state-solution{#}x139-18400012.

[84] PISO, 2014. URL https://openfoamwiki.net/index.php/PISO.

[85] OpenFOAMWiki. OpenFOAM guide/The SIMPLE algorithm in OpenFOAM (date accessed: 07.02.2020), 2020. URL https://openfoamwiki.net/index.php/OpenFOAM{_}guide/The{_}SIMPLE{_}algorithm{_}in{_}OpenFOAM.

[86] Hayat El Baamrani, Lahcen Bammou, Ahmed Aharoune, and Abdallah Boukhris. Volume of fluid (VOF) modeling of liquid film evaporation in mixed convection flow through a vertical channel. *Mathematical Problems in Engineering*, 2021, 2021. ISSN 15635147. doi: 10.1155/2021/9934593.

[87] J. G. Williams, L. Goldsmith, D. E. Moulton, S. L. Waters, and B. W. Turney. A temperature model for laser lithotripsy. *World Journal of Urology*, 39(6):1707–1716, 2020. ISSN 14338726. doi: 10.1007/s00345-020-03357-y. URL https://doi.org/10.1007/s00345-020-03357-y.

Appendix A

Parameter values

All physical parameter values are given for water in SI units. Where helpful for clarity, the Chapter in which a parameter appears is given.

Symbol	**Definition**	**Value**
b	Specific gas constant of vapour	460 J Kg^{-1} K^{-1}
$c_{p,l}$	Specific heat capacity at constant pressure of liquid	3.8×10^3 J Kg^{-1} K^{-1}
$c_{p,v}$	Specific heat capacity at constant pressure of vapour	1.9×10^3 J Kg^{-1} K^{-1}
$c_{V,l}$	Specific heat capacity at constant volume of liquid	4.2×10^3 J Kg^{-1} K^{-1}
$c_{V,v}$	Specific heat capacity at constant volume of vapour	1.9×10^3 J Kg^{-1} K^{-1}
K_l	Thermal conductivity of liquid	0.62 W m^{-1} K^{-1}
K_v	Thermal conductivity of vapour	2.5×10^{-2} W m^{-1} K^{-1}
L	Latent heat of vaporisation	2.3×10^6 J kg^{-1}
$p_v^*(t_{\mathrm{nucl}}^*)$	Dimensionless vapour pressure at time of nucleation	2.4
p_∞	Far-field pressure	10^5 Pa
R_{nucl}^*	Dimensionless radius at time of nucleation	5×10^{-3}
$\dot{R}(t_{\mathrm{nucl}}^*)$	Dimensionless velocity of bubble wall at time of nucleation	0.0

Symbol	Definition	Value
T^*_{nucl}	Dimensionless vapour temperature at which nucleation occurs	6.3
$T_{\text{vap},\infty}$	Vaporisation temperature at far-field pressure in Chapters 3 and 4	373 K
T_{vap}	Vaporisation temperature in Chapter 5	400 K
T_∞	Far-field temperature	310 K
T^*_∞	Dimensionless far-field temperature	3.5
α	Fitting parameter in Chapters 3 and 4	0.2
β	Fitting parameter	2.7
ϵ_p	Dimensionless parameter group, $1/(\Theta b \tau^2 \mu^2)$	3.4×10^{-3}
ϵ_T	Dimensionless parameter group, $c_{p,v} p_\infty/(K_v \tau \Theta b \mu^2)$	Taken as $\leq \epsilon_p$
Θ	Reference temperature, $T_{\text{vap}} - T_\infty$	88 K
λ_1	Dimensionless parameter group, $K_l \tau \mu^2/(c_{p,l}\rho_l)$	1.5×10^{-4}
λ_2	Dimensionless parameter group, $P_{\max}\mu^3\tau/(4\pi\Theta\rho_l c_{p,l})$	$1 - 10$ for clinically relevant parameters
λ_3	Dimensionless parameter group, $b\Theta/L$	1.3×10^{-2}
λ_4	Dimensionless parameter group, $2\sigma\mu/p_\infty$	7.0×10^{-3}
λ_5	Dimensionless parameter group, $K_l\Theta\tau\mu^2/p_\infty$	0.2
μ	Absorption coefficient of 2100 nm light in liquid	5.0×10^3 m^{-1}
ρ_l	Density of liquid	10^3 kg m^{-3}
σ	Coefficient of surface tension between liquid and vapour	2.0×10^{-5} s
τ	Reference time, $\tau := \sqrt{\rho_l/(p_\infty\mu^2)}$, in Chapters 3 and 4	2.0